

An Experimental and Numerical Investigation on Strengthening the Upright Component of Thin- Walled Cold-Formed Steel Rack Structures

Ehsan Taheri

A thesis submitted to fulfil the requirements of the degree of
Doctor of Philosophy

Centre for Infrastructure Engineering (CIE)

WESTERN SYDNEY
UNIVERSITY



October 2021

Copyright 2021, Ehsan Taheri. This document is copyrighted material. Under copyright law, no parts of this document may be reproduced without the expressed permission of the author.

Abstract

Cold-formed steel (CFS) racking systems are widely used for storing products in warehouses. However, as commonly used structures in storage systems, thin-walled open sections are subjected to stability loss because of various buckling modes, including flexural, local, torsional and distortional. This research proposes a novel technique to increase the ultimate capacity of uprights, utilising bolts and spacers, under flexural and compressive loads. The proposed components are attached externally to the sections in certain pitches along the length. In this regard, axial tests were performed on 72 upright frames and nine single uprights with various lengths and thicknesses. Also, the impact of using reinforcing elements was evaluated by investigating the failure modes and ultimate load results. It was concluded that the reinforcement technique is able to restrain upright flanges and therefore improve the upright profiles' strength.

For testing the flexural behaviour, 18 samples of three types were made, including non-reinforced sections and two types of sections reinforced along the upright length at different pitches. After that, monotonic loading was applied along both the minor and major axes of the samples. The suggested reinforcing method leads to increasing the flexural capacity of the upright sections about both the major and minor axes. Also, by using reinforcing system, the flexural performance was improved, and buckling and deformation were constrained.

In addition, the reinforcement technique was evaluated by Finite Element (FE) method. Moreover, Artificial Intelligence (AI) and Machine Learning (ML) algorithms were deployed to predict the normalised ultimate load and deflection of the profiles.

Following the empirical tests, the axial and flexural performance of different CFS upright profiles with various lengths, thicknesses and reinforcement spacings were simulated and examined. Finite element (FE) method was utilised to assess the proposed reinforcement technique in various upright profiles and produce a verified database for the analytical study. Also, in order to determine the most influential parameter on the strength, the Feature Selection technique was carried out on the results of FEM. Then, to predict the normalised ultimate load, by feature selection method, a hybrid AI network, which was a combination of Multi-Layer Perceptron (MLP) algorithm and Particle Swarm Optimisation method (PSO) was developed. The correlation coefficient (R), root mean square error (RMSE), Nash–Sutcliffe efficiency (NSE), mean absolute error (MAE) and

Wilmot's index of agreement (WI) are employed as the measure of accuracy. It was indicated that the geometrical parameters contribute to the capacity and deflection of the specimens. Based on the performance evaluation criteria, the detection and optimisation process for the best model were performed through tuning other algorithm parameters. Obtained results showed that the normalised ultimate load and deflection could be predicted using the hybrid intelligent model.

Finally, it was shown that the reinforcing technique improved the capacity of the samples. Consequently, the proposed reinforcements could be considered a highly effective and low-cost technique to strengthen the axial and flexural behaviour of open CFS sections considering a trade-off between performance and cost of utilising the approach.

Acknowledgment

I would like to express my sincere gratitude to my supervisor Prof. Bijan Samali for his patience, motivation, and immense knowledge. He unconditionally helped me academically, personally, and spiritually. He believed in me at the beginning of my journey and gave me the opportunity to start my PhD. I had his ongoing guidance, support and encouragement during my candidature; no words can express my appreciation.

I would also like to acknowledge Dr Ahmad Firouzianhaji, and Mr Reza Bani Ardalan who I am gratefully indebted to for their precious guidance and support in this research.

I want to extend my gratitude to the Centre for Infrastructure Engineering (CIE) and School of Engineering, Design and Built Environment at Western Sydney University for giving me the opportunity and the funds to explore my area of interest and present my findings in distinguished journals and conferences.

I would also like to convey my thanks to the Western Sydney University Laboratories staff, and Dexion Australia who kindly supported me in the project's experimental stages.

I should extend my most profound appreciation to my family for their unconditional, deep and genuine love, without whom I would not be here. To my mum for her dedication, infinite love, and compassion. To my dad for his ever-present support, patience, motivation, and encouragement. To my sister and brother for their emotional support and always being there for me. To my parents-in-law for providing me with unfailing support and continuous encouragement throughout my years of study.

Last but not least, I would like to extend my warmest gratitude to my wife, Nasim, for her unconditional love and support and putting up with me being tired during my PhD. She has always been the main source of energy and the reason for me to continue even in difficulties.

Statement of Authentication

The work presented in this thesis is, to the best of my knowledge and belief, original except as acknowledged in the text. I hereby declare that I have not submitted this material, either in full or in part, for a degree at this or any other institution.

Ehsan Taheri



Anthology of dissemination

The present thesis is prepared based on publications. The following three published articles and one submitted article (in production) are included in the thesis to satisfy the WSU requirement of PhD by Publication:

1. Taheri, E.; Firouzianhaji, A.; Usefi, N.; Mehrabi, P.; Ronagh, H.; Samali, B. Investigation of a Method for Strengthening Perforated Cold-Formed Steel Profiles under Compression Loads. *Appl. Sci.* **2019**, *9*, 5085. <https://doi.org/10.3390/app9235085>
2. Taheri, E.; Firouzianhaji, A.; Mehrabi, P.; Vosough Hosseini, B.; Samali, B. Experimental and Numerical Investigation of a Method for Strengthening Cold-Formed Steel Profiles in Bending. *Appl. Sci.* **2020**, *10*, 3855. <https://doi.org/10.3390/app10113855>
3. Taheri, E.; Esgandarzadeh Fard, S.; Zandi, Y.; Samali, B. Experimental and Numerical Investigation of an Innovative Method for Strengthening Cold-Formed Steel Profiles in Bending throughout Finite Element Modeling and Application of Neural Network Based on Feature Selection Method. *Appl. Sci.* **2021**, *11*, 5242. <https://doi.org/10.3390/app11115242>
4. Taheri, E.; Mehrabi, P.; Rafiei, Sh.; Samali, B. Numerical Evaluation of the Upright Columns with Partial Reinforcement along with the Utilisation of Neural Networks with Combining Feature-Selection Method to Predict the Load and Displacement. *Appl. Sci.* **2021**, *11*, 11056. <https://doi.org/10.3390/app112211056>

The journal articles have been published under my name, Ehsan Taheri, as the first and corresponding author, and I was responsible for preparing the first full draft of each paper. I reviewed the body of research, prepared the literature review, conducted the experimental tests and numerical simulations, analysed the data, and prepared the results and discussions.

The following conference paper was also prepared and presented based on the studies undertaken during this research project.

1. Samali, B.; Taheri, E.; Firouzianhaji, A.; Ronagh, H. Strengthening the upright component of thin-walled cold-formed steel rack structures under axial loads. *13th International Conference on Steel, Space and Composite Structures (SS18)*. 2018: Perth, Australia.

Contents

Abstract.....	II
Acknowledgment	IV
Statement of Authentication.....	V
Anthology of dissemination.....	VI
List of Figures.....	XI
List of Tables.....	XV
Nomenclature.....	XVII
1. Introduction.....	1
1.1. Reinforcement Method	2
1.2. Axial Experimental Test.....	3
1.3. Flexural Experimental Test	5
1.4. Finite Element (FE) Modelling.....	5
1.5. Strength and Displacement Prediction using Artificial Intelligence.....	6
2. Literature Search Summary	8
3. Investigation of a Method for Strengthening Perforated Cold-Formed Steel Profiles under Compression Loads (Journal Article 1)	13
3.1. Abstract	14
3.2. Introduction.....	14
3.3. Reinforcement Method	17
3.4. Experimental Test	18
3.4.1 Test Specimens.....	19
3.4.2 Material Properties.....	22
3.4.3 Test Rig and Test Setup.....	22
3.4.4 Test Procedure.....	25
3.5. Preliminary Elastic Buckling.....	26
3.6. Results.....	27
3.7. Discussion.....	36
3.8. Finite Element (FE) Modelling.....	39
3.8.1 Material Properties.....	39
3.8.2 Connections and Interactions.....	40
3.8.3 Boundary Conditions and Loading	41
3.8.4 Mesh.....	42
3.8.5 Validation of the FE Model.....	42

3.8.6 Effect of Different Reinforcement Spacing	44
3.9. Conclusions.....	47
3.10. References.....	48
4. Experimental and Numerical Investigation of a Method for Strengthening Cold-Formed Steel Profiles in Bending (Journal Article 2)	51
4.1. Abstract	52
4.2. Introduction.....	52
4.3. Reinforcement Method	54
4.4. Experimental Campaign.....	56
4.4.1 Test Specimens.....	56
4.4.2 Material Properties.....	59
4.4.3 Test Set-Up.....	60
4.4.4 Data Acquisition and Instrumentation	66
4.5. Test Results and Discussion.....	66
4.5.1 Major Axis Test.....	67
4.5.2 Minor Axis Test.....	74
4.5.3 Remarks on the Results.....	81
4.6. Finite Element Models Arrangement.....	82
4.6.1 Element Type, Mesh Size and Material Model.....	83
4.6.2 Connections and Interactions.....	84
4.6.3 Boundary Conditions and Loading	85
4.6.4 Validation of the Finite Element Results	86
4.6.4.1 Minor Axis	86
4.6.4.2 Major Axis	90
4.7. Conclusions.....	93
4.8. References.....	94
5. Experimental and Numerical Investigation of an Innovative Method for Strengthening Cold-Formed Steel Profiles in Bending throughout Finite Element Modeling and Application of Neural Network Based on Feature Selection Method (Journal Article 3)	97
5.1. Abstract	98
5.2. Introduction.....	98
5.3. Finite Element Modeling	101
5.3.1 Material Properties.....	102
5.3.2 Connections and Interactions.....	103
5.3.3 Boundary Conditions and Loading	103

5.3.4 Mesh.....	104
5.3.5 FE Model Verification.....	104
5.3.5.1 Verification under Minor Axis Loading.....	105
5.3.5.2 Verification under Major Axis Loading.....	107
5.3.6 Parametric Finite Element Study.....	108
5.3.6.1 Parametric Study: Results of Major Axis.....	108
5.3.6.2 Parametric Study: Results of Minor Axis.....	112
5.4. Artificial Intelligence Prediction.....	118
5.4.1 Algorithm Methodology.....	119
5.4.1.1 Multi-Layer Perceptron (MLP) Algorithm.....	119
5.4.1.2 Particle Swarm Optimization (PSO).....	120
5.4.1.3 Feature Selection Technique (FS).....	121
5.4.1.4 MLP–PSO–FS Architecture.....	122
5.4.2 Performance Evaluation.....	123
5.4.3 Algorithm Results and Discussion.....	124
5.4.3.1 Normalized Ultimate Load Prediction.....	126
5.4.3.2 Deflection Prediction.....	132
5.5. Conclusions.....	139
5.6. References.....	140
6. Numerical Evaluation of the Upright Columns with Partial Reinforcement along with the Utilisation of Neural Networks with Combining Feature-Selection Method to Predict the Load and Displacement (Journal Article 4).....	143
6.1. Abstract.....	144
6.2. Introduction.....	144
6.3. Finite Element (FE) Modelling.....	147
6.3.1 Material Properties.....	148
6.3.2 Connections and Interactions.....	148
6.3.3 Boundary Conditions, Loading and Mesh.....	149
6.3.4 FE Model Verification.....	150
6.3.5 Result and discussion.....	152
6.4. Artificial Intelligence Prediction.....	161
6.4.1 Algorithm methodology.....	161
6.4.1.1 Multi-layer perceptron (MLP).....	161
6.4.1.2 Particle swarm optimisation (PSO).....	162
6.4.1.3 Feature selection (FS) technique.....	163

6.4.1.4 MLP-PSO-FS architecture	164
6.4.1.5 Performance Evaluation.....	166
6.4.1.6 Algorithm results and discussion	168
6.5. Displacement prediction	170
6.6. Ultimate Load Prediction.....	175
6.7. Conclusion	181
6.8. References.....	183
7. Conclusion and Future Works.....	187
8. Refrences.....	190

List of Figures

Figure 1-1: Schematic of the proposed reinforcing method.	3
Figure 1-2: Section and perforation details.....	4
Figure 1-3: Schematic of a 3600 mm long specimen.	4
Figure 3-1: Schematic of the proposed reinforcing method.	18
Figure 3-2: Designation of specimens (values in mm).	19
Figure 3-3: Section and perforation details (mm).....	20
Figure 3-4: Schematic of specimens with different heights (mm).....	20
Figure 3-5: Reinforcement along the upright length by bolts and spacers.	21
Figure 3-6: Coupon test results for uprights with 1.6 mm and 2.5 mm thickness.	22
Figure 3-7: (a) Schematic of compressive test on uprights; (b) testing rig.....	23
Figure 3-8: (a) Ball bearing; (b) cap plate.	23
Figure 3-9: Adjustable cap connection supports.....	25
Figure 3-10: 3600 mm specimen and boundary conditions.....	25
Figure 3-11: Preliminary elastic buckling analyses for the individual un-perforated upright gross sections (stress values have not been disclosed due to confidentiality).....	27
Figure 3-12: Load displacement curves for 2.5 mm thick specimens.	28
Figure 3-13: Failure modes of upright frames with 2.5 mm thickness.	31
Figure 3-14: Load displacement curves for 1.6 mm thick specimens.	33
Figure 3-15: Failure modes of upright frames with 1.6 mm thickness.....	34
Figure 3-16: Comparison of normalized ultimate load capacity.....	36
Figure 3-17: Effect of reinforcement by increasing the upright height.	37
Figure 3-18: Effect of reinforcement on the different upright thickness.	38
Figure 3-19: Interaction of the frame elements as well as bolt modelling.....	41
Figure 3-20: (a) Full frame meshing, (b) meshing around the polygon perforations, and (c) meshing around the circular perforations.	42
Figure 3-21: Comparison of the finite element (FE) model against the experimental data for 1.6 mm thick uprights.	43
Figure 3-22: Comparison of the FE model against the experimental data for 2.5 mm thick uprights.	43
Figure 3-23: Comparison of failure modes, (a) 1800L-1.6T, (b)1800L-2.5T, (c)1800L-1.6T-400B.	44
Figure 3-24: Load-displacement curves of uprights with different reinforcement spacing.....	45
Figure 3-25: The normalized ultimate load of 1800L uprights with different reinforcement ratio.	46
Figure 3-26: Percentage of increased ultimate load of 1800L uprights with different reinforcement spacing.	47
Figure 4-1: Reinforcement by bolts and spacers: (A) Schematic view; (B) Along the upright....	55
Figure 4-2: Configuration of the details: (A) Upright configuration; (B) Frame configuration (L and W in the Table 4-1).....	57
Figure 4-3: Designation of specimens.	59
Figure 4-4: Stress-strain diagram for 1.6 mm thickness specimen.....	60
Figure 4-5: Typical schematic four-point bending test.	61
Figure 4-6: Minor axis test set-up details: (A) Test specimen; (B) schematic front view; (C) schematic side view.....	62

Figure 4-7: Major axis test set-up details: (A) Test specimen; (B) schematic front view; (C) schematic side view.....	64
Figure 4-8: Crippling of load points: (A) Typical crippling at flanges; (B) Specific crippling reinforcement.	65
Figure 4-9: Test set-up: (A) minor axis test, (B) major axis test.	66
Figure 4-10: Normalized bending moment–deflection about major axis curves: (A) SMJM; (B) 200RMJM; (C) 300RMJM.	68
Figure 4-11: The observed failure mode for unreinforced specimens during the major axis test: (A) SMJM-test1; (B) SMJM-test2; (C) SMJM-test3.....	70
Figure 4-12: The observed failure mode for reinforced specimens with 200 mm reinforcing pitch during the major axis test: (A) 200RMJM-test1; (B) 200RMJM-test2; (C) 200RMJM-test3.....	71
Figure 4-13: The observed failure modes for reinforced specimens with 300 mm reinforcing space during the major axis test: (A) 300RMJM-test1; (B) 300RMJM-test2; (C) 300RMJM-test3.	72
Figure 4-14: The normalized major axis test average curves.	73
Figure 4-15: The ultimate normalized moment for major axis test with respect to the reinforcement type.	74
Figure 4-16: Normalized bending moment–deflection about minor axis test curves: (A) SMIM; (B) 200RMIM; (C) 300RMIM.....	75
Figure 4-17: The observed failure mode for unreinforced specimens during the minor axis test: (A) SMIM-test1; (B) SMIM-test2; (C) SMIM-test3.	77
Figure 4-18: The observed failure mode for reinforced specimens with 200 mm reinforcing pitch during the minor axis test: (A) 200RMIM-test1; (B) 200RMIM-test2; (C) 200RMIM-test3.	78
Figure 4-19: The observed failure mode for reinforced specimens with 300 mm reinforcing pitch during the minor axis test: (A) 300RMIM-test1; (B) 300RMIM-test2; (C) 300RMIM-test3.	80
Figure 4-20: The normalized minor axis average curves.....	80
Figure 4-21: The ultimate normalized moment for the minor axis test by reinforcement type....	81
Figure 4-22: The finite element model arrangement: (A) major axis; (B) minor axis.....	83
Figure 4-23: Typical finite element mesh of an upright section.	84
Figure 4-24: Interactions of the model components and bolt modelling.....	85
Figure 4-25: Finite element model and experimental curves for minor axis test set-up: (A) non-reinforced types; (B) 200 mm reinforced types; (C) 300 mm reinforced types.....	87
Figure 4-26: Comparison of finite element model against minor axis test results along with the linear regression: (A) and (B) non-reinforced model; (C) and (D) 200 mm reinforced model; (E) and (F) 300 mm reinforced model.	88
Figure 4-27: Comparison of failure modes: (A) non-reinforced upright type; (B) 300 mm reinforced upright type.....	90
Figure 4-28: Finite element model and experimental curves for major axis test set-up: (A) non-reinforced frame types; (B) 200 mm reinforced frame types; (C) 300 mm reinforced frame types.	90
Figure 4-29: Comparison of finite element model against major axis test results along with the linear regression: (A) and (B) non-reinforced model; (C) and (D) 200 mm reinforced model; (E) and (F) 300 mm reinforced model.	91
Figure 4-30: Comparison of failure mode: (A) non-reinforced upright type; (B) 300 mm reinforced upright type.....	93
Figure 5-1: Schematic of models.	101

Figure 5-2: Coupon test results for uprights: (a) with 1.6 mm and (b) with 2.5 mm thickness [9].	102
Figure 5-3: Interactions between frame elements.	103
Figure 5-4: (a) Minor axis test setup. (b) Major axis test setup [9].	104
Figure 5-5: Typical FE mesh of an upright section.	104
Figure 5-6: Comparison of the FE model against the minor-axis test results for (a) non-reinforced model, (b) 200 mm reinforced model and (c) 300 mm reinforced model.	106
Figure 5-7: . Linear regression diagram for (a) non-reinforced model, (b) 200 mm reinforced model, and (c) 300 mm reinforced model.	106
Figure 5-8: Comparison of FE model against major-axis test results for (a) non-reinforced model, (b) 200 mm reinforced model and (c) 300 mm reinforced model.	107
Figure 5-9: . Linear regression diagram for; (a) non-reinforced model, (b) 200 mm reinforced model, and (c) 300 mm reinforced model.	107
Figure 5-10: Designation of models.	108
Figure 5-11: Normalized moment-deflection curves for 1800 mm models about major axis....	109
Figure 5-12: Normalized moment-deflection curves for 2400 mm models about major axis....	109
Figure 5-13: Normalized moment-deflection curves for 3000 mm models about major axis....	110
Figure 5-14: Normalized moment-deflection curves for 3600 mm models about major axis....	110
Figure 5-15: The normalized ultimate moment of 1800, 2400, 3000, and 3600 mm models about major axis with respect to reinforcement spacing.....	111
Figure 5-16: Percentage of increased ultimate load of major axis analysis with different reinforcement spacing in length order.....	112
Figure 5-17: Normalized moment-deflection curves for 1800 mm models about minor axis....	113
Figure 5-18: Normalized moment-deflection curves for 2400 mm models about minor axis....	114
Figure 5-19: Normalized moment-deflection curves for 3000 mm models about minor axis....	114
Figure 5-20: Normalized moment-deflection curves for 3600 mm models about minor axis....	115
Figure 5-21: The normalized ultimate moment of 1800, 2400, 3000, 3600 mm models about minor axis with respect to reinforcement spacing.	117
Figure 5-22: Percentage of increased ultimate load with different reinforcement.	118
Figure 5-23: Schematic representation of MLP neuron.....	119
Figure 5-24: Visualization of a single hidden layer MLP network.....	120
Figure 5-25: PSO sequential flowchart.....	121
Figure 5-26: Feature selection technique steps.....	122
Figure 5-27: Flowchart of the sequential combination of hybrid MLP–PSO–FS algorithm.....	123
Figure 5-28: Comparison of the predicted and measured load: (a) One input, (b) two inputs, (c) three inputs, (d) four input, (e) five inputs, (f) six inputs through MLP–PSO–FS model.....	130
Figure 5-29: MLP–PSO–FS (4 inputs) prediction vs. experimental diagram: (above) train phase, (below) test phase.	131
Figure 5-30: MLP–PSO–FS (4 inputs) Error histograms: (above) train phase, (below) test phase.	132
Figure 5-31: MLP–PSO–FS regression charts (iteration = 100): (a) P150, (b) P250, (c)P350..	135
Figure 5-32: MLP–PSO–FS regression charts (iteration = 75): (a) P150, (b) P250, (c)P350....	136
Figure 5-33: MLP–PSO–FS regression charts (iteration = 45): (a) P150, (b) P250, (c)P350....	136
Figure 5-34: MLP–PSO–FS (6 inputs) prediction vs. experimental diagram: (above) train phase, (below) test phase.	138
Figure 5-35: PSO–FS (6 inputs) error histograms: (above) train phase, (below) test phase.	139

Figure 6-1: The reinforcement system and the constituent elements.	147
Figure 6-2: Interaction and connection properties of a typical model.....	149
Figure 6-3: A typical model with a Mesh matrix view on the polygon and circular perforations	150
Figure 6-4: Comparison of test and numerical results of normalised load for (a) 3600L-1.6T, (b)3600L-2.5T.....	151
Figure 6-5: Comparison of test and numerical results of normalised load for (a) 3000L-1.6T, (b) 3000L-2.5T	151
Figure 6-6: Comparison of test and numerical results of normalised load for (a) 2400L-1.6T, (b) 2400L-2.5T	152
Figure 6-7: Comparison of test and numerical results of normalised load for (a) 1800L-1.6T, (b) 1800L-2.5T	152
Figure 6-8: Designation of models.	153
Figure 6-9: Normalised load-displacement diagrams of the FE results for: (a) 3600L-1.6T, (b) 3600L-2.0T, (c) 3600L-2.5T, and (d) 3600L-3.0T models.	154
Figure 6-10: Normalised load-displacement diagrams of the FE results for: (a) 3000L-1.6T, (b) 3000L-2.0T, (c) 3000L-2.5T, and (d) 3000L-3.0T models.	155
Figure 6-11: Normalised load-displacement diagrams of the FE results for: (a) 2400L-1.6T, (b) 2400L-2.0T, (c) 2400L-2.5T, and (d) 2400L-3.0T models.	156
Figure 6-12: Normalised load-displacement diagrams of the FE results for: (a) 1800L-1.6T, (b) 1800L-2.0T, (c) 1800L-2.5T, and (d) 1800L-3.0T models.	157
Figure 6-13: Normalised load-displacement diagrams of the FE results for: (a) 3600L-50B, (b) 3000L-50B, (c) 2400L-50B, and (d) 1800L-50B models.....	158
Figure 6-14: Ultimate load capacities based on thickness and reinforcement spacing for (a) 1800mm models and (b) 2400mm models.....	158
Figure 6-15: Ultimate load capacities based on thickness and reinforcement spacing for (a) 3000mm models and (b) 3600mm models.....	159
Figure 6-16: Schematic representation of MLP neuron.....	162
Figure 6-17: Flowchart of typical single line hidden layer MLP for identifying a problem.	162
Figure 6-18: PSO sequential flowchart.....	163
Figure 6-19: Feature selection technique steps.....	164
Figure 6-20: flowchart of the sequential combination of hybrid MLP-PSO-FS algorithm.....	166
Figure 6-21: Regression of the train (above charts) and test (below charts) phase results with measured values of displacement for (a) One input, (b) Two inputs, (c) Three inputs, (d) Four input, (e) Five inputs.....	173
Figure 6-22: The MPF (five inputs) prediction vs experimental diagram: (above) train phase, (bellow) test phase	174
Figure 6-23: The MPF (five inputs) Error histograms: (above) train phase, (bellow) test phase	175
Figure 6-24: Regression of the train (above charts) and test (below charts) phase results with measured values of normalized load for (a) One input, (b) Two inputs, (c) Three inputs, (d) Four input, (e) Five inputs.....	179
Figure 6-25: The MPF (five inputs) prediction vs experimental diagram: (above) train phase, (bellow) test phase	180
Figure 6-26: The MPF (five inputs) Error histograms: (above) train phase, (bellow) test phase	181

List of Tables

Table 3-1: Specimen details.....	21
Table 3-2: Material properties of upright sections.....	22
Table 3-3: The average normalized ultimate capacity of uprights with 2.5 mm thickness.....	29
Table 3-4: The average normalized ultimate capacity of uprights with 1.6 mm thickness.....	35
Table 4-1: Specimen configurations.....	58
Table 4-2: Material properties of the upright section.....	60
Table 4-3: The ultimate normalized bending capacity of specimens in the major axis test.:	68
Table 4-4: The ultimate normalized bending capacity of specimens in the minor axis tests.....	75
Table 4-5: Finite element model vs experimental results details in terms of evaluation criteria..	89
Table 4-6: Finite element model vs experimental results accuracy details in terms of evaluation criteria.....	92
Table 5-1: Geometrical features of models.....	102
Table 5-2: Material properties of upright sections.....	103
Table 5-3: FEM vs. experimental results accuracy details in terms of evaluation criteria.....	106
Table 5-4: FEM vs. experimental results accuracy details in terms of evaluation criteria.....	107
Table 5-5: Best achieved results in deflection estimation.....	125
Table 5-6: Best achieved results in normalized load estimation.....	125
Table 5-7: Parameter characteristics used for PSO in this study.....	126
Table 5-8: Parameter characteristics used for MLP and FS in this study.....	126
Table 5-9: The calculated accuracy criteria for the performance of the implemented models (Iteration = 150).....	127
Table 5-10: The calculated accuracy criteria for the performance of the implemented models (population = 250).....	127
Table 5-11: The calculated accuracy criteria for the performance of the implemented models for different inputs.....	127
Table 5-12: Most effective inputs based on feature selection.....	128
Table 5-13: The calculated accuracy criteria for the performance of the implemented models (iteration = 45).....	133
Table 5-14: The calculated accuracy criteria for the performance of the implemented models (population = 250).....	133
Table 5-15: The calculated accuracy criteria for the performance of the implemented models for different inputs.....	134
Table 5-16: Most effective inputs based on feature selection.....	134
Table 6-1: Ultimate normalized compressive capacities for 3600 mm models based on reinforcement spacing.....	159
Table 6-2: Ultimate normalized compressive capacities for 3000 mm models based on reinforcement spacing.....	160
Table 6-3: Ultimate normalized compressive capacities for 2400 mm models based on reinforcement spacing.....	160
Table 6-4: Ultimate normalized compressive capacities for 1800 mm models based on reinforcement spacing.....	160
Table 6-5: Best achieved results for displacement estimation.....	168
Table 6-6: Best achieved results for normalised load estimation.....	169
Table 6-7: Parameter characteristics were used for PSO in this study.....	169

Table 6-8: Parameter characteristics used for MLP and FS..... 169
Table 6-9: Selected input composition based on feature-selection method for deflection case. 170
Table 6-10: Calculated accuracy criteria for the performance of the implemented models
(Iteration = 45). 170
Table 6-11: Selected input composition based on feature-selection method for load case..... 176
Table 6-12: Calculated accuracy criteria for the performance of the implemented models
(Iteration = 150). 176

Nomenclature

Symbols

A_g	Gross cross-section area
B	Bolt Spacing
C_i	Acceleration coefficients
E	Module of elasticity
F_u	Ultimate load
F_y	Yield load
L	Length
N	Number of data
nf	Number of functions
O_i	Observed values
P	Bolt pitch
P_i	Predicted value
R	Correlation coefficient
Sp	Reinforcement spacing
T	Thickness
U_x	Translation in X direction
U_y	Translation in Y direction
U_z	Translation in Z direction
w	Inertia weight
W_i	Synaptive weights
Z	Shape factor
α_i	Linear weights
ε	Strain
σ	Stress
σ_u	Ultimate stress
σ_y	Yield stress
Φ	Non-linear activation function

$\hat{y}(x)$	Model predictions
\bar{O}_i	Average of observed values
\bar{P}_i	Average of predicted values
x_i	Multi-dimensional input data
y_i	Multi-dimensional outputs
$\phi_i \rightarrow$	Uniformly-distributed random vectors
$p_i \rightarrow$	Most appropriate position
$s_i \rightarrow$	Particle's position
$V_i \rightarrow$	Particle's velocity

Acronyms

AI	Artificial Intelligence
ANFIS	Adaptive Neuro-Fuzzy Inference System
ANN	Artificial Neural Networks
BC	Boundary Condition
BP	Backpropagation
CFS	Cold-Formed Steel
FE	Finite Element
FEM	Finite Element Modelling
FS	Feature Selection
LMBP	Levenberg–Marquardt Backpropagation
MAE	Mean Absolute Error
ML	Machine Learning
MLP	Multi-Layer Perceptron
MVO	Multi-Verse Optimiser
NSE	Nash–Sutcliffe Efficiency
PSO	Particle Swarm Optimisation
RMI	Rack Manufacturers Institute
RMSE	Root Mean Square Error
STD	Standard Deviation.

WI

Wilmot's Index of Agreement

1. Introduction

Rapid development in different industries has led to high demand for improving the quality of warehousing systems to store the products in secure places before distributing them to the market. To this end, the progress in CFS storage rack systems has been notably increased in various industries. Uprights are recognised as one of the crucial sections of the racking systems, which play a significant role in supporting the loads like columns in buildings. The performance of racking frames is affected by the general behaviour of the uprights since these thin-walled structures are subjected to stability loss because of combined various failure modes such as the interaction of local, distortional and flexural buckling. In addition, extreme loading conditions have a significant effect on the stability of uprights in racking systems.

Recent research indicates that buckling modes of CFS uprights have been studied more than the weaknesses of the uprights under loading. To improve the ultimate capacity of open CFS sections using partial closure, several studies have been performed; however, many experimental investigations were still required to be applied for enhancing the capacity of uprights. Hence, this research is aimed to present a new technique for increasing the strength of uprights in racking structures and controlling buckling, utilising reinforcements along the upright length. In fact, the main purpose is to identify solutions that can be applied by the industry rapidly and without any considerable cost and changes in performance or the procedure of assembly. In this regard, full-scale experiential studies have been performed on uprights with various thicknesses and heights to evaluate the performance and strength of upright frames with and without reinforcement. The findings consist of ultimate capacities, failure mechanisms and deformation modes, followed by a discussion of the experimental data.

In order to examine the influence of various reinforcement spacing on the upright strength, finite element (FE) modelling has also been deployed. Different types of FE models have been designed and explained comprehensively, and their unique characteristics are mentioned. Besides, to predict the axial and flexural performance of upright frames and verify the FE models, artificial intelligence (AI) techniques were employed. As the properties of CFS sections have been

successfully predicted by neural networks in the past, a multi-layer perceptron (MLP) approach is considered as the principal core of the AI technique. In this investigation, to determine the most influential property on the capacity, a feature selection based algorithm is considered and also deployed as another numerical method for verifying, optimising and predicting. The prediction of ultimate axial and flexural load and displacement has been successfully performed using the hybrid AI model on the basis of the feature selection method. The validation of FE results was also demonstrated successfully. In addition, a new MLP algorithm has been developed and combined with particle swarm optimisation, and the results have been discussed extensively.

1.1. Reinforcement Method

Upright sections experience different instability modes under loadings such as local, distortional, and flexural or flexural-torsional buckling. Distortional buckling considerably affects the uprights' design, which has led to restricting the applicability of thin-walled CFS profiles.

In general, the resistance of closed sections is remarkably higher than the flexural and compressive strength of open sections. This is due to the susceptibility of open sections to buckling compared to closed ones. However, the production of closed sections requires more cost and time since a complex overhaul of current practices and procedures is required on the part of CFS industry to achieve the intended outcome. Consequently, a partially closed section that is more cost-effective can improve the capacity of upright frames. For this purpose, in this research, a simple and innovative technique has been used for partially closing upright sections. The failure mode can be controlled by utilising this approach and effect a considerable change in its overall performance.

A regular pattern of perforations is present on both the webs and the flanges of the racking upright profiles. To create a fast interconnection between beams and uprights, web perforation is employed, while the connection of brace components to uprights is allowed using perforations of flanges. Perforations that are not utilised to assemble the frame can be used for partial closing of sections. Hence, in the current study, at the location of perforations, connectors employing bolts, nuts and spacers are applied to connect flanges of open sections and then provide a partially closed section, which has much greater load capacity. Spacers as transverse elements are used for bracing of racking frames and are built up of plastic materials. A schematic of the considered reinforcing technique on the open CFS upright frame is shown in Figure 1-1.

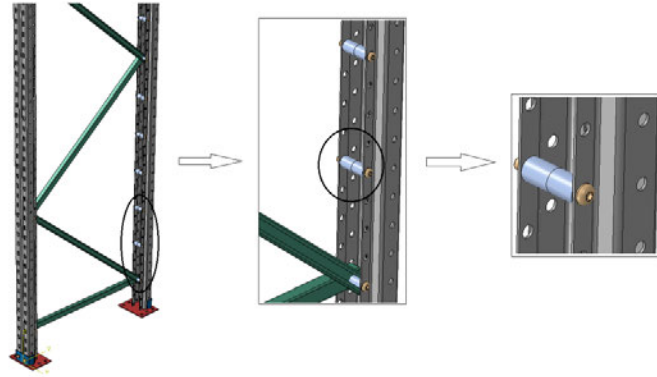


Figure 1-1: Schematic of the proposed reinforcing method.

Commonly, in the racking industry, single long uprights are deployed to reach the required height because cutting and splicing the elements require high cost and ample time. In the higher levels of racking structures where the exerted loads are lower than those at bottom levels, the sections' thickness is the same as the thickness at the lower height for simplicity. But, this strategy is not economical. In other words, for the higher levels, the upright section would be oversized, which is uneconomical. On the other hand, the proposed approach can be employed to overcome excess steel utilisation. Storage racks can be designed with thinner upright sections, which are strengthened by the proposed technique in their lower levels. The construction cost of these structures can be reduced considerably using this method.

Also, to examine the workability and ability of the considered technique, an initial numerical analysis was implemented, and it was shown that the load-bearing capacity of standard uprights could be improved using this method. In this study, the proposed reinforcement technique is a straightforward, cost-effective and timesaving method that can be used for different CFS open sections.

1.2. Axial Experimental Test

At the structural laboratory of Western Sydney University, a comprehensive experimental investigation was designed and performed to evaluate the influence of reinforcement on the upright capacity. Experiments using two scenarios of reinforcements (utilising reinforcement at 200 mm and 400 mm spacing) on different upright lengths from short to long with two thicknesses were conducted. In order to determine the buckling load and failure mode of the upright frames, at first,

the test was applied on samples without reinforcement as control specimens. Thereafter, to examine the influence of the reinforced system, the samples strengthened by bolts and spacers were tested once more.

Nine single uprights and 72 upright frames, each consisting of two uprights connected by diagonal bracing, were made using available rack sections in the market. In order to investigate the impact of thickness on the results, a standard section with two thicknesses (1.6 mm and 2.5 mm) was used for racking frames. Figure 1-2 depicts the geometry of the section and the details of perforation. A sample specimen is shown in Figure 1-3, and several lengths, including 1200 mm, 1800 mm, 2400 mm, 3000 mm, and 3600 mm, have been deployed to obtain various modes of failure and their corresponding interaction.

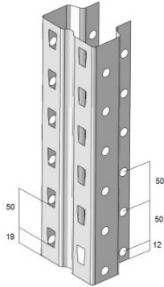


Figure 1-2: Section and perforation details.

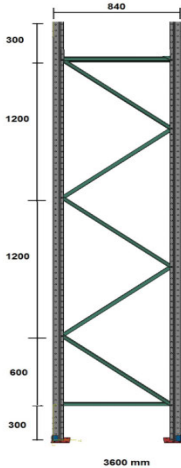


Figure 1-3: Schematic of a 3600 mm long specimen.

The influence of reinforcement on the compressive capacity of uprights was examined by attaching bolts and spacers to the upright at 400 mm and 200 mm spacing along the upright length. The details of experiments and obtained results in the study are given in Chapter 2 and published in an article entitled "Investigation of a Method for Strengthening Perforated Cold-Formed Steel Profiles under Compression Loads".

1.3. Flexural Experimental Test

In order to determine the ultimate moment capacity of the specified reinforced uprights about their major and minor axes, and examine its improvement using suggested reinforcement, several four-point bending tests were carried out. To measure the flexural capacity and failure modes of the reinforced sections, which comprised conventional upright frames and upright frames strengthened by bolt and spacer systems, monotonic tests were performed.

To perform the tests, eighteen specimens, including nine single uprights and nine frames, were considered. The bending frames were built from two upright columns connected by diagonal bracing. Two groups of specimens were constructed with or without reinforcements. The flexural behaviour of the samples without reinforcements was examined throughout the monotonic test. The direction of loading was about the minor and major axes, respectively. Samples with reinforcements located at 200 mm and 300 mm spacing along the upright length have also been examined about their minor and major axes. The study details and results are given in Chapter 3 and was published in a paper entitled "Experimental and Numerical Investigation of a Method for Strengthening Cold-Formed Steel Profiles in Bending".

1.4. Finite Element (FE) Modelling

FE modelling in this research was applied to examine the influence of different reinforcement spacings, lengths and thicknesses on the uprights' strength. The employed numerical technique is presented thoroughly and then validated by experimental results. In the end, the influence of various reinforcement spacings is examined by the verified numerical model. To demonstrate the accuracy of the FEM findings, a comparison between each simulated load-deflection curve and the corresponding test curve was performed, and for each model, linear regression is depicted. The

numerical and experimental results are compared, and accuracy and compatibility between them were investigated.

In order to achieve a validated database for the AI method, a parametric FE study was performed on the suggested reinforcement system, examining the effect of different reinforcement spacings on the strength of the profiles with various thicknesses. All FE modellings are carried out using ABAQUS software. In addition, to obtain a comprehensive dataset, various upright lengths were modelled. The results of FE models are presented in details in Chapter 4 and Chapter 5 and were published as journal articles.

1.5. Strength and Displacement Prediction using Artificial Intelligence

Artificial intelligence (AI) consists of several intelligent techniques that examine each problem based on a designated intelligence algorithm. In engineering problems, most of the applications of AI methods have concentrated on the prediction and verification of data. The accuracy of prediction is affected by different factors such as type of technique, error, evaluating the problems before prediction and so on. Backpropagation (BP) method, as a classic approach, is commonly presented to train artificial neural networks (ANNs). Machine learning is a subset of AI algorithms, which takes advantage of a learning circuit.

In this study, a multi-layer perceptron (MLP) neural network is combined with a particle swarm optimisation (PSO) algorithm which is based on the random production of the initial population. In this hybrid neural network, the feature selection technique is used instead of outdated approaches to identify the most influential input. The main purpose of the current study is to employ the feature selection technique to determine the most influential factors on the flexural and axial capacity of CFS uprights for predicting and identifying deflection and ultimate load simultaneously.

The results of several experiments and FE models have been considered as the dataset of this study. This dataset includes several inputs and one target output. Also, selecting the combination of the effective inputs for the prediction matrix, which is tuned by PSO, is performed as the main neural network model.

MLPs can solve the problems stochastically, which are very useful for research. This advantage provides approximate solutions for highly complicated issues, such as fitness approximation. In this study, MLP is fitted based on the selected data in the training phase throughout trial and test procedure that has been discussed in the related sections. Hence, MATLAB software was employed to predict the output, utilising hybrid PSO-MLP. The population size, iterations, damping ratio, personal and global learning coefficient and inertia weight are the parameters of PSO. Besides, the hidden layers and training function are the parameters of MLP neural network. Also, the characteristics of the parameter employed for FS have been demonstrated in the study.

A dataset can contain a large number of input data; however, definitely, all inputs are not appropriate to be utilised in the neural network since some of them have almost no influence on the prediction of the output. On the other hand, other ones may lead to deviating the network. Consequently, if there are many inputs, finding the best combination is prolonged considerably. It should be mentioned that for this case, with a large number of repetitions, implementing the neural network and analysing its results is not possible due to various combinations of neural network settings. Hence, the best option to choose the multiple input modes and settings is based on prior experiences and primary suppositions.

The application of AI in predicting the behaviour of sections and their properties have been explained in details in Chapter 4 and Chapter 5 and was published as journal articles.

2. Literature Search Summary

In recent years, the development of cold-formed steel (CFS) racking structures has been widely increased, worldwide, because of its structural advantages and workability, particularly in warehouse and storage usage (Shariati et al., 2019). In this regard, different methods have been used by researchers to improve the performance of these systems.

The performance of uprights, as one of the most important components of racking structures, subjected to axial and flexural loading has been widely investigated. In order to achieve a set of coefficients for the optimal length of the uprights under compressive loads, Koen (2008) performed experimental studies on stub uprights and full upright frames. Davies et al. (1997) examined the local buckling of stub columns subjected to axial loads. They compared the obtained results with theoretical relations and the numerical approach. It was deduced that comprehensive experimental tests are not necessary for the design phase of the racking uprights. Trouncer and Rasmussen (2014) found that using EN 15512 (2009) to predict the ultimate load capacity of upright sections can provide more accurate results compared to predicting by Rack Manufacturers Institute (RMI) specifications. Gilbert & Rasmussen (2010) performed extensive experimental studies on individual parts of racking configurations, and some clarifications of the guidance provided by EN15512 (2009) were indicated to precisely obtain the in-plane global stiffness of the upright frames.

In recent years, researchers have focused on the interaction of buckling modes of racking upright members. In an experimental study, Pedro et al. (2014) examined the local-distortional buckling interaction in fixed-end CFS uprights. Also, Roure et al. (2011) evaluated this parameter for short upright columns using the concept of reduced thickness of the stiffeners. It was found that the present design codes are not accurate, and the influence of buckling interaction should also be regarded. In another experimental investigation, the distortional buckling of upright frames with various heights was studied by Casafont et al. (2011). They obtained design formulations according to the combination of distortional and global buckling modes.

The effect of perforations, as an important factor that influences the behaviour of upright sections under loading, was examined by Zhao et al. (2017). It was concluded that the load-bearing

capacity and buckling failure mode of the structure can be highly governed by the perforations. Rhodes and Schneider (1994) investigated the effect of perforation position, dimensions, quantity, and patterns on the compressive performance of upright frames. Moen and Schafer (2008) evaluated the influence of perforation on the stability performance of upright frames using various experimental tests. They also showed that as well as the direct strength technique to design the rack systems, the experimental test is necessary (Moen & Shafer, 2009). Therefore, the design method for upright sections should be based on empirical approaches. Also, the axial loads were applied on perforated and non-perforated uprights having different lengths and load eccentricities to investigate the influence of perforations and loading on the strength of the upright (Baldassino et al., 1999).

In general, perforated CFS elements are also sensitive against bending forces. Following the previous researches on the flexural performance of the perforated CFS profiles, cyclic and monotonic loadings were applied to these sections undergoing various types of deformations, especially buckling types (Chen et al., 2019). Various four-point bending tests were carried out by Yu and Schafer (2006) and Calderoni et al. (2009) to examine the flexural and distortional behaviour of C and Z-shaped built-up cold-formed steel sections. Rogers et al. (1997) investigated the bending moment of validated experimental data with various code provisions. A new design method was introduced by Hancock (1997) for distortional buckling strength of C and Z-shaped cold-formed steel sections. In an experimental and analytical study, C-shaped cold-formed steel beams with or without edge stiffeners were evaluated by Wang et al. (2009). It was found that stiffeners can considerably improve the flexural stiffness and buckling resistivity of the beams subjected to pure and non-pure bending tests. In another study, cold-formed steel built-up beams with web perforations were tested using a four-point bending method by Wang et al. (2015). Also, imperfections of local geometry were estimated. In several experimental and analytical studies, the behaviour of perforated cold-formed steel channel section beams was evaluated considering the influences of web-hole ratio. The more increase in the hole area led to more decrease in the ultimate distortional buckling moment (Yuan et al., 2017; Moen & Shafer, 2009; Zhao et al., 2019; Zhao et al., 2015; Dai et al., 2018; Yu et al. 2019). Besides, the findings showed that the size of the web holes has a direct effect on the distortional buckling moment so that by increasing the hole size, the buckling moment decreased.

The validity of Australia/New Zealand Standard (AS/NZS 4673:2001) for the flexural strength design of rectangular tubes made by cold-rolling steel was evaluated by Zhou et al. (2005). It was reported that the design code is reliable for normal strength steel and unreliable for high strength steel. Laim et al. (2013) performed different bending experiments and FE modellings on the flexural performance of cold-formed steel beams. Muftah et al. (2018) carried out several four-point flexural tests on bolted built-up cold-formed steel beams while employing bolts and nuts systems. Based on the obtained results, by applying the loads on the webs, the flexural performance of the beams was only affected by bolt distances. Huang et al. (2018) suggested a new model to determine the distortional buckling moment of CFS channel sections with various stiffened webs. The obtained results had an acceptable agreement with those of the finite strip approach. The bearing capacity and distortional buckling moment can be increased using flange stiffeners (Wu et al., 2019). Also, the shear rigidity and distortional buckling load can be affected by slots, and the flexural performance is enhanced by the web stiffeners (Shafaei et al., 2019).

Since the upright frames are vulnerable to failure under compressive and bending loads, different approaches have been developed in recent years to address this problem. Talikoti and Bajoria (2005) used spacers as partial reinforcement for open sections. It was reported that the capacity of uprights increases by setting spacers at proper intervals. Also, the failure mode and buckling could be changed concurrently. Veljkovic and Johansson (2008) examined the influence of partially closed CFS thin-walled sections. They worked on improving the torsional stiffness of the sections when utilised as columns. Manikandan and Arun (2016) studied the performance of the thin-walled channels having partially closed sections subjected to axial loading employing various stiffener plates. They found that utilising cover plates for partially reinforcing the systems leads to change of the distortional buckling to a combination of local and flexural-torsional buckling. Other researchers have recently performed some numerical evaluations to enhance the axial capacity of the upright (Anbarasu et al. 2013, 2014).

Experimental studies require costly as well as time-consuming processes, which have inspired researchers to find other alternatives like numerical approaches. Considering the priority of the finite element method (FEM) compared to other numerical techniques, in recent years, this method has been widely deployed in various engineering applications, particularly CFS structures. The flexural performance of stiffened CFS slotted beams under various loading conditions was studied

by Visy et al. (2019). Nandini and Kalyanaraman (2010) numerically investigated the performance and strength of lipped channel beams with different lengths. They proposed a method for designing the mentioned beams under the interaction of local, distortional, and overall lateral-torsional buckling based on the Euro code provisions. In the literature, many studies have been carried out to simulate the performance and strength of CFS racking systems using FEM (Chu et al., 2004; Ye et al., 2016; Gilbert et al., 2012).

In addition, neural networks have been recognised as accurate methods to predict the different characteristics of structural elements employing experimental results (Shariati et al., 2019; 2020). Different factors such as linearity or nonlinearity of data, the number of inputs and outputs and the novelty of the study are considered to select a specific type of neural network (Shariati et al., 2019; Shahgoli et al., 2020; Toghroli et al., 2020). The process of developing the network relies on trial and error identification, which the basic algorithm and possible supplementary methods detect (Armaghani et al., 2019; Mehrabi et al., 2021).

In general, AI models have several advantages which lead to providing more accurate results in comparison with classic approaches (Shariati et al., 2019; 2020; Toghroli et al., 2020, Xu et al., 2019, Li et al., 2021). Two important features of AI are learning and mocking, which make these techniques desirable for researchers (Armaghani et al., 2019; Guo et al., 2019; Xiao et al., 2021; Mousavi et al., 2021; Xiang et al., 2021). A raw model of ANNs is developed generally by using optimisation methods like back-propagation algorithms (Ao et al., 2016). ANN is able to address three types of problems: (1) classification, (2) function-approximation and (3) time series prediction (Mi et al., 2021; Zhang et al., 2021; Shariati et al., 2020; El-Kassas et al., 2001; Liu et al., 2021). However, classical approaches have some problems finding relations and directions of numbers at maximum or minimum values. Therefore, Metaheuristic (MT) optimisation algorithms such as GA (Shariati et al., 2019), particle swarm optimisation (PSO) (Shariati et al., 2019) and imperialist competitive algorithm (ICA) (Perera et al., 2009) can be employed to solve mentioned shortcomings.

The performance of ANN in some cases can be enhanced using the global search feature of these techniques. Recently, ANNs and several optimisation methods have been used to solve complicated engineering problems. Adaptive Neuro-Fuzzy Inference System (ANFIS) is a subset

of ANNs, which has been identified as a reliable technique in the prediction process (Shahgoli et al., 2020). In medical investigations, the prediction capability of ANFIS has been proven in various applications (Yadollahpour et al., 2018; Ozkan et al., 2010). In China, a developed model of ANFIS was deployed for the prediction of infected cases with Covid-19 (Al-Qaness et al., 2020). Moreover, hybrid intelligent models are usually used to address multi-objective problems (Mehrabi et al., 2021; Feng et al., 2021). Hence, various optimisation algorithms can be hybridised with ANFIS to improve the precision and performance of the deployed technique. For example, the multi-verse optimiser (MVO) method was integrated with ANFIS to determine the consumption rate of materials using experimental data (Mehrabi et al., 2021).

In this research, a combination of experimental tests, FE modelling and AI methods are used to investigate the proposed method for strengthening cold-formed open sections under axial and flexural loads.

In addition to this summary, a complete list of relevant literature is included at the end of published papers comprising Chapters 3,4 and 5, respectively.

3. Investigation of a Method for Strengthening Perforated Cold-Formed Steel Profiles under Compression Loads (Journal Article 1)

A reprint of this study entitled ‘Investigation of a Method for Strengthening Perforated Cold-Formed Steel Profiles under Compression Loads’, Taheri, E.; Firouzianhaji, A.; Usefi, N.; Mehrabi, P.; Ronagh, H.; Samali, B. is published by *Applied Sciences*. 2019; 9(23):5085. <https://doi.org/10.3390/app9235085>.

3.1. Abstract

Cold-formed steel (CFS) storage rack structures are extensively used in various industries to store products in safe and secure warehouses before distribution to the market. Thin-walled open profiles that are typically used in storage rack structures are prone to loss of stability due to different buckling modes such as local, distortional, torsional and flexural, or any interaction between these modes. In this paper, an efficient way of increasing ultimate capacity of upright frames under compression load is proposed using bolts and spacers which are added externally to the section with certain pitches along the height. Hereinto, experimental tests on 81 upright frames with different thicknesses and different heights were conducted, and the effect of employing reinforcement strategies was examined through the failure mode and ultimate load results. Non-linear finite element analyses were also performed to investigate the effect of different reinforcement spacing on the upright performance. The results showed that the reinforcement method could restrain upright flange and consequently increase the distortional strength of the upright profiles. This method can also be effective for any other light gauged steel open section with perforation. It was also observed that the reinforcement approach is much more useful for short length upright frames compared to the taller frames.

Keywords: upright; cold-formed steel; compression behavior; bolt and spacer; reinforcement

3.2. Introduction

By increasing the speed of development in various industries, there is a need for well-engineered warehousing systems to store the products in safe and secure warehouses before they are distributed to the market. For this purpose, cold-formed steel (CFS) storage rack structures have widely been developed to be used in different industries. Uprights are one of the main parts of the racking structures which have the important role of bearing loads like what columns do in buildings. The performance of racking frames depends on the overall behavior of the uprights, as these thin-walled structures are subjected to loss of stability due to the combination of different failure modes, such as the interaction of distortional and flexural buckling [1,2]. The stability of uprights in racking systems also becomes more critical under extreme loading scenarios [3,4,5,6].

The compressive behavior of upright racking systems has been extensively studied in recent years. Experimental tests on stub uprights and full upright frames were carried out by Koen [7] in order to obtain a set of reduction coefficients for the effective length of the uprights under compression. Local buckling of stub column members under axial load was experimentally investigated by Davies et al. [8] and the results were compared with theoretical relations as well as the numerical method. They concluded that for the design stage of racking uprights, extensive experimental testing is not necessarily required. In another study, Trouncer and Rasmussen [9] investigated that the predicting ultimate load capacity of upright sections provided by EN 15512 [10] specification is more accurate than predictions by Rack Manufacturers Institute (RMI) specifications. Comprehensive experimental tests on individual components of racking systems were also carried out by Gilbert & Rasmussen [11], and some clarifications of the guidance provided by EN15512 [10] were presented in order to accurately determine the in-plane global stiffness of the upright frame.

The interaction of buckling modes of racking upright members has also been under the attention of researchers in recent years. The local-distortional buckling interaction in fixed-end CFS uprights was experimentally assessed by Pedro et al. [12]. In another project, local-distortional buckling interaction of short upright columns was studied by Roure et al. [13] through the concept of reduced thickness of the stiffeners. They reported that the current design codes are not accurate and the effect of buckling interaction needs to be also considered. In another study, Casafont et al. [14] experimentally evaluated the distortional buckling of upright frames with different heights and provided design formulations based on the combination of distortional and global buckling modes.

In terms of perforation, which is an important parameter that can affect the performance of upright sections under compressive load, Zhao et al. [15] investigated the effect of perforation on compressive behavior of storage rack uprights. They showed that the perforation could significantly affect the load-bearing capacity as well as buckling failure mode of the system. The influence of perforation pattern including of perforation position, dimensions, and quantity on the compressive behavior of upright frames were also assessed by Rhodes and Schneider [16]. A series of experimental tests were conducted by Moen and Schafer [17] to examine the effect of perforation on the stability behavior of upright frames. In another study [18], they indicated that

direct strength method is not enough for the design of rack structures and the experimental test is also required; accordingly, the design approach for upright sections must be based on experimental test procedures. Baldassiono [19] also determined the effect of perforations and applying load on the upright strength through the axial tests on both perforated and non-perforated uprights with various length and load eccentricities.

Considering the weaknesses of the upright frames under compressive loads, in recent years several methods have been proposed in order to improve the compressive behavior of racking uprights. Partial reinforcement of open sections using spacers was proposed by Talikoti and Bajoria [20]. They concluded that by installing spacers at appropriate intervals, the capacity of the uprights is improved and the mode of failure and buckling can be changed at the same time. Veljkovic and Johansson [21] also studied the effect of partially closing CFS thin-walled sections. They focused on increasing the torsional stiffness of these sections when used as columns in structures. An investigation for analyzing the behavior of thin-walled channels with partially closed sections under axial forces using different stiffener plates was conducted by Manikandan and Arun [22]. The result indicated that by partially reinforcing the sections using cover plates, the buckling mode changes from distortional to a combination of local and flexural torsional buckling. Recently, a few studies on improving the upright axial capacity have also been carried out by other researchers [23,24,25,26,27] which are mainly based on numerical parametric studies.

Review of the past studies shows that a great number of research projects have been conducted on the investigation of buckling modes for CFS uprights and little attention has been given to address the weaknesses of the uprights under compressive load. Although some attempts have been made in order to increase the ultimate capacity of open CFS sections using partially closed methods, extensive experimental studies for increasing upright capacity is still required. Therefore, this study aims to propose a new approach in order to improve the strength of the uprights in racking systems and to control buckling issues using reinforcements along the upright length. The main idea is to gain solutions that can be implemented by the industry immediately without any major modifications to the way the industry operates or to the assembly procedure. Hereinto, a total of 81 full-scale experimental tests were conducted on uprights with different heights and thicknesses in order to examine the compressive behavior and strength of upright frames with and without reinforcement. The results include the deformation modes, the failure mechanisms, and ultimate

capacities, followed by a discussion on the experimental data. A finite element (FE) model was also employed to investigate the effect of different reinforcement spacing on the upright strength.

3.3. Reinforcement Method

Upright sections can undergo three modes of instabilities under compressive load: Local, distortional, and flexural or flexural-torsional buckling. The design of uprights is remarkably affected by distortional buckling, which has limited the applicability of thin-walled CFS profiles.

Generally, the compressive strength of open sections is significantly lower than the compressive resistance of closed sections since open sections are more prone to warping and buckling effects than closed sections. Yet, closed section production is very costly and time-consuming as the CFS industry requires a complicated procedure for providing a section in a closed-form. Therefore, increasing the capacity of upright frames can be obtained by offering a partially closed section which is more straightforward and more cost-effective. To achieve this goal, an innovative and simple approach for partially closing of upright sections was employed in this study. Using this method, the mode of failure can be controlled to have a significant change in the overall behavior of the compression element.

Each upright frame consists of a regular pattern of perforations which can be placed on both the web and the flanges. The web perforation is used for fast interconnection between beams and uprights, while the flanges' perforations allow for the connection of brace components to uprights. Those perforations which are not in use in the section can also be employed for partial closing of section. Therefore, in this study, connectors using bolts, nuts, and spacers are utilized at the location of perforations to connect the flanges of the open section, and thereafter create a partially closed section offering a higher load capacity system. Spacers are the transverse elements made up of the plastic material, which are commonly used for bracing of racking frames. Figure 3-1 schematically shows the proposed reinforcing method on the open CFS upright frame.

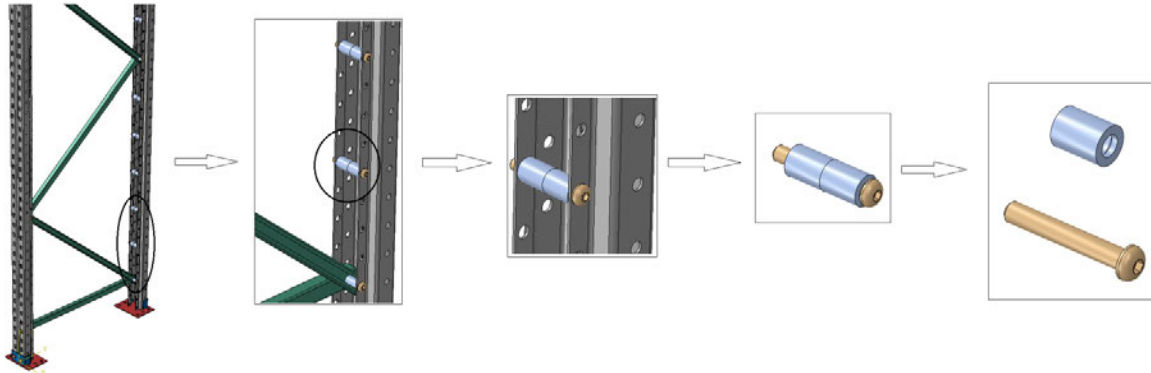


Figure 3-1: Schematic of the proposed reinforcing method.

It should be noted that in the racking industry, usually a single long upright is employed for the total height since it is costly and time-consuming to cut and splice the element. This strategy is uneconomical because for higher levels of racking systems, where the applied loads are low compared to those at bottom levels, the thickness of sections is considered to be the same as thickness at the lower height. In other words, the upright section is overdesigned for the higher levels which causes some economic issues. The proposed method on the other hand can be used to overcome this unnecessary steel usage. Low thick upright sections can be utilized for storage rack in which the lower level is strengthened by the proposed method to provide higher capacity. This approach can significantly reduce the cost of making these structures.

Preliminary numerical analysis was also performed in order to check the feasibility and capability of the proposed method, and it was found that this approach can increase the load-bearing capacity of standard uprights. The reinforcement method proposed in this study is a simple, time and cost-effective approach which can be employed for many CFS open sections [28,29,30,31].

3.4. Experimental Test

An extensive experimental study was planned and carried out at the structural laboratory of Western Sydney University in order to investigate the effect of reinforcement on the upright capacity. Experimental tests on various upright lengths from short to long (as is used in the industry) with two different thicknesses were carried out using two scenarios of reinforcements (employing reinforcement at 200 mm and 400 mm). First, specimens without reinforcement were tested to capture the buckling strength and mode of failure of currently-in use upright frames.

Then, the specimens reinforced by bolts and spacers were tested again for evaluation of the effect of the reinforced system.

3.4.1 Test Specimens

Nine single uprights and 72 upright frames, each comprising two upright columns attached by diagonal bracing were constructed from commercially available rack sections. The convention used for designation of specimens is explained in Figure 3-2.

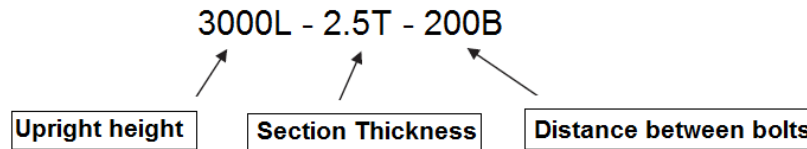


Figure 3-2: Designation of specimens (values in mm).

The test arrangement comprises a frame assembly with 840 mm width from the back of one upright's web to the back of the other upright's web in the frame. A standard section with two different thicknesses of 1.6 mm and 2.5 mm were utilized for the racking frames to examine the effect of thickness on the results. The geometry of the section as well as the perforation details are indicated in Figure 3-3. Due to commercial confidentiality reasons, all geometries are presented in non-dimensional form. In order to determine different failure modes and their corresponding interaction, different lengths of 1200 mm, 1800 mm, 2400 mm, 3000 mm, and 3600 mm were considered, as shown in Figure 3-4. Single upright profile was employed for 1200 mm length because of the limitation on having a full-frame with this length. To consider and prevent the effects of probable specimen geometric imperfections on the test results, each specimen was carefully checked, and all the dimensions were measured at the time of testing in order to identify any defects before the test procedure. So it was confirmed that geometric imperfections do not influence the final results.

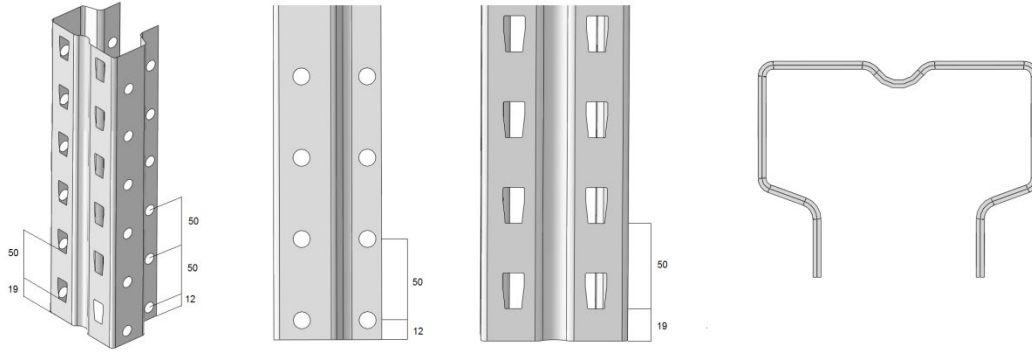


Figure 3-3: Section and perforation details (mm).

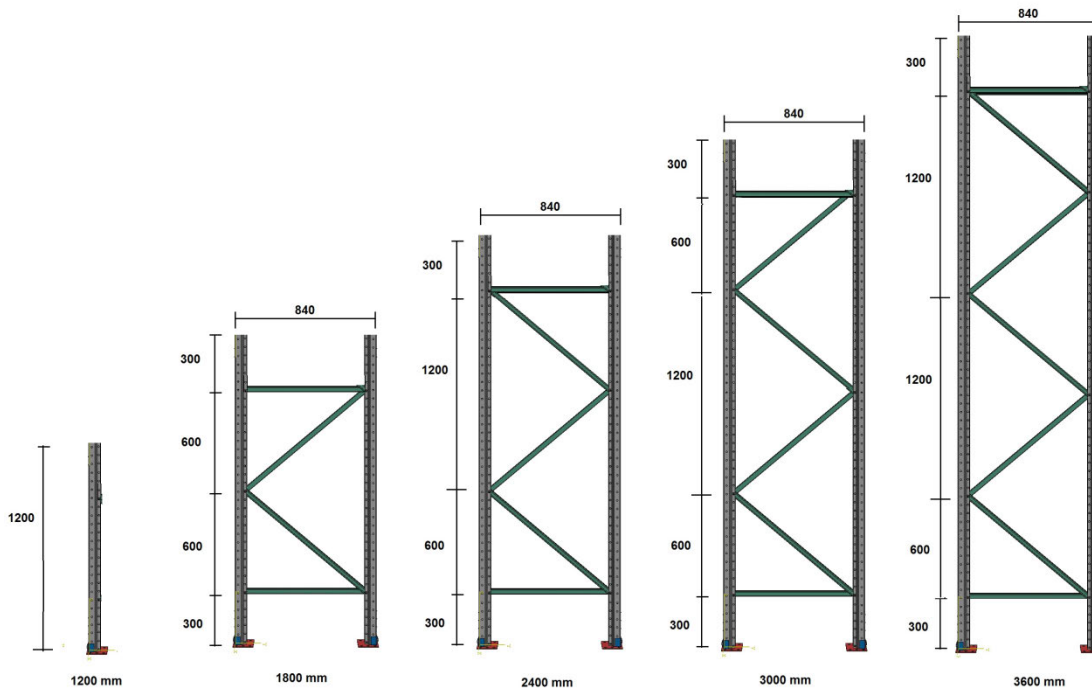


Figure 3-4: Schematic of specimens with different heights (mm).

In order to evaluate the effect of reinforcement on the compressive behavior of uprights, bolts and spacers were attached to the upright at 400 mm and 200 mm space along the upright length. Figure 3-5 shows the example pattern of bolt and spacer attachment for reinforcing of the sections. The details of each specimen including length, thickness, and reinforcement type are also provided in Table 3-1.



Figure 3-5: Reinforcement along the upright length by bolts and spacers.

Table 3-1: Specimen details.

Specimen Designation	Length (mm)	Reinforcement Type	Thickness (mm)
1200L-1.6T		-	
1200L-1.6T-400B	1200	@ 400 mm	
1200L-1.6T-200B		@ 200 mm	
1800L-1.6T		-	
1800L-1.6T-400B	1800	@ 400 mm	
1800L-1.6T-200B		@ 200 mm	
2400L-1.6T		-	
2400L-1.6T-400B	2400	@ 400 mm	1.6
2400L-1.6T-200B		@ 200 mm	
3000L-1.6T		-	
3000L-1.6T-400B	3000	@ 400 mm	
3000L-1.6T-200B		@ 200 mm	
3600L-1.6T		-	
3600L-1.6T-400B	3600	@ 400 mm	
3600L-1.6T-200B		@ 200 mm	
1800L-2.5T		-	
1800L-2.5T-400B	1800	@ 400 mm	
1800L-2.5T-200B		@ 200 mm	
2400L-2.5T		-	
2400L-2.5T-400B	2400	@ 400 mm	
2400L-2.5T-200B		@ 200 mm	2.5
3000L-2.5T		-	
3000L-2.5T-400B	3000	@ 400 mm	
3000L-2.5T-200B		@ 200 mm	
3600L-2.5T		-	
3600L-2.5T-400B	3600	@ 400 mm	
3600L-2.5T-200B		@ 200 mm	

3.4.2 Material Properties

Tensile coupon tests were also carried out to obtain the material properties including yield stress, ultimate stress, and elongation of the specimens. Three coupon samples for each thickness were cut from the flange of the upright where there was no perforation. A 300 kN capacity MTC Sintech testing machine with a rate of 0.01 mm/s was employed for coupon tests following the AS4600 [32] procedures. Figure 3-6 shows the stress-strain curves for both 2.5 mm and 1.6 mm sections. The mean value of the ultimate tensile strength (σ_u), yield stress (σ_y), and elongation are also presented in Table 3-2.

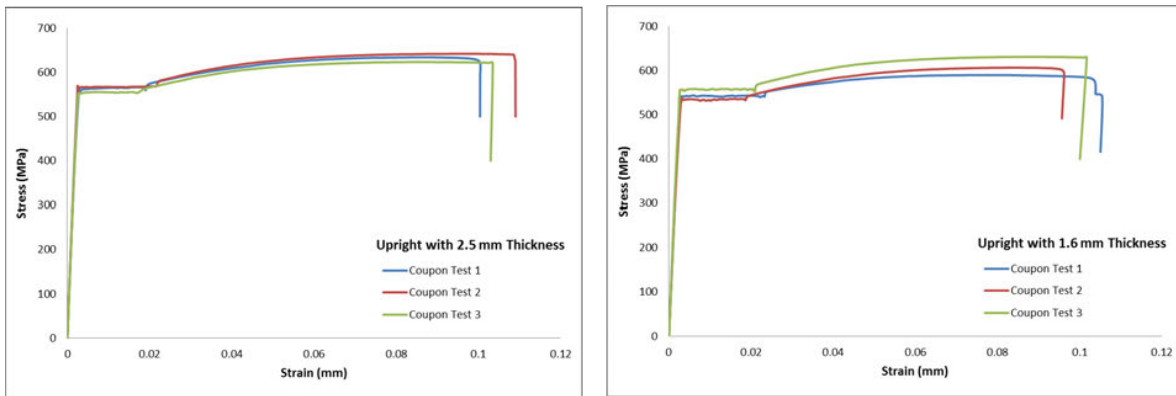


Figure 3-6: Coupon test results for uprights with 1.6 mm and 2.5 mm thickness.

Table 3-2: Material properties of upright sections.

Section Type	Yield Stress, σ_y (MPa)	Ultimate Stress, σ_u (MPa)	Elongation (%)
Upright with 2.5 thickness	572	608	13
Upright with 1.6 thickness	563	591	11

3.4.3 Test Rig and Test Setup

The test rig was prepared according to AS 4084:2012 [33] section C.7.3.2 titled: Compression tests on uprights—determination of buckling curves. The test rig includes a frame assembly in which one of the two uprights is loaded axially, as shown in Figure 3-7. According to the code, the upright is loaded through ball bearings and fitted with base and cap plates. Specimens were free to rotate

about both axes due to the pin-ended bearing, while rotations about the y-axis, as well as torsion, were constrained by the bracing and its connection.

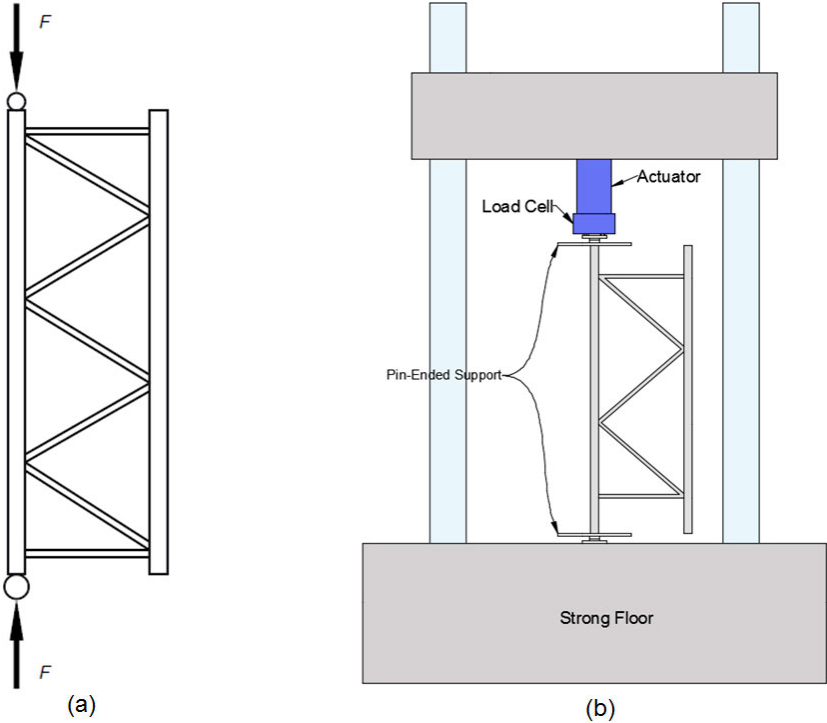


Figure 3-7: (a) Schematic of compressive test on uprights; (b) testing rig.

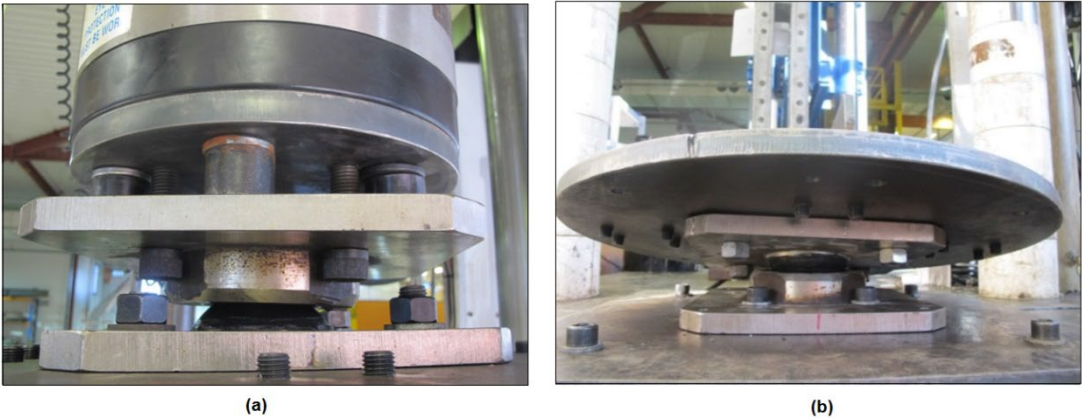


Figure 3-8: (a) Ball bearing; (b) cap plate.

For each test, the upright frame was assembled and positioned in the test rig between the two cap plates, which were designed to ensure uniform load distribution during the test. In order to

minimize any eccentricity of loading, the upright centroid coincided with the centroid of the ball bearing. One of the uprights of each frame was loaded through hemisphere and socket joint fitted with adjustable caps, as shown in Figure 3-9. The upright was free to move on both ends, and the cap did not restrain it as it was not touching the upright on the sides. The other upright was connected by loose bolts to a support column. There was clearance between the support column and the whole frame in order to be free to displace and deflect laterally. Figure 3-10 illustrates the test setup on a typical frame (3600 mm) and depicts the support and connection system used on both ends of one upright.

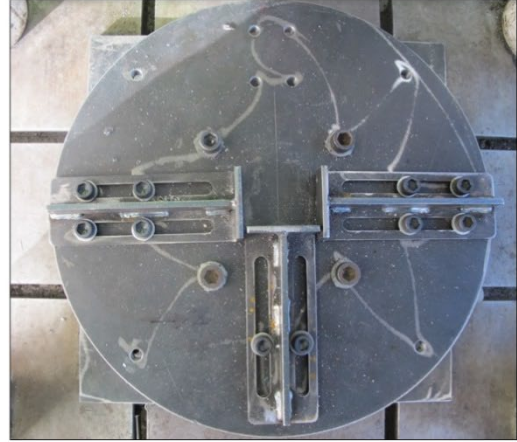


Figure 3-9: Adjustable cap connection supports.



Figure 3-10: 3600 mm specimen and boundary conditions.

3.4.4 Test Procedure

According to the Australian Racking Code, AS4084: 2012 [33], a minimum of three tests are required for each specimen to determine the test data of each upright profile. The tests were carried

out by a universal testing machine, Instron 8506 with a 3000 kN compression capacity hydraulic jack. A load cell of 500 kN capacity was also attached to the jack equipped with a linear variable differential transformer (LVDT) positioned there to record the deformation. Axial load was applied to each of the specimens using a displacement rate of 0.02 mm/s. The applying load was continued until a significant drop in the load-displacement curve of the specimens was observed.

3.5. Preliminary Elastic Buckling

In order to better understand the performance of a single upright member under compressive load, elastic buckling analyses for single upright with both thicknesses (1.6 mm and 2.5 mm) were conducted using the CUFSM package. Figure 3-11 shows the half-wavelength of sections after buckling analysis. It can be observed that for the different ranges of lengths in this study (1200 mm to 3600 mm), the dominant elastic buckling modes are distortional or flexural-torsional modes. In addition, local buckling rarely occurs in these length ranges. This paper aims to investigate the uprights of the in-use commercial rack systems. The so-called signature curves shown in Figure 3-11 refer to a single un-perforated profile and do not accurately predict the behavior of the perforated sections in a system. Besides, in a full upright frame, the connections at the location of bracings provide a restraint for distortional buckling which may change the buckle half-wavelength associated with the distortional buckling mode.

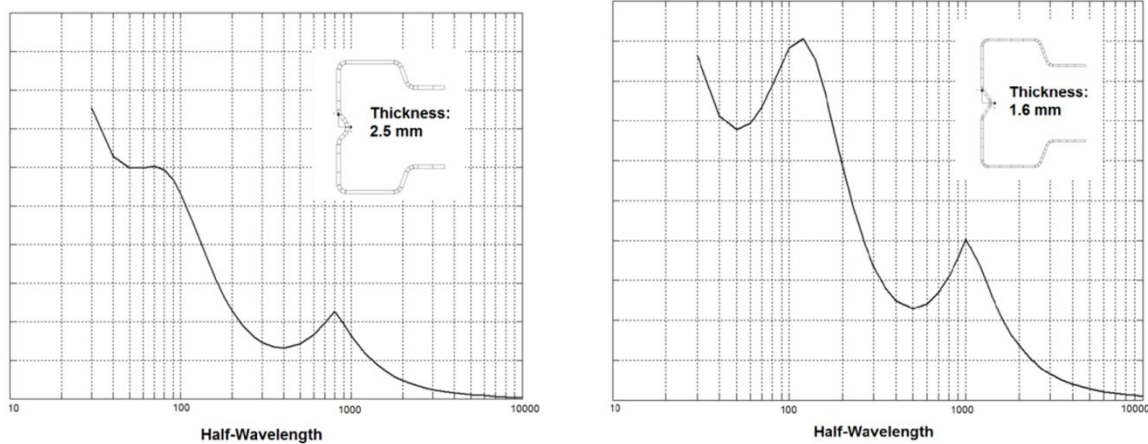


Figure 3-11: Preliminary elastic buckling analyses for the individual un-perforated upright gross sections (stress values have not been disclosed due to confidentiality).

It is expected that the favorable influence of the proposed reinforcement (attaching bolt and spacer) decreases by increasing the length of the element. This can be justified by the fact that the dominant mode of buckling will gradually change from distortional to flexural or flexural-torsional buckling for which the proposed reinforcement method will not be as effective.

3.6. Results

Compression tests were performed on the upright frames with two different thicknesses and five lengths, and the effect of reinforcement at 400 mm and 200 mm was investigated. Ultimate load capacities, as well as failure modes, were recorded from the compression tests and the results were accurately analyzed. At the end of the test, failure modes were investigated based on the experimental observations. For some specimens, it was relatively difficult to detect which mode of failure is dominant since the interaction of two or three buckling modes had occurred.

The ultimate load capacity of each test was extracted and normalized with respect to the gross cross-section (A_g) and the mean yielding strength (σ_y) due to the confidentiality matters. The normalized load-displacement curves of the specimens with 2.5 mm thickness are shown in Figure 3-12. The normalized load value is related to the compressive load applied on top of the upright, while the displacement value shows the deformation of the top head of the upright measured by LVDT. For each specimen type, at least three tests were carried out as recommended by the Australian Racking code (AS4084: 2012) [33]. The reason for the different ultimate values for

these three tests of each specimen can be attributed to the fact that upright elements have different initial geometrical imperfections associated with the manufacturing processes [34].

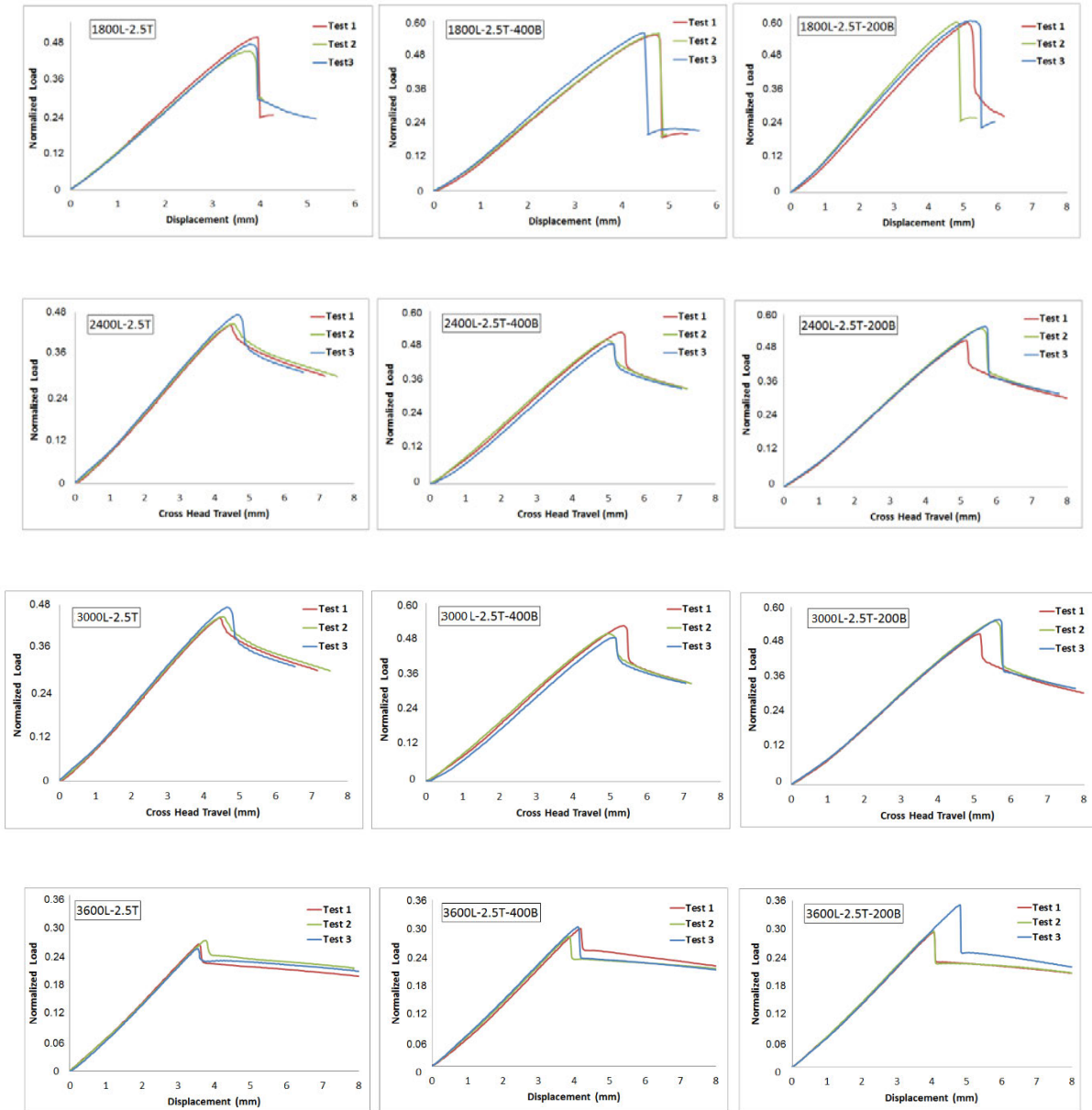


Figure 3-12: Load displacement curves for 2.5 mm thick specimens.

The normalized ultimate load capacity of each test, average value, and standard deviation for each specimen are provided in Table 3-3. In general, three types of failure modes were observed in the experimental tests: (a) Distortional buckling failure which was dominant for specimens with 1800 mm length; (b) flexural or torsional mode or combination of them was also dominant for specimens

with 3000 mm and 3600 mm length; and (c) transition from distortional buckling to flexural buckling failure which happened for specimens with 2400 mm length. Local buckling was also observed in some specimens, especially for 200 mm reinforcement pitch in which the buckle half-wavelength was limited to 200 mm.

Table 3-3: The average normalized ultimate capacity of uprights with 2.5 mm thickness.

Test Specimen	Normalized Buckling Load ($\frac{f}{\sigma_y \times A_g}$)		
	Without Bolt	Reinforcement at 400 mm	Reinforcement at 200 mm
1800L-2.5T-Test 1	0.478	0.548	0.624
1800L-2.5T-Test 2	0.442	0.552	0.639
1800L-2.5T-Test 3	0.457	0.555	0.615
Ave. *	0.457	0.550	0.627
Std. **	0.018	0.004	0.012
2400L-2.5T-Test 1	0.443	0.522	0.510
2400L-2.5T-Test 2	0.446	0.495	0.551
2400L-2.5T-Test 3	0.472	0.482	0.556
Ave.	0.454	0.499	0.538
Std.	0.016	0.020	0.025
3000L-2.5T-Test 1	0.385	0.431	0.445
3000L-2.5T-Test 2	0.361	0.422	0.426
3000L-2.5T-Test 3	0.360	0.365	0.422
Ave.	0.370	0.403	0.433
Std.	0.013	0.035	0.012
3600L-2.5T-Test 1	0.270	0.294	0.292
3600L-2.5T-Test 2	0.273	0.279	0.294
3600L-2.5T-Test 3	0.258	0.302	0.350
Ave.	0.269	0.289	0.310
Std.	0.008	0.012	0.033

* Average
 ** Standard Deviation

According to Figure 3-13, the buckling mode of specimens with 3600 mm and 3000 mm, was hardly affected by employing bolts and spacers at either 200 mm or 400 mm. Therefore, it was concluded that the load capacity for specimens with and without reinforcement at higher length is not affected as significantly as shorter specimens. This is mainly because the buckling mode of failure in high length upright is governed by flexural and torsional flexural buckling, and utilizing reinforcement strategy does not necessarily change or control the buckling mode. It can be noted that one of the most effective parameters that determine the failure mode of the uprights under compression is the upright height and reinforcement might not overcome this issue.



3600L-2.5T



3600L-2.5T-400P



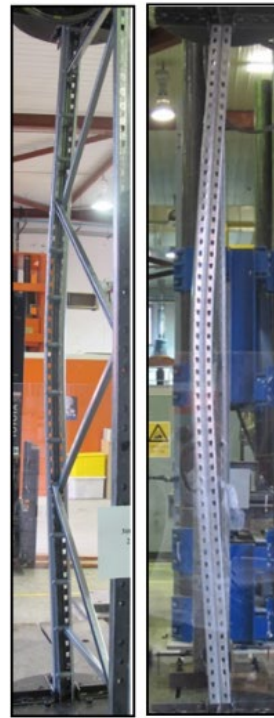
3600L-2.5T-200P



3000L-2.5T



3000L-2.5T-400P



3000L-2.5T-200P

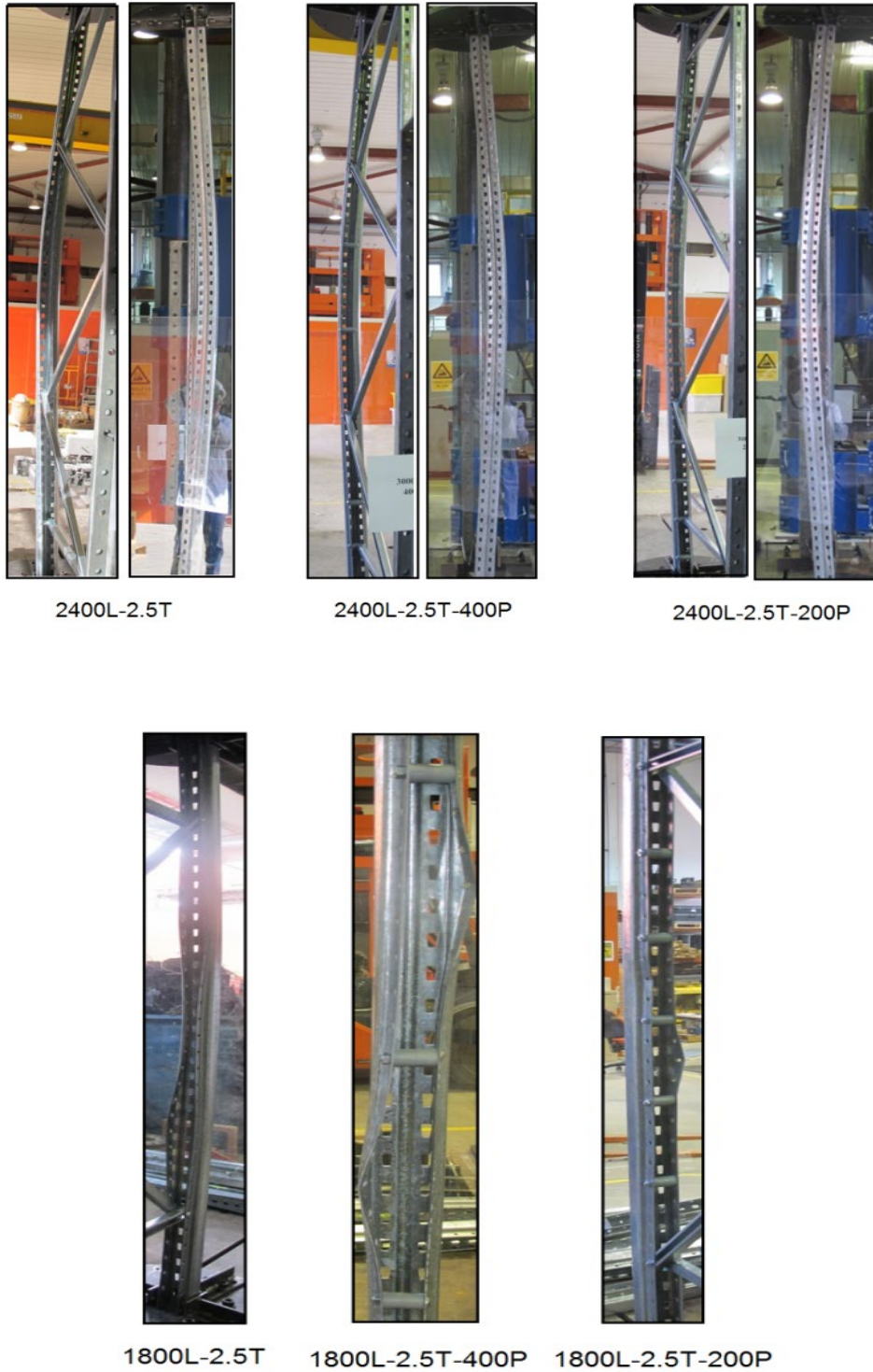
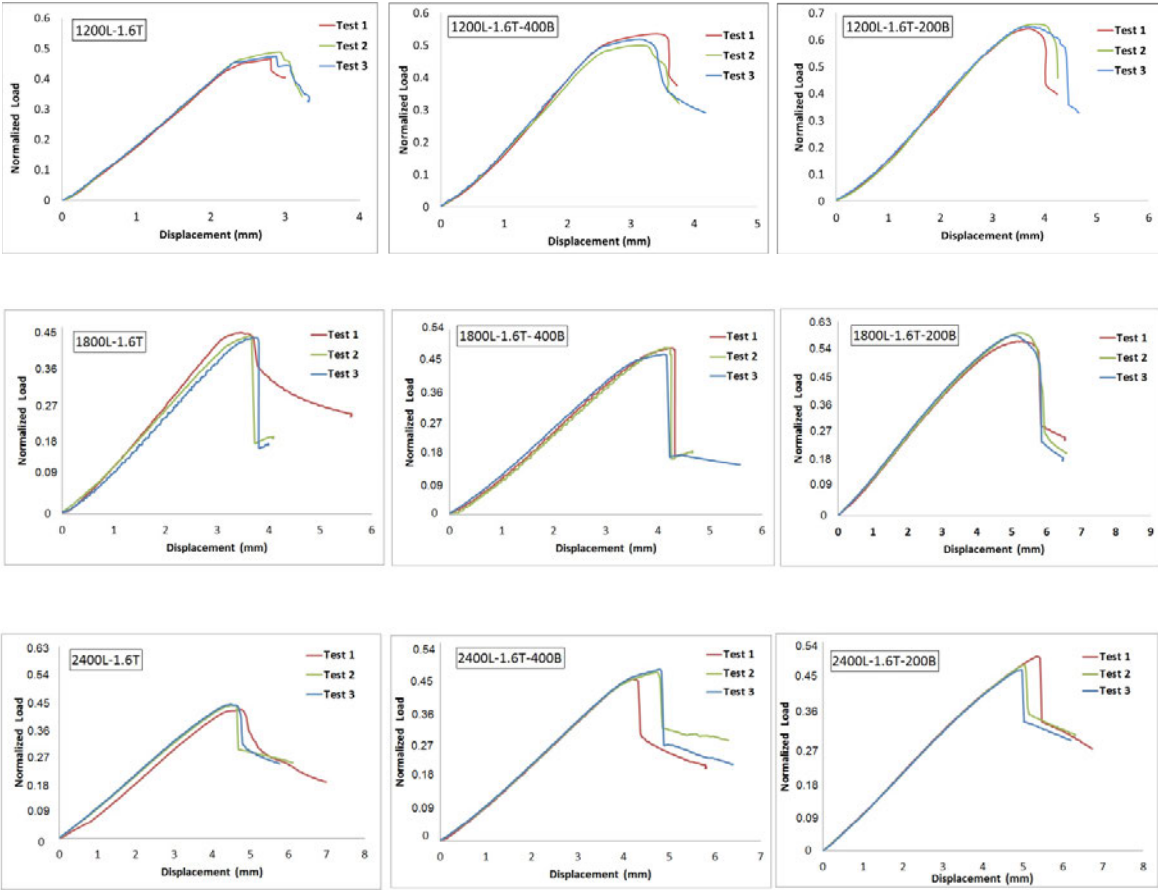


Figure 3-13: Failure modes of upright frames with 2.5 mm thickness.

Interestingly, for the short specimens with 1800 mm and 2400 mm length, the reinforcement system was extremely effective. Distortional buckling was the primary failure mode for these

specimens and utilizing reinforcement could shorten the half-wavelength of the specimen resulting in capturing higher capacity when 400 mm and 200 mm bolts were used. The failure of the short specimens was primarily dominated by distortional buckling of the flange; while, for the taller uprights the elements were vulnerable to flexural-torsional buckling at mid-span where the uprights had low rigidity.

The effect of section thickness on the performance of an upright is considerable and should be investigated through experimental tests. Hereinto, the uprights with lower thickness were also experimentally tested in order to have a better comparison with thicker uprights. The normalized load-displacement curves of specimens with 1.6 mm thickness and their failure modes are shown in Figure 3-14 and Figure 3-15. The average values of normalized ultimate capacity, as well as standard deviations, are also provided in Table 3-4. It was observed that in terms of thickness effect, as the cross-section area of this type of upright is smaller than the area of 2.5 mm thick upright, the ultimate load is significantly reduced.



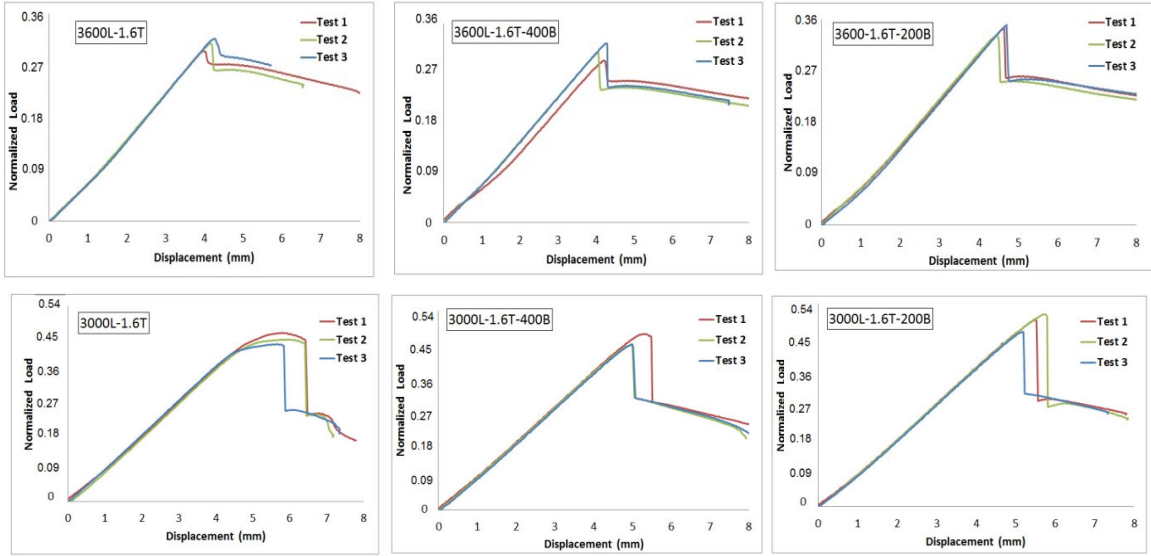


Figure 3-14: Load displacement curves for 1.6 mm thick specimens.



3600L-1.6T 3600L-1.6T-400P 3600L-1.6T-200P 3000L-1.6T 3000L-1.6T-400P 3000L-1.6T-200P



3000L-1.6T



3000L-1.6T-400P



3000L-1.6T-200P



1800L-1.6T



1800L-1.6T-400P



1800L-1.6T-200P



1200L-1.6T



1200L-1.6T-200P

Figure 3-15: Failure modes of upright frames with 1.6 mm thickness.

Table 3-4: The average normalized ultimate capacity of uprights with 1.6 mm thickness.

Test Specimen	Normalized Buckling Load ($\frac{f}{\sigma_y \times A_g}$)		
	Without Bolt	Reinforcement at 400 mm	Reinforcement at 200 mm
1200L-1.6T-Test 1	0.471	0.542	0.646
1200L-1.6T-Test 2	0.483	0.504	0.665
1200L-1.6T-Test 3	0.476	0.520	0.650
Ave.	0.476	0.522	0.653
Std.	0.005	0.018	0.009
1800L-1.6T-Test 1	0.451	0.503	0.576
1800L-1.6T-Test 2	0.444	0.503	0.610
1800L-1.6T-Test 3	0.440	0.485	0.593
Ave.	0.446	0.497	0.590
Std.	0.005	0.010	0.017
2400L-1.6T-Test 1	0.440	0.454	0.525
2400L-1.6T-Test 2	0.450	0.475	0.504
2400L-1.6T-Test 3	0.451	0.482	0.484
Ave.	0.446	0.469	0.501
Std.	0.006	0.014	0.020
3000L-1.6T-Test 1	0.472	0.492	0.513
3000L-1.6T-Test 2	0.469	0.465	0.533
3000L-1.6T-Test 3	0.455	0.468	0.485
Ave.	0.464	0.473	0.506
Std.	0.009	0.014	0.024
3600L-1.6T-Test 1	0.308	0.303	0.346
3600L-1.6T-Test 2	0.320	0.328	0.339
3600L-1.6T-Test 3	0.330	0.342	0.349
Ave.	0.320	0.325	0.343
Std.	0.011	0.019	0.004

As shown in Figure 3-14 and Figure 3-15, the load-displacement trends and failure mode patterns for uprights with 1.6 mm thickness are somewhat similar to those observed in the tests for uprights with 2.5 mm thickness. For the 1.6 mm thick specimens, distortional buckling was the primary buckling failure for specimens with 1200 mm and 1800 mm length, while for the specimen with 2400 mm the failure was followed by flexural buckling or flexural-torsional buckling mode. For specimens with 3000 mm and 3600 mm length, the primary failure was flexural-torsional buckling of upright about the weak axis.

Similar to uprights with 2.5 mm thickness, the failure mode observation reveals that the reinforcement has a slight influence on the ultimate load-bearing capacity of uprights with 3000 mm and 3600 mm and the best application of reinforcement method is for lower lengths of 1200 mm and 1800 mm due to the improvements in local and distortional buckling modes.

3.7. Discussion

In order to compare the capacity of different uprights, the average value of normalized ultimate loads was determined according to the test results. Figure 3-16 shows the normalized ultimate load capacity of uprights for both 1.6 mm and 2.5 mm thicknesses. The values of normalized ultimate loads are grouped by upright length and the type of reinforcement (bolt at 200 mm and 400 mm). As indicated in this figure, the ultimate load capacity improvement due to the reinforcement of the uprights, with different thickness and reinforcement, is decreased by increasing the upright length. This can be justified by this fact that at higher length the dominant buckling mode is flexural buckling failure mode which is not much affected by the proposed reinforcement method; therefore, increasing the ultimate capacity of the upright at higher lengths could not be achieved considerably. Figure 3-16 also indicates that employing bolt and spacer at 200 and 400 mm provides higher ultimate capacity compared to uprights without bolt and spacer which represents the capability of the proposed simple reinforcement method for increasing the load-bearing capacity of uprights.

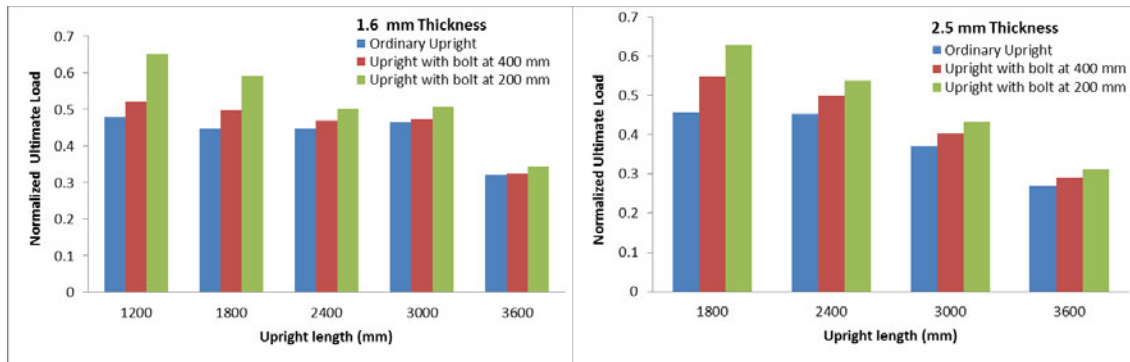


Figure 3-16: Comparison of normalized ultimate load capacity.

The effect of reinforcement spacing on the ultimate load capacity of uprights is also illustrated in Figure 3-17. As shown in this figure, a significant difference in the increase of the ultimate load capacity is observed for specimens 1800L-1.6T and 1800L-2.5T with reinforcement spacing of 200 mm compared to the 400 mm. For 1800L-1.6T upright, 33% and 12% increase in ultimate capacity resulted by employing bolts at 200 mm and 400 mm, respectively. A similar trend was

also observed for 1800L-2.5T upright with 37% and 20% increase in ultimate capacity by employing bolts at 200 mm and 400 mm, respectively.

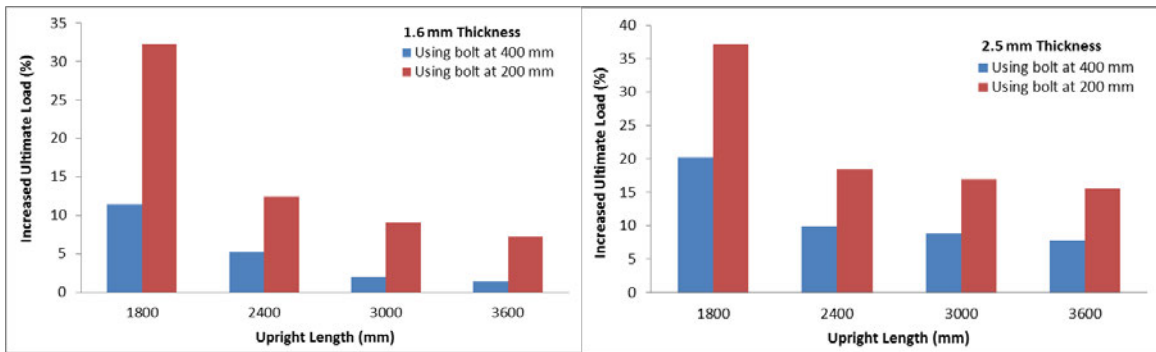


Figure 3-17: Effect of reinforcement by increasing the upright height.

As shown in Figure 3-17, the effect of employing bolt and spacer in uprights ultimate capacity is decreased by increasing the upright height. Comparing 1800L-1.6T and 3600L-1.6T specimens show that the difference between the increase in load capacity of two types of reinforcement (bolt at 400 mm and 200 mm) decreases from 23% for 1800 mm upright to 5% for 3600 mm upright. The same behavior was also captured for 2.5 mm thickness upright (1800L-2.5T and 3600L-2.5T) showing that the difference between the increased ultimate loads for the two types of reinforcement is 17% and 5% for 1800 mm and 3600 mm uprights, respectively. This indicates that the application of bolt reinforcement in shorter pitches (200 mm) in longer uprights does not offer extra resistance as much as it provides for shorter uprights since the failure of longer uprights is dominated by flexural buckling mode. Therefore, it can be concluded that although reducing the spacing of the bolts and spacers can improve the distortional buckling capacity considerably; as discussed earlier, the effect of the reinforcement spacing on buckling mode change for higher lengths uprights is not considerable.

Figure 3-18 shows the effect of section thickness on the results of reinforced uprights. As shown in this figure, the reinforcement in 2.5 mm thick upright could increase the ultimate load capacity of upright much more than reinforcement in uprights with 1.6 mm thickness. A similar trend was observed in both types of uprights with 200 mm and 400 mm bolt and spacer; however, the difference between increased ultimate load for specimens with 200B is less than the difference between increased ultimate loads for specimens with 400B, for both thicknesses. In other words,

when uprights were reinforced with bolts at 200 mm, the increased ultimate load percentage for 2.5 mm upright was closer to the increased ultimate load for upright with 1.6 mm compared to the other type of reinforcement (at 400 mm).

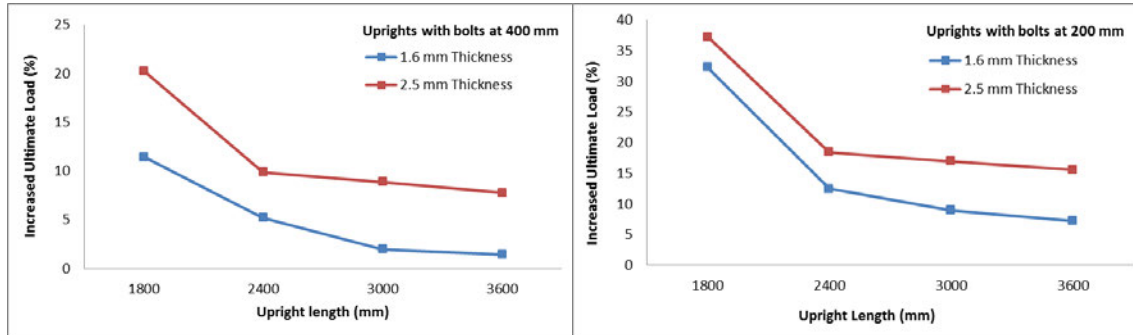


Figure 3-18: Effect of reinforcement on the different upright thickness.

For the 1800L-1.6T-400P and 1800L-2.5T-400P uprights, the increased ultimate load capacity was 10% and 20%, respectively. Nevertheless, the values for the condition of having bolts spaced at 200 mm were 33% and 37% for uprights with 1.6 mm and 2.5 mm thickness. Similar behavior was observed for the other upright heights showing that the 200 mm attachment of bolts can decrease the weakness of having a low thickness section. Yet, the decrease in ultimate capacity is lower when 2.5 mm thickness section is employed. For 3600L-2.5T uprights, the application of bolts at 200 mm and 400 mm could increase the ultimate resistance by 15% and 7%, respectively; while for the same height and lower thickness (3600L-1.6T) the increased values are 7% (for bolts at 200 mm) and 3% (for bolts at 200 mm) which indicates the weakness of reinforcement for low thickness sections at high length.

According to the experimental results, it is recommended to use the reinforcement system for currently-in use racking frames in order to improve their performance under compression load. In addition, the steel tonnage of the frame and consequently, the cost of the rack system could be significantly decreased when thinner gauged sections with reinforcement are employed. It should be noted that this method is not limited to rack uprights and can also be used for any CFS C profile with flange perforations. For other CFS profiles such as L and T sections, further evaluation on the reinforcing method is required. As a future study, other reinforcement approaches can also be examined in order to find other feasible approaches for controlling torsional or flexural-torsional buckling modes which are the dominant failure modes for long uprights. Optimization techniques

can also be performed in order to determine the sufficient distance of the reinforcement with bolt and spacer [35,36].

3.8. Finite Element (FE) Modelling

In this paper, FE model is also employed in order to investigate the effect of other reinforcement spacing including 50 mm, 100 mm, 150 mm, 250 mm, 300 mm, and 350 mm on the strength of the upright frames. According to the experimental results, the reinforcement method was most effective for the uprights with lower height in which the distortional buckling could significantly be controlled. Therefore, the detailed FE model with the simulation of all perforations is developed here for frames with 1800 mm height using ABAQUS package [37]. First, the numerical method is well presented in details and then verified against the experimental data provided in Section 3.6. Finally, the effect of the different reinforcement spacing is assessed through the validated numerical model.

3.8.1 Material Properties

The stress-strain data from the coupon tests were utilized for the simulation of the material properties. The true stress-strain relationship is used to account for the change in cross-section area of the coupon resulting from Poisson's effects in numerical models [38,39]. The true stress (σ_{true}) and true strain (ϵ_{true}) can be obtained using the following equations:

$$\sigma_{\text{true}} = \sigma(1 + \epsilon) \quad (1.1)$$

$$\epsilon_{\text{true}} = \ln(1 + \epsilon) - \frac{\sigma_{\text{true}}}{E} \quad (1.2)$$

where σ and ϵ are the stresses and strains obtained from the coupon tests. The von Mises yield criteria with isotropic hardening were also considered for the simulation. In addition, the Poisson ratio and the module of elasticity were assumed equal to 0.3 and 200 GPa, respectively.

3.8.2 Connections and Interactions

Generally, two types of interactions need to be defined for the numerical model of upright frames under compression load: (a) The interaction between the upright flange edges and bracing web, and (b) the interaction between the webs of two braces at the location of the bolt connections. The surface to surface interaction with hard contact for normal behavior, as well as penalty method with the friction coefficient of 0.3 for the tangential behavior were adopted for model interactions. Coupling method and beam connectors were also utilized for modelling of the bolts. At each bolt location, a reference point was created at the center of the hole where the upright flange (at the hole region) was restrained to this reference point using the coupling method [37]. Then the reference points at two opposite sides of the upright section were connected to each other using a beam connector. This type of connector constrains the axial translational degree of freedom between connecting nodes, simulating the actual bolt behavior in the upright frame. Figure 3-19 shows the interaction between frame elements as well as the modelling of the bolt in the upright frame.

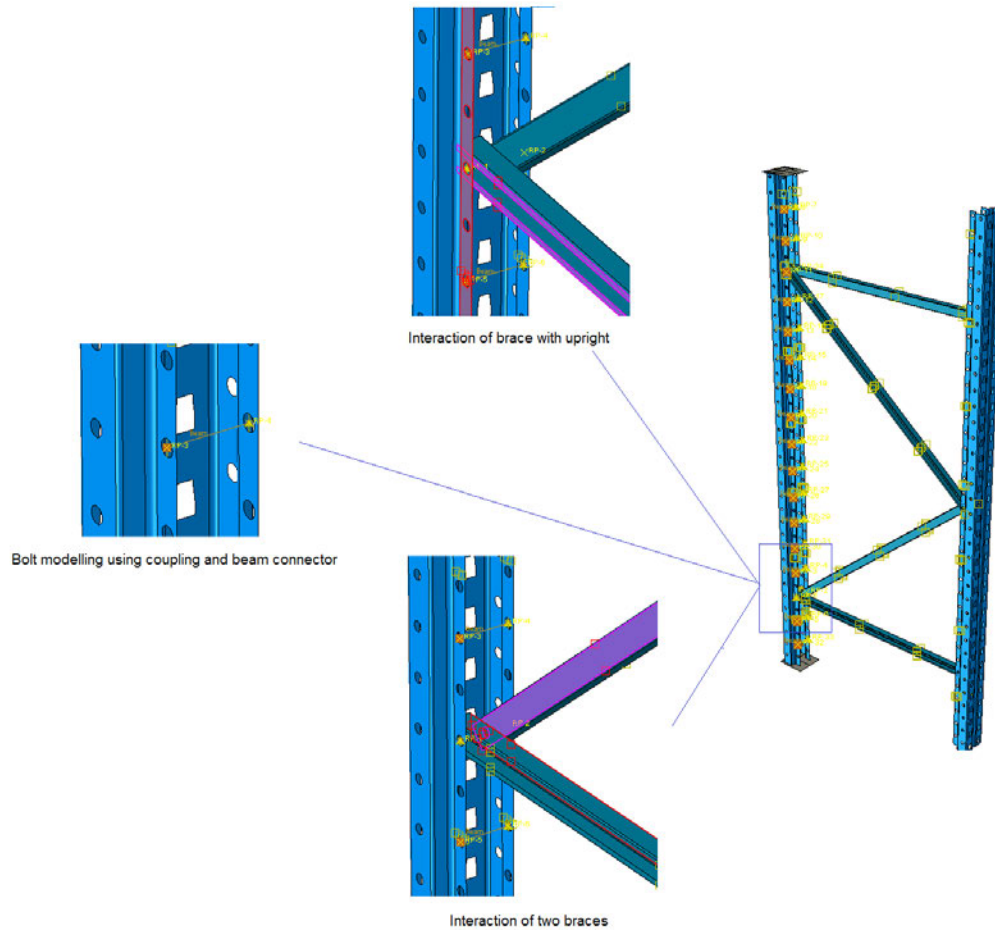


Figure 3-19: Interaction of the frame elements as well as bolt modelling.

3.8.3 Boundary Conditions and Loading

Similar to the experimental test, the pinned-end condition was also adopted for modelling of the upright frame. All element edges at the top and bottom of the upright were constrained to a reference point at the cross-section neutral axis with coupling method in order to simulate the center of the ball bearings. This means that all the displacements of the cross-section at the end are tied to the centroid by coupling constraint. The concentrated load with displacement method was applied at the top reference point. At the other end of the upright, all three translations together were restrained ($U_x = U_y = U_z = 0$), while the rotations about the maximum and minimum moment of inertia axes were allowed to simulate the actual test conditions.

3.8.4 Mesh

Shell elements were employed in this study since the thickness of the open CFS members is very small compared to their width and length; thus, buckling deformations could be explicitly modelled [37,40]. The four-noded shell element with reduced integration (S4R) was utilized for modelling of the frame elements. Convergence study was performed to capture the optimum mesh size for the upright and bracing members and it was observed that quad dominated meshes (type of mesh in the visual mode of ABAQUS) with dimensions of 10 mm were deemed satisfactory for frame elements. The final mesh used for the upright models is shown in Figure 3-20.

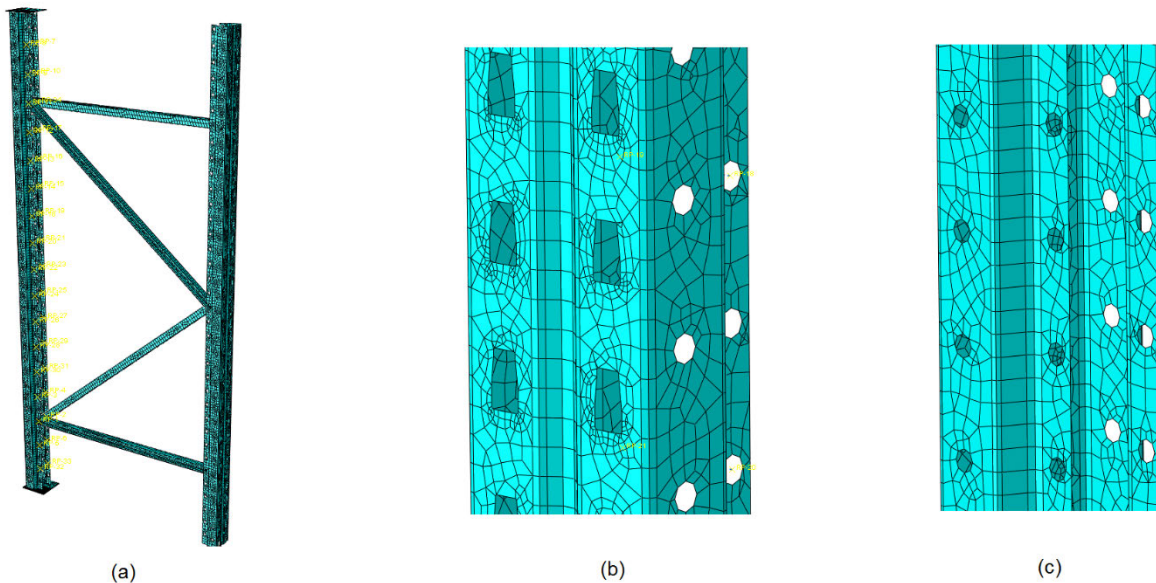


Figure 3-20: (a) Full frame meshing, (b) meshing around the polygon perforations, and (c) meshing around the circular perforations.

3.8.5 Validation of the FE Model

Experimental results obtained from upright with 1800 mm height for both thicknesses were used to evaluate the validity and accuracy of the numerical model. Figure 3-21 and Figure 3-22 show the comparisons between the numerical and test results in terms of load-displacement curves for uprights with 1.6 mm and 2.5 mm thickness, respectively. As indicated in these figures, the developed FE model predicts well the overall load-displacement curve of the specimens. The slight

differences between the numerical and the experimental results can be attributed to this point that the load in the actual test could not precisely be applied at the centroid of the section which can cause a different eccentricity compared to numerical inputs.

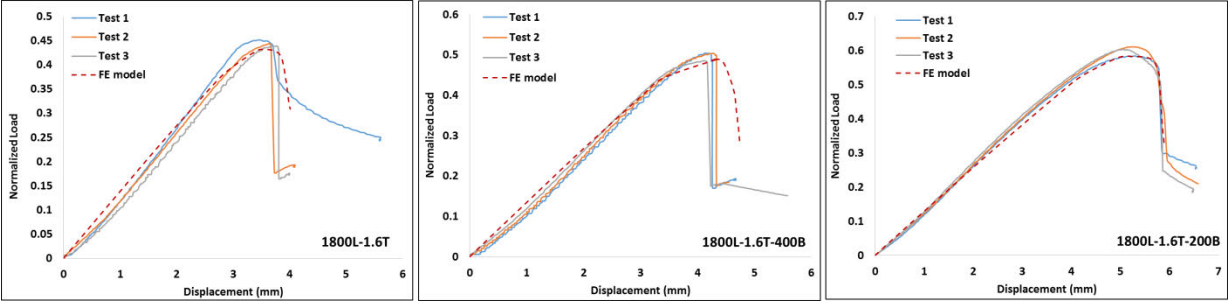


Figure 3-21: Comparison of the finite element (FE) model against the experimental data for 1.6 mm thick uprights.

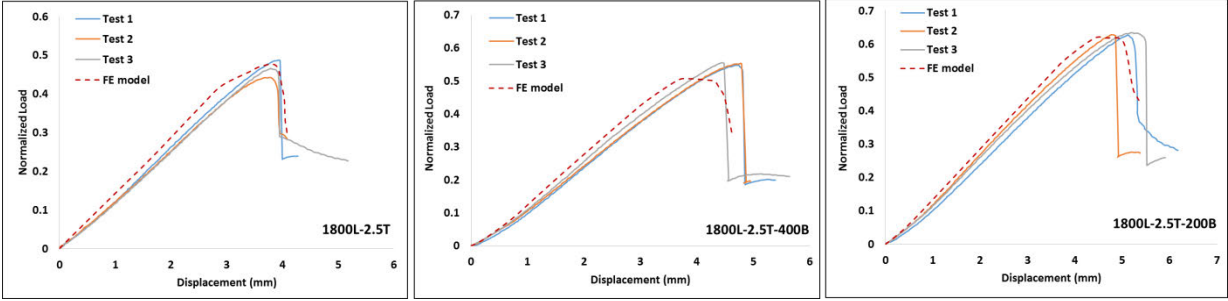


Figure 3-22: Comparison of the FE model against the experimental data for 2.5 mm thick uprights.

Figure 3-23 also illustrates the final deformation of uprights for both numerical model and experimental test. Similar to the experimental deformations, the figure shows that the FE method is able to capture the overall behavior of the upright frames.

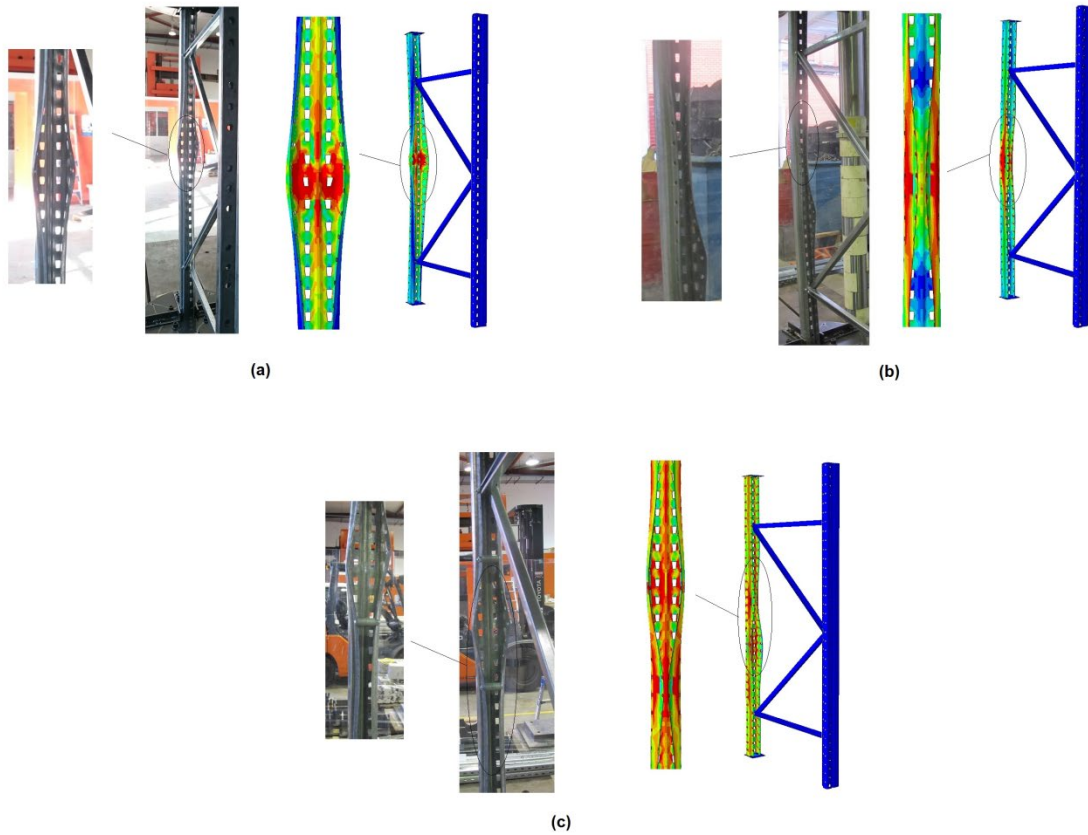


Figure 3-23: Comparison of failure modes, (a) 1800L-1.6T, (b)1800L-2.5T, (c)1800L-1.6T-400B.

Comparing FE and experimental results in terms of the load-displacement curve and deformation contours shows that the FE model is capable of estimating the overall behavior of the upright frame. Therefore, the numerical modelling is reliable enough to undertake a further study for investigating the effects of different reinforcement spacing on the buckling behavior of uprights.

3.8.6 Effect of Different Reinforcement Spacing

Overall, eight different reinforcement spacings including 50 mm, 100 mm, 150 mm, 200 mm, 250 mm, 300 mm, 350 mm, and 400 mm were considered for the parametric study. Due to the location of the perforations, the spacing allocation was limited to 50 mm intervals. The numerical analyses were performed for both 1.6 mm and 2.5 mm thick upright frames and the results were compared with each other. Figure 3-24 shows the normalized load-displacement curves of the numerical models for both thicknesses. It can be observed that, employing more reinforcement to partially

close the section leads to increase in the strength of the upright, which means that reinforcement should be taken into account, especially for uprights with a shorter length.

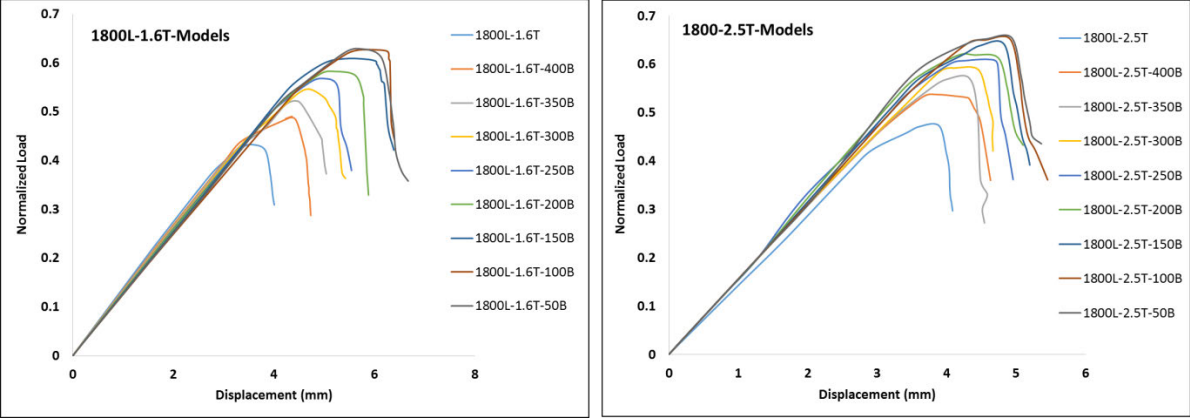


Figure 3-24: Load-displacement curves of uprights with different reinforcement spacing.

The normalized ultimate strength of the uprights with different reinforcement spacing is also represented in Figure 3-25. From this figure, it is concluded that by employing shorter reinforcement spacing, the ultimate strength of the sections increases, which may contribute to the reduction in the buckling length of the section and enhancement of load sharing between the bolts. In fact, the distortional buckling behavior is improved, and section failure is changed from distortional buckling to overall buckling mainly due to partial closing of the upright section. A similar outcome is observed for both thicknesses in which increasing the number of reinforcement improves the ultimate strength of the upright for both the type of sections.

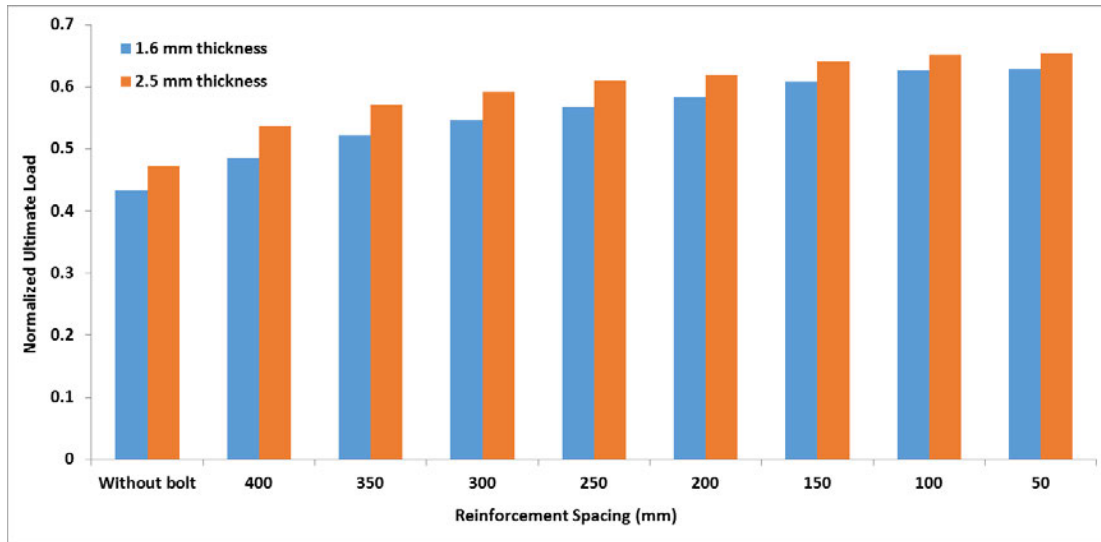


Figure 3-25: The normalized ultimate load of 1800L uprights with different reinforcement ratio.

Figure 3-26 also shows the percentage of increased ultimate strength using different reinforcement spacing in respect to upright without reinforcement condition. Generally, the reinforcement method could have a reasonable effect on the ultimate capacity of the upright frame through increasing its capacity to the range 10% to 45%. As indicated in this figure, the addition of reinforcement from 400 mm spacing to 50 mm spacing in 1800L models can enhance the frame's strength around 35% and 40% for uprights with 1.6 and 2.5 thicknesses, respectively. It is also shown that up to 100 mm reinforcement spacing, decreasing the reinforcement spacing can noticeably increase the ultimate strength of the upright under compression load; however, less difference in increased ultimate load is observed when reinforcement spacing decreased from 100 mm to 50 mm.

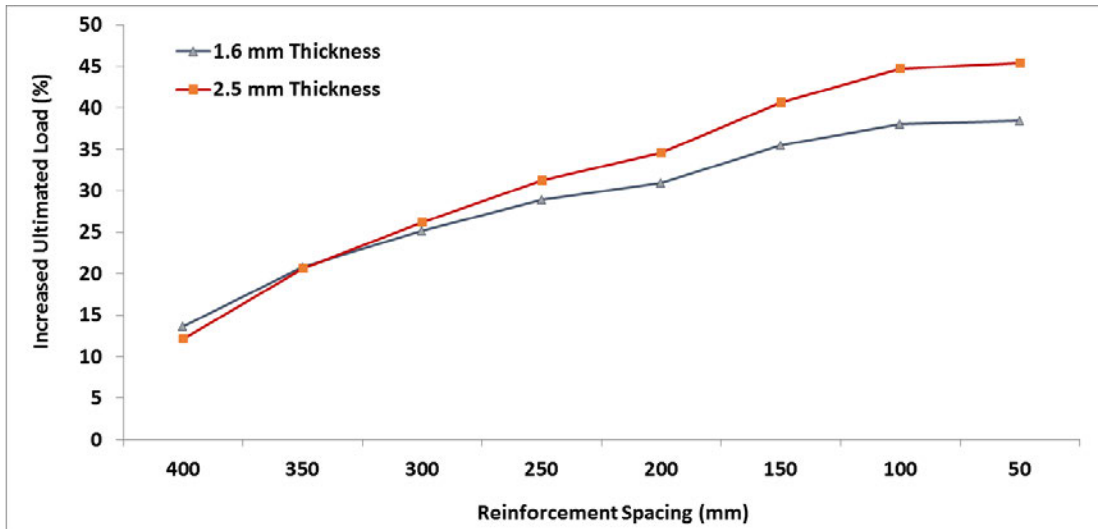


Figure 3-26: Percentage of increased ultimate load of 1800L uprights with different reinforcement spacing.

3.9. Conclusions

This study investigated the effect of a proposed reinforcement method on the compressive performance of upright frames. An extensive experimental program was conducted on 75 upright frames, and 9 single uprights with different thicknesses and heights, and the corresponding results obtained from the tests were analyzed. The reinforcement system was proposed in such a way that bolts and spacers were attached along the upright height. Experimental tests showed that the application of the reinforcement system is significantly effective for increasing the load-bearing capacity when distortional buckling failure mode governs. However, the application of this method is not particularly useful for taller frames. This justifies the fact that this reinforcing method (i.e., using bolts and spacers to partially close off the open profile) is predominantly effective on distortional buckling mode and has minimal effect on other buckling modes (torsional, flexural/torsional, local, and flexural). In addition, compared to thinner uprights (1.6 mm thick), thicker uprights (2.5 mm thick) showed higher capacity improvement (percentage of increased load compared to unreinforced frame) when reinforced with bolts and spacers. The results also showed that the reinforcement has a significant influence not only on the ultimate load capacity but also on the buckling failure mode of low length upright frames (1200 mm, 1800 mm, and 2400 mm). Numerical simulation was also employed in order to investigate the effect of different reinforcement spacing on the performance of the upright frame. It was indicated that up to 100 mm

reinforcement spacing, decreasing the reinforcement spacing can increase the ultimate strength of the upright under compression load; while less improvement was observed when reinforcement spacing decreased from 100 mm to 50 mm.

Further experimental and theoretical attempts are required in order to better understand the behavior of open perforated profiles reinforced with bolts and spacers as well as other materials. Finite element method is also needed for a parametric study of different types of reinforcement systems.

3.10. References

1. Yang, N.; Bai, F. Damage Analysis and Evaluation of Light Steel Structures Exposed to Wind Hazards. *Appl. Sci.* **2017**, *7*, 239.
2. Sharafi, P.; Mortazavi, M.; Usefi, N.; Kildashti, K.; Ronagh, H.; Samali, B. Lateral force resisting systems in lightweight steel frames: Recent research advances. *Thin-Walled Struct.* **2018**, *130*, 231–253.
3. Javidan, M.M.; Kang, H.; Isobe, D.; Kim, J. Computationally efficient framework for probabilistic collapse analysis of structures under extreme actions. *Eng. Struct.* **2018**, *172*, 440–452.
4. Ahmadi, R.; Rashidian, O.; Abbasnia, R.; Nav, F.M.; Usefi, N. Experimental and numerical evaluation of progressive collapse behavior in scaled RC beam-column subassembly. *Shock Vib.* **2016**, *2016*, Article ID 3748435.
5. Shayanfar, M.A.; Javidan, M.M. Progressive Collapse-Resisting Mechanisms and Robustness of RC Frame–Shear Wall Structures. *J. Perform. Constr. Facil.* **2017**, *31*, 04017045.
6. Javidan, M.M.; Kim, J. Variance-based global sensitivity analysis for fuzzy random structural systems. *Comput. Aided Civ. Infrastruct. Eng.* **2019**, *34*, 602–615.
7. Koen, D.J. *Structural Capacity of Light Gauge Steel Storage Rack Uprights*; University of Sydney: Sydney, Australia, 2008.
8. Michael Davies, J.; Leach, P.; Taylor, A. The design of perforated cold-formed steel sections subject to axial load and bending. *Thin-Walled Struct.* **1997**, *29*, 141–157.
9. Trouncer, A.N.; Rasmussen, K.J.R. Flexural–torsional buckling of ultra light-gauge steel storage rack uprights. *Thin-Walled Struct.* **2014**, *81*, 159–174.
10. Standard, B. Steel static storage systems—Adjustable pallet racking systems—Principles for structural design. *BS EN* **2009**, *15512*, 15512.
11. Gilbert, B.P.; Rasmussen, K.J.R. Bolted moment connections in drive-in and drive-through steel storage racks. *J. Constr. Steel Res.* **2010**, *66*, 755–766.
12. Dinis, P.B.; Young, B.; Camotim, D. Strength, interactive failure and design of web-stiffened lipped channel columns exhibiting distortional buckling. *Thin-Walled Struct.* **2014**, *81*, 195–209.
13. Roure, F.; Pastor, M.M.; Casafont, M.; Somalo, M.R. Stub column tests for racking design: Experimental testing, FE analysis and EC3. *Thin-Walled Struct.* **2011**, *49*, 167–184.
14. Casafont, M.; Pastor, M.M.; Roure, F.; Peköz, T. An experimental investigation of distortional buckling of steel storage rack columns. *Thin-Walled Struct.* **2011**, *49*, 933–946.
15. Zhao, X.; Ren, C.; Qin, R. An experimental investigation into perforated and non-perforated steel storage rack uprights. *Thin-Walled Struct.* **2017**, *112*, 159–172.

16. Rhodes, J.; Schneider, F.D. *The Compressional Behaviour of Perforated Elements*; Saint Louis, Missouri, USA, 1994.
17. Moen, C.D.; Schafer, B.W. Experiments on cold-formed steel columns with holes. *Thin-Walled Struct.* **2008**, *46*, 1164–1182.
18. Moen, C.D.; Schafer, B.W. Elastic buckling of cold-formed steel columns and beams with holes. *Eng. Struct.* **2009**, *31*, 2812–2824.
19. Baldassino, N.; Hancock, G. Distortional Buckling of Cold-Formed Steel Storage Rack Section including Perforations. In Proceedings of the 4th International Conference on Steel and Aluminum Structures, Espoo, Finland, 20-23 June 1999..
20. Talikoti, R.; Bajoria, K. New approach to improving distortional strength of intermediate length thin-walled open section columns. *Electron. J. Struct. Eng.* **2005**, *5*, 69–79.
21. Veljkovic, M.; Johansson, B. Thin-walled steel columns with partially closed cross-section: Tests and computer simulations. *J. Constr. Steel Res.* **2008**, *64*, 816–821.
22. Manikandan, P.; Arun, N. Behaviour of Partially Closed Stiffened Cold-Formed Steel Compression Member. *Arab. J. Sci. Eng.* **2016**, *41*, 3865–3875.
23. Anbarasu, M.; Amali, D.; Sukumar, S. New approach to improve the distortional strength of intermediate length web stiffened thin walled open columns. *KSCE J. Civ. Eng.* **2013**, *17*, 1720–1727.
24. Anbarasu, M.; Kumar, S.B.; Sukumar, S. Study on the effect of ties in the intermediate length cold formed steel (CFS) columns. *Struct. Eng. Mech.* **2013**, *46*, 323–335.
25. Anbarasu, M.; Sukumar, S. Effect of connectors interaction in behaviour and ultimate strength of intermediate length cold formed steel open columns. *Asian J. Civ. Eng. (BHRC)* **2013**, *14*, 305–317.
26. Anbarasu, M.; Sukumar, S. Finite Element-Based Investigation on Performance of Intermediate Length Thin-walled Columns with Lateral Stiffeners. *Arab. J. Sci. Eng.* **2014**, *39*, 6907–6917.
27. Anbarasu, M.; Sukumar, S. Influence of Spacers on Ultimate Strength of Intermediate Length Thin walled Columns. *Steel Compos. Struct. Int. J.* **2014**, *16*, 437–454.
28. Ye, J.; Jiang, L.; Wang, X. Seismic Failure Mechanism of Reinforced Cold-Formed Steel Shear Wall System Based on Structural Vulnerability Analysis. *Appl. Sci.* **2017**, *7*, 182.
29. Ye, J.; Wang, X. Piecewise Function Hysteretic Model for Cold-Formed Steel Shear Walls with Reinforced End Studs. *Appl. Sci.* **2017**, *7*, 94.
30. Usefi, N.; Sharafi, P.; Ronagh, H. Numerical models for lateral behaviour analysis of cold-formed steel framed walls: State of the art, evaluation and challenges. *Thin-Walled Struct.* **2019**, *138*, 252–285.
31. Shafaei, S.; Ronagh, H.; Usefi, N. Experimental evaluation of CFS braced-truss shear wall under cyclic loading. In *Advances in Engineering Materials, Structures and Systems: Innovations, Mechanics and Applications, Proceedings of the 7th International Conference on Structural Engineering, Mechanics and Computation (SEMCC 2019), Cape Town, South Africa, 2–4 September 2019*; CRC Press: Boca Raton, FL, USA, 2019.
32. Hancock, G.J. *Design of Cold-formed Steel Structures: To Australian/New Zealand Standard AS/NZS 4600: 1996*; Institute of Steel Construction: Sydney, Australian, 1998.
33. AS 4084. *Steel Storage Racking*; Standards Australia: Sydney, Australia, 2012.
34. Shen, Y.; Chacón, R. Effect of Uncertainty in Localized Imperfection on the Ultimate Compressive Strength of Cold-Formed Stainless Steel Hollow Sections. *Appl. Sci.* **2019**, *9*, 3827.
35. Kaveh, A.; Vaez, S.R.H.; Hosseini, P.; Fathali, M.A. A New Two-Phase Method for Damage Detection in Skeletal Structures. *Iran. J. Sci. Technol. Trans. Civ. Eng.* **2019**, *43*, 49–65.
36. Kaveh, A.; Vaez, S.H.; Hosseini, P. Simplified dolphin echolocation algorithm for optimum design of frame. *Smart Struct. Syst.* **2018**, *21*, 321–333.
37. Abaqus, V. *6.14 Documentation*; Dassault Systemes Simulia Corporation: Johnston, RI, USA 2014; Volume 651.
38. Usefi, N.; Ronagh, H.R.; Mohammadi, M. Finite element analysis of hybrid cold-formed steel shear wall panels. In *Streamlining Information Transfer between Construction and Structural Engineering, Proceedings of the Fourth Australasia and South-East Asia Structural Engineering and Construction Conference, ISEC Press, Brisbane, Australia, 3–5 December 2018*.

39. Cardoso, F.S.; Rasmussen, K.J. Finite element (FE) modelling of storage rack frames. *J. Constr. Steel Res.* **2016**, *126*, 1–14.
40. Usefi, N.; Ronagh, H.; Kildashti, K.; Samali, B. Macro/micro analysis of cold-formed steel members using ABAQUS and OPENSEES. In Volume of Abstracts, Proceedings of the 13th International Conference on Steel, Space and Composite Structures (SS18), The University of Western Australia, Perth, Australia, 31 January–2 February 2018.

4. Experimental and Numerical Investigation of a Method for Strengthening Cold-Formed Steel Profiles in Bending (Journal Article 2)

A reprint of this study entitled 'Experimental and Numerical Investigation of a Method for Strengthening Cold-Formed Steel Profiles in Bending', Taheri, E.; Firouzianhaji, A.; Mehrabi, P.; Vosough Hosseini, B.; Samali, B. published by Applied Sciences. 2020; 10(11):3855. <https://doi.org/10.3390/app10113855>

4.1. Abstract

Perforated cold-formed steel (CFS) beams subjected to different bending scenarios should be able to deal with different buckling modes. There is almost no simple way to address this significant concern. This paper investigates the bending capacity and flexural behavior of a novel-designed system using bolt and nut reinforcing system through both experimental and numerical approaches. For the experiential program, a total of eighteen specimens of three types were manufactured: a non-reinforced section, and two sections reinforced along the upright length at 200 mm and 300 mm pitches. Then, monotonic loading was applied to both the minor and major axes of the specimens. The finite element models were also generated and proved the accuracy of the test results. Using the proposed reinforcing system the flexural capacity of the upright sections was improved around either the major axis or minor axis. The 200 mm reinforcement type provided the best performance of the three types. The proposed reinforcing pattern enhanced flexural behavior and constrained irregular buckling and deformation. Thus, the proposed reinforcements can be a very useful and cost-effective method for strengthening all open CFS sections under flexural loading, considering the trade-off between flexural performance and the cost of using the method.

Keywords: cold-formed steel; upright; monotonic loading

4.2. Introduction

Steel pallet racking systems have been widely used around the world since the industrial revolution. Over the years, steel pallet racking has evolved from hot-rolled profiles to cold-formed steel (CFS) profiles in order to increase the structural performance in terms of engineering optimization. The benefit of steel pallet racking is its flexibility in using limited space in warehouses. The increase in popularity of steel storage racking means more types of applications are now required to meet the demands of customers [1]. However, the performance of the proposed sections needs to be well understood by full-scale testing. Generally, perforated CFS components are susceptible to bending forces. Following the previous study on the flexural behavior of the perforated CFS profiles, these sections have been subjected to cyclic and monotonic forces where they have experienced different kinds of deformations, notably different types of buckling [2].

There are three primary types of buckling modes for CFS sections including local, distortional and global. Therefore, it is vital to find suitable ways to speed up constraining the buckling process.

Yu and Schafer [3] and Calderoni et al. [4] performed a series of four-point bending tests to investigate the distortional and flexural performance of C and Z-shaped section built-up cold-formed steels. Rogers et al. [5] evaluated the bending moment of existing authentic experimental results with different code provisions. Hancock et al. [6] proposed a new design approach of distortional buckling strength for C and Z-shaped cold-formed steel sections. Wang et al. [7] experimentally and analytically investigated C-shaped cold-formed steel beams with or without edge stiffeners. Using the stiffeners significantly enhanced the flexural stiffness and buckling resistivity of the beam under pure and non-pure bending tests. Wang et al. [8] performed a four-point bending test program on cold-formed steel built-up section beams with web perforations. Local geometric imperfections were also measured. When the hole diameter to web depth ratio (d_h/d_w) increased from 0.25 to 0.5, the moment rotation capacity reduced slightly by 6%. However, increasing the ratio up to 0.7 reduced the capacity by 16%. The effects of the web-hole ratio on the performance of the perforated cold-formed steel channel section beams were experimentally and analytically investigated. The greater the increase in the hole area, the more reduction in the ultimate distortional buckling moment [9,10,11,12,13,14]. The reported results also illustrated that the size of the web holes directly affected the distortional buckling moment, with the bigger the hole, the lower the buckling moment. Zhou et al. [15] examined the authenticity of the Australia/New Zealand Standard (AS 1391) on the flexural strength design of rectangular tubes manufactured with cold-rolling steel, where the Australian standard has shown reliable design code and unreliable design procedure for normal and high strength steel, respectively. Laim et al. [16] conducted a series of bending tests and also finite element modellings on flexural behaviour of cold-formed steel beams. The authors reported that the dominant failure mode was distortional buckling. Folded-flange sections were developed to present the best performance under bending investigation compared to other typical and industrial sections (the flexural capacity increased by up to 50%), and using partial reinforcing significantly increased the beam strength against the lateral-torsional buckling [17,18]. Muftah et al. [19] performed a series of four-point flexural tests on bolted built-up cold-formed steel beams while using bolts and nuts system. According to the reported conclusions, when the loads were applied on the webs, the flexural behaviour of the beams was dependent just on bolt distances. Huang et al. [20] proposed a novel solution to the distortional

buckling moment for stiffened CFS beams based on the minimum potential energy rules and using web and flange stiffeners. The presence of flange stiffeners enhanced the bearing capacity and increased the distortional buckling moment [21]. The presence of slots affected both the shear rigidity and distortional buckling load and the web stiffeners improved the flexural behavior [22].

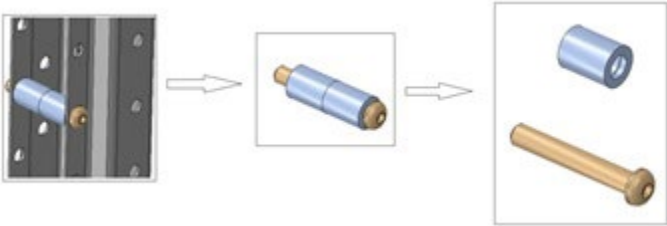
Following the literature, perforated CFS beams subjected to different bending scenarios should be able to deal with different buckling modes [23]. There is almost no simple way to address this significant concern. Hence, this study proposed a simple and low-cost reinforcing system for CFS uprights consisting of a bolt, nut and spacer. A series of four-point bending tests were performed on the specific stiffened perforated beams to measure the buckling-resistant moment of an upright section about its major and minor axes and to evaluate its improvement by proposed reinforcement. A total of eighteen monotonic tests were conducted to determine both the flexural capacity and failure modes of the reinforced sections, which consisted of uprights with 1.6 mm thickness strengthened by bolt and spacer systems. Finite element (FE) analysis was also performed by ABAQUS program and was verified by the experimental results. The comparison of the parametric study and test study showed both outstanding accuracy for the experimental results, and the proficiency of the proposed reinforcing system.

4.3. Reinforcement Method

Three principal buckling modes for upright sections observed during the flexural test are distortional, flexural and flexural-torsional. However, the distortional buckling is the governing mode in the design of uprights, where excessive deformation occurs about a weaker principal axis.

The typical upright frame consists of a regular pattern of perforations which can be placed on both the web and the lips. Web perforations are used for fast interconnection between beams and uprights, while lip perforations allow the connection of the brace components to uprights. The location of perforations which are not in use in the section lip can also be used to partially close off the section. Therefore, in this study, stiffeners comprised of fasteners, nuts and spacers were used at the location of perforations to connect the lips of the open sections and to improve the moment capacity of the system. These stiffeners are commonly used to attach the brace to uprights; hence, no further design is required for these connectors.

Time-consuming and costly stiffening methods, such as plate stiffeners and partially closing the sections, are not practical for upright frames already in use. Preliminary numerical analyses were also performed in order to check the feasibility and capability of the proposed reinforcing method, and it was found that this approach can increase the load-bearing capacity of standard uprights. The strengthening method proposed in this study is a handy and cost-effective approach that can be used for all racking systems, especially those which are currently in use in storage locations. This approach can be employed for all CFS open sections as well [24,25]. The reinforcement arrangement consisted of a bolt, nut and double spacer, where the spacer was the transverse element made up of the plastic material commonly used for bracing of racking by attaching to the lips of the section. The reinforcing details are demonstrated in Figure 4-1.



(A)



(B)

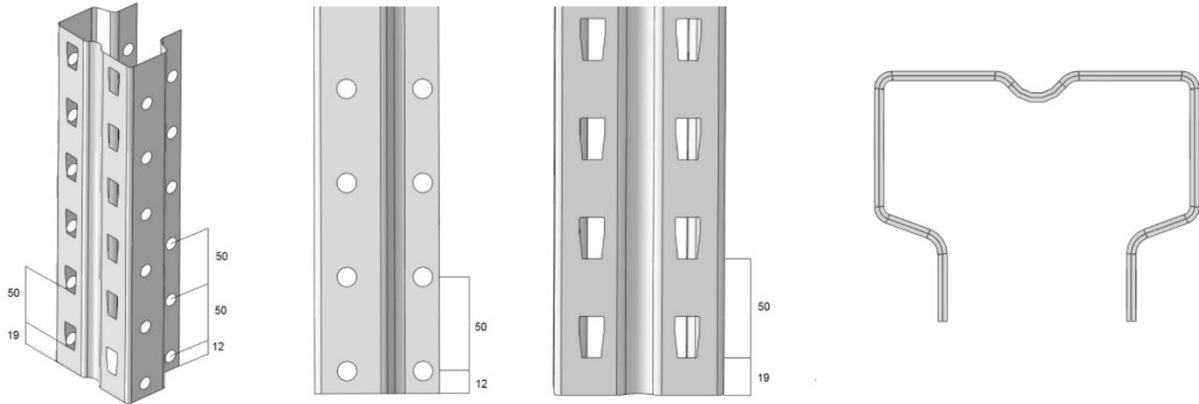
Figure 4-1: Reinforcement by bolts and spacers: (A) Schematic view; (B) Along the upright.

4.4. Experimental Campaign

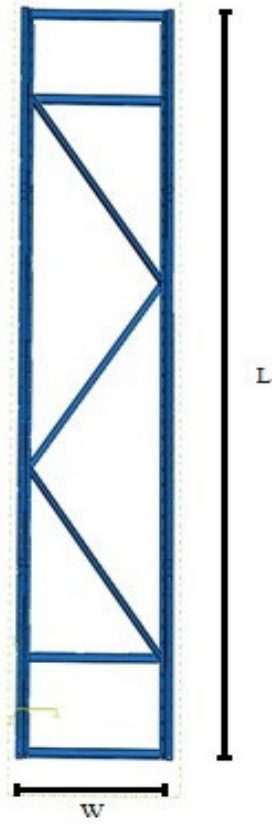
The experimental investigation was performed at the structural laboratory of Western Sydney University in order to determine the moment capacity of an upright section about its major and minor axes of bending and its improvement by different patterns of reinforcement by adding bolts, spacers and partially closing the sections. The experimental test details are discussed in the next section.

4.4.1 Test Specimens

Eighteen specimens consisting of nine single-upright and nine bending frames were prepared for testing. The bending frames including two upright columns attached by diagonal bracing were constructed from commercially available rack sections, and the ends of the frame were constrained by back-to-back bracing to avoid twisting. Specimens were produced in two groups, with or without reinforcements. The specimen specifications are tabulated in Table 4-1. Figure 4-2 indicates the section and the perforation details as well as the frame configurations.



(A)



(B)

Figure 4-2: Configuration of the details: (A) Upright configuration; (B) Frame configuration (L and W in the Table 4-1).

Table 4-1: Specimen configurations.

Specimen Type	Geometry (mm)				Reinforcement	Loading Direction	
	* Length	** Thickness	*** Width	**** Sp		Major Axis	Minor Axis
SMIM				-	No		•
SMIM				-	No		•
SMIM				-	No		•
SMJM				-	No	•	
SMJM				-	No	•	
SMJM				-	No	•	
200RMIM				200	Yes		•
200RMIM				200	Yes		•
200RMIM	2400	1.6	600	200	Yes		•
200RMJM				200	Yes	•	
200RMJM				200	Yes	•	
200RMJM				200	Yes	•	
300RMIM				300	Yes		•
300RMIM				300	Yes		•
300RMIM				300	Yes		•
300RMJM				300	Yes	•	
300RMJM				300	Yes	•	
300RMJM				300	Yes	•	

* Length = upright length. ** Thickness = upright thickness. *** Width = frame width (distance between two upright). ****

Sp = distance between reinforcement bolts (reinforcement space).

The convention used to designate the specimens is explained in Figure 4-3. The SMIM and SMJM specimens were manufactured without reinforcements, and their flexural behaviour was investigated during the monotonic test. Their loading direction was carried out on the minor and major axes, respectively. The 200RMIM and 200RMJM specimens were produced with reinforcements placed at 200 mm spacing along the upright length and were investigated about their minor and major axes respectively. The 300RMIM and 300RMJM specimens were developed according to the previous patterns except that their reinforcement spaces were 300 mm.

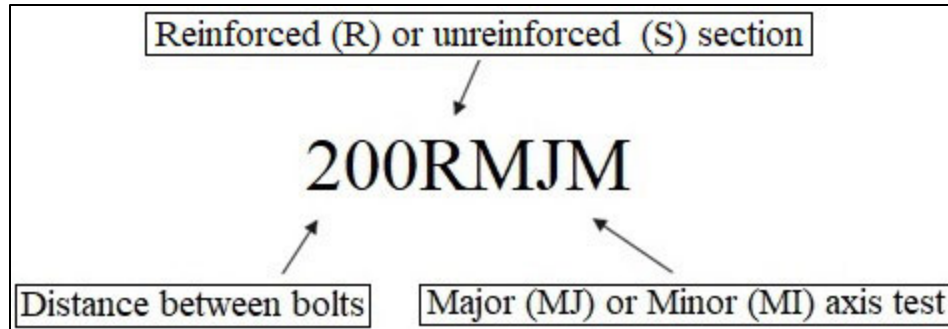


Figure 4-3: Designation of specimens.

4.4.2 Material Properties

The tensile coupon test is essential to identify the actual material properties of the test specimen. Three coupons from the upright flanges with no perforations were prepared for the coupon test. The CFS channel section was cleaned, cleared and cut into coupon-shaped flexural specimens. The tensile test was conducted according to AS4600 procedures [26].

The tensile test results were used for developing finite element models that are presented later in this paper. An MTS Sintech testing machine (TestResources Inc., Shakopee, MN, USA) with 300 kN capacity and a rate of 0.01 mm/s was used for the coupon tests. Figure 4-4 shows the stress-strain curves for 1.6 mm thickness sections. The mean values of the ultimate tensile strength (σ_u), and yield stress (σ_y) and elongation are presented in Table 4-2.

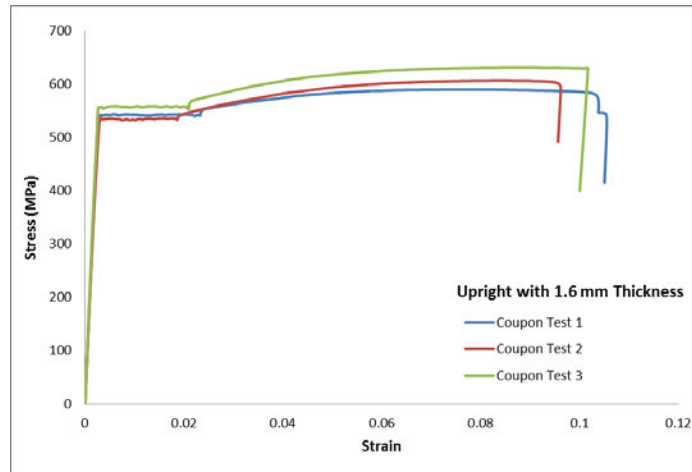


Figure 4-4: Stress-strain diagram for 1.6 mm thickness specimen.

Table 4-2: Material properties of the upright section.

Section Type	Yield Stress, σ_y (MPa)	Ultimate Stress, σ_u (MPa)	Elongation (%)
Upright with 1.6 mm thickness (Test 1)	561	578	10.3
Upright with 1.6 mm thickness (Test 2)	557	585	9.6
Upright with 1.6 mm thickness (Test 3)	571	610	10.1
Average	563	591	10

4.4.3 Test Set-Up

The purpose of the four-point bending test is to determine the flexural moment capacity of an upright section about its major and minor axes of bending and its improvement by different patterns of reinforcement by adding bolts, spacers and partially closing its sections. The flexural test was carried out to simulate the pure bending using a four-point bending test according to AS 4084:2012 [27] Section 7.3.4: Bending tests on upright sections (Figure 4-5).

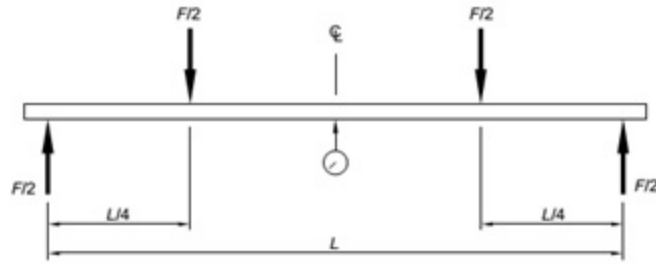
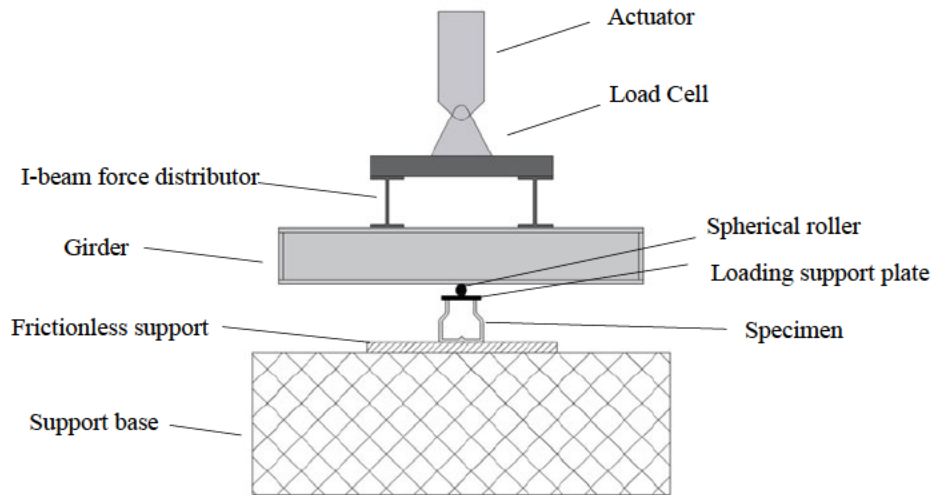


Figure 4-5: Typical schematic four-point bending test.

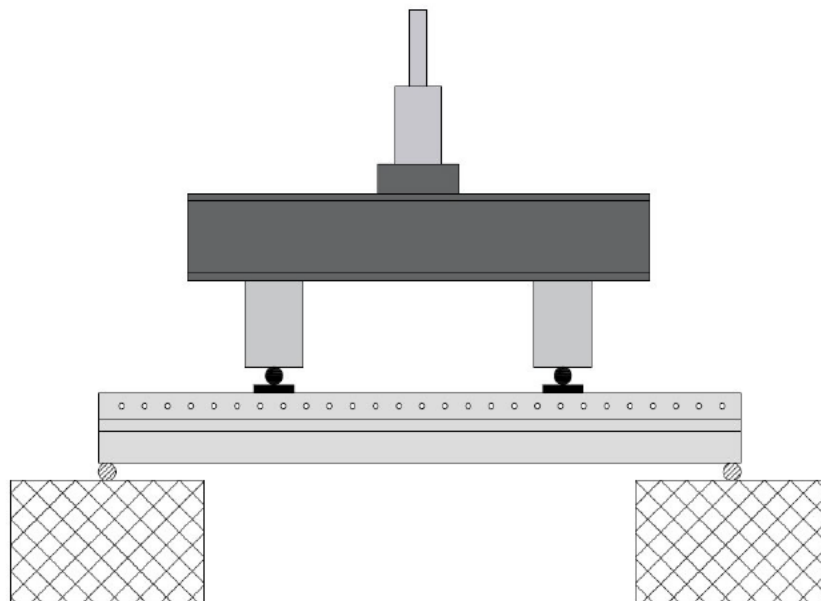
In the test section, the actuator was placed on two steel I-beams, and the I-beams were settled on the steel girders to transmit the applied force on spherical rollers. The steel spherical rollers were placed on the test specimen to facilitate the movement of the specimen not only to show the potential deformations but to simulate the real condition for pure bending. The rollers were placed on two perforated steel plates. The details and the schematic views of the minor axis test set-up are shown in Figure 4-6.



(A)



(B)



(C)

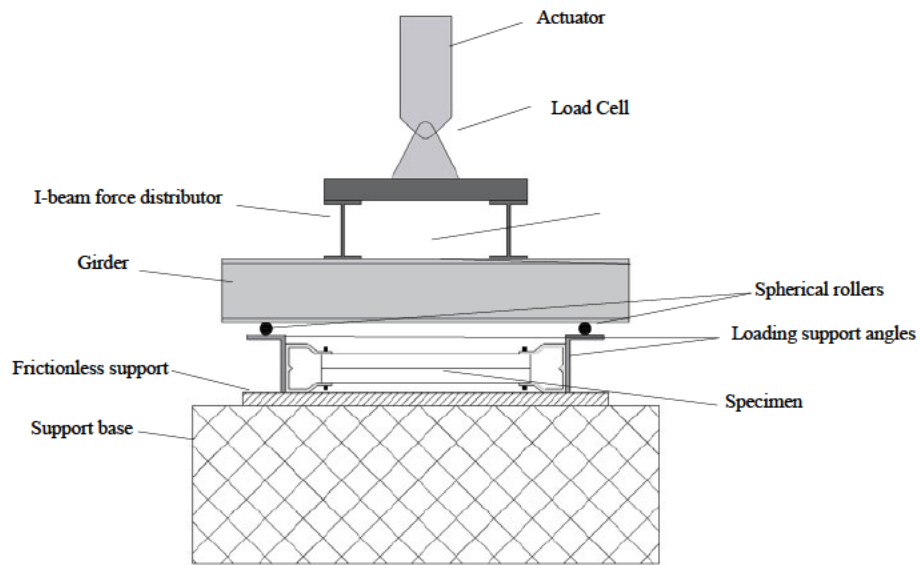
Figure 4-6: Minor axis test set-up details: (A) Test specimen; (B) schematic front view; (C) schematic side view.

The major axis test was designed to measure both the bending strength of the upright about the major axis and the buckling modes. Because of the potential distortion and torsional displacement of the section, as shown in Figure 4-7 the designed major axis test specimens contained two studs

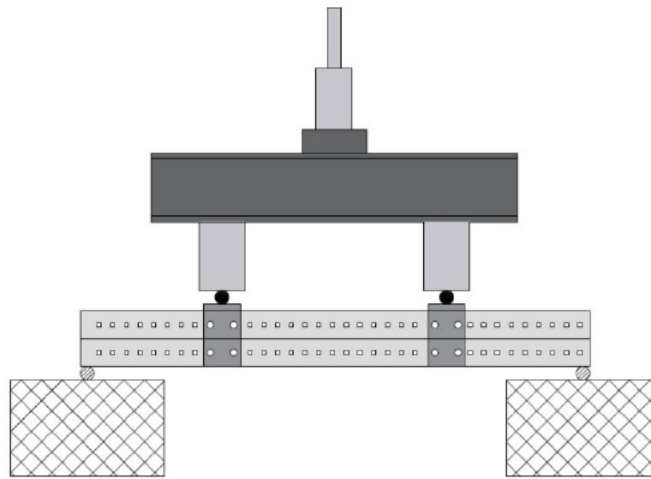
as a single frame so that the specimens would demonstrate appropriate flexural behaviour during the monotonic loading. Also, the actuator was placed on two steel I-beams, and the I-beams were settled on two steel girders which transmitted the force onto the roller supports. Put et al. [28] performed a series of eccentrically and concentrically loading on the channel steel upright connections. The more eccentricity increases, the more beam strength decreases. Therefore, for the major axis tests, the rollers settled on four perforated steel angles attached to the web of the channel by four fasteners designed to exert the load to the shear center of the profile section. That being the case, the spherical rollers and loading angles were designed to let any possible displacement, especially the distortional buckling, happen. Also, the specimen was free to twist on the frictionless supports. By this means, this test arrangement permits buckling modes to occur similar to the real modes developed by the upright in its normal usage. Three tests for each type of the specimens and about each axis were carried out including unreinforced profiles and reinforced ones.



(A)



(B)



(C)

Figure 4-7: Major axis test set-up details: (A) Test specimen; (B) schematic front view; (C) schematic side view.

Although the roller supports were designed to be at the shear centre of the uprights and act delicately in case of load transfer, the preliminary tests faced the problem of local crushing and

cripling in the vicinity of the loading angles and rollers. This issue was addressed by using reinforcement just underneath the supports, as shown in Figure 4-8.



Figure 4-8: Crippling of load points: (A) Typical crippling at flanges; (B) Specific crippling reinforcement.

In total, 18 monotonic tests (single directional force) were conducted during the investigation based on AS 4084: 2012, Section 7.3.4: Bending tests on upright sections [27] to determine the failure moment and mode of the pallet racking's uprights (Figure 4-9).



(A)



(B)

Figure 4-9: Test set-up: (A) minor axis test, (B) major axis test.

4.4.4 Data Acquisition and Instrumentation

The experiments were conducted using a Universal Testing Machine, Instron 8506 (Instron, Norwood, MA, USA) with 3000 kN capacity. The loading rate of 0.5 mm/min was applied to the specimens. The reading of the forces was measured by the load cell, whereas the deflection of the uprights was measured by linear variable differential transformers (LVDTs). The data was collected via data logger and sent to the computer then processed with Microsoft Excel. The data was measured at a frequency of 2 Hz, which means every 0.5 s.

4.5. Test Results and Discussion

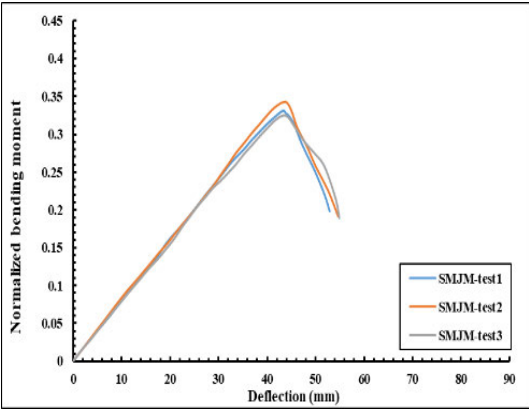
Eighteen specimens with 2400 mm length and 1.6 mm thickness were tested in three reinforcement compositions: without reinforcement, and with reinforcements at 200 mm and 300 mm. The tests aimed to investigate the reinforcement effect on flexural performance. The tests were designed to acquire both the flexural capacity and the failure modes during the loading process.

The flexural moment capacity for each specimen was recorded and due to confidentiality matters, it was normalised with respect to the normalization factor ($N_f = Z \cdot \sigma_y$), where Z was the shape factor of the section, and σ_y was the yield-stress extracted by the coupon tests. On the other hand, the deflection value represents the displacement of the mid-point in each specimen recorded by

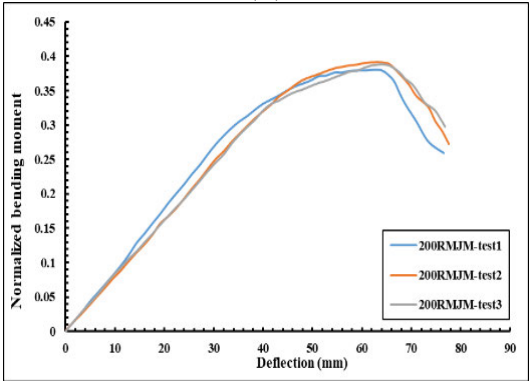
LVDTs. For each specimen type, three tests were conducted to ensure the accuracy of the results for the upright flexural behaviour.

4.5.1 Major Axis Test

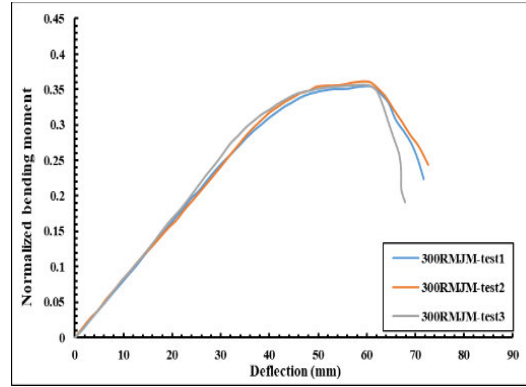
Figure 4-10 demonstrates the normalised bending moment versus deflection for unreinforced, 200 mm and 300 mm reinforcement types under monotonic flexural tests. The 200 mm reinforcement type provided the highest flexural strength compared to the other two types. The normalized bending moment capacity for each specimen is tabulated in Table 4-3. Factors responsible for some differences in the results for the same specimen types could be related to the typical shortcomings during the set-up adjustment.



(A)



(B)



(C)

Figure 4-10: Normalized bending moment–deflection about major axis curves: (A) SMJM; (B) 200RMJM; (C) 300RMJM.

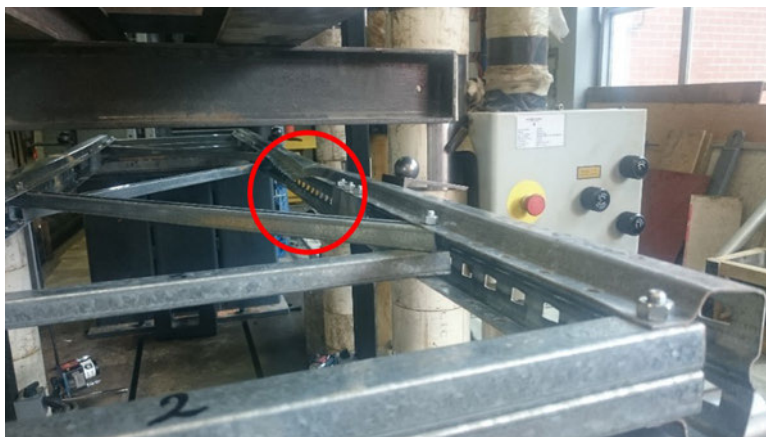
Table 4-3: The ultimate normalized bending capacity of specimens in the major axis test.:

Test Specimen	Normalised Ultimate Bending moment ($\frac{M}{\sigma_y \times Z}$)
SMJM-Test1	0.330
SMJM-Test2	0.342
SMJM-Test3	0.325
Average	0.332
Standard deviation	0.008
200RMJM-Test1	0.379
200RMJM-Test2	0.391
200RMJM-Test3	0.388
Average	0.386
Standard deviation	0.005
300RMJM-Test1	0.354
300RMJM-Test2	0.361
300RMJM-Test3	0.356
Average	0.357
Standard deviation	0.003

Both the distortional and local buckling were observed during major axis testing of the unreinforced frames (Figure 4-11). According to the observations, some notches were observed along with the failure mechanism at the local buckling zones.



(A)



(B)



(C)

Figure 4-11: The observed failure mode for unreinforced specimens during the major axis test: (A) SMJM-test1; (B) SMJM-test2; (C) SMJM-test3.

When the reinforced specimens with 200 mm reinforcing pitch were subjected to the monotonic displacement control test on the major axis, local buckling, as well as a combination of both local and distortional buckling, occurred during the experiments. The yielding notches were also observed as crippling signs in some areas (Figure 4-12).



(A)



(B)



(C)

Figure 4-12: The observed failure mode for reinforced specimens with 200 mm reinforcing pitch during the major axis test: (A) 200RMJM-test1; (B) 200RMJM-test2; (C) 200RMJM-test3.

Following the experimental investigation, the reinforced specimens with 300 mm reinforcing pitch were subjected to the major axis displacement control monotonic test (Figure 4-13). The governing failure mode at these tests was also the distortional and local buckling.



(A)



(B)



(C)

Figure 4-13: The observed failure modes for reinforced specimens with 300 mm reinforcing space during the major axis test: (A) 300RMJM-test1; (B) 300RMJM-test2; (C) 300RMJM-test3.

To compare the flexural behaviour of the uprights, the mean curves shown in Figure 4-14 presented the effect of reinforcements with respect to the average normalized bending. According Figure 4-14, it is clear that using reinforcements improves both the ultimate capacity and deflection of the specimens; however, this improvement has been enhanced by using the 200 mm reinforcement type. Figure 4-14 shows the 200 mm pitch improved the flexural behaviour of the uprights and also increased the bending capacity.

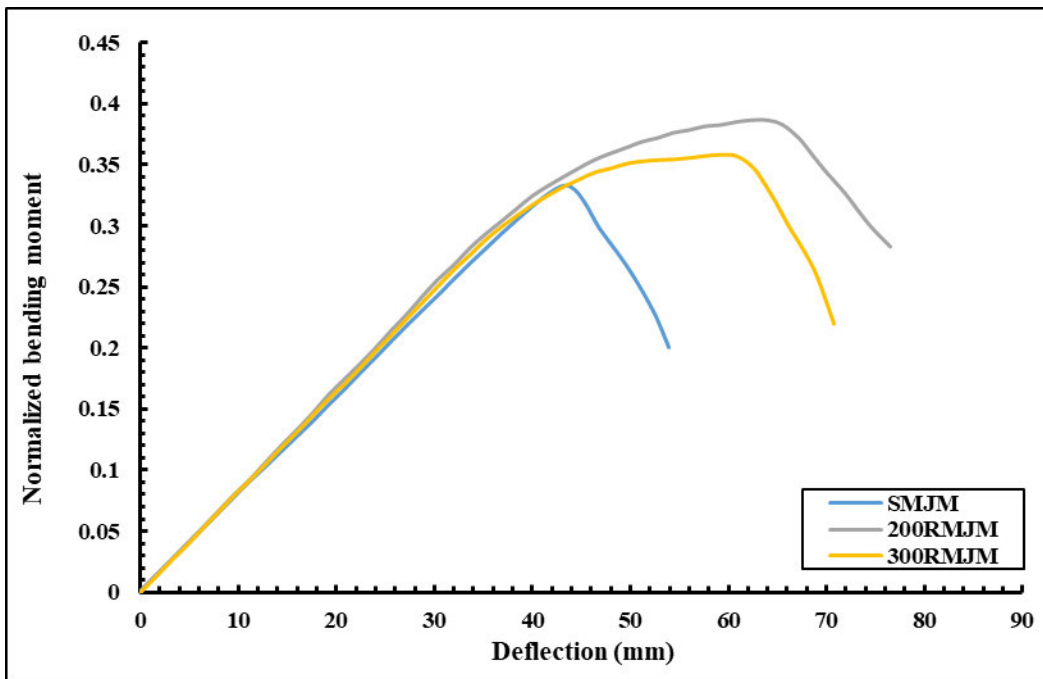


Figure 4-14: The normalized major axis test average curves.

The reported experimental results show the effectiveness of the presence of reinforcements. Figure 4-15 compares the different reinforcement types used. In Figure 4-15, the 200 mm reinforcement type showed 13.8% and 7.35% enhanced capacity compared to the non-reinforced and 300 mm reinforcement type, respectively. The 300 mm type showed 6.97% improvement in bending capacity compared to the unreinforced specimen. Typically, the failure modes which were observed in the major axis experimental tests were local and distortional bucklings.

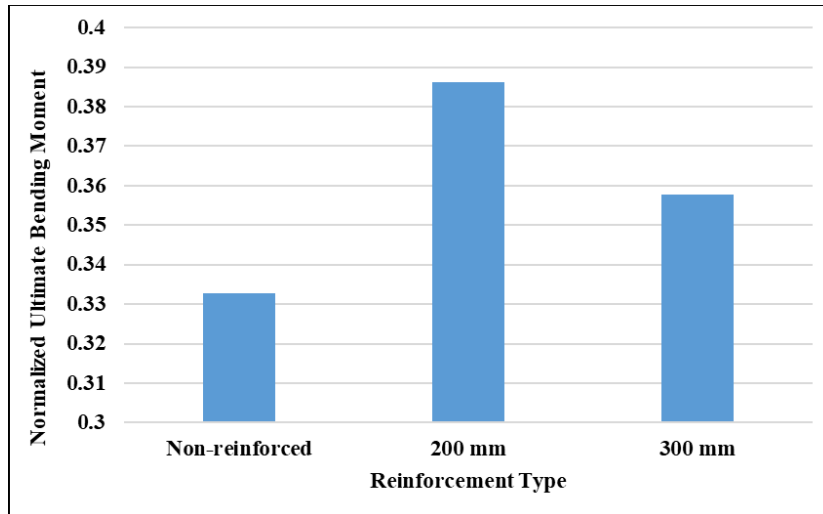
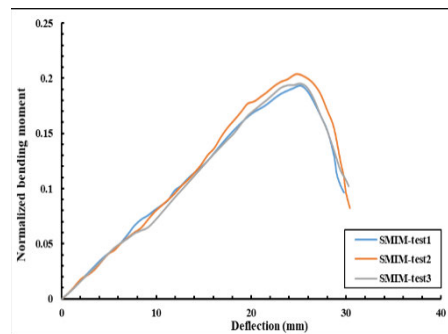


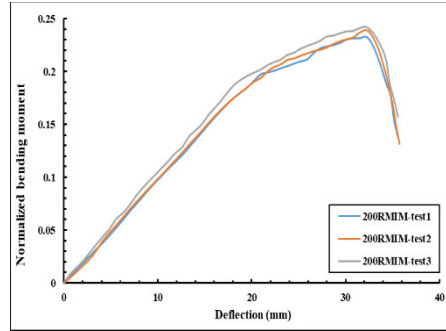
Figure 4-15: The ultimate normalized moment for major axis test with respect to the reinforcement type.

4.5.2 Minor Axis Test

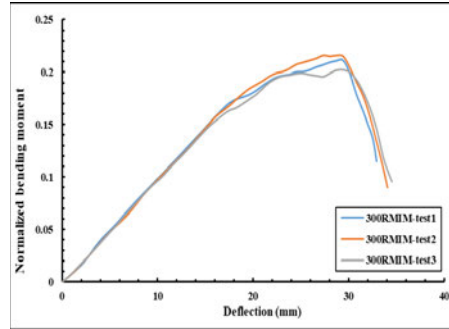
Figure 4-16 presents the normalized bending moment–deflection curves for unreinforced, 200 mm and 300 mm reinforcement types where the flexural behaviour of the specimens under minor axis tests has been reported.



(A)



(B)



(C)

Figure 4-16: Normalized bending moment–deflection about minor axis test curves: (A) SMIM; (B) 200RMIM; (C) 300RMIM.

The 200 mm reinforcement type captured the best flexural performance compared to the other two types. The normalized bending capacity for each specimen is also tabulated in Table 4-4.

Table 4-4: The ultimate normalized bending capacity of specimens in the minor axis tests.

Test Specimen	Normalized Ultimate Bending Moment $\left(\frac{M}{\sigma_y \times Z}\right)$
SMIM-Test1	0.193
SMIM-Test2	0.203
SMIM-Test3	0.195
Average	0.197
Standard deviation	0.005
200RMIM-Test1	0.232
200RMIM-Test2	0.239
200RMIM-Test3	0.242
Average	0.238
Standard deviation	0.004
300RMIM-Test1	0.211
300RMIM-Test2	0.215
300RMIM-Test3	0.202
Average	0.209
Standard deviation	0.006

Figure 4-17 represents the minor axis test for the single unreinforced uprights, showing the uprights' distortional buckling in the tests.



(A)



(B)



(c)

Figure 4-17: The observed failure mode for unreinforced specimens during the minor axis test: (A) SMIM-test1; (B) SMIM-test2; (C) SMIM-test3.

The reinforced specimens with 200 mm reinforcing space were subjected to the minor axis tests as shown in Figure 4-18. Based on the test observations, the mid-span deflections were much higher than the unreinforced specimens. The reinforced specimens exhibited no sudden torsion or twisting, but the bending capacity was enhanced significantly in the 200 mm reinforcing type.



(A)



(B)



(C)

Figure 4-18: The observed failure mode for reinforced specimens with 200 mm reinforcing pitch during the minor axis test: (A) 200RMIM-test1; (B) 200RMIM-test2; (C) 200RMIM-test3.

The minor axis test was performed on 300 mm reinforced specimens. Observations proved that increasing the reinforcing space decreases the section flexural capacity compared to the 200 mm specimens as well as the ultimate deflection of the sections at the time of failure (Figure 4-19).



(A)



(B)



(C)

Figure 4-19: The observed failure mode for reinforced specimens with 300 mm reinforcing pitch during the minor axis test: (A) 300RMIM-test1; (B) 300RMIM-test2; (C) 300RMIM-test3.

The normalized mean bending moment versus deflection curves demonstrated in Figure 4-20 represent the effects of the reinforcements in the minor axis tests. According to Figure 4-20, non-reinforced specimens had lower bending capacity. However, 200 and 300 mm reinforcement types presented improved behaviour, especially in the ultimate capacity and deflection.

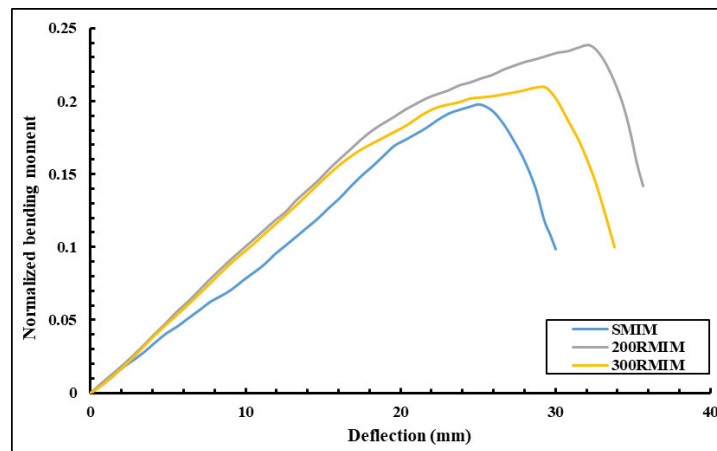


Figure 4-20: The normalized minor axis average curves.

Figure 4-21 presents the influence of performed reinforcement types. The 200 mm reinforcement type resulted in 12% and 17% improvement in ultimate bending capacity compared to the 300 mm reinforcement and non-reinforced types, respectively. The 300 mm type showed a 5.5% improvement in ultimate bending capacity compared to the non-reinforced specimen.

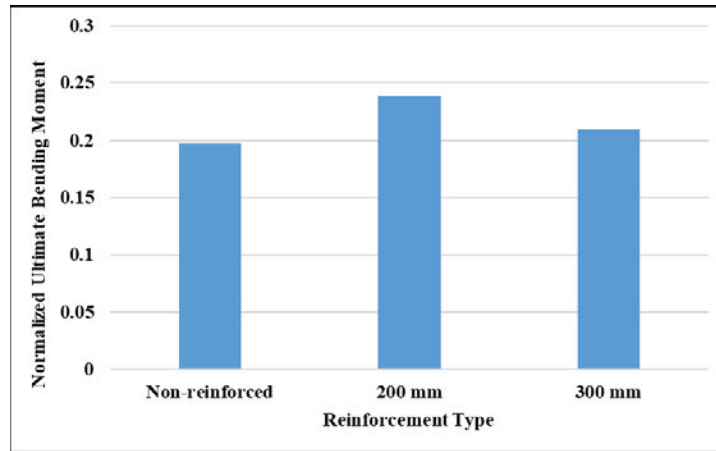


Figure 4-21: The ultimate normalized moment for the minor axis test by reinforcement type.

4.5.3 Remarks on the Results

Based on the results of both experimental and numerical investigations, the governing failure mechanisms can be categorized into two main types: buckling or crippling. First of all, local and distortional bucklings happened in almost every unreinforced specimen's major axis test. These failure mechanisms were located near the weakest zone of the beam, which was typically the mid-span of the specimens. Local bucklings were mostly observed in 200 mm type reinforced specimens, but the presence of condense reinforcing was acting as the constraining factor. As the reinforcing pitch was enlarged, the distortional buckling became the dominant failure mode as observed in the 300 mm reinforcing types. The change in the section's half-wavelength resulted in the change of buckling mode and failure load. Reducing the half-wavelength by decreasing the reinforcement pitch increases the distortional buckling capacity as well as changing the mode from distortional to local–distortional in some cases.

Secondly, in the case of crippling as another factor of failure, the unreinforced specimens failed due to this factor, especially in the major axis tests. The 200 mm and 300 mm reinforcing types also failed through the crippling mechanism; however, the ultimate load of crippling was different from the unreinforced specimens. The crippling failure mechanism was initiated by a yielding

notch which was exhibited on the flange. Then, due to the represented notch, the section became weak at that specific zone. Finally, this shortcoming led to the crippling and the frame collapsed.

Regarding the presented results, the reinforced frames and single-uprights showed a much better flexural performance in both the major and minor axes monotonic tests, especially the ones with 200 mm reinforcements. Furthermore, the specific reinforcements increased the section stiffness, and strengthened the uprights, especially where the uprights tend to deform or initiate buckling failure. For a better understanding, the observed buckling failure modes are demonstrated in the following sections using FE models.

4.6. Finite Element Models Arrangement

Different techniques are available for data validations and predictions such as artificial neural networks [29,30,31,32,33,34], FE method [1,35,36], and finite strip method [37,38]. The FE method, which is generally carried out by FE programs such as ABAQUS and ANSYS, was performed in the current study as a reliable technique for empirical data validation and response prediction. Two different FE models were used in order to simulate the experimental results of reinforcement spacing, including 200 mm, 300 mm, and without reinforcement, on the flexural strength of the upright frames about either major or minor axes. Two different arrangements were considered:

- Bending frame: The frame was modelled to simulate the major axis test, and other parts of the set-up were simulated throughout boundary condition and interaction descriptions.
- Single beam: The beam was modelled to simulate the minor axis test, and the other components of the test were simulated using appropriate stiffeners and boundary conditions.

Figure 4-22(A) shows the overall arrangement for the bending frame model and Figure 4-22(B) shows the same arrangement for single-uprights. The software ABAQUS/CAE v.12.1 was used to model the presented test specimens. The FE models were adjusted to replicate the tests.

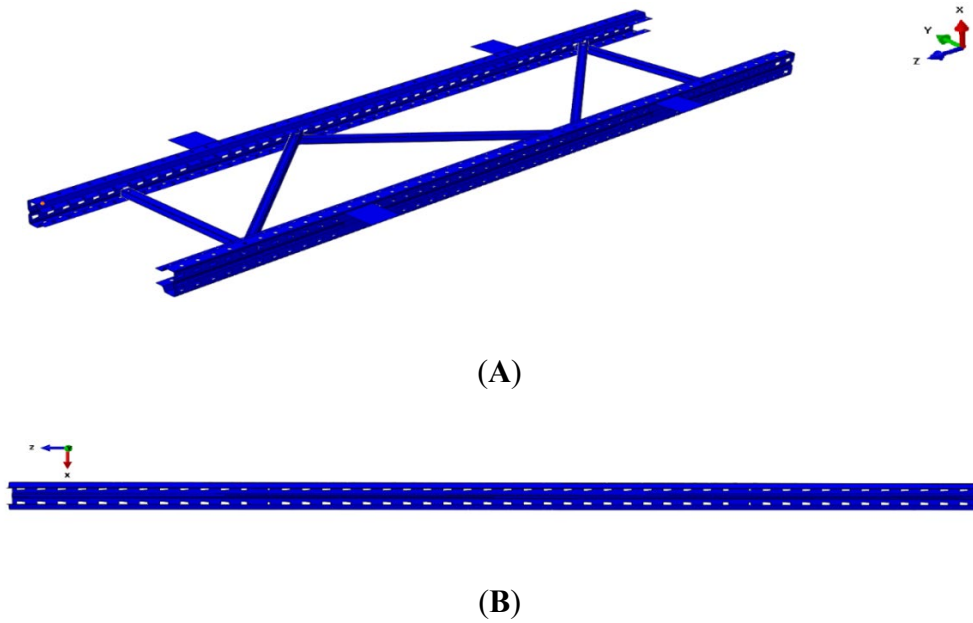


Figure 4-22: The finite element model arrangement: (A) major axis; (B) minor axis.

4.6.1 Element Type, Mesh Size and Material Model

Both models were simulated using four-node shell element S4R available in ABAQUS [1]. This element is a thin, shear flexible, isometric quadrilateral shell with four nodes and five degrees of freedom per node, using reduced integration and bilinear interpolation scheme (Figure 4-23).

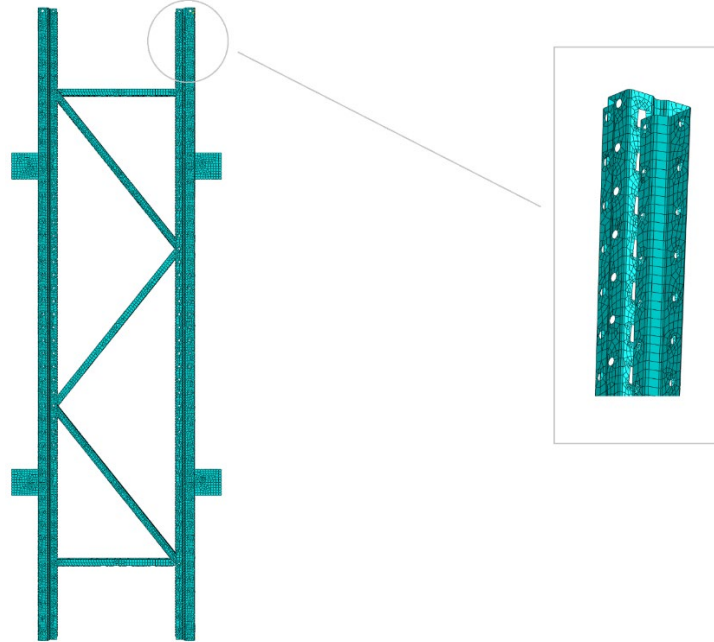


Figure 4-23: Typical finite element mesh of an upright section.

The stress-strain results from the tensile tests were used to model the material properties. To consider the necking phenomena in the tensile tests, the true stress-strain relationship was used for the models [39,40] with the following

$$\sigma_{\text{true}} = \sigma(1 + \epsilon) \quad (4.1)$$

$$\epsilon_{\text{true}} = \ln(1 + \epsilon) - \frac{\sigma_{\text{true}}}{E} \quad (4.2)$$

where σ and ϵ are the stresses and strains from the tensile tests. The von Mises yield criteria with isotropic hardening were also taken into account for the modelling. The modulus of elasticity was considered equal to 200 GPa and the Poisson ratio as 0.3 [1].

4.6.2 Connections and Interactions

For a decisive simulation, two types of interactions were defined for the FE models of the uprights subjected to loading either about the major axis or the minor axis: (a) the existing interaction of flange edges and bracing, and (b) the interaction of bracing webs at bolt connections. The surface to surface interaction with hard contact for normal behaviour, as well as the penalty method with

the friction coefficient of 0.3 for the tangential behaviour, were adopted for the model interactions [41,42,43,44]. The coupling method and beam connectors were also used to model the bolts. At each bolt location, a reference point was created at the centre of the hole where the upright flange (at the hole region) was restrained to this reference point using the coupling method [45]. The end beam restraints have also been considered as a beam using the contact pairs between the elements at two opposite sides of the sections. This type of connector constrains the axial translational degree of freedom between connecting nodes, simulating the actual bolt behaviour in the upright frame. Figure 4-24 indicates the existing interactions between frame elements as well as the modelling of the bolt in the upright frame.

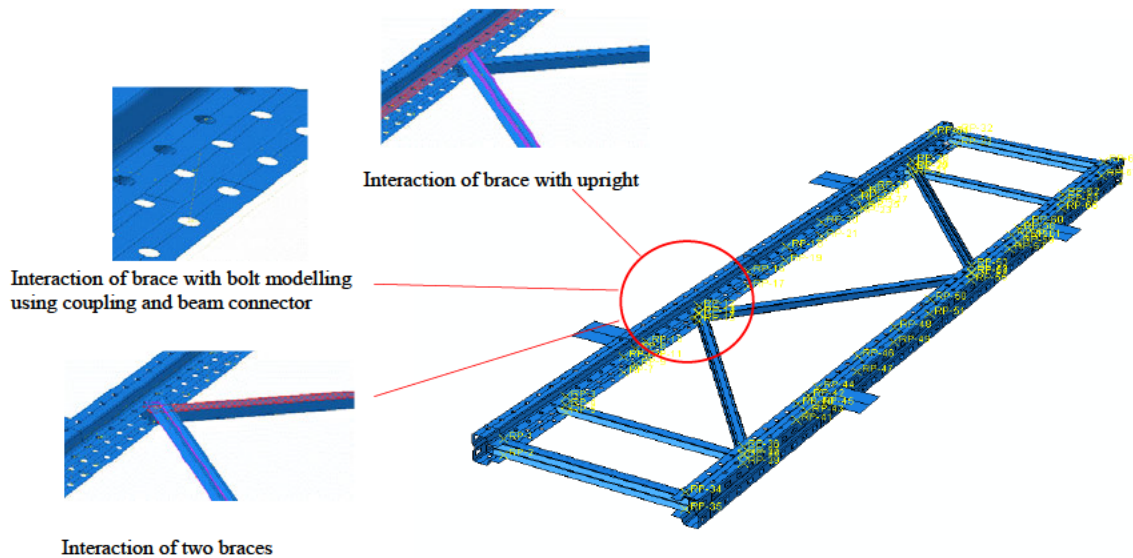


Figure 4-24: Interactions of the model components and bolt modelling.

4.6.3 Boundary Conditions and Loading

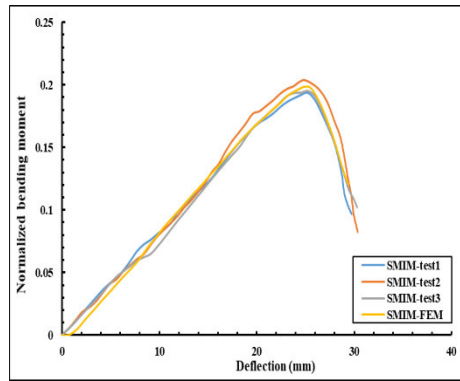
Similar to the experimental test, all boundary conditions in the FE model were also adopted in a way to represent the testing situation. The concentrated load with displacement method was applied at the shear centre of the uprights on loading support plates in the vertical direction while the translation and rotation in every direction were allowed to simulate the real testing conditions. At frictionless supports, the vertical translation was restrained to illustrate the actual support behaviour.

4.6.4 Validation of the Finite Element Results

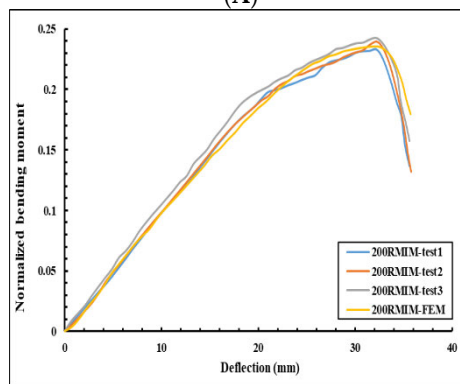
According to the details in the previous sections, the FE models were generated, and the experimental simulations were carried out. The numerical results were extracted and compared with the existing test results and failure modes to be verified. Linear regression is a powerful tool to develop predicting models for estimating the engineering properties of different materials. In this section, linear regression analyses were performed on the FE model results to help validate the results obtained from the numerical models.

4.6.4.1 Minor Axis

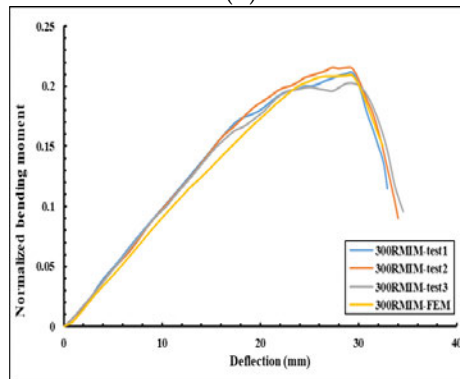
The single-upright configuration for FE modelling has been used in this section. Figure 4-25 compares the normalized bending moment–deflection curves of the FE model and experimental results. Figure 4-26 also illustrates the linear regression of the FE model mean curve with the experimental mean curve. Table 4-5 presents the evaluation criteria of the accuracy of the FE model predictions.



(A)

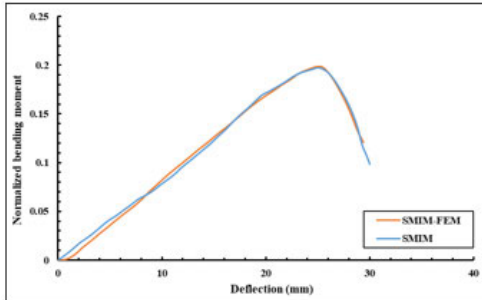


(B)

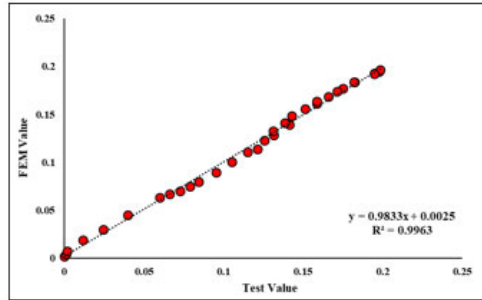


(C)

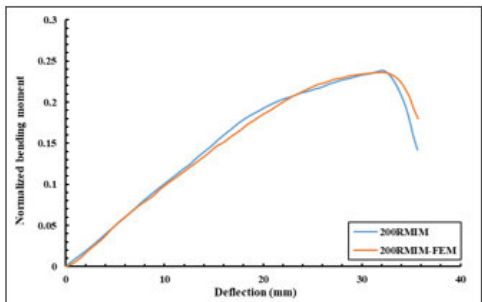
Figure 4-25: Finite element model and experimental curves for minor axis test set-up: (A) non-reinforced types; (B) 200 mm reinforced types; (C) 300 mm reinforced types.



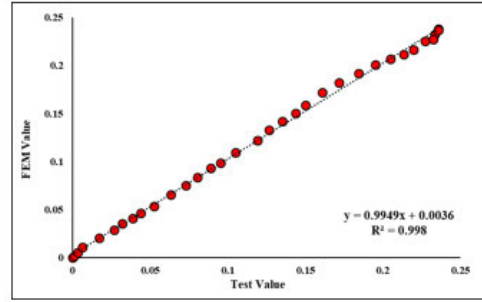
(A)



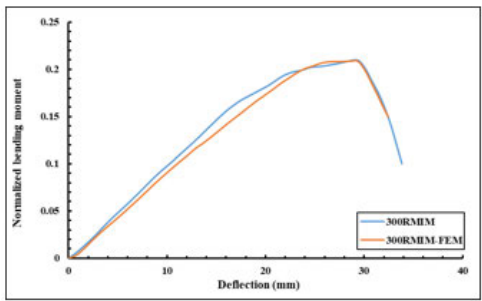
(B)



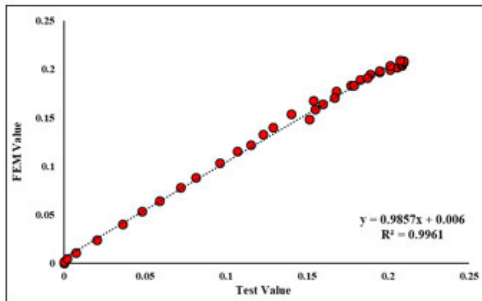
(C)



(D)



(E)



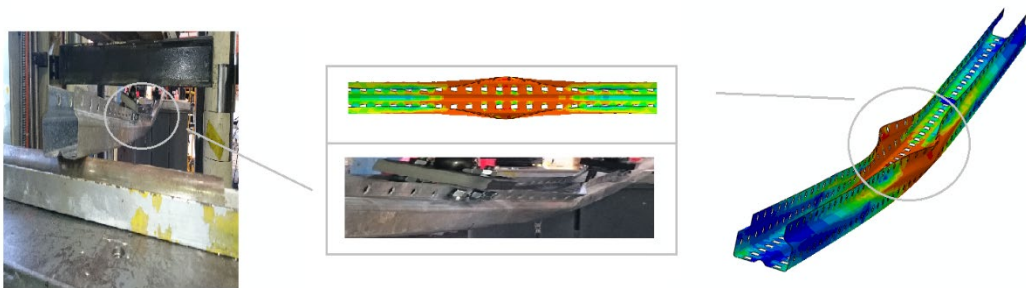
(F)

Figure 4-26: Comparison of finite element model against minor axis test results along with the linear regression: (A) and (B) non-reinforced model; (C) and (D) 200 mm reinforced model; (E) and (F) 300 mm reinforced model.

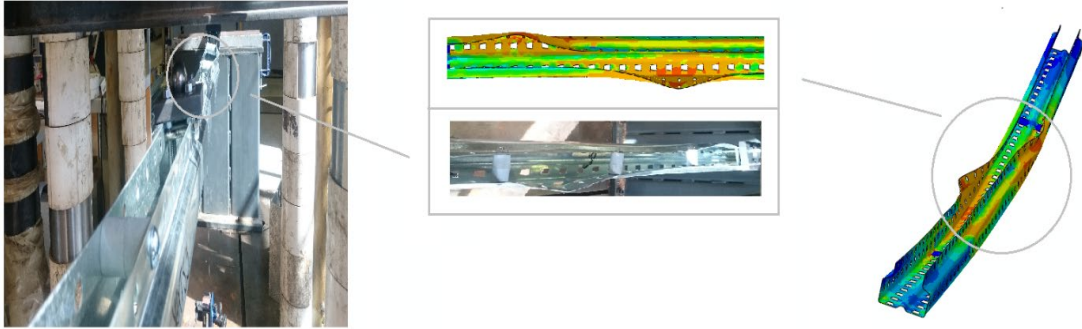
Table 4-5: Finite element model vs experimental results details in terms of evaluation criteria.

	Evaluation criteria	
Non-reinforced model	Standard deviation	0.061
	Pearson (r)	0.998
	R ²	0.996
	Evaluation criteria	
200 mm reinforced model	Standard deviation	0.080
	Pearson (r)	0.993
	R ²	0.998
	Evaluation criteria	
300 mm reinforced model	Standard deviation	0.069
	Pearson (r)	0.998
	R ²	0.9961

According to Figure 4-26 and Table 4-5, the FE model results achieved outstanding accuracy and compatibility with the test results. In addition, Figure 4-27 compares the FE model failure modes of the uprights to the experimental failure modes where the developed FE model has well predicted the overall deformed shape. These uprights failed in distortional and local buckling mode.



(A)

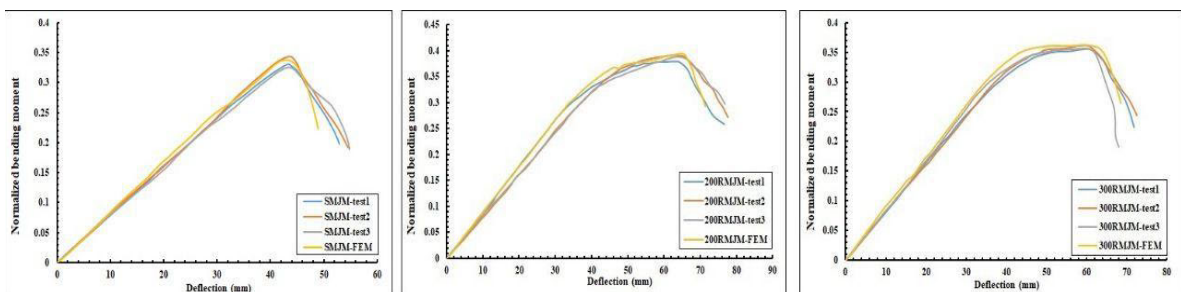


(B)

Figure 4-27: Comparison of failure modes: (A) non-reinforced upright type; (B) 300 mm reinforced upright type.

4.6.4.2 Major Axis

A bending frame arrangement was used for the numerical assessment of the upright major axis test. Figure 4-28 compares the normalized bending moment–deflection curves between the FE model and experimental results. Figure 4-29 illustrates the linear regression of the FE model mean curve with the experimental mean curve. Table 4-6 presents the evaluation criteria for the accuracy of the FE model predictions.



(A)

(B)

(C)

Figure 4-28: Finite element model and experimental curves for major axis test set-up: (A) non-reinforced frame types; (B) 200 mm reinforced frame types; (C) 300 mm reinforced frame types.

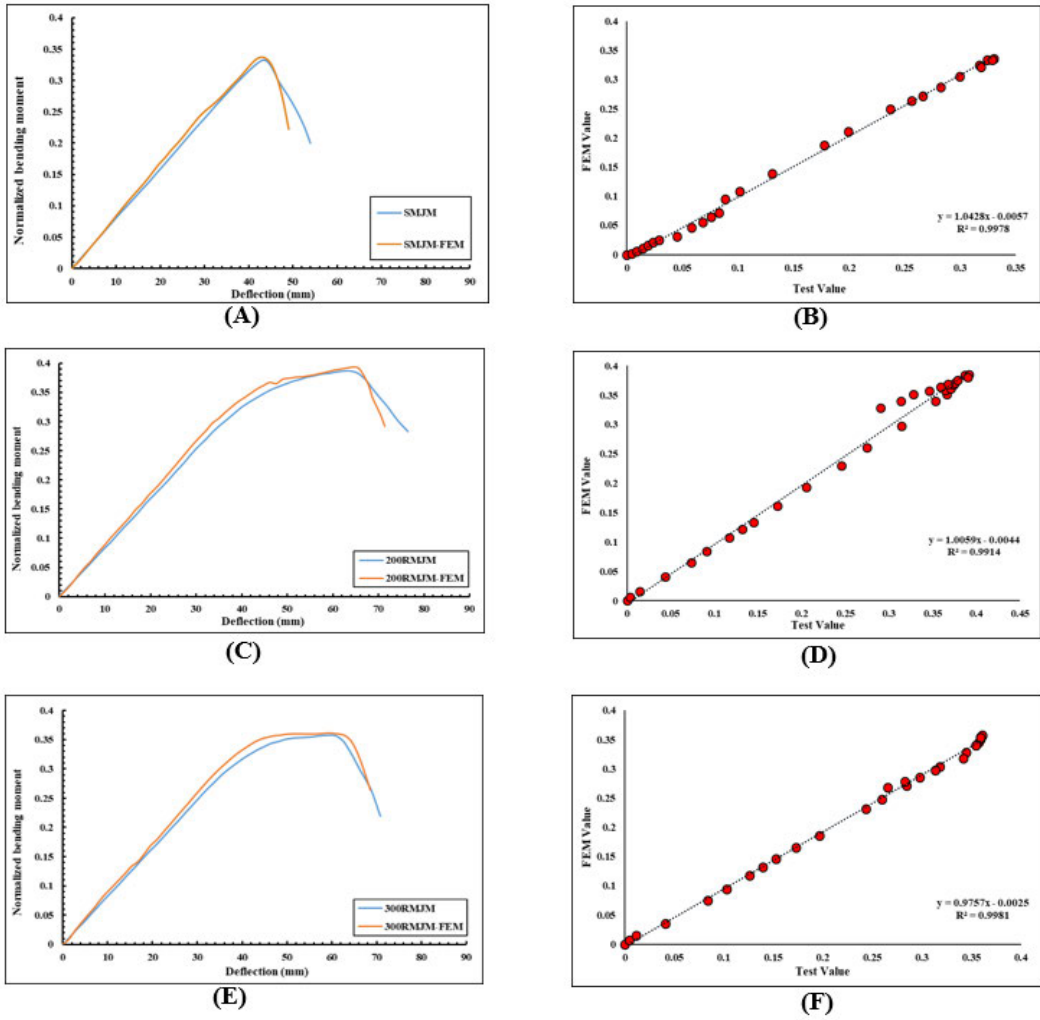
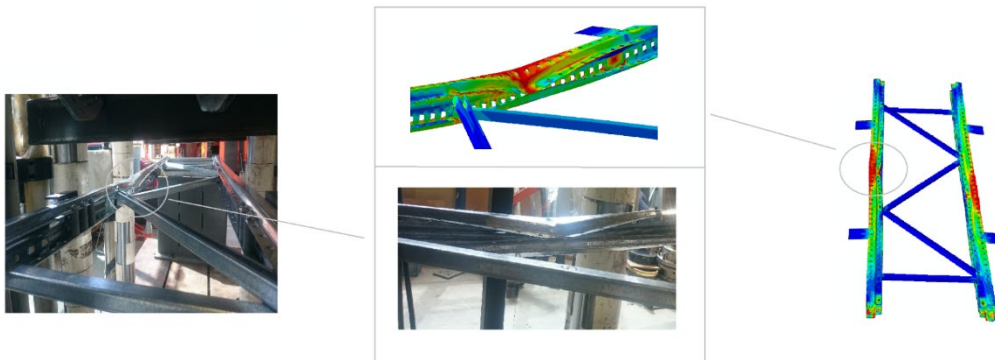


Figure 4-29: Comparison of finite element model against major axis test results along with the linear regression: (A) and (B) non-reinforced model; (C) and (D) 200 mm reinforced model; (E) and (F) 300 mm reinforced model.

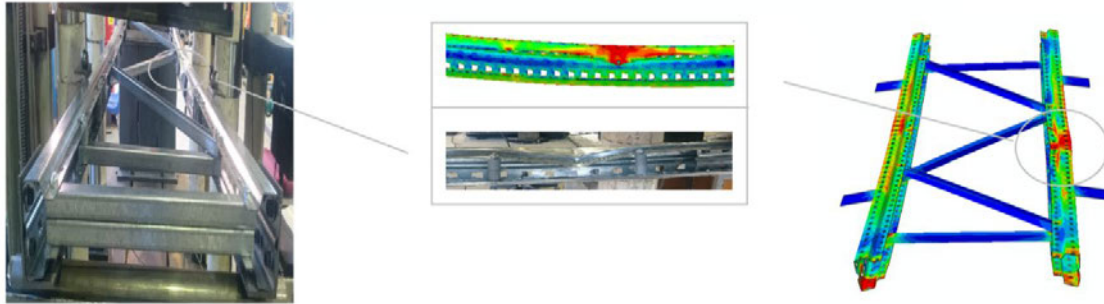
Table 4-6: Finite element model vs experimental results accuracy details in terms of evaluation criteria.

	Evaluation criteria	
Non-reinforced model	Standard deviation	0.124
	Pearson (r)	0.998
	R ²	0.997
	Evaluation criteria	
200 mm reinforced model	Standard deviation	0.135
	Pearson (r)	0.995
	R ²	0.991
	Evaluation criteria	
300 mm reinforced model	Standard deviation	0.122
	Pearson (r)	0.999
	R ²	0.998

According to Figure 4-29 and Table 4-6, the FE results had appropriate convergence with the test results. Figure 4-30 compares the FE failure modes of the frame with the experimental failure modes where the developed FE model has well predicted the overall deformed shape. These upright frames failed by distortional and local buckling mode.



(A)



(B)

Figure 4-30: Comparison of failure mode: (A) non-reinforced upright type; (B) 300 mm reinforced upright type

4.7. Conclusions

This study proposed a specific reinforcement system to enhance the flexural strength of CFS upright/beam sections. Eighteen specimens were fabricated and standard monotonic four-point bending displacement control experimental tests were performed to evaluate their bending capacity. All the specimens were made of perforated CFS uprights with 2400 mm length and 1.6 mm thickness. Specimens without reinforcement and specimens with reinforcement at 200 mm and 300 mm pitches were tested about their minor and major axes. The specimens for the minor axis test consisted of single uprights, while the tested specimens for the major axis tests were produced by combining two uprights as a frame employing conventional diagonal bracing to keep the set-up stable for accurate estimation of the flexural strength of reinforced and unreinforced uprights.

Based on the reported observations, the governing failure modes were local, distortional and a combination of these modes of buckling both in the minor axis and major axis tests. Using the proposed reinforcements increases the bending moment capacity of the specimens by changing the half wavelength of the sections. Reinforcement at 200 mm pitches improves the ultimate flexural capacity compared to the unreinforced specimens by around 13.8% and 17% in major axis and minor axis tests, respectively. Using reinforcement at 300 mm pitches increases the bending moment capacity compared to the unreinforced specimens by 6.97% and 5.5% for the major axis and minor axis tests, respectively. The study emphasized that the proposed

reinforcements can be a very useful and cost-effective method for strengthening all open CFS sections under flexural loading, considering the trade-off between flexural performance and the cost of using the method.

4.8. References

1. Taheri, E.; Firouzianhaji, A.; Usefi, N.; Mehrabi, P.; Ronagh, H.; Samali, B. Investigation of a Method for Strengthening Perforated Cold-Formed Steel Profiles under Compression Loads. *Appl. Sci.* **2019**, *9*, 5085, doi:10.3390/app9235085.
2. Chen, C.; Shi, L.; Shariati, M.; Toghroli, A.; Mohamad, E.T.; Bui, D.T.; Khorami, M. Behavior of steel storage pallet racking connection—A review. *Steel Compos. Struct.* **2019**, *30*, 457–469, doi:10.31224/osf.io/jzdpq.
3. Yu, C.; Schafer, B.C. Distortional Buckling Tests on Cold-Formed Steel Beams. *J. Struct. Eng.* **2006**, *132*, 515–528, doi:10.1061/(asce)0733-9445(2006)132:4(515).
4. Calderoni, B.; De Martino, A.; Formisano, A.; Fiorino, L. Cold formed steel beams under monotonic and cyclic loading: Experimental investigation. *J. Constr. Steel Res.* **2009**, *65*, 219–227, doi:10.1016/j.jcsr.2008.07.014.
5. Rogers, C.; Schuster, R. Flange/web distortional buckling of cold-formed steel sections in bending. *Thin Walled Struct.* **1997**, *27*, 13–29, doi:10.1016/0263-8231(96)00017-1.
6. Hancock, G. Design for distortional buckling of flexural members. *Thin Walled Struct.* **1997**, *27*, 3–12, doi:10.1016/0263-8231(96)00020-1.
7. Wang, H.; Zhang, Y. Experimental and numerical investigation on cold-formed steel C-section flexural members. *J. Constr. Steel Res.* **2009**, *65*, 1225–1235, doi:10.1016/j.jcsr.2008.08.007.
8. Wang, L.; Young, B. Beam tests of cold-formed steel built-up sections with web perforations. *J. Constr. Steel Res.* **2015**, *115*, 18–33, doi:10.1016/j.jcsr.2015.08.001.
9. Yuan, W.-B.; Yu, N.-T.; Li, L.-Y. Distortional buckling of perforated cold-formed steel channel-section beams with circular holes in web. *Int. J. Mech. Sci.* **2017**, *126*, 255–260, doi:10.1016/j.ijmecsci.2017.04.001.
10. Moen, C.D.; Schafer, B. Elastic buckling of cold-formed steel columns and beams with holes. *Eng. Struct.* **2009**, *31*, 2812–2824, doi:10.1016/j.engstruct.2009.07.007.
11. Zhao, J.; Sun, K.; Yu, C.; Wang, J. Tests and direct strength design on cold-formed steel channel beams with web holes. *Eng. Struct.* **2019**, *184*, 434–446, doi:10.1016/j.engstruct.2019.01.062.
12. Zhao, O.; Rossi, B.; Gardner, L.; Young, B. Behaviour of structural stainless steel cross-sections under combined loading—Part I: Experimental study. *Eng. Struct.* **2015**, *89*, 236–246, doi:10.1016/j.engstruct.2014.11.014.
13. Dai, L.; Zhao, X.; Rasmussen, L.J. Flexural behaviour of steel storage rack beam-to-upright bolted connections. *Thin Walled Struct.* **2018**, *124*, 202–217, doi:10.1016/j.tws.2017.12.010.
14. Yu, N.-T.; Kim, B.; Yuan, W.-B.; Li, L.-Y.; Yu, F. An analytical solution of distortional buckling resistance of cold-formed steel channel-section beams with web openings. *Thin Walled Struct.* **2019**, *135*, 446–452, doi:10.1016/j.tws.2018.11.012.
15. Zhou, F.; Young, B. Tests of cold-formed stainless steel tubular flexural members. *Thin Walled Struct.* **2005**, *43*, 1325–1337, doi:10.1016/j.tws.2005.06.005.
16. Laím, L.; Rodrigues, J.P.; Da Silva, L.S. Experimental and numerical analysis on the structural behaviour of cold-formed steel beams. *Thin Walled Struct.* **2013**, *72*, 1–13, doi:10.1016/j.tws.2013.06.008.
17. Ye, J.; Hajirasouliha, I.; Becque, J.; Pilakoutas, K. Development of more efficient cold-formed steel channel sections in bending. *Thin Walled Struct.* **2016**, *101*, 1–13, doi:10.1016/j.tws.2015.12.021.
18. Chu, X.-T.; Kettle, R.; Li, L.-Y. Lateral-torsion buckling analysis of partial-laterally restrained thin-walled channel-section beams. *J. Constr. Steel Res.* **2004**, *60*, 1159–1175, doi:10.1016/j.jcsr.2003.11.001.

19. Muftah, F.; Sani, M.S.H.M.; Kamal, M.M.M. Flexural Strength Behaviour of Bolted Built-Up Cold-Formed Steel Beam with Outstand and Extended Stiffener. *Int. J. Steel Struct.* **2018**, *19*, 719–732, doi:10.1007/s13296-018-0157-0.
20. Huang, X.; Yang, J.; Liu, Q.-F.; Zhu, J.; Bai, L.; Wang, F.-L.; Wang, J.-H. A simplified flange–lip model for distortional buckling of cold-formed steel channel-sections with stiffened web. *Int. J. Mech. Sci.* **2018**, *136*, 451–459, doi:10.1016/j.ijmecsci.2017.12.034.
21. Wu, M.-J.; Huang, X.-H.; Zhu, J. Distortional buckling of a CFS channel section with and without stiffened flanges. *J. Mech. Sci. Technol.* **2019**, *33*, 2623–2632, doi:10.1007/s12206-019-0510-z.
22. Visy, D.; Szedlák, M.; Geleji, B.B.; Ádány, S. Flexural buckling of thin-walled lipped channel columns with slotted webs: Numerical and analytical studies. *Eng. Struct.* **2019**, *197*, 109399, doi:10.1016/j.engstruct.2019.109399.
23. Shafaei, S.; Ronagh, H.; Usefi, N. Experimental evaluation of CFS braced-truss shear wall under cyclic loading. In Proceedings of the Advances in Engineering Materials, Structures and Systems: Innovations, Mechanics and Applications, Proceedings Of The 7Th International Conference On Structural Engineering, Mechanics And Computation, September 2-4, 2019, Cape Town, South Africa, UK, 2019; pp. 192–196.
24. Ye, J.; Jiang, L.; Wang, X. Seismic Failure Mechanism of Reinforced Cold-Formed Steel Shear Wall System Based on Structural Vulnerability Analysis. *Appl. Sci.* **2017**, *7*, 182, doi:10.3390/app7020182.
25. Ye, J.; Wang, X. Piecewise Function Hysteretic Model for Cold-Formed Steel Shear Walls with Reinforced End Studs. *Appl. Sci.* **2017**, *7*, 94, doi:10.3390/app7010094.
26. Hancock, G.; Rogers, C. Design of cold-formed steel structures of high strength steel. *J. Constr. Steel Res.* **1998**, *46*, 167–168, doi:10.1016/s0143-974x(98)80013-8.
27. AS 4084. *Steel Storage Racking*; Standards Australia: Sydney, Australia, 2012.
28. Put, B.M.; Trahair, N.S.; Pi, Y.-L. Bending and Torsion of Cold-Formed Channel Beams. *J. Struct. Eng.* **1999**, *125*, 540–546, doi:10.1061/(ASCE)0733-9445(1999)125:5(540).
29. Shariati, M.; Mafipour, M.S.; Mehrabi, P.; Zandi, Y.; Deghani, D.; Bahadori, A.; Shariati, A.; Trung, N.T.; Shek, P. Application of Extreme Learning Machine (ELM) and Genetic Programming (GP) to design steel-concrete composite floor systems at elevated temperatures. *Steel Compos. Struct.* **2019**, *33*, 319.
30. Shariati, M.; Trung, N.T.; Wakil, K.; Mehrabi, P.; Safa, M.; Khorami, M. Estimation of moment and rotation of steel rack connection using extreme learning machine. *Steel Compos. Struct.* **2019**, *31*, 427–435.
31. Xu, C.; Zhang, X.; Mehrabi, P.; Shariati, A.; Mohamad, E.T.; Hoang, N.; Wakil, K. Using genetic algorithms method for the paramount design of reinforced concrete structures. *Struct. Eng. Mech.* **2019**, *71*, 503–513.
32. Trung, N.T.; Shahgoli, A.F.; Zandi, Y.; Shariati, M.; Wakil, K.; Safa, M.; Khorami, M. Moment-rotation prediction of precast beam-to-column connections using extreme learning machine. *Struct. Eng. Mech.* **2019**, *70*, 639–647.
33. Sedghi, Y.; Sedghi, Y.; Zandi, Y.; Shariati, M.; Ahmadi, E.; Azar, V.M.; Toghroli, A.; Safa, M.; Mohamad, E.T.; Khorami, M.; Wakil, K. Application of ANFIS technique on performance of C and L shaped angle shear connectors. *Smart Struct. Syst.* **2018**, *22*, 335–340.
34. Safa, M.; Shariati, M.; Ibrahim, Z.; Toghroli, A.; Bin Baharom, S.; Nor, N.M.; Petkovic, D. Potential of adaptive neuro fuzzy inference system for evaluating the factors affecting steel-concrete composite beam's shear strength. *Steel Compos. Struct.* **2016**, *21*, 679–688, doi:10.12989/scs.2016.21.3.679.
35. Shariati, M.; Faegh, S.S.; Mehrabi, P.; Bahavarnia, S.; Zandi, Y.; Masoom, D.R.; Toghroli, A.; Trung, N.T.; Salih, M.N.A. Numerical study on the structural performance of corrugated low yield point steel plate shear walls with circular openings. *Steel Compos. Struct.* **2019**, *33*, 569–581.
36. Usefi, N.; Sharafi, P.; Ronagh, H. Numerical models for lateral behaviour analysis of cold-formed steel framed walls: State of the art, evaluation and challenges. *Thin Walled Struct.* **2019**, *138*, 252–285, doi:10.1016/j.tws.2019.02.019.
37. Sharafi, P.; Mortazavi, M.; Usefi, N.; Kildashti, K.; Ronagh, H.; Samali, B. Lateral force resisting systems in lightweight steel frames: Recent research advances. *Thin Walled Struct.* **2018**, *130*, 231–253, doi:10.1016/j.tws.2018.04.019.

38. Sharafi, P.; Rashidi, M.; Samali, B.; Ronagh, H.; Mortazavi, M. Identification of Factors and Decision Analysis of the Level of Modularization in Building Construction. *J. Archit. Eng.* **2018**, *24*, 04018010, doi:10.1061/(asce)ae.1943-5568.0000313.
39. Usefi, N.; Ronagh, H.; Mohammadi, M. Finite Element Analysis of Hybrid Cold-Formed Steel Shear Wall Panels. In *International Structural Engineering and Construction*, 2018; ISEC Press: Fargo, ND, USA, 2018; Volume 5.
40. Cardoso, F.S.; Rasmussen, L.J. Finite element (FE) modelling of storage rack frames. *J. Constr. Steel Res.* **2016**, *126*, 1–14, doi:10.1016/j.jcsr.2016.06.015.
41. Lakusic, S.; Usefi, N.; Nav, F.M.; Abbasnia, R. Finite element analysis of RC elements in progressive collapse scenario. *J. Croat. Assoc. Civ. Eng.* **2016**, *68*, 1009–1022, doi:10.14256/JCE.1550.2016.
42. Majidi, L.; Usefi, N.; Abbasnia, R. Numerical study of RC beams under various loading rates with LS-DYNA. *J. Central South Univ.* **2018**, *25*, 1226–1239, doi:10.1007/s11771-018-3820-x.
43. Usefi, N.; Ronagh, H.; Kildashti, K.; Samali, B. Macro/Micro Analysis of Cold-Formed Steel Members Using ABAQUS and OPENSEES. In *Volume of Abstracts, Proceedings of the 13th International Conference on Steel, Space and Composite Structures (SS18)*; The University of Western Australia: Perth, Australia, 2018.
44. Nav, F.M.; Usefi, N.; Abbasnia, R. Analytical investigation of reinforced concrete frames under middle column removal scenario. *Adv. Struct. Eng.* **2017**, *21*, 1388–1401, doi:10.1177/1369433217746343.
45. Abaqus, V. *6.14 Documentation*; Dassault Systemes Simulia Corporation: Johnston, RI, USA, 2014; Volume 651.

5. Experimental and Numerical Investigation of an Innovative Method for Strengthening Cold-Formed Steel Profiles in Bending throughout Finite Element Modeling and Application of Neural Network Based on Feature Selection Method (Journal Article 3)

A reprint of this study entitled ‘Experimental and Numerical Investigation of an Innovative Method for Strengthening Cold-Formed Steel Profiles in Bending throughout Finite Element Modeling and Application of Neural Network Based on Feature Selection Method’, Taheri, E.; Esgandarzadeh Fard, S.; Zandi, Y.; Samali, B. published by Applied Sciences. 2021; 11(11):5242. <https://doi.org/10.3390/app11115242>

5.1. Abstract

This study evaluates an innovative reinforcement method for cold-formed steel (CFS) upright sections through finite element assessment as well as prediction of the normalized ultimate load and deflection of the profiles by artificial intelligence (AI) and machine learning (ML) techniques. Following the previous experimental studies, several CFS upright profiles with different lengths, thicknesses and reinforcement spacings are modeled and analyzed under flexural loading. The finite element method (FEM) is employed to evaluate the proposed reinforcement method in different upright sections and to provide a valid database for the analytical study. To detect the most influential factor on flexural strength, the “feature selection” method is performed on the FEM results. Then, by using the feature selection method, a hybrid neural network (a combination of multi-layer perceptron algorithm and particle swarm optimization method) is developed for the prediction of normalized ultimate load. The correlation coefficient (R), root mean square error (RMSE), Nash–Sutcliffe efficiency (NSE), mean absolute error (MAE) and Wilmot’s index of agreement (WI) are used as the measure of precision. The results show that the geometrical parameters have almost the same contribution in the flexural capacity and deflection of the specimens. According to the performance evaluation indexes, the best model is detected and optimized by tuning other algorithm parameters. The results indicate that the hybrid neural network can successfully predict the normalized ultimate load and deflection.

Keywords: cold-formed steel; upright; finite element method; feature selection method; multi-layer perceptron; particle swarm optimization; neural network

5.2. Introduction

Employing cold-formed steel (CFS) racking systems has been extensively developed around the world due to their valuable structural benefits and workability, especially for storage and warehouse applications [1]. In recent years, various researchers and engineers have investigated different approaches to enhance the overall performance of these systems by utilizing different CFS upright strengthening methods.

In this regard, many studies indicated that CFS racking systems under flexural loading experience different types of failures, including distortional buckling failure modes [2], which can affect the

stability status of upright frames [3]. Various studies worked to improve different characteristics of uprights not only to enhance the bearing capacity, but also to extend the application of these systems. Following the study of racking system performances, Put et al. [4] applied a series of eccentrically and concentrically loading on the CFS upright connections and reported that by increasing the eccentricity, the beams strength decreases. Wang and Young [5] investigated novel CFS channel sections with double and single stiffeners and showed that local and distortional buckling can be controlled using this method. In another study, Calderoni et al. [6] conducted a series of monotonic and cyclic experiments on CFS members. Their results indicated that the CFS channels could not resist the buckling deformations due to the lack of flexural stiffness. Wang and Zhang [7] studied C-shaped CFS elements with or without edge stiffeners. They employed two types of stiffeners and reported an increase in the capacity of CFS members due to applying stiffeners. Taheri et al. [8] evaluated the influence of a new reinforcement approach on the compressive capacity of racking upright profiles. In another study, Taheri et al. [9] also performed a series of flexural tests on CFS sections with or without the reinforcement approach. The results indicated that the proposed reinforcements considerably improved the ultimate flexural capacity.

The expensive and time-consuming nature of actual experimental tests has encouraged researchers to employ other types of approaches for structural evaluations, such as numerical methods. Since the finite element method (FEM) has major priorities in comparison to other numerical approaches, employing this technique has drastically increased for a variety of engineering problems, especially CFS racking systems. Visy et al. [10] numerically studied the flexural behavior of stiffened CFS slotted beams subjected to different loading scenarios. Nandini and Kalyanaraman [11], in a numerical investigation, studied the behavior and strength of Lipped channel beams of various lengths. They suggested an approach to design these beams under the interaction of local, distortional and overall lateral–torsional buckling based on the Euro code provisions. There are several other studies in the literature that simulated the behavior and strength of CFS racking frames through FEM [12–14].

Artificial intelligence is a group of techniques related to intelligent methods that consider each problem with a defined intelligence algorithm. Most of the applications of these techniques in engineering problems are focused on either predicting or verifying a problem. Prediction accuracy depends on a variety of variables, such as error, soft computing approach, estimation of the

problems before the prediction process, etc. Backpropagation (BP) approaches, which are considered among classic techniques, are generally proposed to train artificial neural networks (ANN). Machine learning is another type of these algorithms that benefits from a learning circuit. Some of the rotational properties of CFS racking systems have been successfully estimated by the machine learning method in the past years [15]. In order to address classic algorithm deficiencies, some approaches, including genetic algorithm (GA) [16], particle swarm optimization (PSO) [17], and multi-layer perceptron (MLP) [18], have been proposed and utilized in different prediction cases in recent years. Generally, the PSO algorithm has been proved as a reliable technique to be combined with other types of intelligence algorithms based on different studies [19,20].

In this paper, the proposed reinforcement method for CFS uprights (previously presented by the authors [8,9]) is further investigated through FEM and machine learning algorithms. First, a finite element model is developed in ABAQUS software to simulate and analyze the CFS upright frames under flexural loading. Then, the FEM results are compared and verified by the experimental test data in the literature [9]. Thereafter, the verified FEM is employed for a parametric study to evaluate the performance of upright frames with different lengths, thicknesses and reinforcement spacing. Considering the FEM and test results (current study and test results in [9]), an artificial intelligence approach is also employed both for predicting the flexural capacity of the proposed system and verifying the FEM models. First, a feature selection based algorithm is used to find the most governing property of flexural strength and then a hybrid neural network (MLP algorithm in combination with PSO) is utilized for verification, optimization and prediction.

5.3. Finite Element Modeling

The proposed reinforcement method for strengthening the upright frame, which was previously discussed by Taheri et al. [8,9], is presented in Figure 5-1. In this paper, a parametric FE study is conducted on the proposed reinforcement system to obtain a reliable database for the artificial intelligence approach. All of the FE modeling is conducted in the ABAQUS computer program. First, the FE modeling approach is presented in detail (Sections 5.3.1 - 5.3.4) and then it is verified by the experimental data (Section 5.3.5) [9]. Finally, the validated FE method is utilized for a parametric study (5.3.6). The parametric study evaluates the influence of various reinforcement spacing, including 50, 100, 150, 250, and 300 mm, on the strength of the profiles with different thicknesses of 1.6, 2, 2.5 and 3 mm. Moreover, in order to achieve a comprehensive dataset, different upright lengths are taken into account in this study. The details of the FE models are provided in Table 5-1 and Figure 5-1. Further details about the experimental setup, specimen specifications, etc., can be found in [8,9].

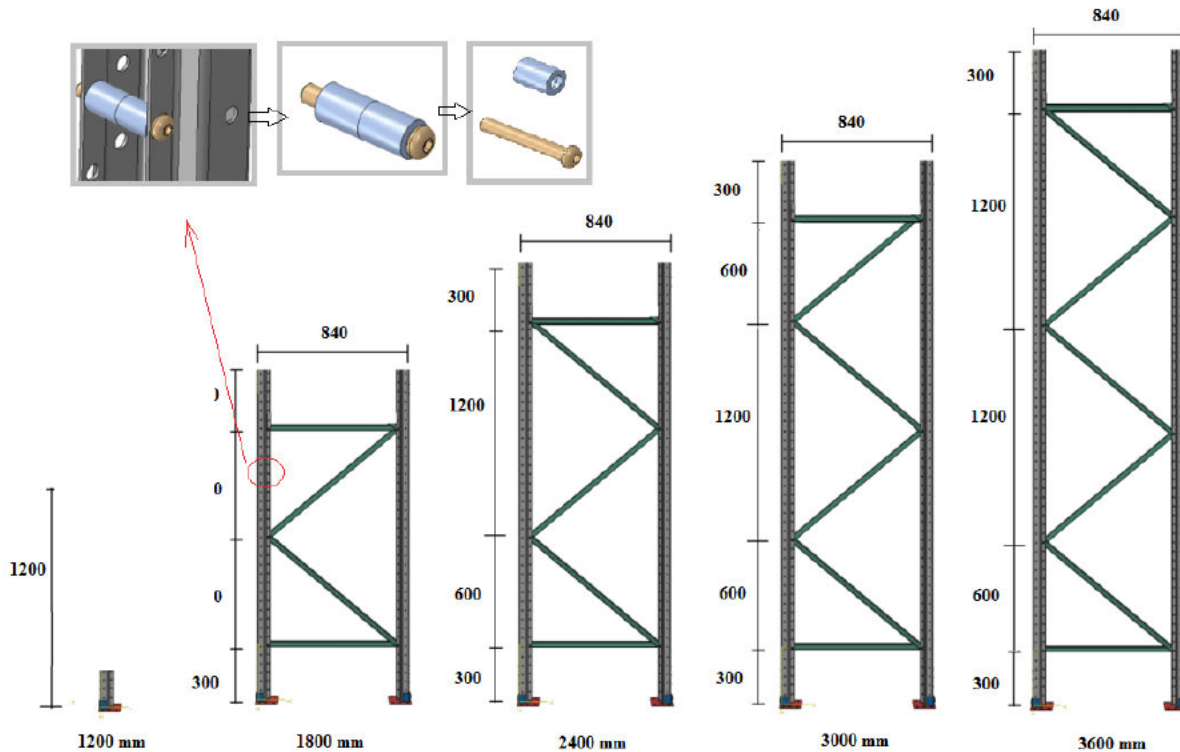


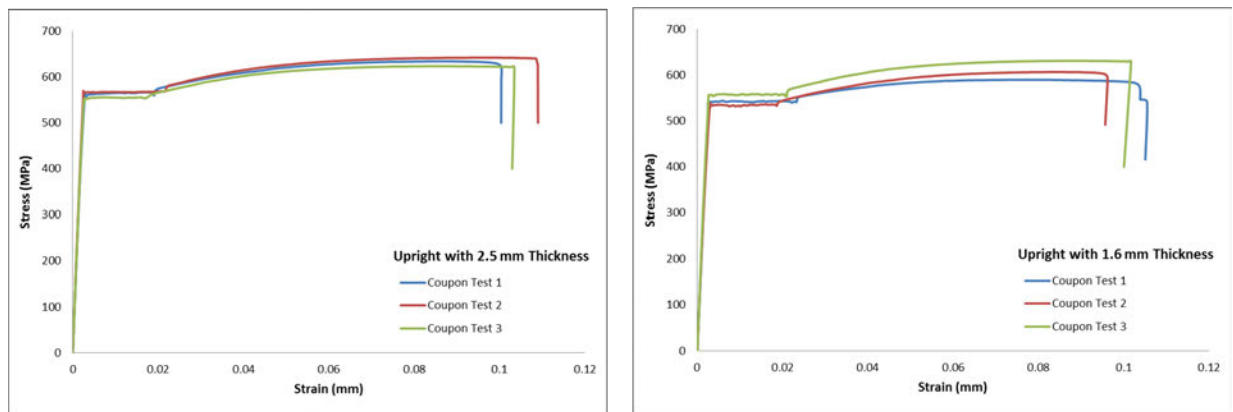
Figure 5-1: Schematic of models.

Table 5-1: Geometrical features of models.

Upright Length (mm)	Upright Thickness (mm)	Reinforcement Spacing (mm)
1800		50
	1.6	100
2400	2.0	150
	2.5	200
3000	3.0	250
3600		300

5.3.1 Material Properties

The Poisson's ratio and the modulus of elasticity are assumed to be 0.3 and 200 GPa, respectively [21]. Additionally, other material properties were derived according to the modified coupon test, which is indicated in Figure 5-2 and Table 5-2. The material law of the frame assembly was modeled using the bi-linear stress-strain relation [21].



(a)

(b)

Figure 5-2: Coupon test results for uprights: (a) with 1.6 mm and (b) with 2.5 mm thickness [9].

Table 5-2: Material properties of upright sections.

Thickness (mm)	Yield Stress, f_y (MPa)	Ultimate Stress, f_u (MPa)	Elongation (%)
2.5	572	608	13
1.6	563	591	11

5.3.2 Connections and Interactions

The penalty method with a surface-to-surface interaction is employed for models, where a friction coefficient of 0.3 is considered for the tangential response [21–23]. Hard contact is also adopted for normal behavior. For simulating the interaction of bolts, the coupling method is employed. A reference point is defined at the center of the bolt hole and then the end beam restraints are considered as a beam, using the contact pairs between the elements at the two opposite sides of the built-up sections. Figure 5-3 shows the existing interactions between the bending frame components model.

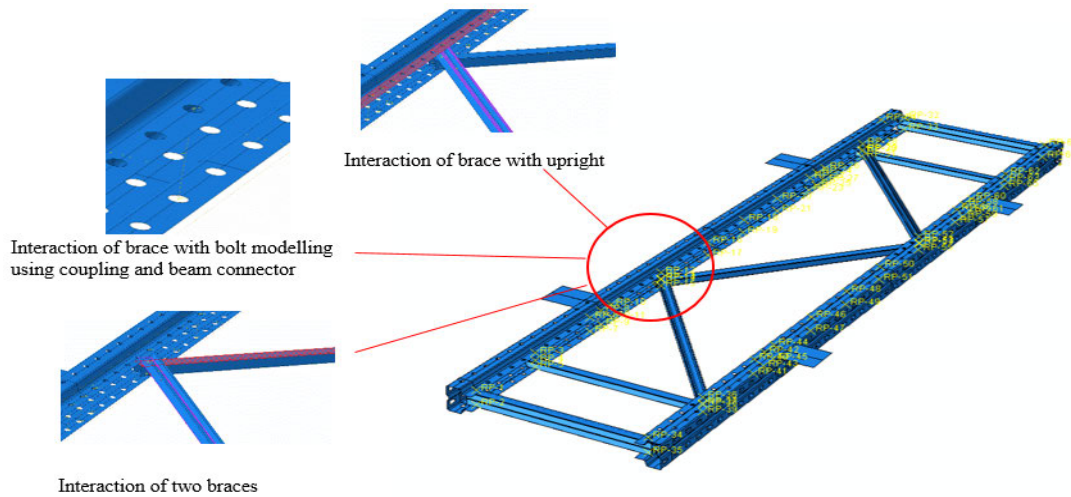


Figure 5-3: Interactions between frame elements.

5.3.3 Boundary Conditions and Loading

All boundary components are constrained to simulate the test setup illustrated in Figure 5-4. The vertical translation on the supports is restrained. The concentrated load with the displacement method is applied at the shear center of the upright section on the loading plates, while the rotations and translation are allowed to simulate the actual test conditions. Details of the test setup about each axis is illustrated in Figure 5-4 [9].

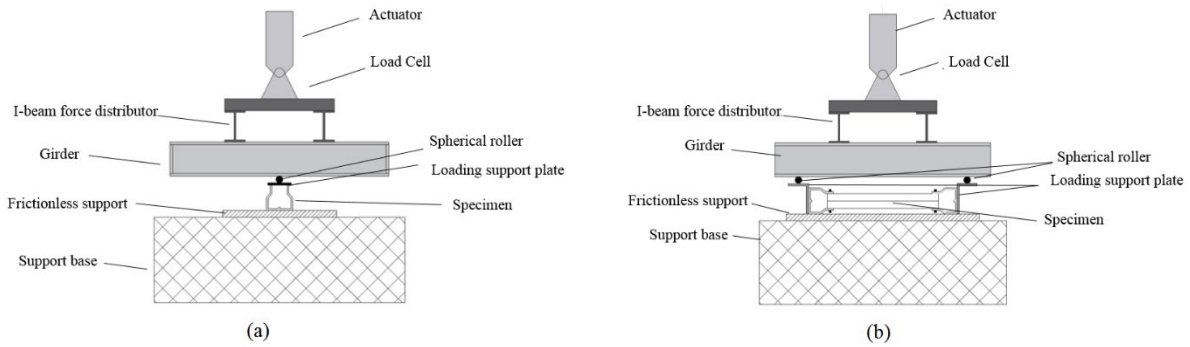


Figure 5-4: (a) Minor axis test setup. (b) Major axis test setup [9].

5.3.4 Mesh

In this paper, shell elements are deployed since the thickness of the open CFS members is very small in comparison with their width and length; thus, buckling deformations can be explicitly modeled. The four-node shell element with reduced integration (S4R) is employed to model the frame elements [24]. A convergence study is performed to capture the optimum mesh size for the upright and bracing members, and it is observed that quad-dominated meshes with dimensions of 10 mm are deemed satisfactory for frame elements. Figure 5-5 shows the final mesh used for the upright models.

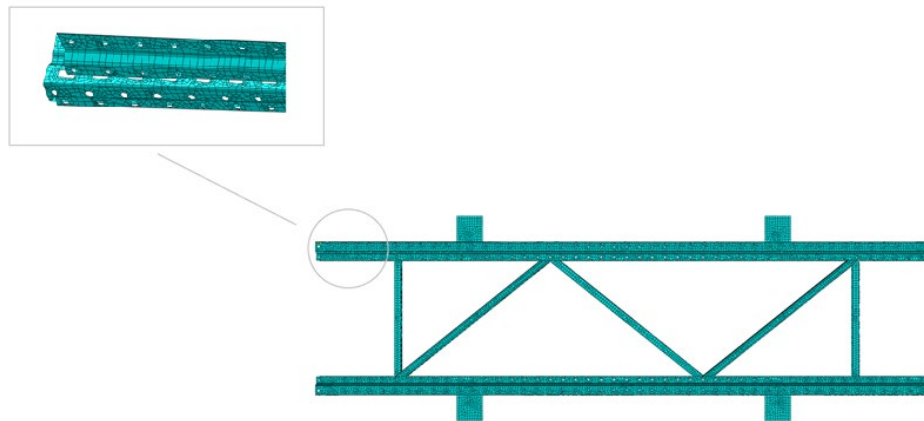


Figure 5-5: Typical FE mesh of an upright section.

5.3.5 FE Model Verification

After establishing the FE models, a loading simulation is conducted through the ABAQUS program. It should be noted that only specimens with 2400 mm length and 1.6 mm thickness are

employed for the verification purpose. In addition, three scenarios of non-reinforcement, reinforcement with 200 mm spacing, and reinforcement with 300 mm spacing are considered. In this part, linear regression analyses are applied to the FE results to assist in validating the obtained results of the numerical models. Additionally, the verified results are exported to a database for artificial intelligence applications, which will be discussed in Section 3.

5.3.5.1 Verification under Minor Axis Loading

In order to illustrate the accuracy of the FEM results, each curve is compared with the corresponding test curve and a linear regression is drawn for each model [25]. Figure 5-6 compares the normalized bending moment-deflection curves between the FE and experimental results. In addition, Figure 5-7 shows the linear regression of the FEM curve with the experimental curve. Table 5-3 demonstrates the evaluation criteria of the accuracy of the FEM predictions. Comparison of the experimental and numerical results indicates the outstanding accuracy and compatibility between the two methods.

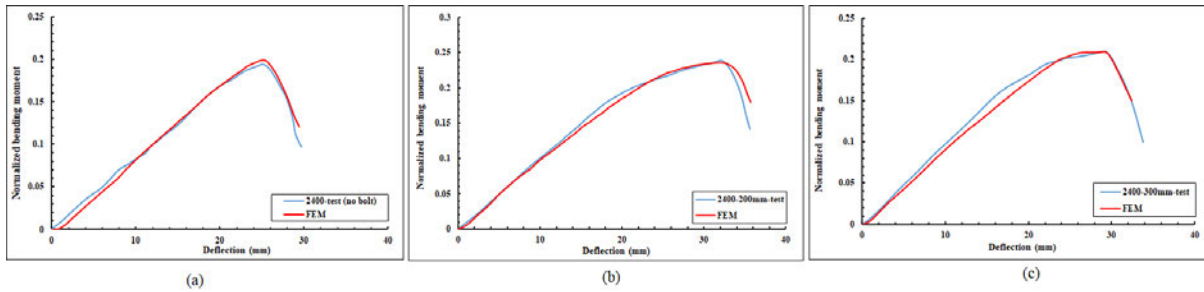


Figure 5-6: Comparison of the FE model against the minor-axis test results for (a) non-reinforced model, (b) 200 mm reinforced model and (c) 300 mm reinforced model.

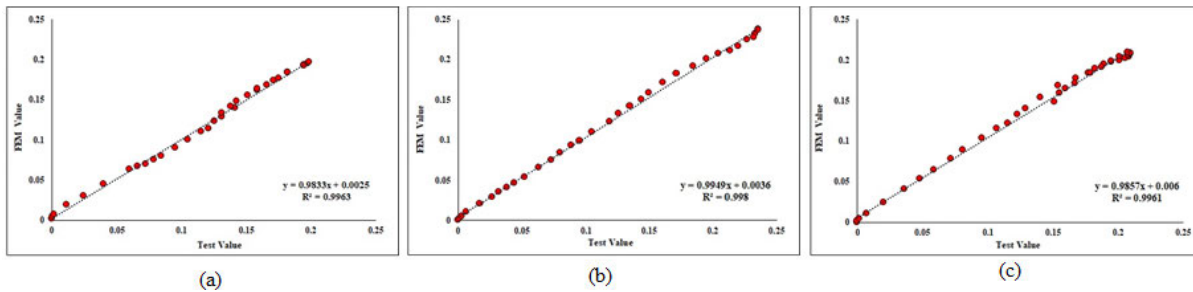


Figure 5-7: . Linear regression diagram for (a) non-reinforced model, (b) 200 mm reinforced model, and (c) 300 mm reinforced model.

Table 5-3: FEM vs. experimental results accuracy details in terms of evaluation criteria.

Non-reinforced model	Evaluation criteria	
	Std *	0.061
	Pearson (r)	0.998
	R ²	0.996
200 mm reinforced model	Evaluation criteria	
	Std	0.080
	Pearson (r)	0.993
	R ²	0.998
300 mm reinforced model	Evaluation criteria	
	Std	0.069
	Pearson (r)	0.998
	R ²	0.996

* Std = standard deviation.

5.3.5.2 Verification under Major Axis Loading

The same technique is also employed for the FE assessment of the upright section under the major axis loading. Figure 5-8 compares the normalized bending moment-deflection curve between the FEM and experimental results of the upright section under major axis loading. Figure 5-9 also indicates the linear regression of the FE results with the experimental curve. The evaluation criteria for the accuracy of the FEM predictions are represented in Table 5-4. Based on Figure 5-9 and Table 5-4, the FEM results indicate high accuracy and compatibility with the experimental results.

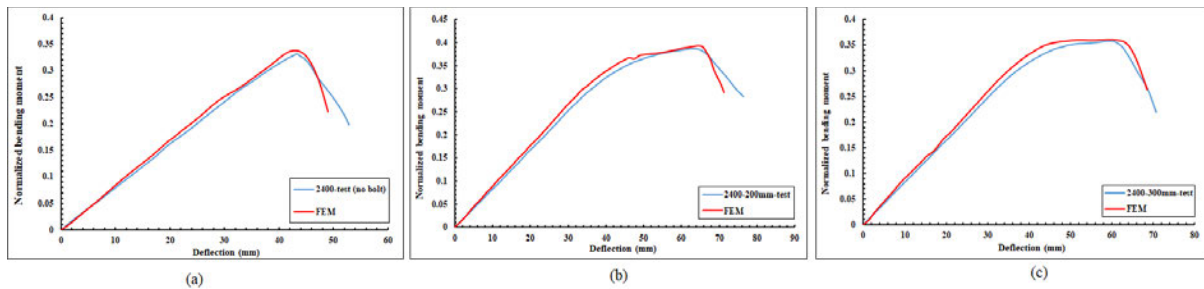


Figure 5-8: Comparison of FE model against major-axis test results for (a) non-reinforced model, (b) 200 mm reinforced model and (c) 300 mm reinforced model.

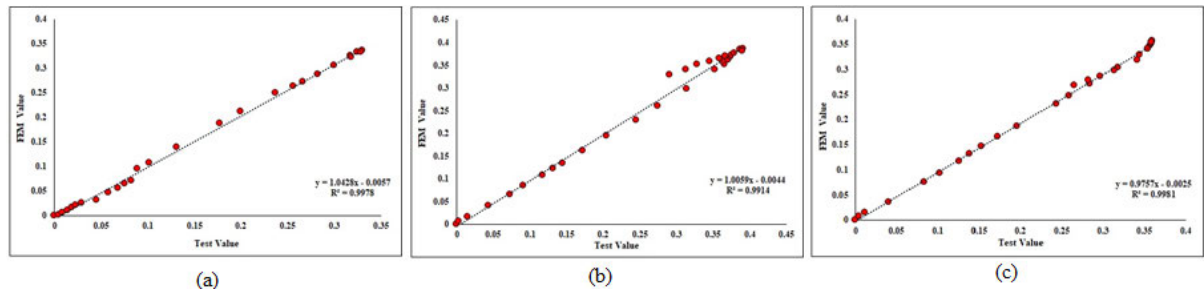


Figure 5-9: . Linear regression diagram for; (a) non-reinforced model, (b) 200 mm reinforced model, and (c) 300 mm reinforced model.

Table 5-4: FEM vs. experimental results accuracy details in terms of evaluation criteria.

Non-reinforced model	Evaluation criteria	
	Std *	0.124
	Pearson (r)	0.998
200 mm reinforced model	Evaluation criteria	
	Std	0.135
	Pearson (r)	0.995
300 mm reinforced model	Evaluation criteria	
	Std	0.122
	Pearson (r)	0.999
	R^2	0.998

* Std = standard deviation.

5.3.6 Parametric Finite Element Study

As discussed in the previous section, the FE model is capable of simulating the actual testing condition with minimum error. Hence, in this section, the verified FE method is utilized for a parametric study to investigate various uprights with different heights and thicknesses as well as different reinforcement spacings under flexural loading. The models for the parametric study are presented in Table 5-1. The results of the parametric study are classified into two groups of loading under major and minor axes, which are presented in the following sections. The convention used to name the specimens is shown in Figure 5-10.

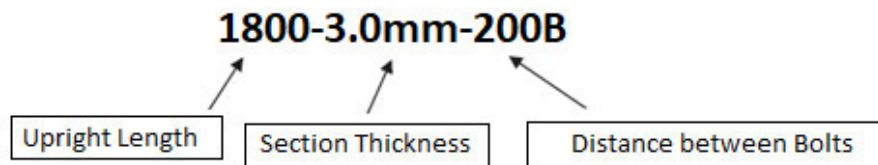


Figure 5-10: Designation of models.

5.3.6.1 Parametric Study: Results of Major Axis

The influence of various reinforcement spacings for the uprights under major axis loading has been discussed in this section. The normalized moment-displacement curves of the numerical models for each thickness are indicated in Figure 5-11, Figure 5-12, Figure 5-13, and Figure 5-14. As it is observed from the figures, using more reinforcement to partially close the section leads to improving the specimen's flexural capacity.

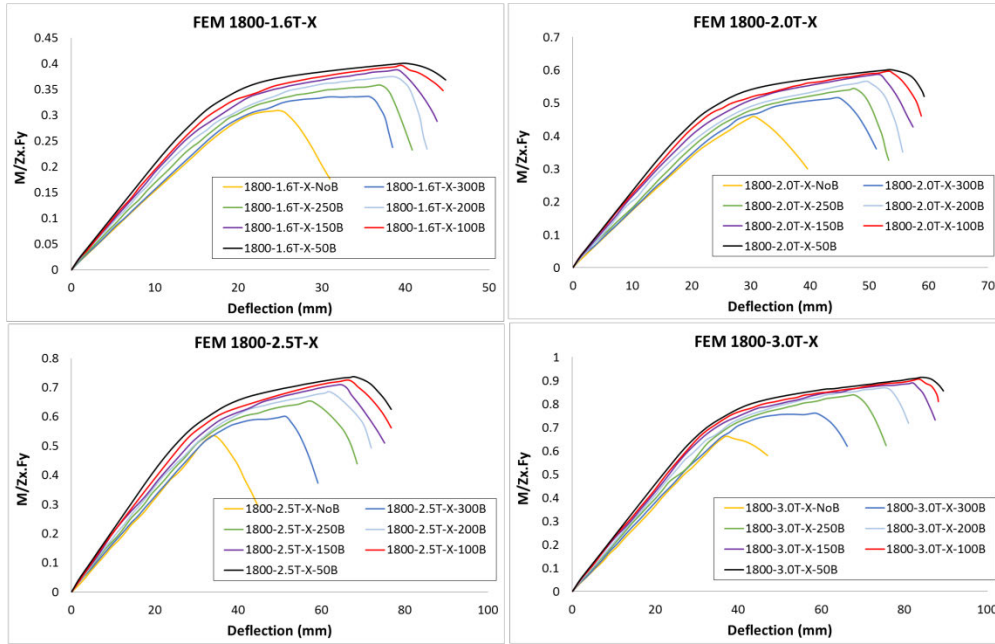


Figure 5-11: Normalized moment-deflection curves for 1800 mm models about major axis.

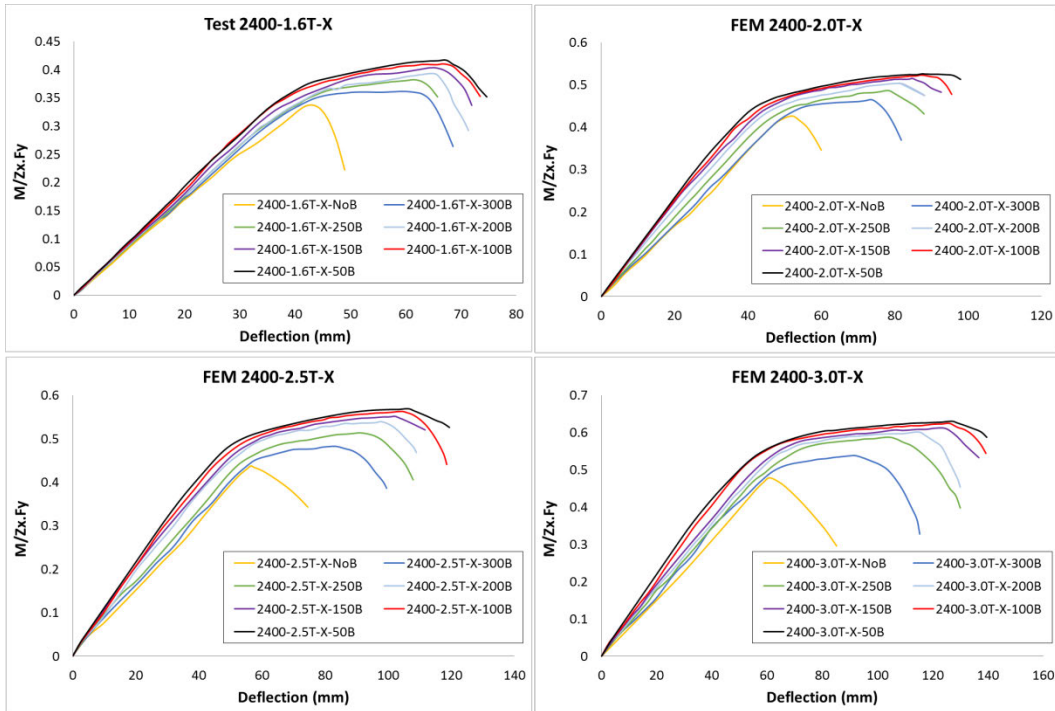


Figure 5-12: Normalized moment-deflection curves for 2400 mm models about major axis.

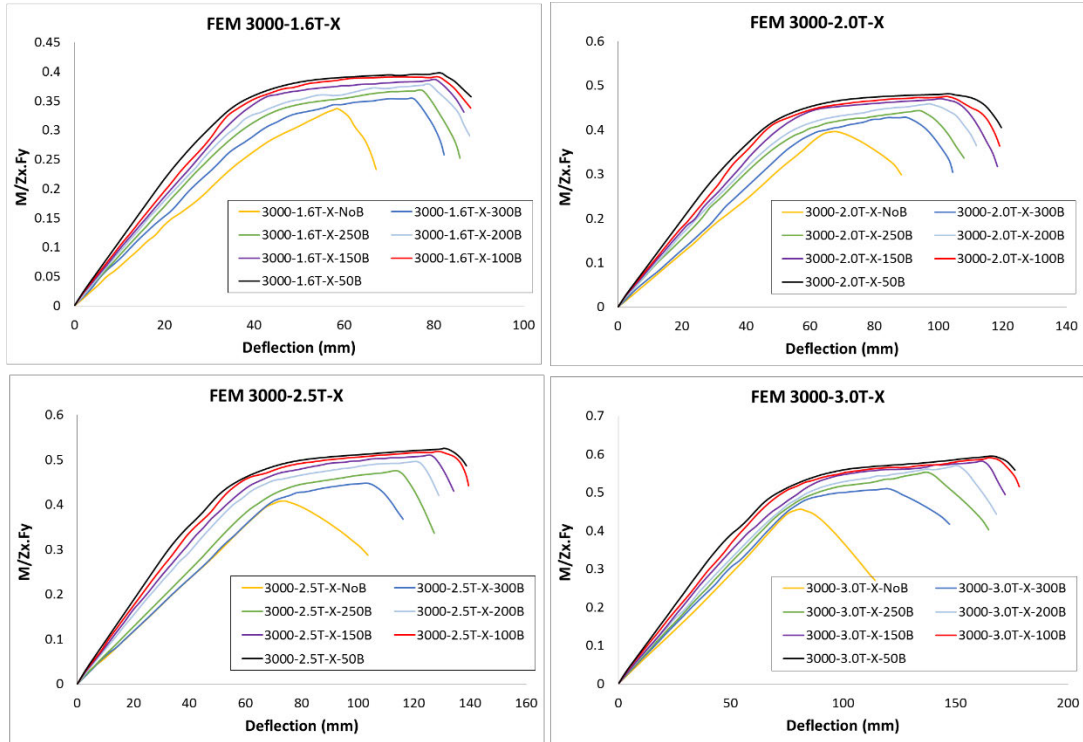


Figure 5-13: Normalized moment-deflection curves for 3000 mm models about major axis.

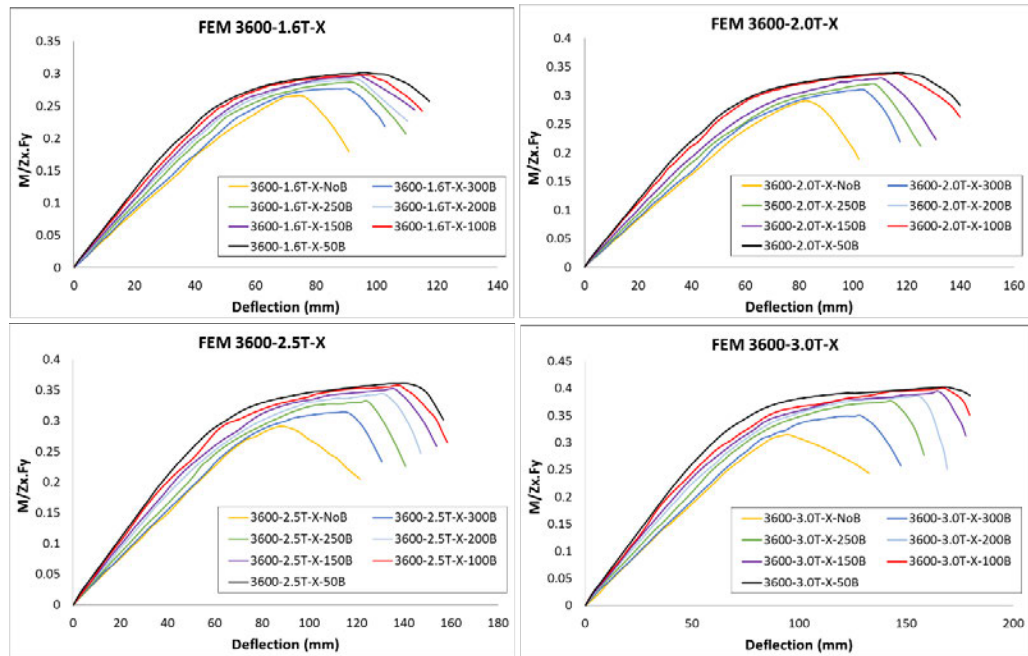


Figure 5-14: Normalized moment-deflection curves for 3600 mm models about major axis.

Figure 5-15 displays the normalized ultimate moment of the sections with various thicknesses at different reinforcement spacings. It is deduced that the shorter reinforcement spacing increases the ultimate bending capacity of the sections.

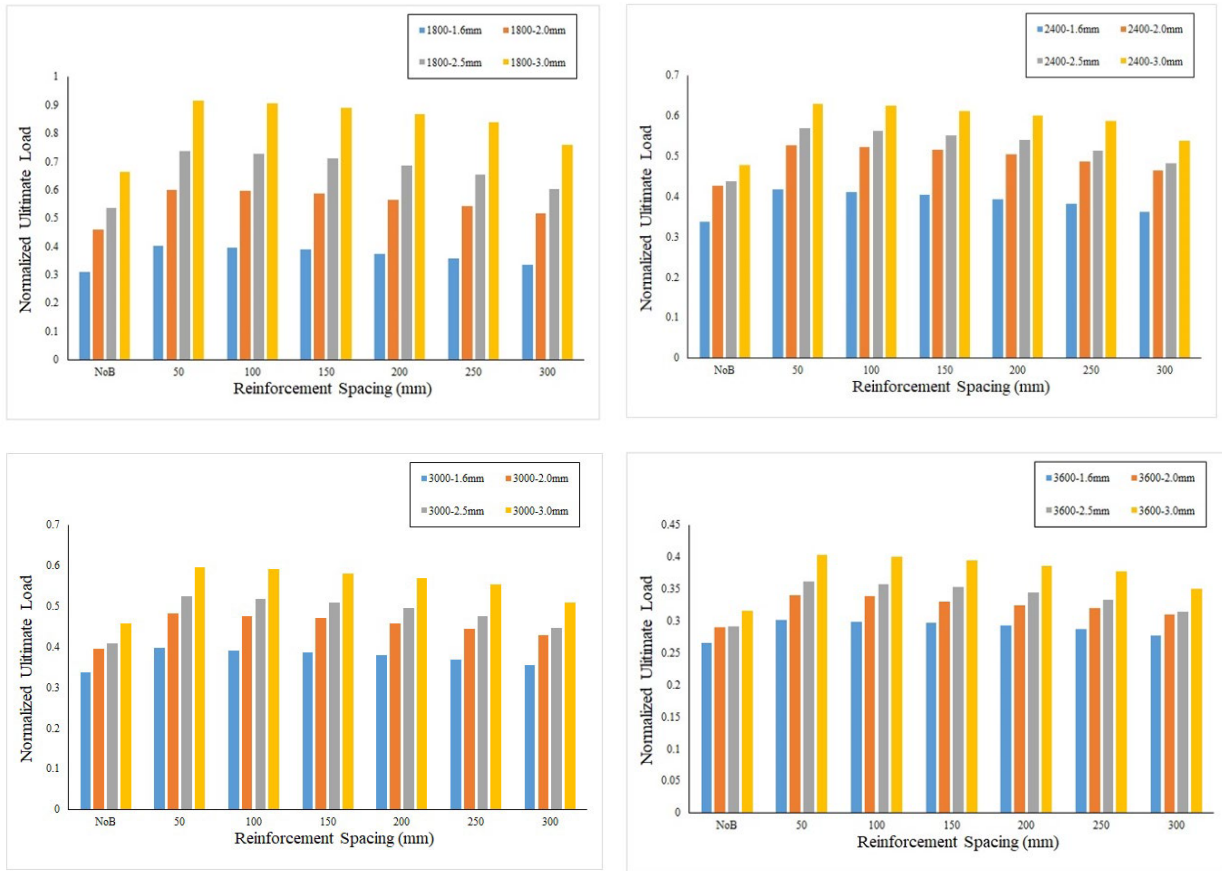


Figure 5-15: The normalized ultimate moment of 1800, 2400, 3000, and 3600 mm models about major axis with respect to reinforcement spacing.

The increased ultimate moment percentage utilizing various reinforcement spacing for the profiles from 1800 mm to 3600 mm length with respect to specimens without reinforcement is presented in Figure 5-16. In general, the reinforcement technique influences the ultimate capacity of the open sections in a range of about 5% to 40%. As it is seen, reinforcement addition from 300 mm spacing to 50 mm spacing can improve the frame’s strength by a significant amount. It is also found that reducing reinforcement spacing (up to 50 mm) can considerably increase the ultimate strength of the upright section under flexural loading.

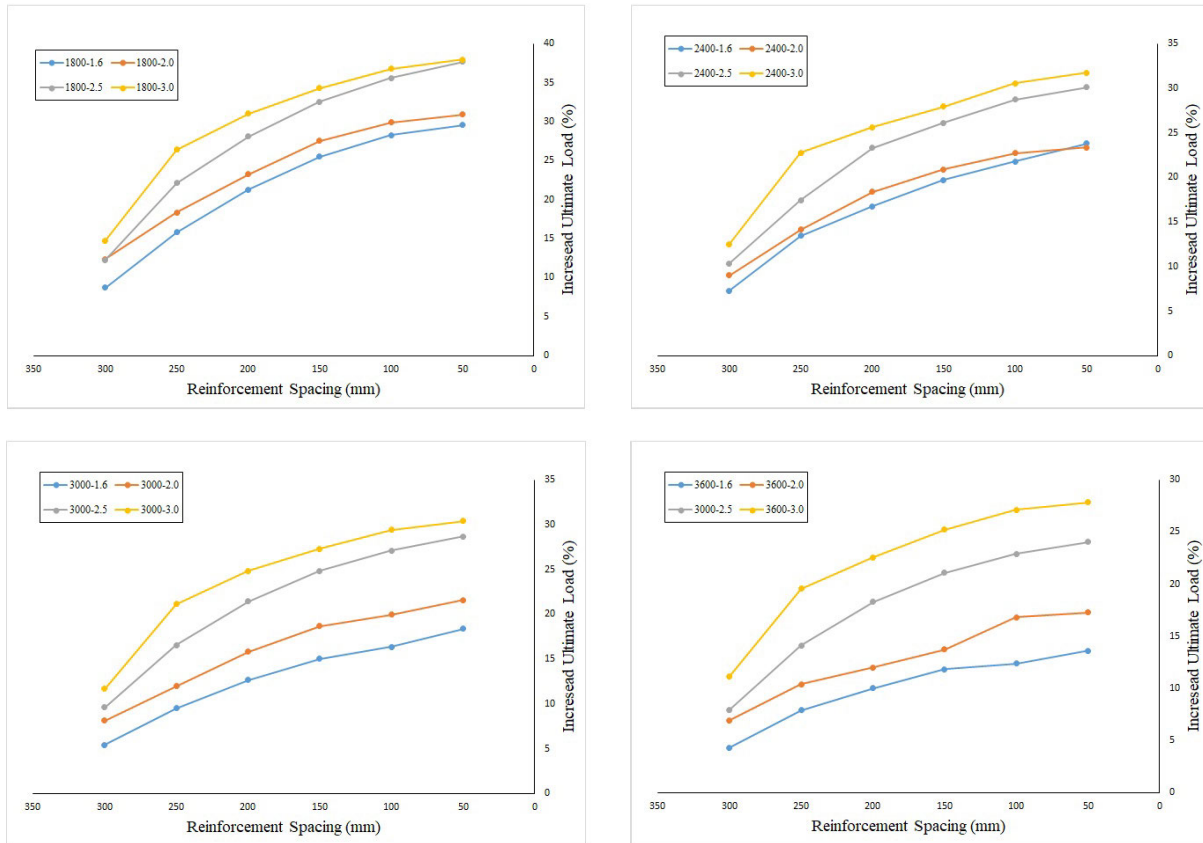


Figure 5-16: Percentage of increased ultimate load of major axis analysis with different reinforcement spacing in length order.

5.3.6.2 Parametric Study: Results of Minor Axis

The effect of different reinforcement spacings for the uprights under minor axis loading is discussed in this section. Minor axis models are provided with the same spacing and the same thickness as the major axis models. Figure 5-17, Figure 5-18, Figure 5-19, and Figure 5-20 indicate the normalized load-displacement curves for different models and thicknesses under minor axis loading. According to the figures, thickness and length play important roles in flexural strength. Additionally, more reinforcement leads to more ultimate strength. These figures show that using reinforcement with shorter spacing increases the strength of the sections. Sections with a shorter length and thicker cross-sections already have higher flexural strength, but this strength is improved noticeably by employing reinforcement. Due to the restrained buckling and better distribution of force along the section's length, specimens with dense reinforcements indicate better distortional buckling behavior. Generally, the distortional buckling behavior is enhanced,

and section failure is changed from general global buckling to local buckling, mostly due to partial closing of the upright section.

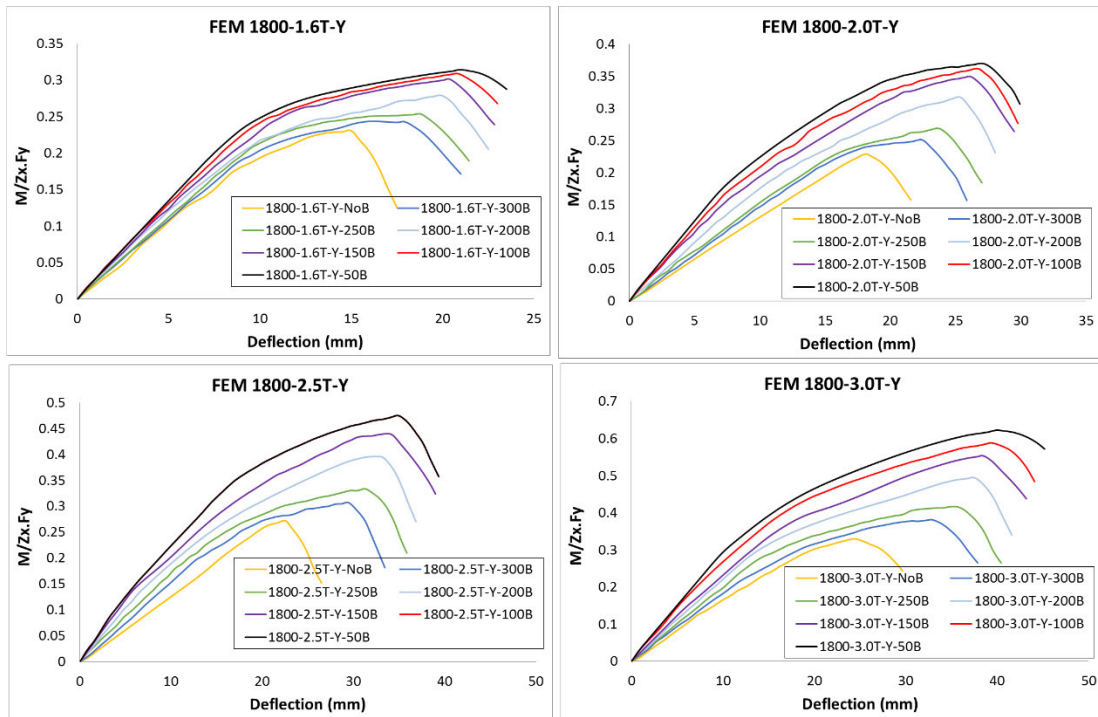


Figure 5-17: Normalized moment-deflection curves for 1800 mm models about minor axis.

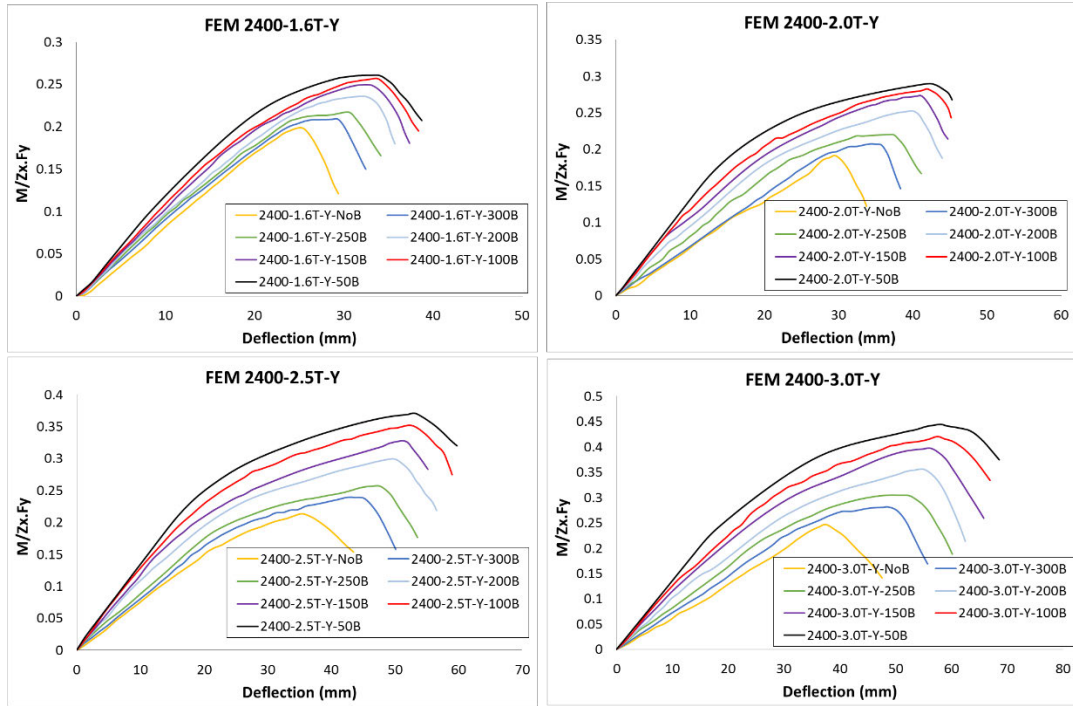


Figure 5-18: Normalized moment-deflection curves for 2400 mm models about minor axis.

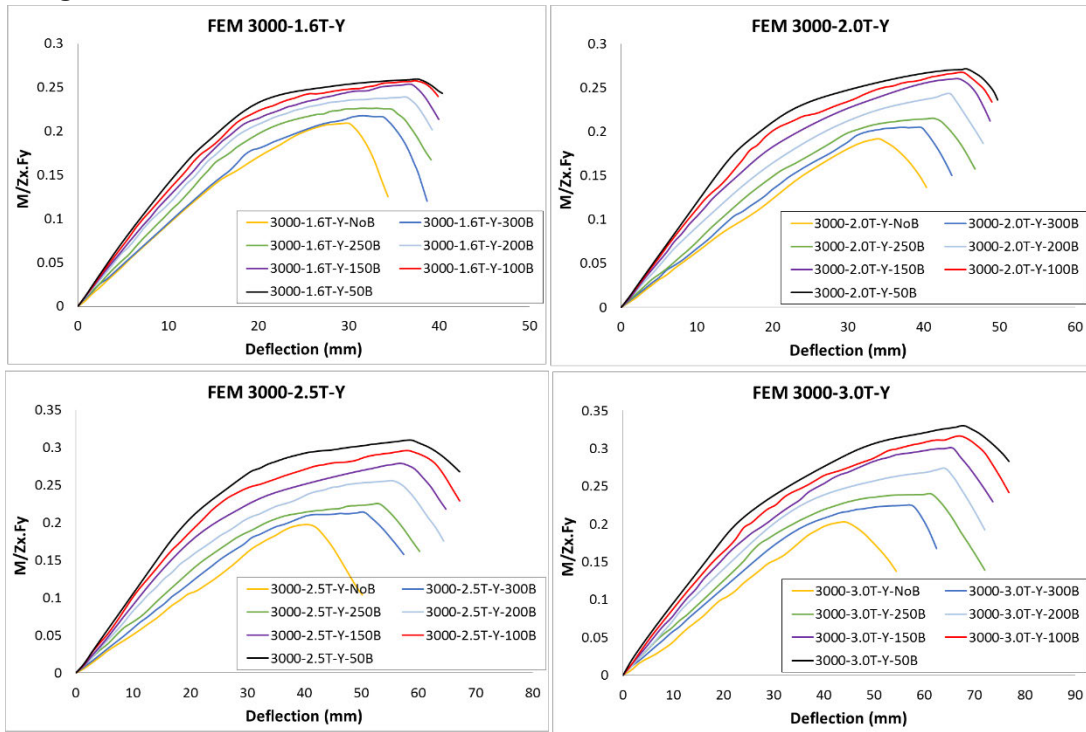


Figure 5-19: Normalized moment-deflection curves for 3000 mm models about minor axis.

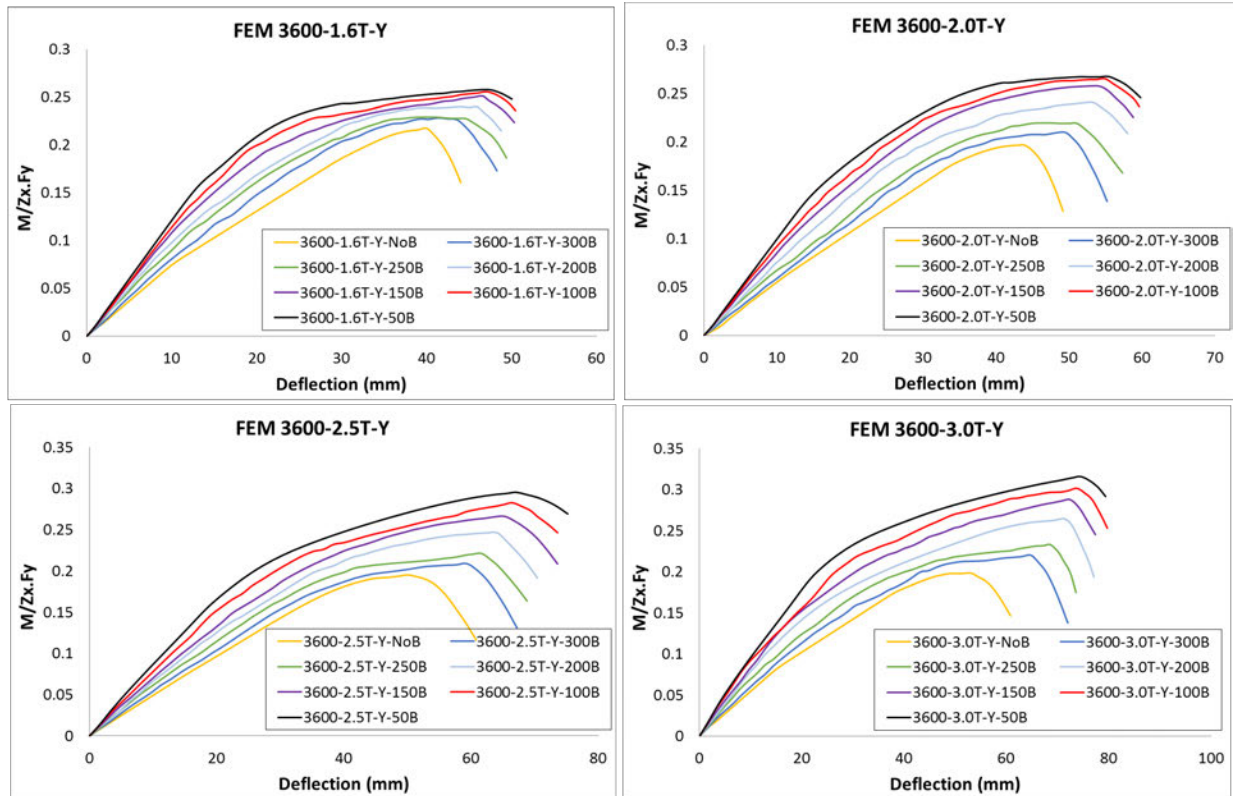
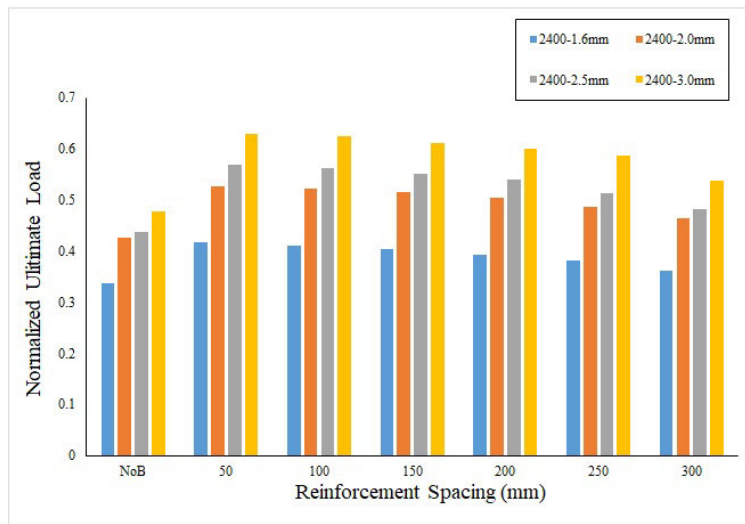
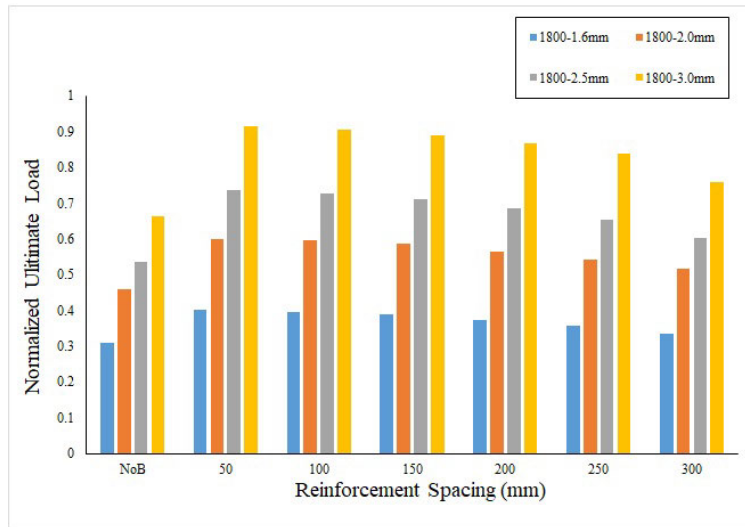


Figure 5-20: Normalized moment-deflection curves for 3600 mm models about minor axis.

Figure 5-21 indicates the normalized ultimate flexural strength with respect to the reinforcement spacing for models under minor axis loading. It can be observed that length has an inverse relation with flexural strength, where both spacing and thickness have a direct relation with the ultimate load. Hence, shorter models with higher thickness and shorter reinforcement spacing indicate higher flexural strength. For example, the model with 1800 mm length and 3 mm thickness (1800–3.0 mm) with 50 mm reinforcement spacing shows the greatest ultimate load.



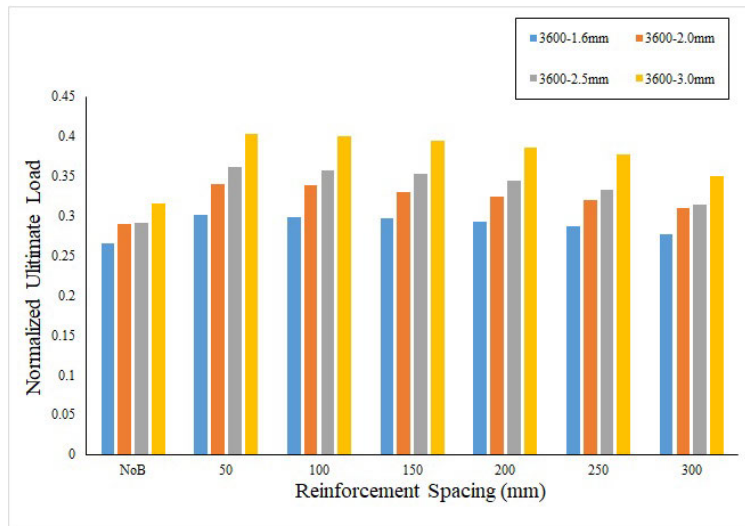
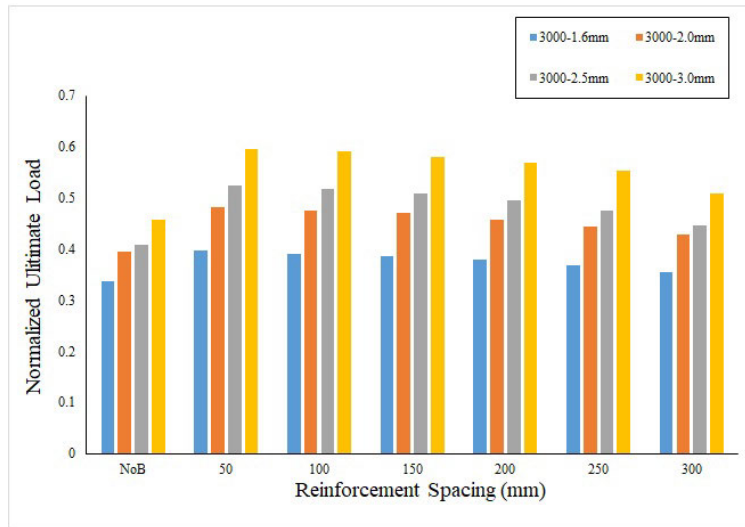


Figure 5-21: The normalized ultimate moment of 1800, 2400, 3000, 3600 mm models about minor axis with respect to reinforcement spacing.

Figure 5-22 illustrates a comparison between different increased ultimate loads with respect to reinforcement spacing with length order. Spacing and thickness are playing a same role in the case of flexural strength where both are enhancing the flexural strength of specimens.

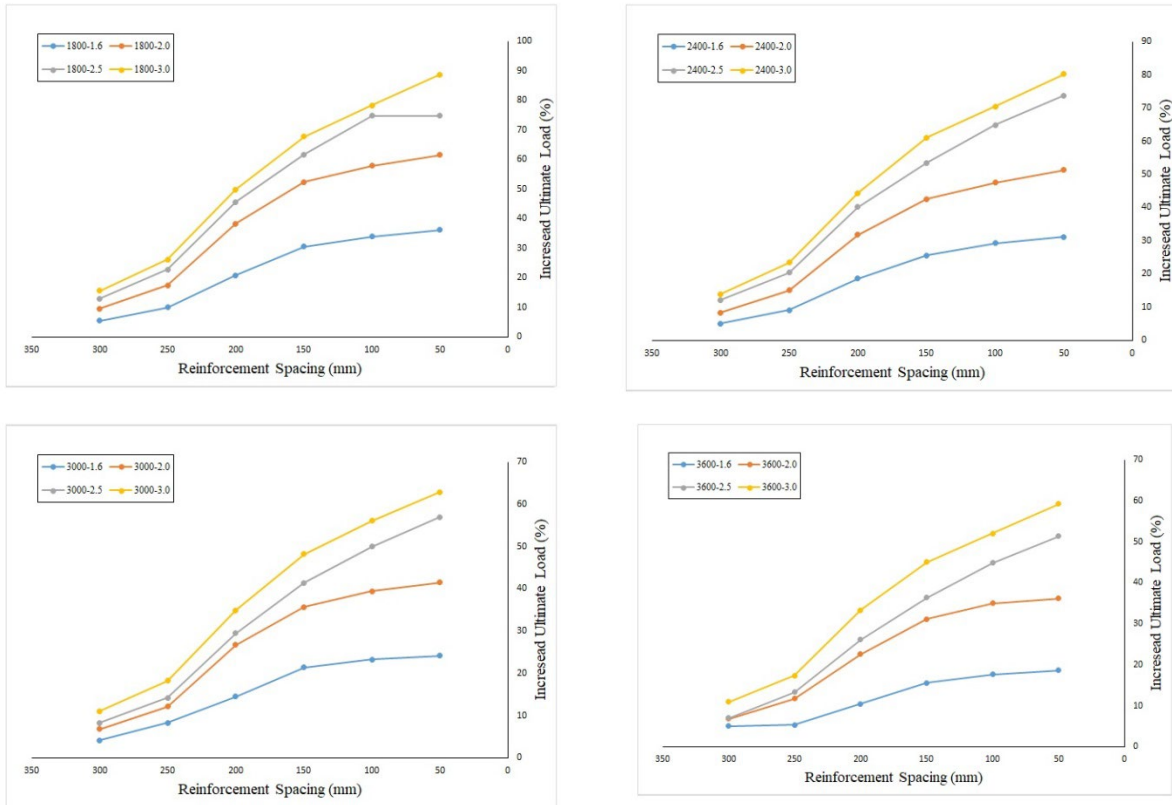


Figure 5-22: Percentage of increased ultimate load with different reinforcement.

5.4. Artificial Intelligence Prediction

Neural network systems are proved as highly valued approaches for data prediction regarding the different numerical research studies [17,20,26]. The strategy for using a specific type of network depends on different factors, including data behavior (linear, non-linear), number of inputs, number of outputs and the research innovation [15,27,28]. The process of developing the network relies on trial and error identification, which the basis algorithm and possible supplementary methods detect [29,30]. The combination of the multi-layer perceptron (MLP) neural network with the particle swarm optimization (PSO) algorithm, which is based on the random production of the initial population, is employed in this study. Based on the hybrid mechanism, in the training phase objective values would be identified in MLP algorithm and put in as objective function of PSO technique. In order to identify the most effective input for this hybrid neural network, instead of traditional methods and manually testing possible scenarios, the feature selection technique, which is the best way to identify the features of an issue, is employed in this paper. The main point of this study is to use the feature selection technique to identify the most effective parameter on the

flexural capacity of the CFS uprights to predict and identify the deflection and ultimate flexural load simultaneously.

5.4.1 Algorithm Methodology

5.4.1.1 Multi-Layer Perceptron (MLP) Algorithm

MLP networks can be used as powerful hyper-surface reconstruction tools, which can successfully map a set of multi-dimensional input data ($\underline{x}_i; i = 1, \dots, N$) onto a set of appropriate multidimensional outputs ($\underline{y}_i; i = 1, \dots, N$). The MLP configuration is extensively used for static regression applications and it consists of one input layer, one or more hidden layer(s) and one output layer. The MLP network utilizes a supervised learning technique called backpropagation for training the network. The basic element of the modified un-stabilized MLP neural network is shown in Figure 5-23, which performs a projection oriented mathematical operation on its inputs.

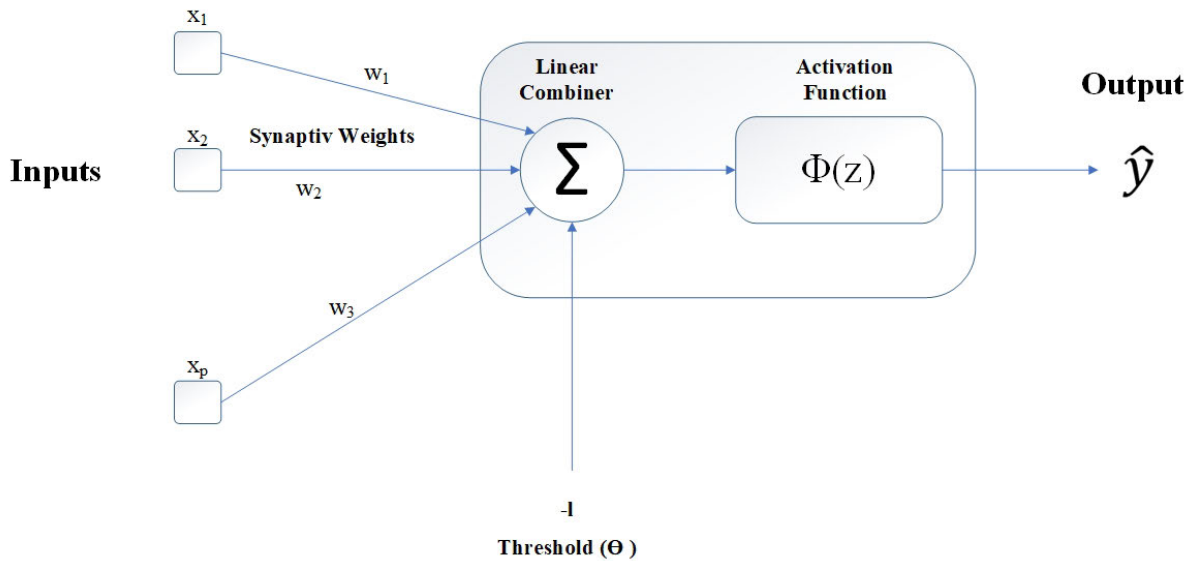


Figure 5-23: Schematic representation of MLP neuron.

Non-linear activation function (ϕ) performs a pre-defined mathematical operation over its argument and provides the model predictions ($\hat{y}(x)$). Sigmoid, hyperbolic tangent, threshold and piecewise-linear basis functions are the most popular activation functions traditionally used for MLP networks. The MLP network is developed by assigning the synaptic weights deriving from a PSO algorithm in this study. As shown in Figure 5-24, additional linear weights ($\alpha_1, \dots, \alpha_M$) are used in our modified MLP network.

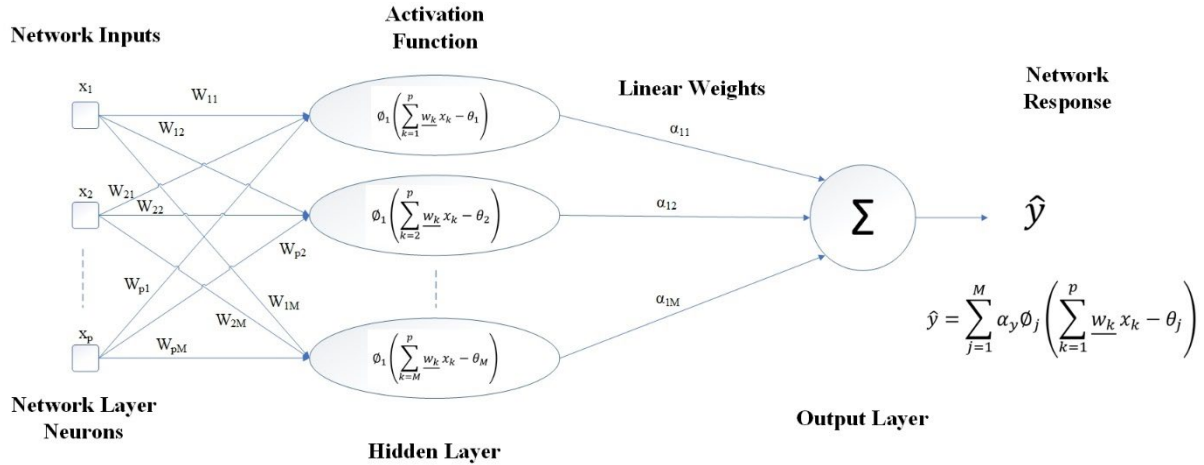


Figure 5-24: Visualization of a single hidden layer MLP network.

In the present study, the MLP algorithm was developed and trained by several bending test data obtained from the experimental tests [9] as well as the FEM results discussed in the previous sections.

5.4.1.2 Particle Swarm Optimization (PSO)

PSO is a powerful algorithm for optimization in nonlinear, non-convex and discontinuous environments. This algorithm is very powerful and efficient while defining many parameters. In this algorithm, particles are the building blocks of the population, and with the intelligence that they have, a certain amount of intelligence is created that is not comparable to the intelligence of each of them. Figure 5-25 indicates the PSO sequential flowchart.

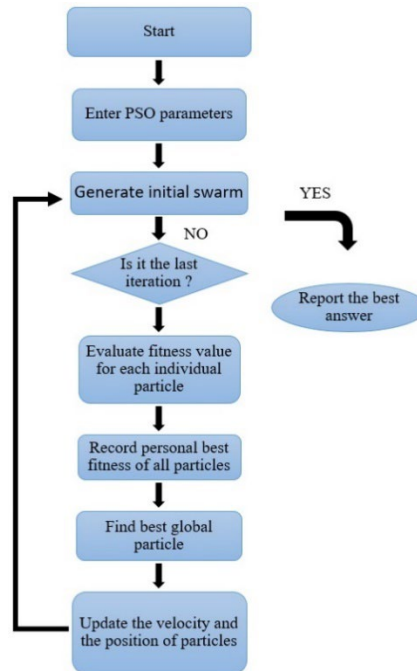


Figure 5-25: PSO sequential flowchart.

In this study, the PSO algorithm is employed along with MLP as a unique intelligence algorithm. The goal of the PSO algorithm is to find the optimal objective function.

5.4.1.3 Feature Selection Technique (FS)

“Feature selection” is a process of selecting a subcategory from a category of features [31]. It is preferable in contexts where readability and interpretability are issues of concern because the discounted values of the main features are preserved in the reduced space. This method of dimension reduction results in a qualitative database, without the removal of useful information. It also allows for features with different data models to be combined. The issue is of importance because a large number of features are often used in different applications. Therefore, the need to select a limited set among them becomes apparent. The feature selection process is divided into four parts as shown in Figure 5-26: generation procedure, evaluation function, stopping criteria and validation procedure.

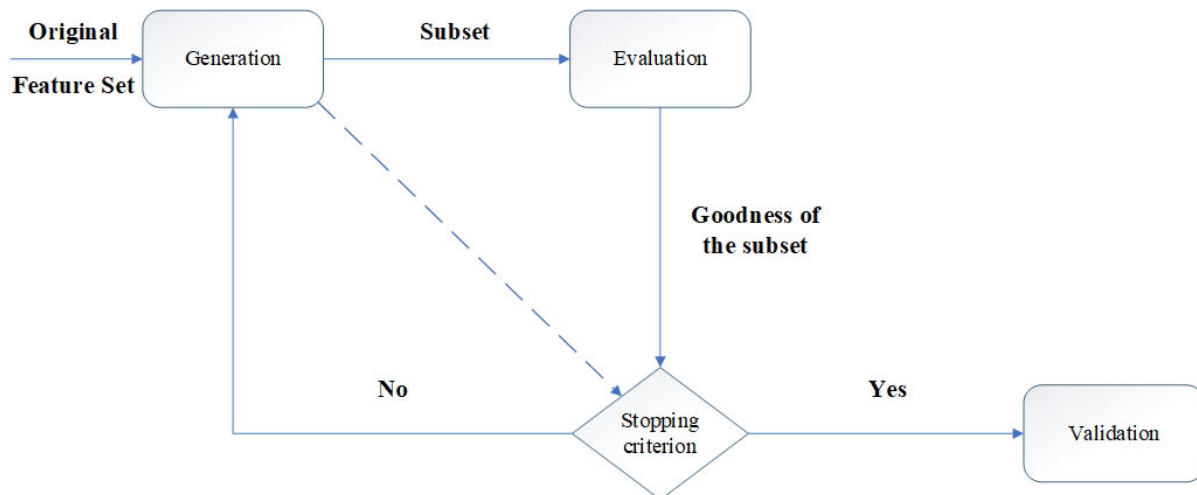


Figure 5-26: Feature selection technique steps.

In this study, some prominent features of CFS racking uprights are produced through one or more conversions on input features. While mapping points from one space with higher dimensions into another space with lower dimensions, a large number of points may overlap. Feature extraction helps to find a new dimension where a minimum number of points overlap. This approach is associated with the problem area and is commonly used in image processing where specific features are extracted in accordance with the requirements of the problem.

5.4.1.4 MLP–PSO–FS Architecture

The way that the algorithm works is that the MLP neural network starts learning based on the initial configuration. For data with relatively high complexity, learning a simple neural network without an optimizer may not be enough, hence using an optimizer technique is required. PSO is one of these techniques that is based on the collective movement of birds and fish. The optimizer runs at a higher level than the neural network, meaning that each MLP neural network calculation itself is one of the PSO optimizer particles. If the feature selection technique is needed to find the best combination, this technique must be performed before executing the MLP–PSO set. In this way, first, FS obtains all possible states from the combination of inputs and then sends the first state to the hybrid neural network. After obtaining the final result, FS sends the second state to the neural network and the results are compared with each other. The best result is maintained and repeated for the third case. This is done until all scenarios are completed, and finally, the best input combination is identified. Figure 5-27 presents the diagram of the sequential PSO–FS and MLP combination.

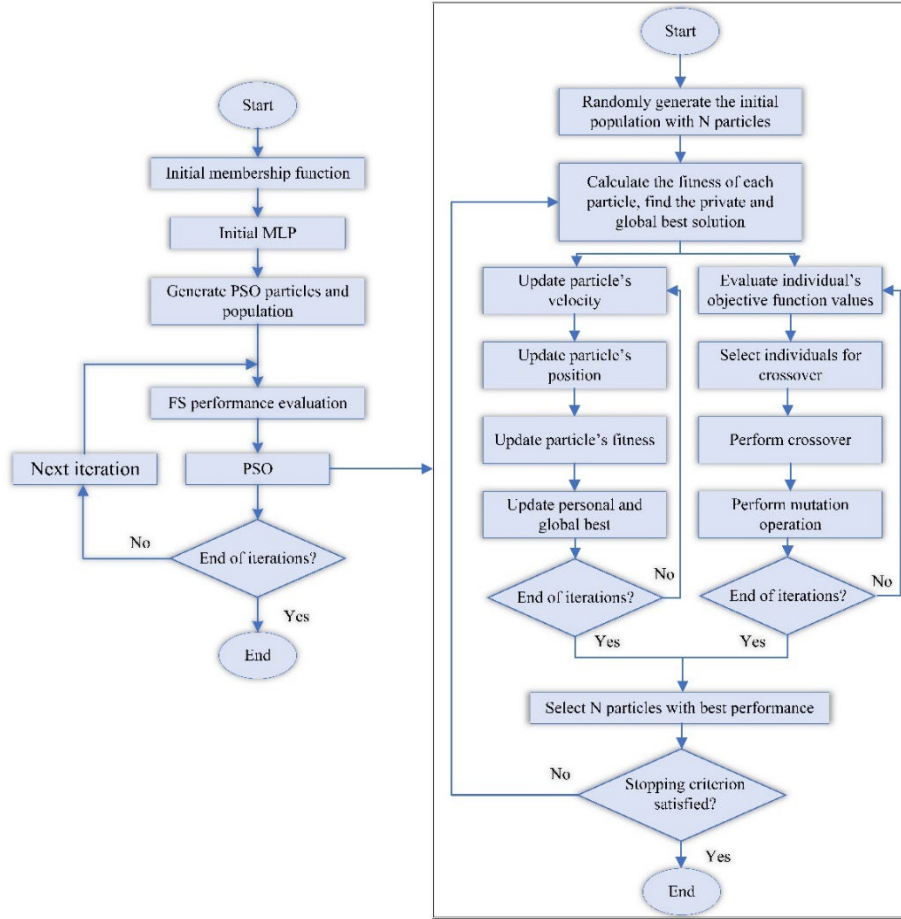


Figure 5-27: Flowchart of the sequential combination of hybrid MLP–PSO–FS algorithm.

5.4.2 Performance Evaluation

In this paper, several performance measures are employed to assess the proposed models. The R , NSE , $RMSE$, MAE and WI [32–36] are employed as the measure of precision in this study, which is represented as follows:

$$R = \frac{\sum_{i=1}^M (O_i - \bar{O}_i) \cdot (P_i - \bar{P}_i)}{\sqrt{\sum_{i=1}^M (O_i - \bar{O}_i)^2 \sum_{i=1}^M (P_i - \bar{P}_i)^2}} \quad (5.1)$$

$$NSE = 1 - \frac{\sum_{i=1}^N (P_i - O_i)^2}{\sum_{i=1}^N (O_i - \bar{O}_i)^2} \quad (5.2)$$

$$RMSE = \sqrt{\frac{1}{N} \sum_{i=1}^N (P_i - O_i)^2} \quad (5.3)$$

$$MAE = \frac{\sum_{i=1}^M |P_i - O_i|}{N} \quad (5.4)$$

$$WI = 1 - \frac{\sum_{i=1}^N (O_i - P_i)^2}{\sum_{i=1}^N (|P_i - \bar{O}_i| + |O_i - \bar{O}_i|)^2} \quad (5.5)$$

where O_i and P_i are the observed and predicted values, respectively; \bar{O}_i and \bar{P}_i indicate the average of the observed and predicted values, respectively, and the number of data is shown by N . The R index [Range = (0–1); ideal value = 1] shows the suitability of the selected predictors applied for the prediction of the target variable. NSE [Range = $(-\infty, 1)$; ideal value = 1] is demonstrated to evaluate the capability of the suggested methods. The highest value of unity reveals an appropriate fit between the actual and measured value for which a negative value shows that the performance of the model is worse than the arithmetic mean of the developed models. The $RMSE$ and MAE [Range = $(0, +\infty)$; ideal value = 0] are measures for assessing the accuracy, which are greater or equal to zero in value. WI [Range = $(0, 1)$; ideal value = 1] is a standardized indicator for model prediction error. The values close to 0 demonstrate poor precision, while the values close to unity reveal the goodness of prediction.

5.4.3 Algorithm Results and Discussion

The dataset used in this research is the result of several experiments that ultimately formed 5111 rows of information. This database has six inputs and one target output. In this investigation, choosing the combination of the influential input for the prediction matrix of the load MLP, which is tuned by PSO, is carried out as the main neural network model. The variables affecting load are indicated in the functional relationship as follows:

$$Load = f(length, bolts, thickness, M/ZY.Fy, Ult Moment, Ult Load)$$

MLPs are useful in research due to their ability to address the problems stochastically, which often allows approximate solutions for extremely complicated problems, such as fitness approximation. In this part, according to the training datasets, MLP is fitted. Therefore, MATLAB software is utilized to predict the load by the use of hybrid PSO with MLP. The best result is given in Table 5-5 and Table 5-6.

Table 5-5: Best achieved results in deflection estimation.

Phase	Network Result				
	R	NSE	RMSE	MAE	WI
Test	0.948	0.886	5.415	3.235	0.972
Train	0.943	0.878	5.702	3.303	0.970

Table 5-6: Best achieved results in normalized load estimation.

Phase	Network Result				
	R	NSE	RMSE	MAE	WI
Test	1.000	1.000	1.000	0.001	0.000
Train	1.000	1.000	1.000	0.000	0.000

The parameters of the PSO algorithm are population size, iterations, inertia weight, damping ratio, personal and global learning coefficient, which are provided in Table 5-7. The MLP neural network parameters are the hidden layers and training function as shown in Table 5-8. The parameter characteristics used for FS are also indicated in Table 5-8.

Table 5-7: Parameter characteristics used for PSO in this study.

FIS Clusters	Population Size	Iterations	Inertia Weight	Damping Ratio	Learning Coefficient	
					Personal	Global
10	150~350	45~100	1	0.99	1	2

Table 5-8: Parameter characteristics used for MLP and FS in this study.

Parameter characteristics used for MLP	
Hidden Layers	Training Function
10	Levenberg–Marquardt Backpropagation (LMBP)
Parameter characteristics used for FS	
Number of runs	Number of functions (n_f)
3	1~6

Before reviewing the results, it is necessary to have a comparison between the feature selection technique and other neural networks and algorithms in selecting the best inputs. A database may have a large amount of input data but, certainly, not all inputs are suitable for use in the neural network, as some of them have virtually no effect on output prediction, and some may cause network deviation. Therefore, finding the best combination is very time consuming and tedious if there is a large number of work inputs. It should be noted that the implementation of the neural network and the study of its results for this number of repetitions is impossible considering the different combinations of neural network settings. Therefore, the only way to select different input modes and settings is based on previous experiences and initial assumptions. Using the feature selection technique, with only six runs, all possible input states are checked and the best combination is determined.

5.4.3.1 Normalized Ultimate Load Prediction

Following the prediction process, to predict the normalized ultimate load, available inputs are tested with different scenarios. As shown in Table 5-9, Table 5-10, and Table 5-11, different prediction patterns are presented by accuracy criteria (by adjusting best population and iteration). From Figure 5-28 to 5-30, it is noted that the normalized ultimate load estimation is perfectly

predicted by the proposed algorithm. Furthermore, as shown in the tables and graphs, the prediction accuracy in this study is 100%.

Table 5-9: The calculated accuracy criteria for the performance of the implemented models (Iteration = 150).

Population	Network Result									
	Training Phase					Testing Phase				
	R*	NSE	RMSE	MAE	WI	R	NSE	RMSE	MAE	WI
150	0.996	0.992	7.193	5.041	0.998	0.905	0.780	7.227	5.035	0.948
250	0.996	0.992	7.244	5.270	0.998	0.907	0.798	7.199	5.246	0.951
350	0.996	0.991	7.381	5.578	0.998	0.900	0.776	7.534	5.679	0.946

*= Pearson's correlation coefficient

Table 5-10: The calculated accuracy criteria for the performance of the implemented models (population = 250).

Iteration	Network Result									
	Training Phase					Testing Phase				
	R	NSE	RMSE	MAE	WI	R	NSE	RMSE	MAE	WI
100	0.995	0.990	7.837	5.751	0.998	0.882	0.711	8.333	5.953	0.934
150	0.996	0.992	7.244	5.270	0.998	0.907	0.798	7.199	5.246	0.951
200	0.995	0.991	7.504	5.339	0.998	0.899	0.762	7.421	5.250	0.944

Table 5-11: The calculated accuracy criteria for the performance of the implemented models for different inputs.

Number of Inputs	Network Result											
	Training Phase						Testing Phase					
	R ²	R	NSE	RMSE	MAE	WI	R ²	R	NSE	RMSE	MAE	WI
1	0.885	0.941	0.870	0.035	0.026	0.969	0.991	0.935	0.854	0.038	0.028	0.965
2	0.971	0.985	0.970	0.018	0.003	0.993	0.997	0.978	0.955	0.022	0.004	0.989
3	1.000	1.000	1.000	0.002	0.000	1.000	1.000	1.000	0.999	0.003	0.001	1.000
4	1.000	1.000	1.000	0.001	0.000	1.000	1.000	1.000	1.000	0.001	0.000	1.000
5	1.000	1.000	1.000	0.000	0.000	1.000	1.000	1.000	1.000	0.001	0.000	1.000
6	0.822	0.996	0.992	7.244	5.270	0.998	0.823	0.907	0.798	7.199	5.246	0.951

After finding the best population, the calculations to find the optimal number of repetitions are performed. According to Table 5-12, the optimal number of repetitions in the test phase is obtained as 150.

Table 5-12: Most effective inputs based on feature selection.

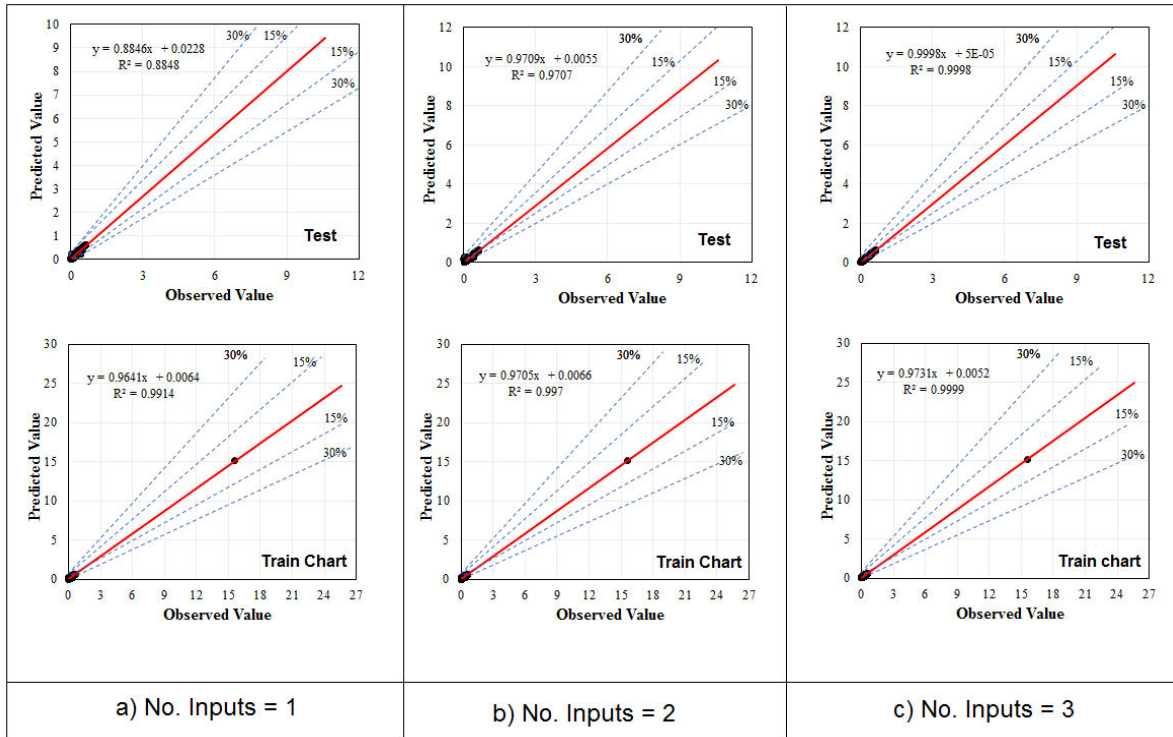
Feature	Number of Inputs					
	1	2	3	4	5	6
Length					X	X
Bolt distance						X
Thickness		X	X	X	X	X
Deflection				X	X	X
Ult moment	X	X	X	X	X	X
Ult load			X	X	X	X

According to the results obtained in the test phase, cases with 4 and 5 inputs obtain the same results. However, because it is more efficient to obtain the result with less number of inputs, the number of optimal inputs is chosen to be four. As shown in Table 5-12, the ultimate moment has the greatest impact on finding results.

Figure 5-28 illustrates the predicted and measured load by the MLP–PSO–FS model in scatter diagrams. Figure 5-28a reveals the train and test phase of the model with a single input for which the performance parameters are shown in Table 5-11 ($R^2_{test} = 0.8848$, $R^2_{train} = 0.9914$). Figure 5-28b shows the testing and training phase of the model with two inputs ($R^2_{test} = 0.9707$, $R^2_{train} = 0.997$). According to this procedure, it is obvious that the MLP–PSO–FS model shows acceptable performance where the number of inputs is increased to five inputs. Nevertheless, the MLP–PSO–FS model with six inputs does not perform well enough in comparison with other models. Figure 5-28d,e represents the best-achieved predictions amongst other models, although there is a little difference between these two models in the prediction capability which is shown in Table 5-11. As can be seen, some improvements in the performance of the MLP is captured by utilizing the PSO algorithm in such a way that the r and R^2 values are increased and the RMSE value is decreased. The testing phase is also improved with respect to the MLP–PSO–FS model.

Figure 5-29 indicates the capability of the models in the testing phase to predict each of the measured values of the test samples. As can be observed, both of the MLP–PSO–FS with four input models are capable of predicting most of the test samples closely. As shown in Table 5-11

and Figure 5-30, the best performance parameters for the PSO-FS neural network are $RMSE = 0.001$, $r = 1.000$, $R^2 = 1.000$, $NSE = 1.000$, $MAE = 0$, and $WI = 1.000$. Considering that the best result for RMSE is the lowest result and for r , the best positive correlation coefficient is 1, then numbers closer to 1 are considered better results. Additionally, for NSE and MAE, smaller results are considered better results and for WI, larger results, indicate better performance.



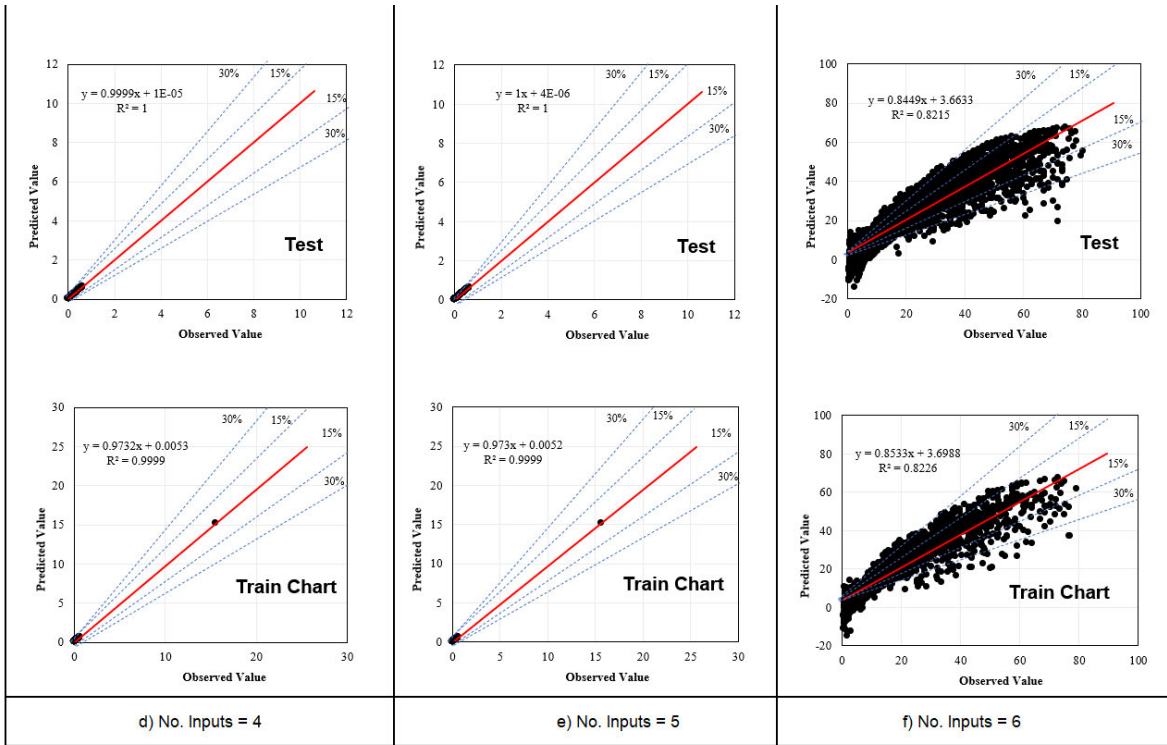


Figure 5-28: Comparison of the predicted and measured load: (a) One input, (b) two inputs, (c) three inputs, (d) four input, (e) five inputs, (f) six inputs through MLP-PSO-FS model.

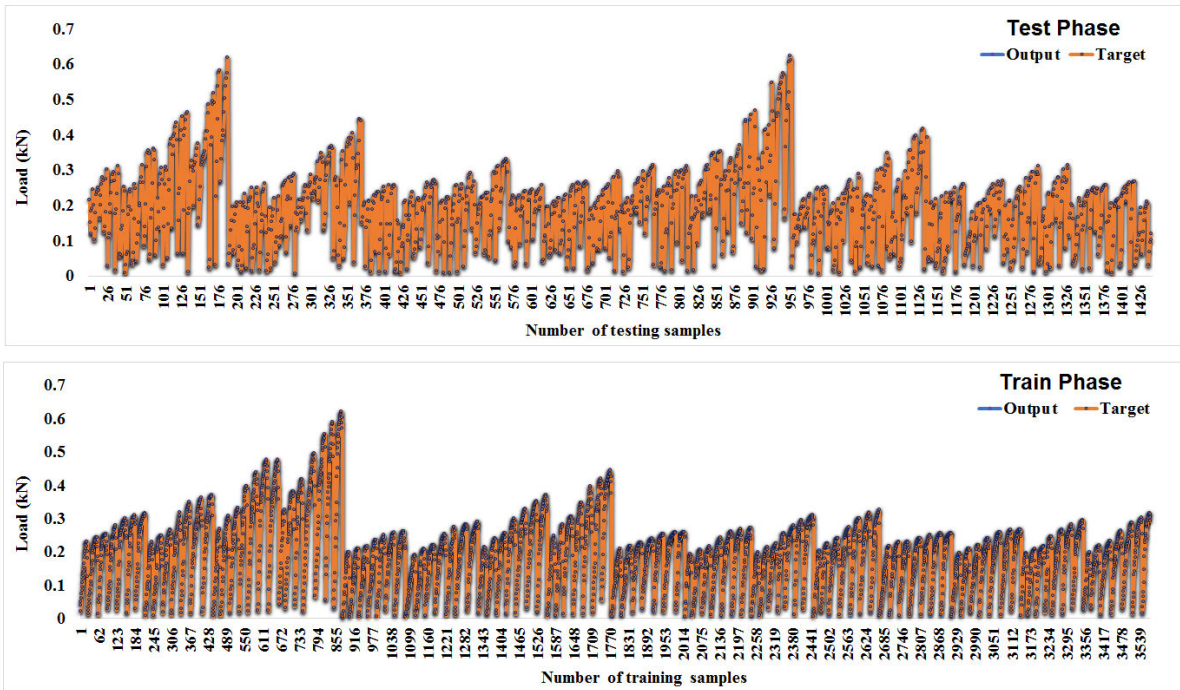


Figure 5-29: MLP-PSO-FS (4 inputs) prediction vs. experimental diagram: (above) train phase, (below) test phase.

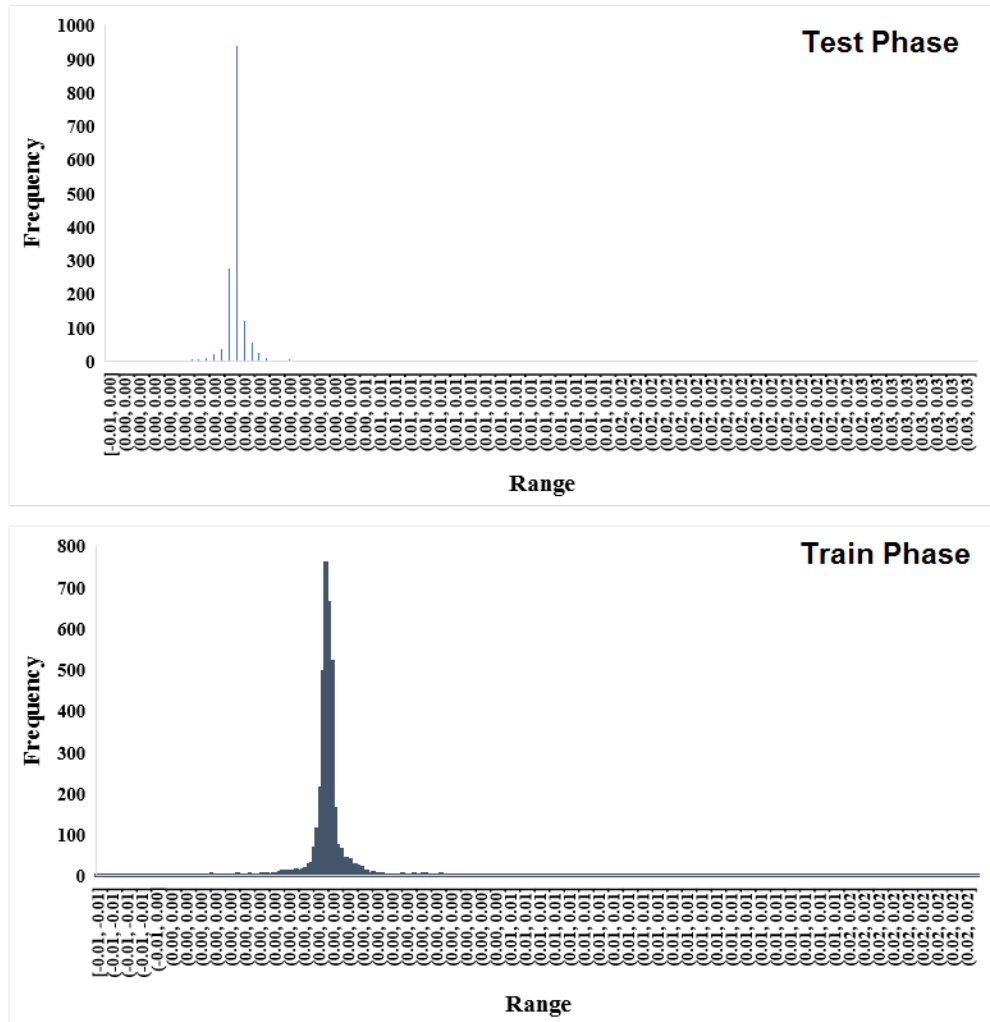


Figure 5-30: MLP-PSO-FS (4 inputs) Error histograms: (above) train phase, (below) test phase.

5.4.3.2 Deflection Prediction

Firstly, the best number of populations needs to be found by considering a constant number of repetitions equal to 45. In Table 5-13, the population of 250 is identified as the best result in the test phase.

Table 5-13: The calculated accuracy criteria for the performance of the implemented models (iteration = 45).

Population	Network Result									
	Training Phase					Testing Phase				
	R	NSE	RMSE	MAE	WI	R	NSE	RMSE	MAE	WI
150	0.948	0.886	5.434	3.186	0.972	0.933	0.852	6.200	3.567	0.964
250	0.942	0.874	5.706	3.409	0.970	0.943	0.878	5.702	1.457	0.970
350	0.944	0.879	5.594	3.354	0.971	0.936	0.856	6.093	3.623	0.966

After finding the best population, the calculations to find the optimal number of repetitions are carried out. According to Table 5-14, the optimal number of repetitions in the test phase is 45.

Table 5-14: The calculated accuracy criteria for the performance of the implemented models (population = 250).

Iteration	Network Result									
	Training Phase					Testing Phase				
	R	NSE	RMSE	MAE	WI	R	NSE	RMSE	MAE	WI
45	0.942	0.874	5.706	3.409	0.970	0.943	0.878	5.702	1.457	0.970
75	0.948	0.886	5.415	3.235	0.972	0.932	0.848	6.297	3.583	0.964
100	0.947	0.884	5.492	3.137	0.972	0.938	0.862	5.936	3.310	0.967

Following finding the best parameters for the neural network, the optimal input combination is found through the feature selection technique. As mentioned earlier, this technique does not require testing all possible combinations, and it is sufficient to test them only once for each set of n (number of inputs). For example, if the best combination of inputs with four members is required to be determined, the network needs to be run only once and the value of n_f needs to be set to six. Additionally, the network of six inputs that has the most impact on the answer should be selected. In Table 5-15 and Figure 5-31, the best value of n is specified.

Table 5-15: The calculated accuracy criteria for the performance of the implemented models for different inputs.

Number of Inputs	Network Result											
	Training Phase						Testing Phase					
	R ²	R	NSE	RMSE	MAE	WI	R ²	R	NSE	RMSE	MAE	WI
1	0.493	0.702	0.046	12.000	8.788	0.807	0.496	0.704	0.097	12.504	3.893	0.803
2	0.783	0.885	0.723	7.993	5.684	0.936	0.782	0.884	0.734	7.889	2.437	0.937
3	0.853	0.924	0.828	6.511	4.034	0.959	0.805	0.897	0.758	7.626	1.914	0.943
4	0.892	0.944	0.880	5.608	3.342	0.971	0.857	0.926	0.831	6.512	1.610	0.960
5	0.897	0.947	0.885	5.441	3.242	0.972	0.870	0.933	0.839	6.279	1.545	0.963
6	0.888	0.942	0.874	5.706	3.409	0.970	0.890	0.943	0.878	5.702	1.457	0.970

As shown in Table 5-16, the results are almost the same for four or more inputs. As it is clear, the ultimate moment has the smallest effect and the effect of the other parameters is almost the same. In Figure 5-31, Figure 5-32, and Figure 5-33, the diagrams related to the six compounds are presented.

Table 5-16: Most effective inputs based on feature selection.

Feature	Number of Inputs					
	1	2	3	4	5	6
Length			X	X	X	X
Bolt			X	X	X	X
Thickness				X	X	X
(M/ZY.Fy)			X	X	X	X
Ult moment		X				X
Ult load	X	X			X	X

Figure 5-31, Figure 5-32, and Figure 5-33 demonstrate the results of the MLP–PSO–FS models in the prediction of the deflection. It is obvious that predicting the deflection is faced with more challenges than flexural load prediction. Figure 5-31 illustrates the training and testing phase of the MLP–PSO–FS model with 100 iterations. Performance indices of the model in Figure 5-31a with 150 show that the population is noticeably better than the other two populations ($R^2_{test} = 0.8804$, $R^2_{train} = 0.89$). Figure 5-32 illustrates optimal regression against two other population

with 75 iterations ($R^2_{test} = 0.8772$, $R^2_{train} = 0.8946$). Figure 5-33 illustrates that the case with 250 population represents an enhanced model in comparison with other population models with 45 iterations ($R^2_{test} = 0.8896$, $R^2_{train} = 0.888$). As can be realized, the MLP-PSO-FS model performs better with 100 iterations in the training phase. The testing phase is also improved in the 45-iteration model. Most importantly, the close values of performance indices in the training and testing phases confirm the high reliability of the models.

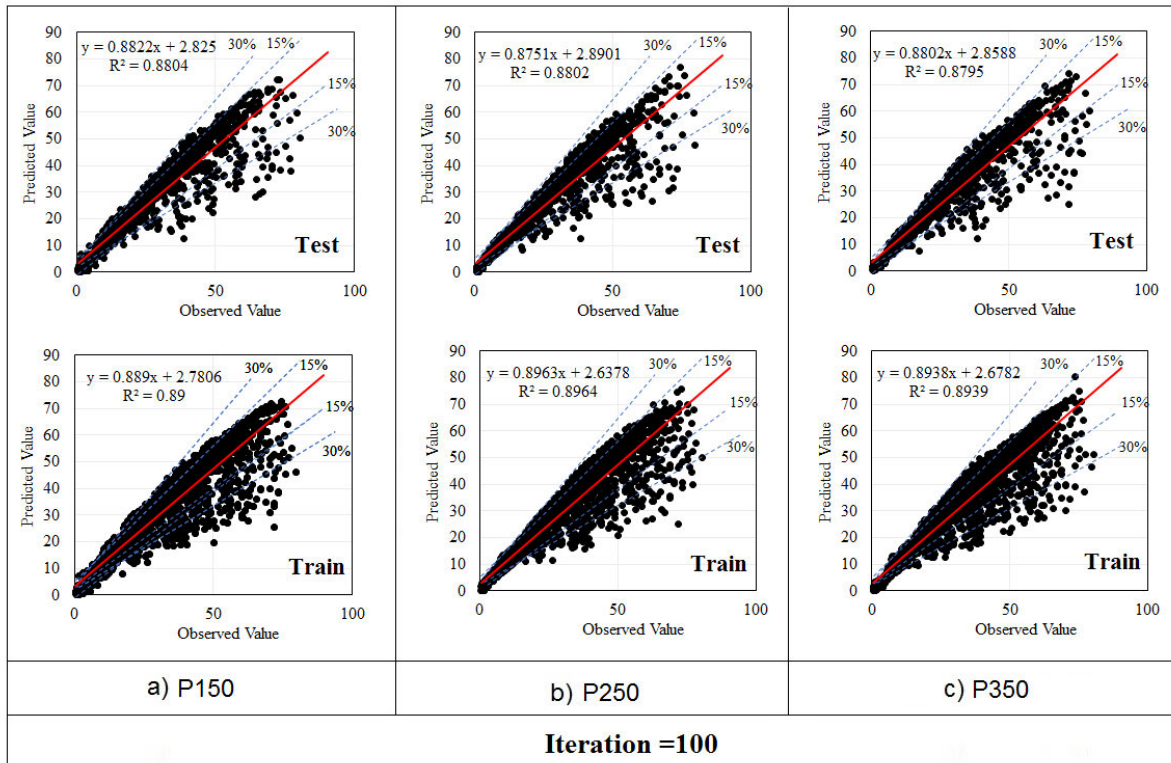


Figure 5-31: MLP-PSO-FS regression charts (iteration = 100): (a) P150, (b) P250, (c) P350.

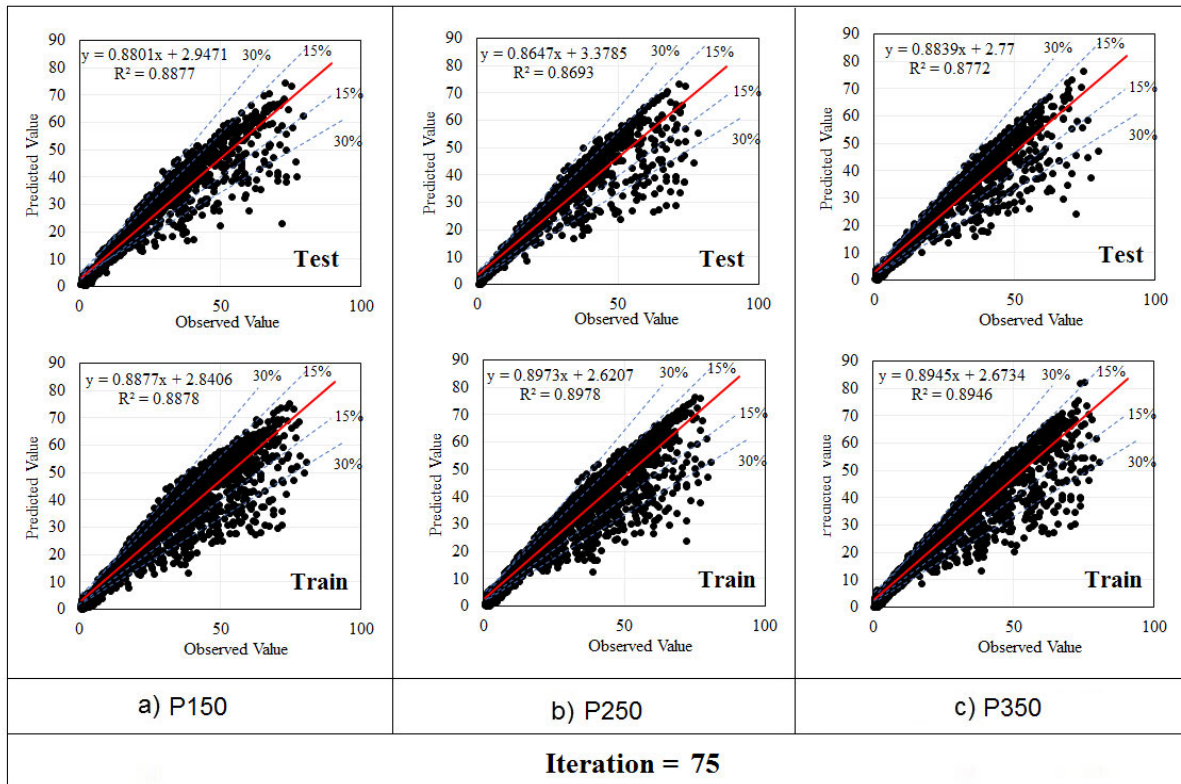


Figure 5-32: MLP-PSO-FS regression charts (iteration = 75): (a) P150, (b) P250, (c)P350.

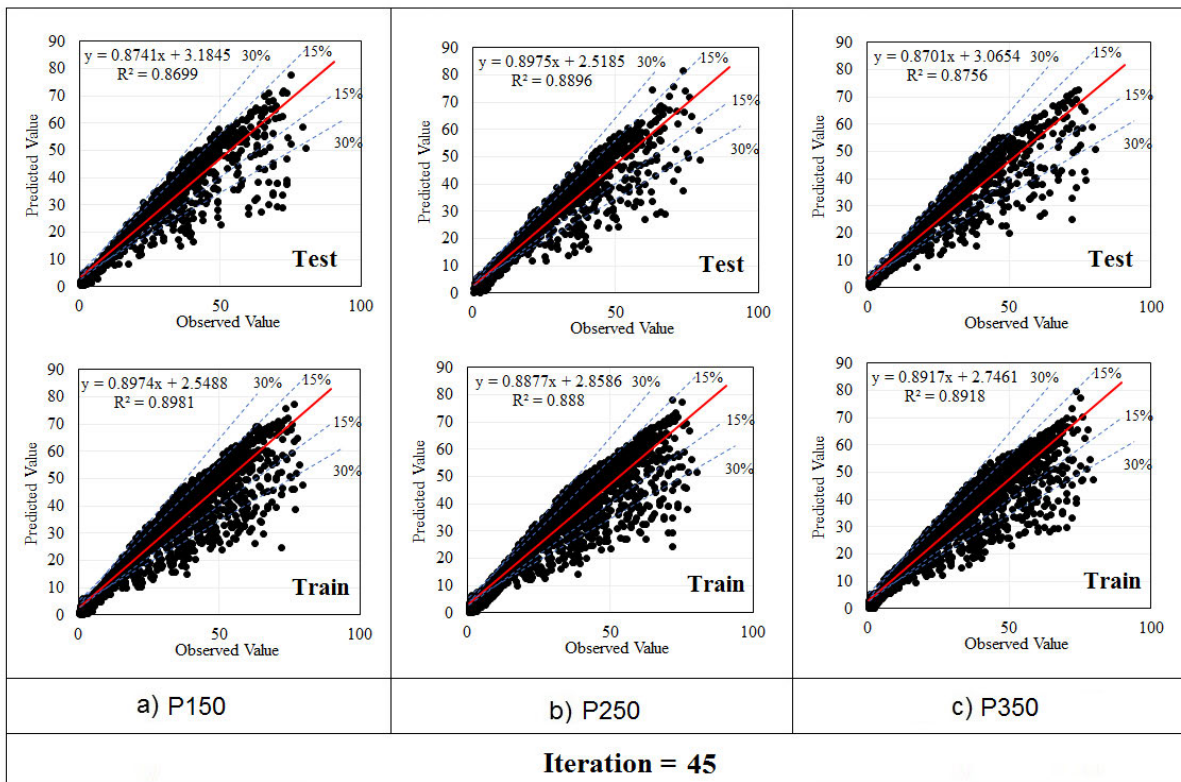


Figure 5-33: MLP-PSO-FS regression charts (iteration = 45): (a) P150, (b) P250, (c)P350.

The capability of the models in the prediction of each test sample is indicated in Figure 5-34. A significantly close prediction of the models and the better performance of the MLP–PSO model can be seen in this figure. As shown in Table 5-13 and Figure 5-35, the best performance parameters for the PSO–FS neural network are $RMSE = 5.702$, $r = 0.943$, $R^2 = 0.890$, $NSE = 0.878$, $MAE = 1.457$, and $WI = 0.970$. The best result for $RMSE$ is the minor value, and for r , the best positive correlation coefficient is 1. The numbers closer to 1 are considered better results. For NSE and MAE , smaller results and for WI , larger results indicate better performance.

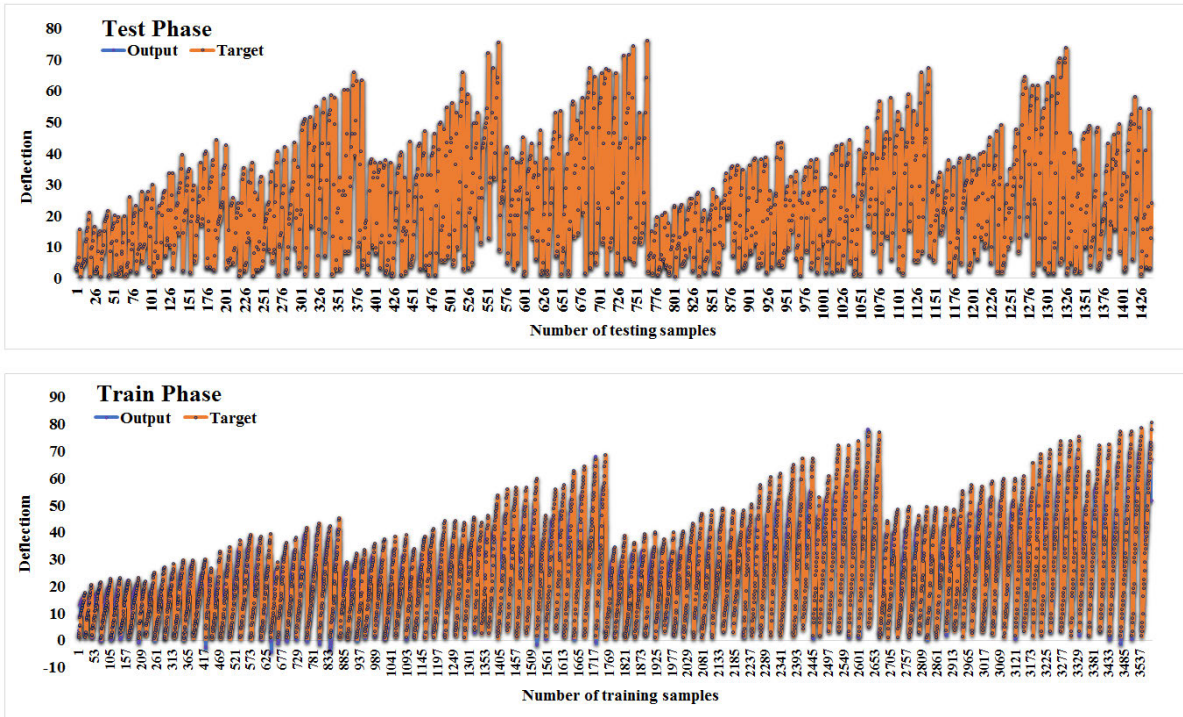
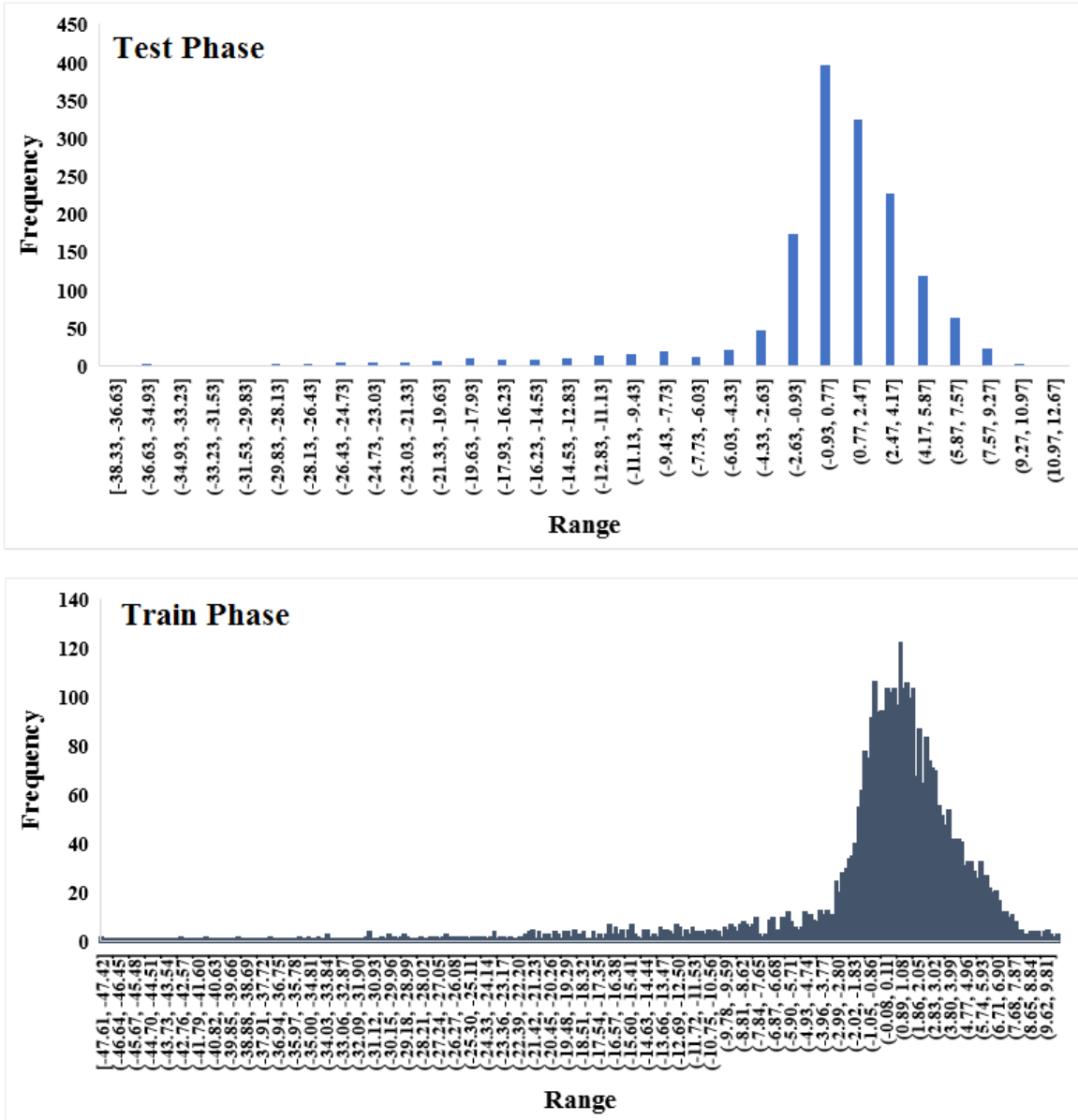


Figure 5-34: MLP-PSO-FS (6 inputs) prediction vs. experimental diagram: (above) train phase, (below) test phase.



of simulating CFS section structural behavior. Additionally, in this study, the MLP–PSO hybrid neural network by combining the evolutionary feature selection technique was used to predict some major characteristics of CFS upright frames, such as “flexural strength” and “deflection”. The feature selection technique was used to avoid trying all possible input modes and wasting time. It provided the best possible input combination that may be overlooked in other methods. The neural network results illustrated noticeable accuracy and a fascinating prediction ability of the MLP algorithm along with the feature selection technique, which has compatibility with the literature.

According to the FEM results, both in major and minor axis simulations, all models indicated a unique behavior with respect to length/thickness variation. The thicker models showed higher flexural capacity, especially those with shorter lengths. Moreover, taller uprights faced capacity loss due to buckling. This deficiency was somehow addressed by the proposed reinforcements. The proposed fasteners played a noticeable role as reinforcement not only in longer uprights, but also in thinner ones. By reducing the fastener spacing, the ultimate load of the models was increased.

According to the analytical study, the FEM results were verified and proved to be authenticated through the training phase of the analytical analysis. The predictions were performed for both the deflection value and ultimate flexural load, and the accuracy of the prediction was evaluated. Employing a hybrid neural network based on the feature-selection technique successfully predicted the normalized ultimate load and the deflection.

5.6. References

1. Shariati, M.; Faegh, S.S.; Mehrabi, P.; Bahavarnia, S.; Zandi, Y.; Masoom, D.R.; Toghroli, A.; Trung, N.T.; Salih, M.N.A. Numerical study on the structural performance of corrugated low yield point steel plate shear walls with circular openings. *Steel Compos. Struct.* **2019**, *33*, 569–581.
2. Zhao, X.; Wang, T.; Chen, Y.; Sivakumaran, K.S. Flexural behaviour of steel storage rack beam-to-upright connections. *J. Constr. Steel Res.* **2014**, *99*, 161–175.
3. Firouzianhaji, A.; Usefi, N.; Samali, B.; Mehrabi, P. Shake Table Testing of Standard Cold-Formed Steel Storage Rack. *Appl. Sci.* **2021**, *11*, 1821, doi:10.3390/app110418214.
4. Put, B.M.; Pi, Y.L.; Trahair, N.S. Bending and torsion of cold-formed channel beams. *J. Struct. Eng.* **1999**, *125*, 540–546.
5. Wang, L.; Young, B. Behavior of cold-formed steel built-up sections with intermediate stiffeners under bending. I: Tests and numerical validation. *J. Struct. Eng.* **2015**, *142*, 04015150.
6. Calderoni, B.; De Martino, A.; Formisano, L.; Fiorino, L. Cold formed steel beams under monotonic and cyclic loading: Experimental investigation. *J. Constr. Steel Res.* **2009**, *65*, 219–227.

7. Wang, H.; Zhang, Y. Experimental and numerical investigation on cold-formed steel C-section flexural members. *J. Constr. Steel Res.* **2009**, *65*, 1225–1235.
8. Taheri, E.; Firouzianhaji, A.; Usefi, N.; Mehrabi, P.; Ronagh, H.; Samali, B. Investigation of a Method for Strengthening Perforated Cold-Formed Steel Profiles under Compression Loads. *Appl. Sci.* **2019**, *9*, 5085.
9. Taheri, E.; Firouzianhaji, A.; Mehrabi, P.; Vosough Hosseini, B.; Samali, B. Experimental and Numerical Investigation of a Method for Strengthening Cold-Formed Steel Profiles in Bending. *Appl. Sci.* **2020**, *10*, 3855, doi:10.3390/app
10. Visy, D.; Szedlák, M.; Geleji, B.B.; Ádány, S. Flexural buckling of thin-walled lipped channel columns with slotted webs: Numerical and analytical studies. *Eng. Struct.* **2019**, *197*, 109399.
11. Nandini, P.; Kalyanaraman, V. Strength of cold-formed lipped channel beams under interaction of local, distortional and lateral torsional buckling. *Thin-Walled Struct.* **2010**, *48*, 872–877.
12. Chu, X.; Kettle, R.; Li, L. Lateral-torsion buckling analysis of partial-laterally restrained thin-walled channel-section beams. *J. Constr. Steel Res.* **2004**, *60*, 1159–1175.
13. Ye, J.; Hajirasouliha, I.; Becque, J.; Pilakoutas, K. Development of more efficient cold-formed steel channel sections in bending. *Thin-Walled Struct.* **2016**, *101*, 1–13.
14. Gilbert, B.P.; Savoyat, T.J.M.; Teh, L.H. Self-shape optimisation application: Optimisation of cold-formed steel columns. *Thin Walled Struct.* **2012**, *60*, 173–184.
15. Shariati, M.; Trung, N.T.; Wakil, K.; Mehrabi, P.; Safa, M.; Khorami, M. Estimation of moment and rotation of steel rack connection using extreme learning machine. *Steel Compos. Struct.* **2019**, *31*, 427–435.
16. Shariati, M.; Mafipour, M.S.; Mehrabi, P.; Ahmadi, M.; Wakil, K.; Trung, N.T.; Toghrli, A. Prediction of concrete strength in presence of furnace slag and fly ash using Hybrid ANN-GA (Artificial Neural Network-Genetic Algorithm). *Smart Struct. Syst.* **2020**, *25*, 183–195.
17. Shariati, M.; Mafipour, M.S.; Mehrabi, P.; Bahadori, A.; Zandi, Y.; Salih, M.N.A.; Nguyen, H.; Dou, J.; Song, X.; Poi-Ngian, S. Application of a Hybrid Artificial Neural Network-Particle Swarm Optimization (ANN-PSO) Model in Behavior Prediction of Channel Shear Connectors Embedded in Normal and High-Strength Concrete. *Appl. Sci.* **2019**, *9*, 5534, doi:10.3390/app
18. Hornik, K.; Stinchcombe, M.; White, H. Multilayer feedforward networks are universal approximators. *Neural Netw.* **1989**, *2*, 359–366.
19. Koopialipoor, M.; Fahimfar, A.; Ghaleini, E.; Momenzadeh, M.; Jahed Armaghani, D. Development of a new hybrid ANN for solving a geotechnical problem related to tunnel boring machine performance. *Eng. Comput.* **2020**, *36*, 1–13.
20. Shariati, M.; Mafipour, M.S.; Mehrabi, P.; Zandi, Y.; Dehghani, D.; Bahadori, A.; Shariati, A.; Trung, N.T.; Shek, P. Application of Extreme Learning Machine (ELM) and Genetic Programming (GP) to design steel-concrete composite floor systems at elevated temperatures. *Steel Compos. Struct.* **2019**, *33*, 319.
21. Firouzianhaji, A. The Effect of Connection Flexibility on the Seismic Performance of Industrial Racking Systems. Ph.D. Thesis, UTS, Sydney, Australia, 2016.
22. Usefi, N.; Sharafi, P.; Ronagh, H. Numerical models for lateral behaviour analysis of cold-formed steel framed walls: State of the art, evaluation and challenges. *Thin-Walled Struct.* **2019**, *138*, 252–285.
23. Usefi, N.; Ronagh, H.; Sharafi, P. Numerical modelling and design of hybrid cold-formed steel wall panels. *Thin-Walled Struct.* **2020**, *157*, 107084.
24. Kasaeian, S.; Usefi, N.; Ronagh, H.; Dareshiry, S. Seismic performance of CFS strap-braced walls using capacity-based design approach. *J. Constr. Steel Res.* **2020**, *174*, 106317.
25. Mehrabi, P.; Shariati, M.; Kabirifar, K.; Jarrah, M.; Rasekh, H.; Thoi Trung, N.; Shariati, A.; Jahandari, S. Effect of pumice powder and nano-clay on the strength and permeability of fiber-reinforced pervious concrete incorporating recycled concrete aggregate. *Constr. Build. Mater.* **2021**, *287*, 122652.
26. Shariati, M.; Mafipour, M.S.; Mehrabi, P.; Shariati, A.; Toghrli, A.; Thoi Trung, N.; Salih, M.N.A. A novel approach to predict shear strength of tilted angle connectors using artificial intelligence techniques. *Eng. Comput.* **2020**, 1–21, doi:10.1007/s00366-019-00930-x.
27. Shahgoli, A.F.; Zandi, Y.; Heirati, A.; Khorami, M.; Mehrabi, P.; Petkovic, D. Optimisation of propylene conversion response by neuro-fuzzy approach. *Int. J. Hydromechatron.* **2020**, *3*, 228–237.
28. Toghrli, A.; Mehrabi, P.; Shariati, M.; Trung, N.; Jahandari, S.; Rasekh, H. Evaluating the use of recycled concrete aggregate and pozzolanic additives in fiber-reinforced pervious concrete with industrial and recycled fibers. *Constr. Build. Mater.* **2020**, *252*, 118997.
29. Armaghani, D.J.; Hasanipanah, M.; Bakhshandeh Amnieh, H.; Bui, D.T.; Mehrabi, P.; Khorami, M. Development of a novel hybrid intelligent model for solving engineering problems using GS-GMDH algorithm. *Eng. Comput.* **2019**, *36*, 1379–1391.

30. Mehrabi, P.; Honarbari, S.; Rafiei, S.; Jahandari, S.; Alizadeh Bidgoli, M. Seismic response prediction of FRC rectangular columns using intelligent fuzzy-based hybrid metaheuristic techniques. *J. Ambient Intell. Humaniz. Comput.* **2021**, 1–19, doi:10.1007/s12652-020-02776-4.
31. Liao, X.; Khandelwal, M.; Yang, H.; Koopialipoor, M.; Murlidhar, B.R. Effects of a proper feature selection on prediction and optimization of drilling rate using intelligent techniques. *Eng. Comput.* **2020**, *36*, 499–510.
32. Yaseen, Z.M.; Deo, R.C.; Hilal, A.; Abd, A.M.; Bueno, L.C.; Salcedo-Sanz, S.; Nehdi, M.L. Predicting compressive strength of lightweight foamed concrete using extreme learning machine model. *Adv. Eng. Softw.* **2018**, *115*, 112–125.
33. Keshtegar, B.; Bagheri, M.; Yaseen, Z.M. Shear strength of steel fiber-unconfined reinforced concrete beam simulation: Application of novel intelligent model. *Compos. Struct.* **2019**, *212*, 230–242.
34. Al-Musawi, A.A.; Alwanas, A.A.H.; Salih, S.Q.; Ali, Z.H.; Tran, M.T.; Yaseen, Z.M. Shear strength of SFRCB without stirrups simulation: implementation of hybrid artificial intelligence model. *Eng. Comput.* **2020**, *36*, 1–11.
35. Sanikhani, H.; Deo, R.C.; Yaseen, Z.M.; Eray, O.; Kisi, O. Non-tuned data intelligent model for soil temperature estimation: A new approach. *Geoderma* **2018**, *330*, 52–64.
36. Broomhead, D.S.; Lowe, D. *Radial Basis Functions, Multi-Variable Functional Interpolation and Adaptive Networks*; Royal Signals and Radar Establishment Malvern: Worcestershire, UK, 1998; RSRE-MEMO-4148

6. Numerical Evaluation of the Upright Columns with Partial Reinforcement along with the Utilisation of Neural Networks with Combining Feature-Selection Method to Predict the Load and Displacement (Journal Article 4)

A reprint of this study entitled ‘Numerical Evaluation of the Upright Columns with Partial Reinforcement along with the Utilisation of Neural Networks with Combining Feature-Selection Method to Predict the Load and Displacement’, Taheri, E.; Mehrabi, P.; Rafiei, Sh.; Samali, B. is published by Applied Sciences. 2021; 11(22): 11056. <https://doi.org/10.3390/app112211056>

6.1. Abstract

This study has evaluated the axial capacity of cold-formed racking upright sections strengthened with an innovative reinforcement method through finite element modelling and artificial intelligence techniques. At the first stage, several specimens with different lengths, thicknesses and reinforcement spacings have been modelled in ABAQUS. The finite element method (FEM) was employed to increase the available datasets and evaluate the proposed reinforcement method in different geometrical types of sections. In order to detect the most influential factors on axial strength, at the second stage, a feature-selection method has been carried out, employing FEM results, using both multi-layer perceptron and particle swarm optimisation for normalised ultimate load capacity prediction. In the case of accuracy evaluation, some of the rolling criteria including the correlation coefficient (R^2), Pearson's correlation coefficient (PR), Nash-Sutcliffe Efficiency (NS), Root Mean Square Error (RMSE), Mean Absolute Error (MAE) and Wilmot Index (WI) were used. Results showed that geometrical parameters have almost the same contribution in compression capacity and displacement of the specimens. According to the performance evaluation indexes, the best model was detected and specified in the paper and optimised by tuning other algorithm parameters. As a result, the normalised ultimate load and displacement were predicted successfully.

Keywords: Artificial Intelligence; Finite Element Method; Cold-Formed; Rack Upright; Feature-Selection Method; Multi-Layer Perceptron; Particle Swarm Optimization; Prediction

6.2. Introduction

Warehousing systems are widely used to manage industrial production. Since cold-formed steel (CFS) sections have been developed in racking systems, steel storage systems are extensively employed in various industries [1-4]. Uprights are critical components of the racking systems, which play the same role as a column in other structures. The stability of the racking systems directly depends on uprights where a combination of different failure modes is probable under service loads [5-10]. Since racking systems typically experience extreme loading scenarios, the design of the uprights has become a vital task [11-16].

The structural performance of the upright racking systems has been widely studied under different axial load scenarios. Koen [17] evaluated stub uprights to identify the effective length of the racking uprights under service loads by obtaining a set of reduction coefficients. Davies et al. [18] experimentally and numerically investigated failure modes of the stub uprights under compression. According to their study, limited tests are promising for designing racking uprights. According to the Trouncer and Rasmussen study [19], the prediction of the capacity of uprights is more decisive by EN 15512 [20] specifications compared to Rack Manufacturers Institute (RMI) ones. Gilbert and Rasmussen [21] performed general tests on racking systems to enhance EN 15512 specifications and presented some clarifications to determine in-plane stiffness.

The combination of different buckling modes in upright frame elements has been studied in the form of research programs. Dinis et al. [22] evaluated the local-distortional buckling combination in fixed-end CFS uprights. Based on the concept of reduced thickness, the interaction of buckling along with short stiffened columns was examined by Roure et al. [23]. According to their reports, the typical design codes were inadequate, which means the interaction of different failures and buckling should be calculated. Distortional buckling of upright columns was studied along different lengths and thicknesses by Casafont et al. [24] who finally derived a set of design configurations and equations for failure modes. The finite element method is a reliable approach for the process of data prediction and validation and is commonly conducted by FE programs such as ANSYS and ABAQUS. Using the relevant programs to evaluate the structural performances has been widely developed out in recent years. Johns Hopkins University and Griffith University have performed a series of optimisation tests on CFS cross-sections to achieve ‘global optimum’ solutions. Numerical evaluation of racking systems currently is a typical approach to derive the optimum values of CFS sections and upright characteristics. Two famous numerical approaches including finite strip method and direct strength method were conducted along the Genetic Algorithm (GA) to obtain the best possible upright columns [25-28]. In this study, various lengths and thicknesses of cold-formed uprights have been modelled by ABAQUS with different reinforcement distances.

Generally, artificial intelligence (AI) techniques are able to address some of the previous engineering issues due to their advantages compared to classic methods [29-34]. Learning and mocking are two significant points of AI, which make these algorithms favourable for researchers

[35-39]. Employing optimisation techniques such as back-propagation algorithms [40], a raw model of Artificial neural networks (ANNs) is generally developed. ANN can solve three types of problems including (1) classification, (2) function-approximation and (3) time series prediction [41-45]. However, local extremums and difficulty in crossing plateaus of error function landscape are common defects of classic approaches [46-50]. In this regard, Metaheuristic (MT) optimisation algorithms such as GA [51], particle swarm optimisation (PSO) [52] and imperialist competitive algorithm (ICA) [53] can be used to address mentioned drawbacks.

In some cases, the ANN performance can be improved by the global search feature of these methods. ANNs and some optimisation techniques have been recently applied for solving nonlinear and sophisticated engineering shortcomings. One of the ANN developments is adaptive neuro-fuzzy inference system (ANFIS) which has become a trending algorithm for prediction [54]. In medical researches, ANFIS also has been conducted for predicting a number of verified patient cases [55,56]. A novel combination set of ANFIS was developed in China to predict the number of contaminated cases from covid-19 [57]. In addition, hybrid algorithms are typically employed to solve multiobjective problems [58,59]. Therefore, different types of optimisation methods can be integrated with ANFIS to increase the accuracy and improve the performance of the employed algorithm. The multi-verse optimiser (MVO) approach has been combined with ANFIS to calculate the consumption of materials. This hybrid algorithm is utilised to solve the consumption rate of material and predict that from a dataset which has been derived from different areas [58].

According to literature few studies has investigated the CFS upright sections by AI and almost none has employed feature-selection method. First, FE models with different configurations were successfully produced and comprehensively discussed, and their noticeable specifications have been mentioned. Secondly, an AI approach is utilised for predicting the compression capacity of the upright frames and verifying the FE models. Since the neural network has a successful background in predicting upright section properties, a multi-layer perceptron (MLP) technique has been selected as the central core of the AI method. In this paper, a feature-selection based algorithm has also been used to find the most governing property of compressive strength and employed another numerical approach for verification, optimisation and prediction. Operating a hybrid neural network based on the feature-selection technique has successfully led to predicting the ultimate normalised load and the displacement. The validity of the FE results was successfully

proven as well. Moreover, a new developed multi-layer perceptron algorithm in combination with particle swarm optimisation was deployed, and obtained results have been discussed comprehensively.

6.3. Finite Element (FE) Modelling

FE models were employed to study the effect of reinforcement spacings, including 50 mm, 100 mm, 150 mm, 200mm, 250 mm, 300 mm, 350 mm and 400 mm, on the strength of the upright frames. All perforations are modeled for frames with 1800 mm, 2400 mm, 3000 mm and 3600 mm heights using the Abaqus package. At the first stage, the FE specifications are described and then, the results are checked against the tests. Finally, the effects of different reinforcement spacings are derived through the final FE model.

Upright profiles are typically perforated along the length, which provides a suitable opportunity to install the reinforcements through their flanges or webs to strengthen racking frames. This paper simulated the novel fastening system, which has already been proposed in [60]. The reinforcement consists of bolts, nuts and spacers to connect the flanges of the open section to partially closing it. Figure 6-1 indicates the reinforcement system and the mechanism of its installation.

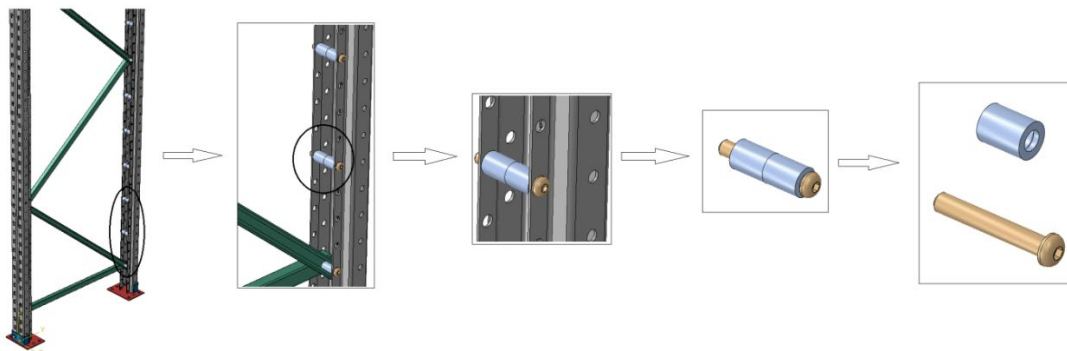


Figure 6-1: The reinforcement system and the constituent elements.

6.3.1 Material Properties

Material specifications have been obtained from the coupon test and deployed to accurately simulate the upright column material. The stress (σ_{true}) and strain (ϵ_{true}) could be derived using the following relations:

$$\sigma_{true} = \sigma(1 + \epsilon) \quad (1) \quad (6.1)$$

$$\epsilon_{true} = \ln(1 + \epsilon) - \frac{\sigma_{true}}{E} \quad (2) \quad (6.2)$$

Where;

σ & ϵ are = stresses and strains derived from the coupon tests.

Poisson ratio = 0.3

E (Module of elasticity) = 200 GPa

6.3.2 Connections and Interactions

In order to specify the compression load capacity for upright frames, three kinds of interactions are required in the models, including upright to bracing, bracing to bracing, and bolt to upright interaction. Therefore, the penalty method has been utilised with 0.3 as the friction coefficient to simulate the tangential behaviour. Also, the surface to surface interaction with hard contact has been selected for the simulation. Figure 6-2 represents the quality of described interactions between elements and the bolt modeling in the upright frame.

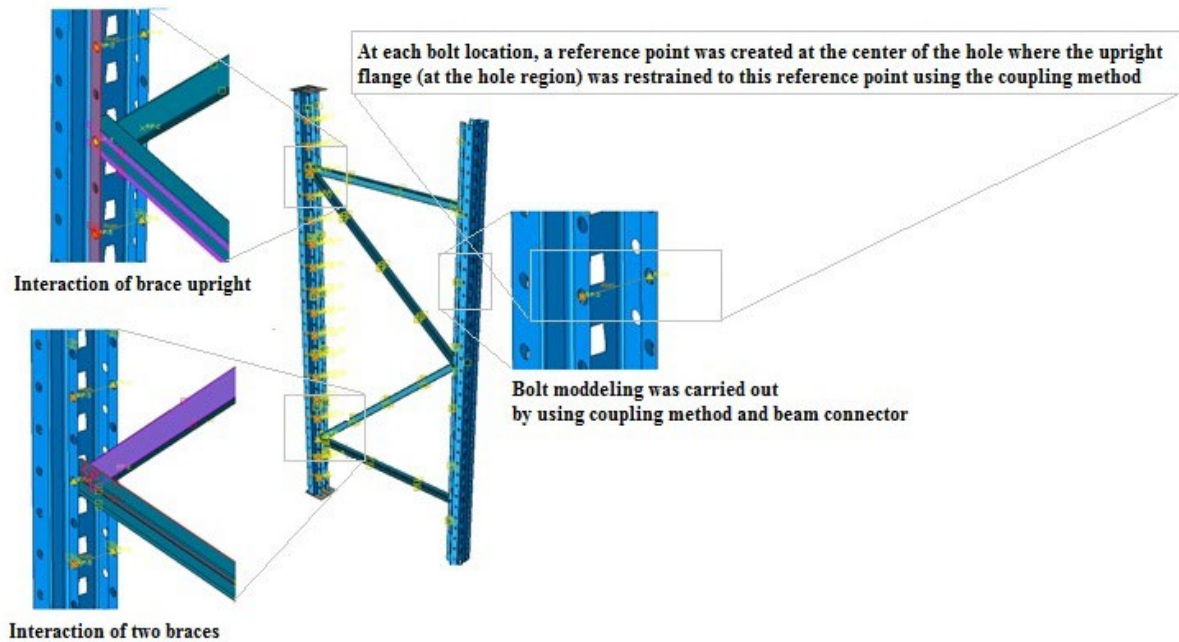


Figure 6-2: Interaction and connection properties of a typical model

6.3.3 Boundary Conditions, Loading and Mesh

The applied load was simulated by a displacement of the reference point on the top of the upright, while at another end of the upright, BCs were set to simulate pinned-end by fixing translation and allowing rotation.

Meshes were selected from shell elements due to the small aspect ratio of the profile sections, which leads to accurate simulation of deformation. Figure 6-3 depicts the employed meshing system of the typical FE model.

A convergence study was performed to capture the optimum mesh size for the upright and bracing members and it was observed that quad dominated meshes with dimensions of 10mm were deemed satisfactory for frame elements.

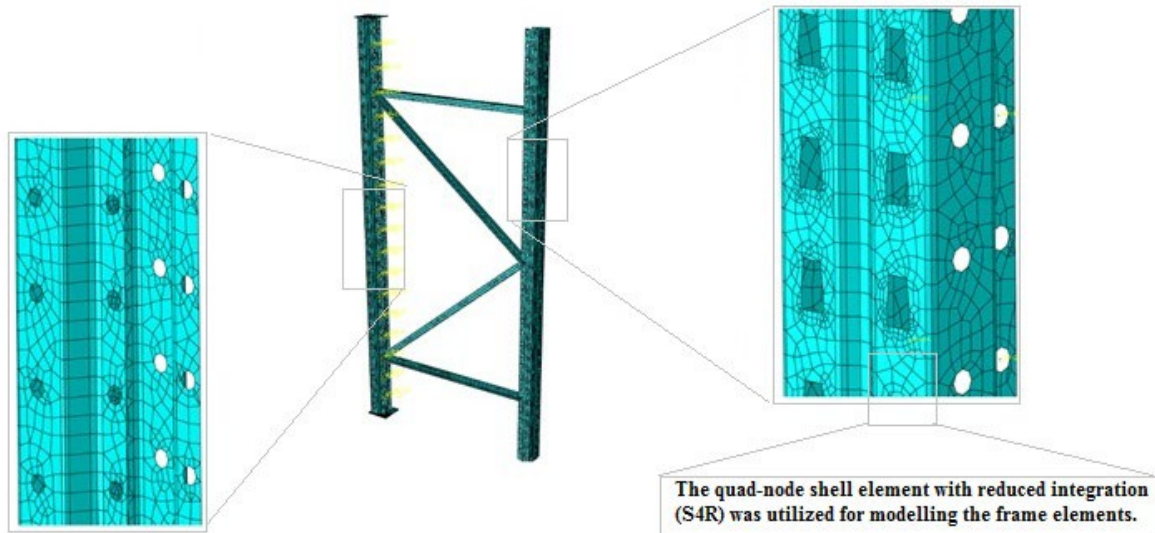
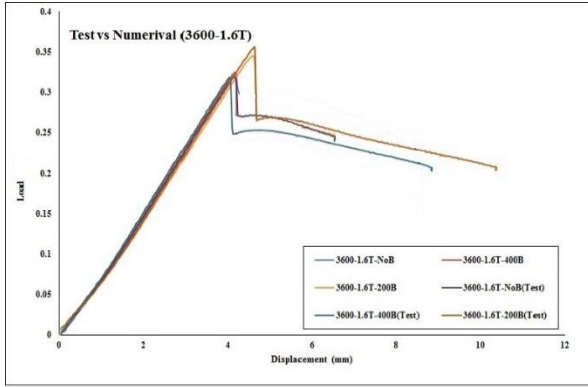


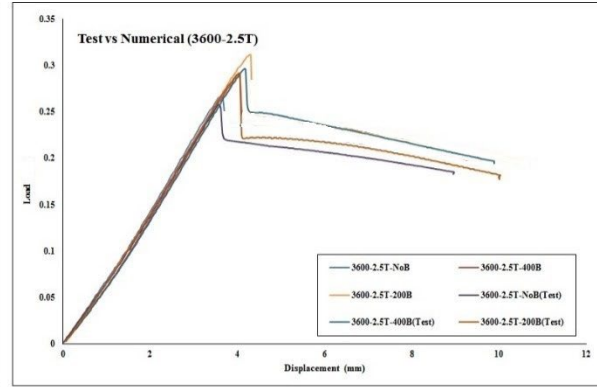
Figure 6-3: A typical model with a Mesh matrix view on the polygon and circular perforations

6.3.4 FE Model Verification

Data were derived from test results of uprights with 1800 mm, 2400 mm, 3000 mm and 3600 mm height for both 1.6 mm and 2.5 mm thicknesses. Because of confidentiality reasons, the normalised ultimate load capacity of the sections to their gross cross-section and the mean yielding strength ($\frac{Load}{A_g \times \sigma_y}$) is presented in this paper. The employed load data is derived from the normalised load in all figures in the article. Figure 6-4, Figure 6-5, Figure 6-6, and Figure 6-7 indicate a comparison between the numerical and experimental data based on normalized load-displacement curves for sections with 1.6 mm and 2.5 mm thicknesses, respectively. According to the diagrams, FE curves cover well enough the test curves, which could prove the reasonable accuracy of the FE results. The slight differences can be attributed to specific FE conservative solutions and possible errors in experimental tests. Therefore, it can be perceived that FE modelling can simulate the accurately performance of upright CFS sections under compression load.

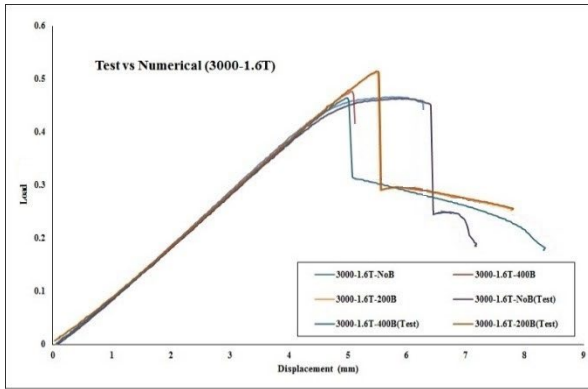


(a)

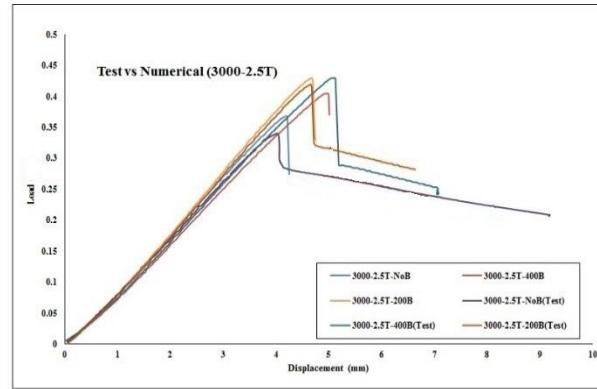


(b)

Figure 6-4: Comparison of test and numerical results of normalised load for (a) 3600L-1.6T, (b)3600L-2.5T



(a)



(b)

Figure 6-5: Comparison of test and numerical results of normalised load for (a) 3000L-1.6T, (b) 3000L-2.5T

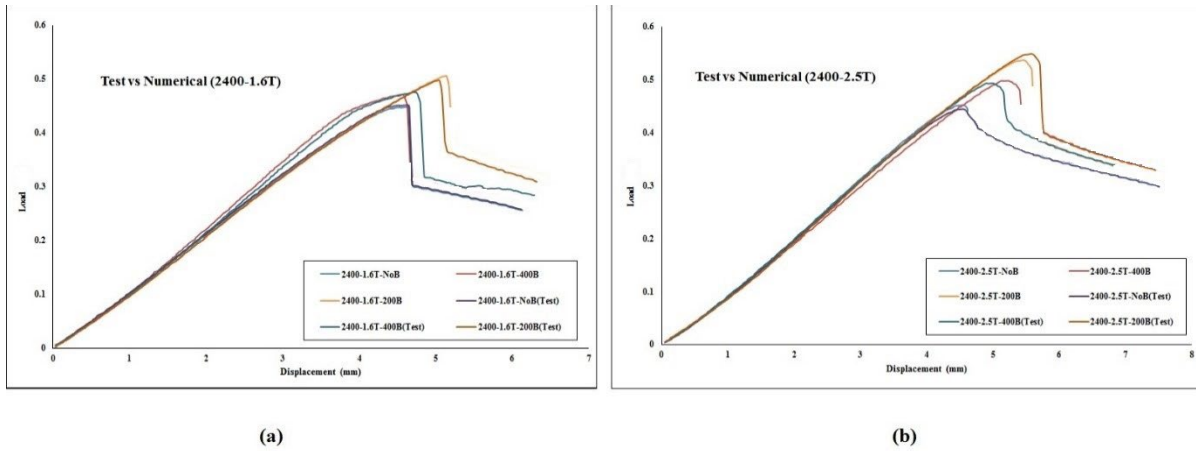


Figure 6-6: Comparison of test and numerical results of normalised load for (a) 2400L-1.6T, (b) 2400L-2.5T

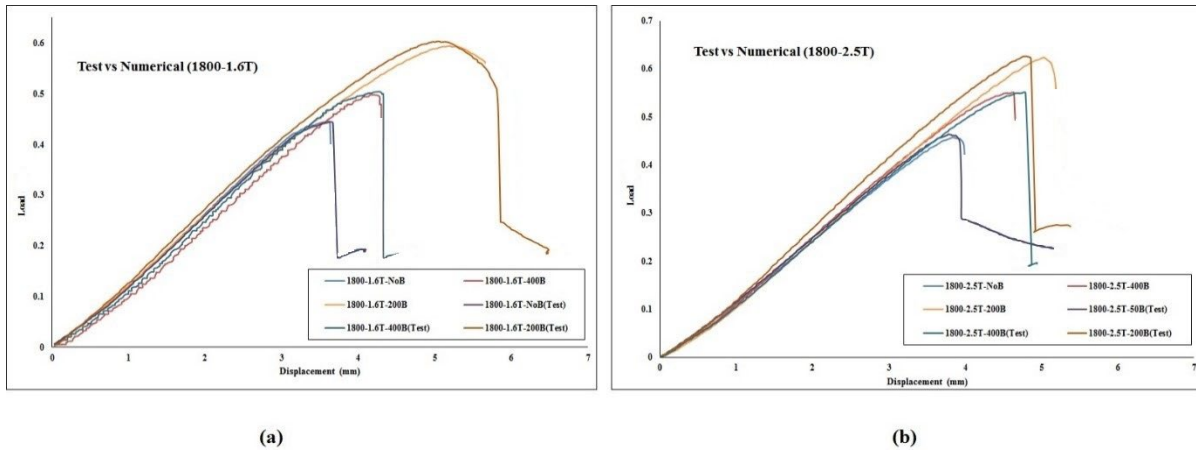


Figure 6-7: Comparison of test and numerical results of normalised load for (a) 1800L-1.6T, (b) 1800L-2.5T

6.3.5 Result and discussion

The numerical model was successfully able to simulate the actual condition with minimum error. Hence, in this section, the verified FE method is utilised for a parametric study to investigate various uprights with different heights and thicknesses as well as different reinforcement spacings under axial loading. In general, eight reinforcement spacings including no-reinforcement, 50 mm, 100 mm, 150 mm, 200 mm, 250 mm, 300 mm, 350 mm and 400 mm were considered for the parametric study. The numerical evaluation was conducted on four various thicknesses of 1.6 mm, 2.0 mm, 2.5 mm and 3.0 mm of profiles as well as four different upright lengths, including

1800mm, 2400mm, 3000mm and 3600mm. For the sake of brevity, the models have been named according to Figure 6-8 in which the values are in mm.

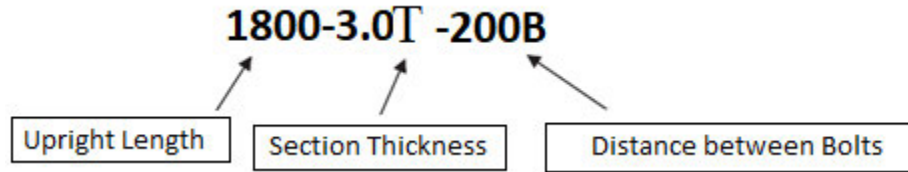
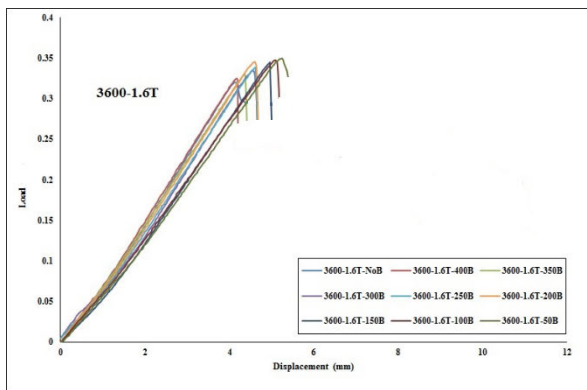


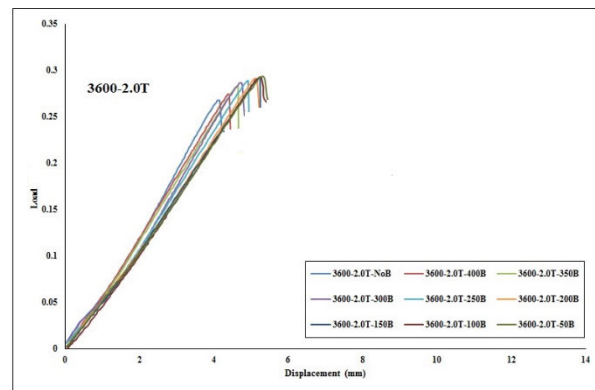
Figure 6-8: Designation of models.

Generally, four lengths (1800 mm, 2400 mm, 3000 mm and 3600 mm) with different reinforcement spacings (50 mm, 100 mm, 150 mm, 200 mm, 250 mm, 300 mm, 350 mm and 400 mm) and web thicknesses (1.6 mm, 2.0 mm, 2.5 mm and 3.0 mm) were considered for modelling of the upright frames.

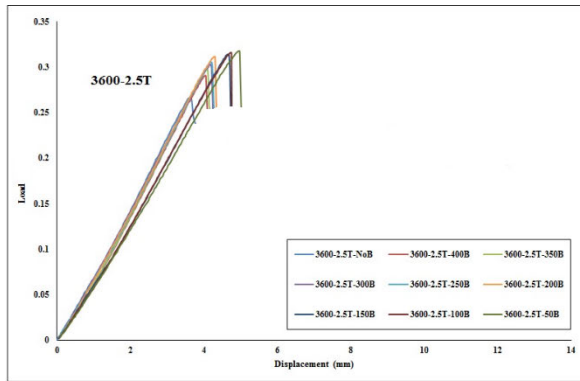
Figures 6-9(a)-(d) illustrate the axial behaviour of 3600 mm length upright frames with 1.6 mm, 2.0 mm, 2.5 mm and 3.0 mm thickness, respectively. According to Figure 6-9, using shorter reinforcement spacing have increased ultimate load capacity among all of the models, especially in model with 3.0 mm thickness. It can also be understood from Figure 6-9 that increasing thickness could control the mode of distortional buckling.



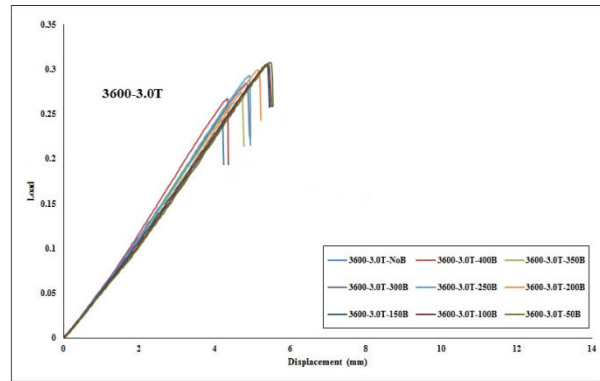
(a)



(b)



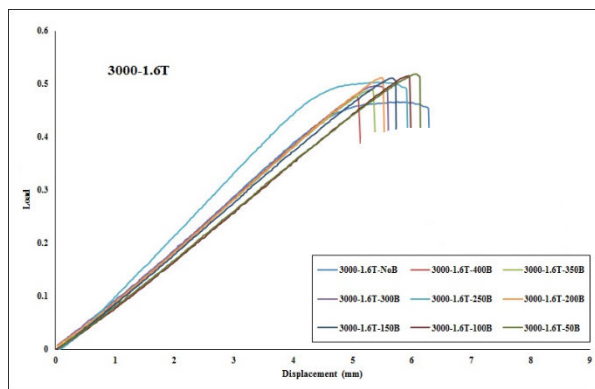
(c)



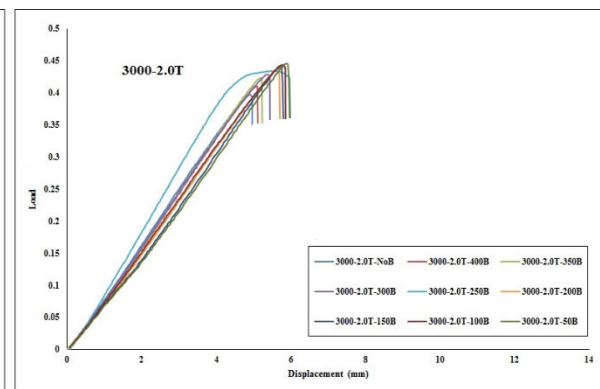
(d)

Figure 6-9: Normalised load-displacement diagrams of the FE results for: (a) 3600L-1.6T, (b) 3600L-2.0T, (c) 3600L-2.5T, and (d) 3600L-3.0T models.

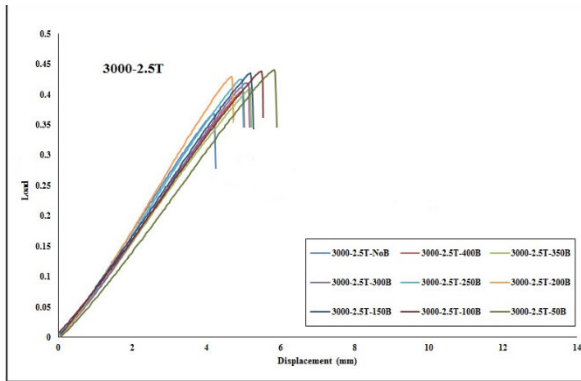
Figure 6-10 (a)-(d) depict the FE results of the 3000mm long models based on the normalized load-displacement diagram. In models with 3000 mm length, upright frames are more strengthened as the reinforcement spacing decreases. The models with 50 mm reinforcement spacing achieved the maximum ultimate capacity in all categories.



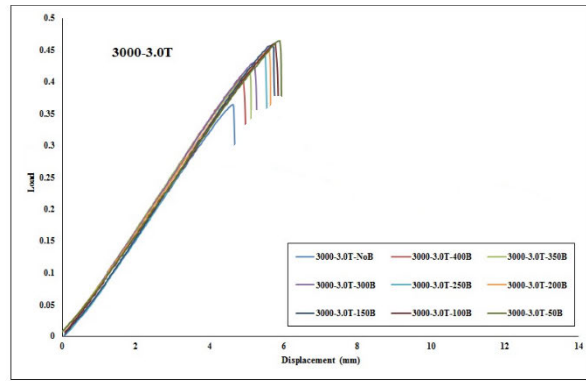
(a)



(b)



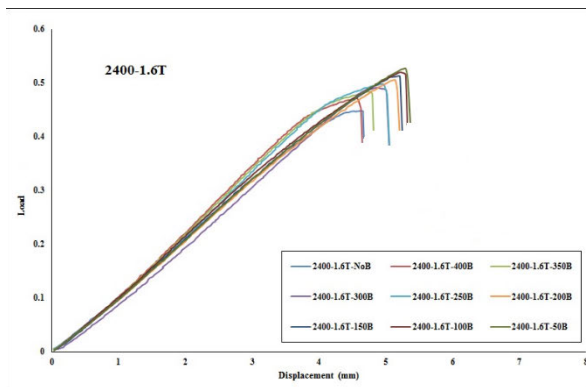
(c)



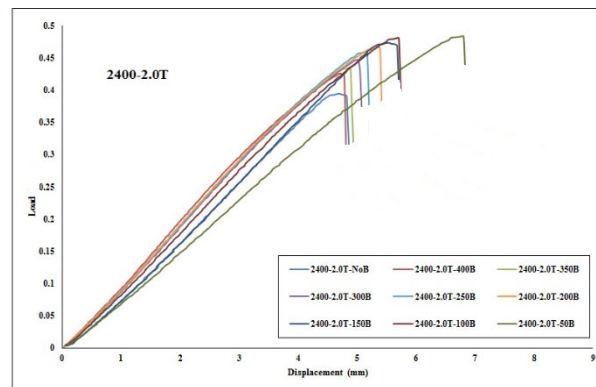
(d)

Figure 6-10: Normalised load-displacement diagrams of the FE results for: (a) 3000L-1.6T, (b) 3000L-2.0T, (c) 3000L-2.5T, and (d) 3000L-3.0T models.

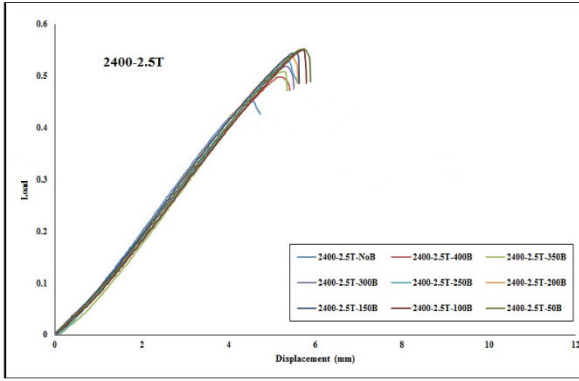
Figure 6-11 (a)-(d) represent the diagrams of the 2400 mm models simulation. It is clearly shown that using 50 mm spacing for reinforcement is the optimum choice to enhance compressive capacity for 2400 mm uprights. By comparing the thicknesses, the models with 2.5 mm thickness presented the highest normalized load capacity among other thicknesses in this case.



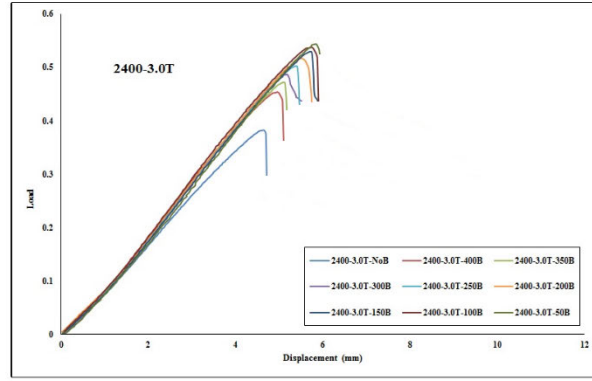
(a)



(b)



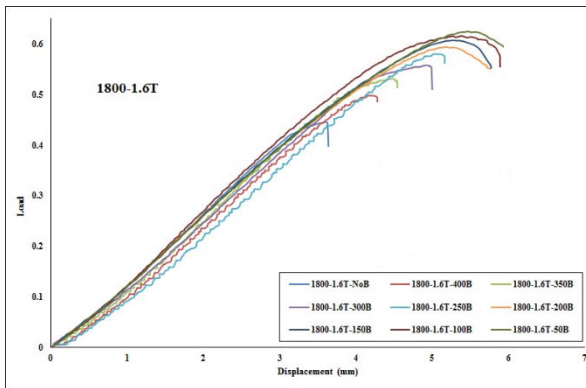
(c)



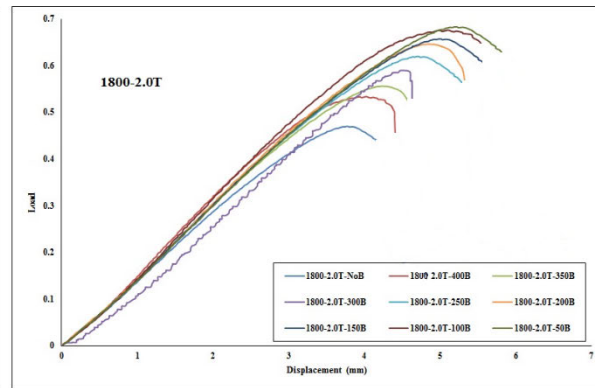
(d)

Figure 6-11: Normalised load-displacement diagrams of the FE results for: (a) 2400L-1.6T, (b) 2400L-2.0T, (c) 2400L-2.5T, and (d) 2400L-3.0T models.

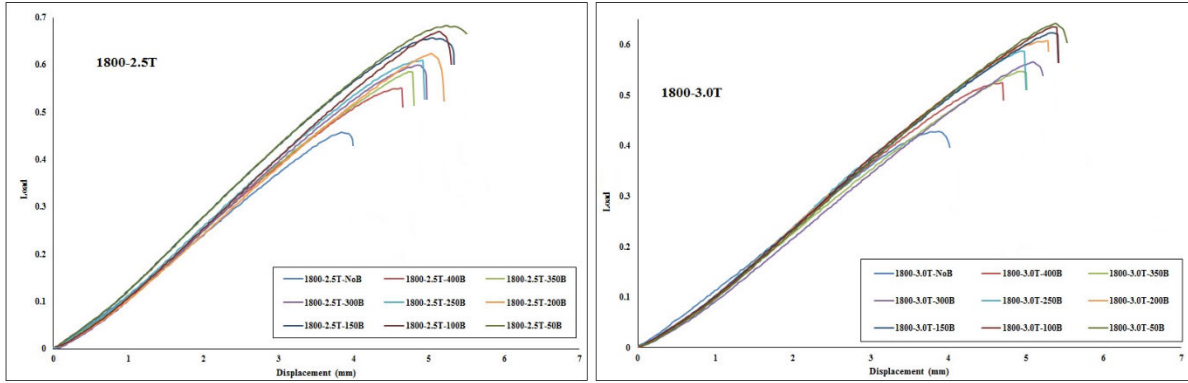
According to Figure 6-12 (a)-(d), simulations have proved that models with 1800 mm length follow the previous trend in the spacing pattern, where 50 mm spacing is the optimum spacing to increase the loading capacity of the frames with 1800 mm length.



(a)



(b)

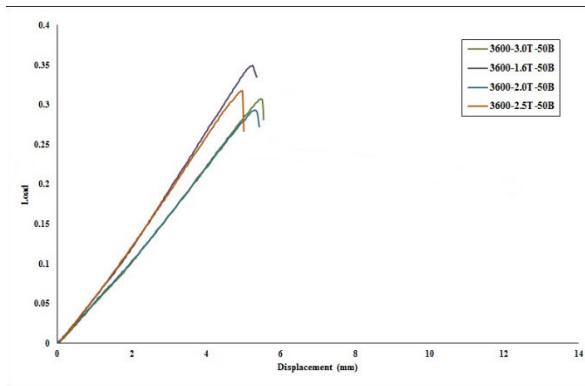


(c)

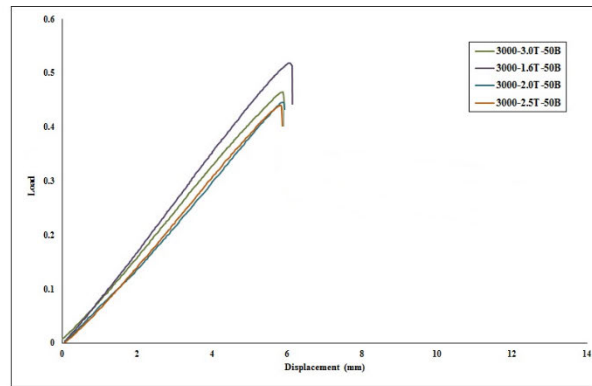
(d)

Figure 6-12: Normalised load-displacement diagrams of the FE results for: (a) 1800L-1.6T, (b) 1800L-2.0T, (c) 1800L-2.5T, and (d) 1800L-3.0T models.

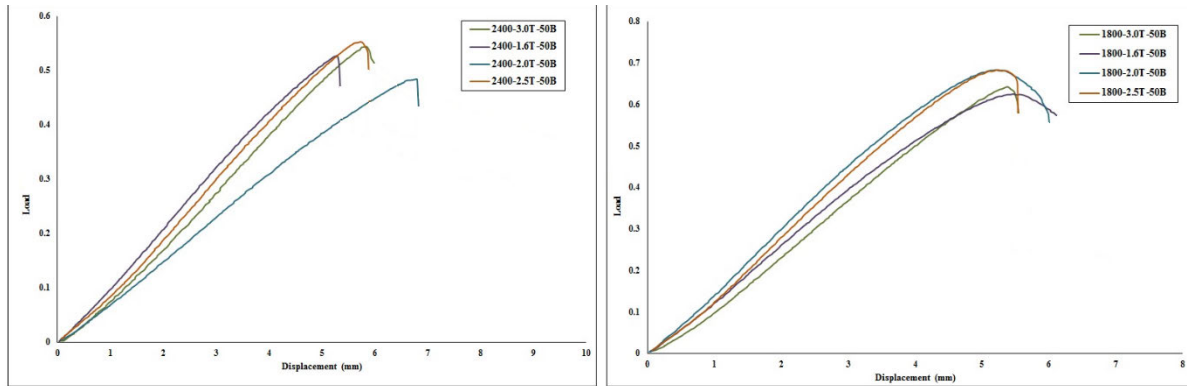
In general, in all four lengths, 50 mm spacing stood in the first rank among other spacing values for increasing the ultimate load capacity. Figure 6-13 (a)-(d) consist of models categorised according to 50 mm reinforcement spacing. According to this figure, models with 1800 mm length and 50 mm spacing represented the highest capacity among other models.



(a)



(b)

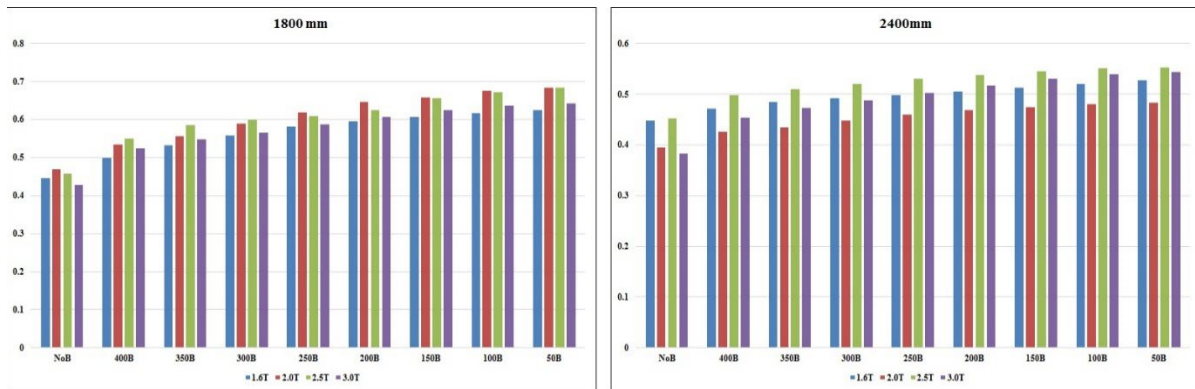


(c)

(d)

Figure 6-13: Normalised load-displacement diagrams of the FE results for: (a) 3600L-50B, (b) 3000L-50B, (c) 2400L-50B, and (d) 1800L-50B models.

According to the FE results, uprights followed almost the same trend of increasing the ultimate load capacities with reinforcement spacing. However, the results did not indicate the same pattern for different thicknesses and lengths. Figure 6-14 and Figure 6-15 represent the normalized ultimate load capacities of each model based on the length and thickness. 2.5 mm thickness is the optimum value for uprights 1800 mm and 2400 mm long. However, 3000mm and 3600mm models presented a different pattern, where models with 1.6 mm thickness showed the highest normalized ultimate capacities among other models and thicknesses, as indicated in Figure 6-15.



(a)

(b)

Figure 6-14: Ultimate load capacities based on thickness and reinforcement spacing for (a) 1800mm models and (b) 2400mm models

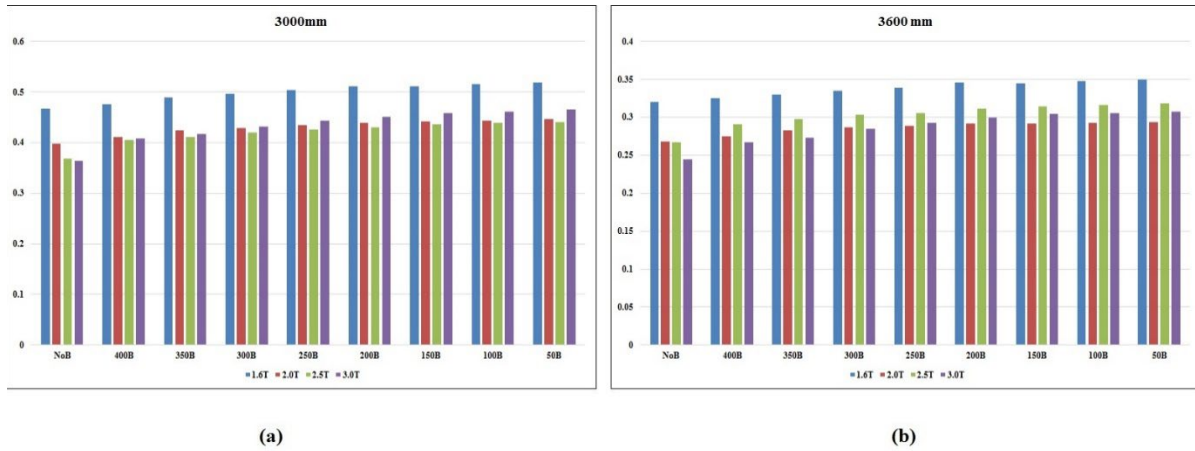


Figure 6-15: Ultimate load capacities based on thickness and reinforcement spacing for (a) 3000mm models and (b) 3600mm models

Ultimate normalised values are given in Table 6-1, Table 6-2, Table 6-3, and Table 6-4 where each table represents the ultimate values in order of thickness and reinforcement spacing. Table 6-1 represented 3600mm model values, where 50 mm spacing is the optimum value for reinforcing pitch along the upright length. According to Table 6-1, 50 mm spacing has increased the ultimate compressive capacity by 9.1%, 9.55%, 19.2% and 25.94% for 1.6mm, 2.0mm, 2.5mm and 3.0mm thicknesses, respectively. Table 6-2 demonstrated the ultimate normalized compressive capacities for 3000 mm models enhanced by 11.24%, 12.21%, 19.8% ,and 27.64% for 1.6mm, 2.0mm, 2.5mm and 3.0mm thicknesses, respectively. However, these values for 2400 mm models are 17.6%, 22.53%, 22.25%, and 42.19%, respectively (Table 6-3). Finally, according to Table 6-4, models with 1800 mm length have represented the best compressive performance with 50 mm spacing. In this case, the increased values are 40%, 45%, 49.1% and 49.9% for 1.6 mm, 2.0 mm, 2.5 mm and 3.0 mm thicknesses.

Table 6-1: Ultimate normalized compressive capacities for 3600 mm models based on reinforcement spacing

3600 mm	NoB	400B	350B	300B	250B	200B	150B	100B	50B
1.6T	0.320	0.324	0.329	0.334	0.338	0.345	0.345	0.347	0.349
2.0T	0.267	0.274	0.283	0.286	0.288	0.291	0.291	0.292	0.293
2.5T	0.266	0.290	0.297	0.302	0.305	0.311	0.314	0.315	0.317
3.0T	0.244	0.266	0.273	0.284	0.292	0.299	0.304	0.305	0.307

Table 6-2: Ultimate normalized compressive capacities for 3000 mm models based on reinforcement spacing

3000mm	NoB	400B	350B	300B	250B	200B	150B	100B	50B
1.6T	0.466	0.476	0.488	0.496	0.503	0.511	0.511	0.514	0.518
2.0T	0.397	0.410	0.423	0.429	0.434	0.438	0.441	0.443	0.445
2.5T	0.367	0.404	0.411	0.419	0.424	0.429	0.435	0.438	0.440
3.0T	0.364	0.407	0.416	0.431	0.442	0.450	0.457	0.461	0.464

Table 6-3: Ultimate normalized compressive capacities for 2400 mm models based on reinforcement spacing

2400mm	NoB	400B	350B	300B	250B	200B	150B	100B	50B
1.6T	0.448	0.471	0.484	0.491	0.498	0.505	0.512	0.520	0.527
2.0T	0.394	0.426	0.434	0.447	0.458	0.468	0.473	0.480	0.483
2.5T	0.452	0.498	0.508	0.519	0.529	0.537	0.545	0.550	0.552
3.0T	0.382	0.454	0.472	0.487	0.502	0.516	0.529	0.538	0.543

Table 6-4: Ultimate normalized compressive capacities for 1800 mm models based on reinforcement spacing

1800mm	NoB	400B	350B	300B	250B	200B	150B	100B	50B
1.6T	0.446	0.498	0.531	0.557	0.580	0.594	0.607	0.615	0.624
2.0T	0.469	0.533	0.555	0.589	0.619	0.645	0.657	0.675	0.682
2.5T	0.457	0.549	0.585	0.599	0.608	0.624	0.656	0.671	0.682
3.0T	0.428	0.523	0.547	0.566	0.587	0.606	0.623	0.635	0.642

Overall, investigation of FE results for uprights under compression loading proves that partially reinforced sections have considerable higher capacities under applied loads, which reveals the outstanding effectiveness of the proposed reinforcement method.

6.4. Artificial Intelligence Prediction

In this paper, a combination of MLP with PSO algorithm based on the random production of the initial population is utilised. PSO is a universal method of minimisation that can be employed to deal with problems whose answer is a point or surface in n-dimensional space. In this case, a random population is assumed, and an initial velocity is assigned to them as well as channels of communication between the particles. These particles then move in the response space, and findings are calculated according to the "competency criterion" after each time interval. Over time, particles accelerate toward the particles with a higher competency standard and are in the same communication group. Although each technique performs well in many problems, it has shown great success in solving ongoing optimisation problems. In order to identify the most influential input, the feature selection technique is employed instead of traditional methods, which is the best way to identify the features of an issue. In other words, the main purpose of this study is to utilise the feature selection technique to determine the most influential parameter on the prediction of compression capacity of the CFS upright columns and verify the displacement and ultimate axial load simultaneously.

6.4.1 Algorithm methodology

6.4.1.1 Multi-layer perceptron (MLP)

Feed-forward multi-layer perceptron (MLP) networks can be used as powerful hyper-surface reconstruction tools which are able to successfully map a set of multi-dimensional input data $(\underline{x}_i; i = 1, \dots, N)$ onto a set of appropriate multi-dimensional outputs $(\underline{y}_i; i = 1, \dots, N)$. The MLP configuration has been extensively utilised for static regression applications, and it consists of one input layer, one or more hidden layer(s) and one output layer. In addition, the MLP network employs a supervised learning technique called backpropagation for training the network.

The fundamental element of the modified un-stabilized MLP neural network is shown in Figure 6-16, which performs a projection oriented mathematical operation on its inputs (Figure 6-17).

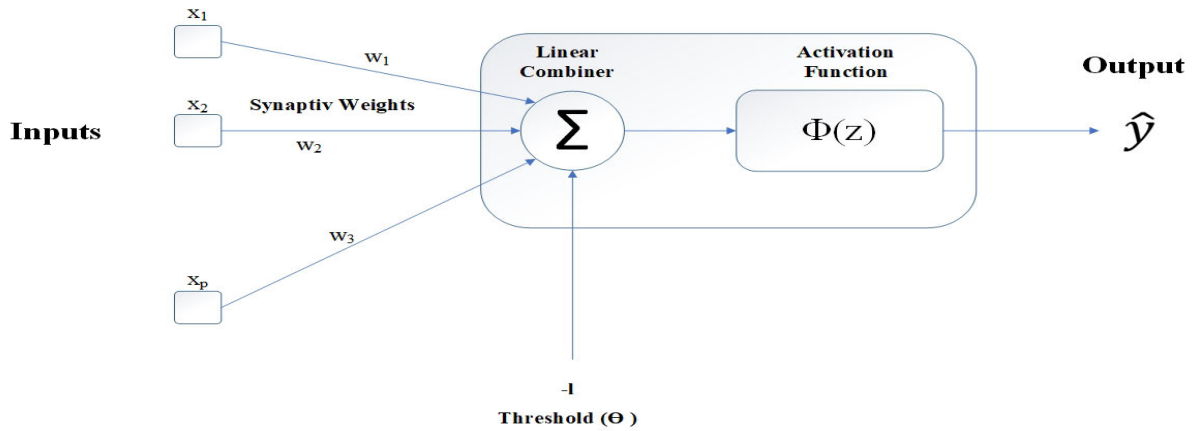


Figure 6-16: Schematic representation of MLP neuron.

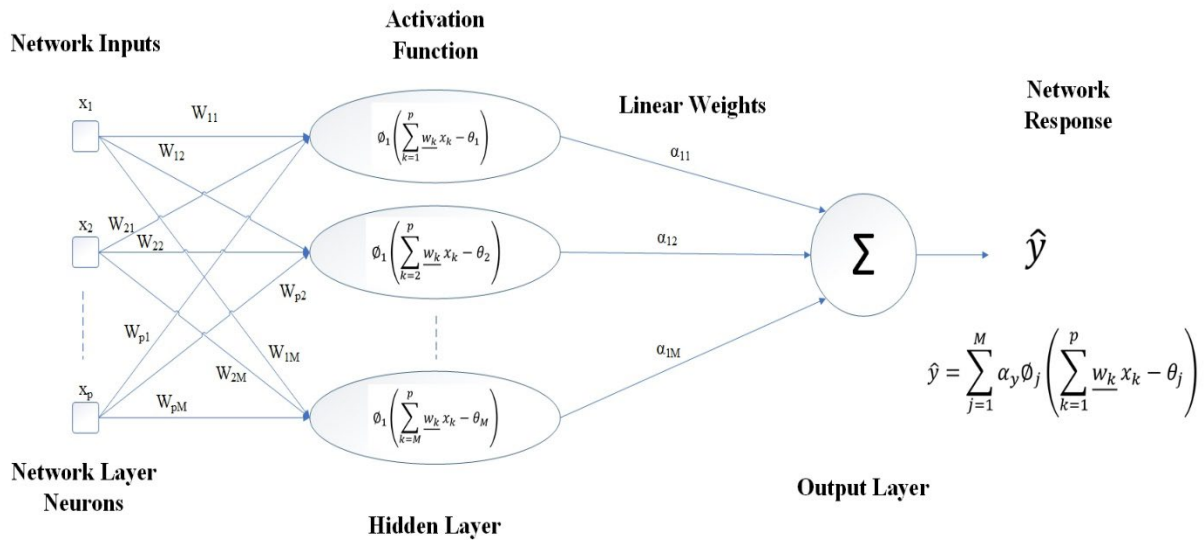


Figure 6-17: Flowchart of typical single line hidden layer MLP for identifying a problem.

In the present study, a particular kind of ANN called multi-layer perceptron (MLP) was developed and trained by data obtained from several experimental tests and FEM models.

6.4.1.2 Particle swarm optimisation (PSO)

PSO is a robust algorithm for optimisation in nonlinear, non-convex and discontinuous environments. Using the PSO algorithm, all kinds of optimisation problems, both continuous and discrete, can be solved. This algorithm has major capabilities and efficiently optimise while defining many parameters. In this algorithm, particles (inputs) are the building blocks of the population and work together. With the intelligence they have, a certain amount of intelligence is

created that is not comparable to the intelligence of each of them. For this reason, it is called swarm intelligence. The most important feature of any particle is its position, and the critical issue is what indicator or target the particle offers and how fast it moves (Figure 6-18).

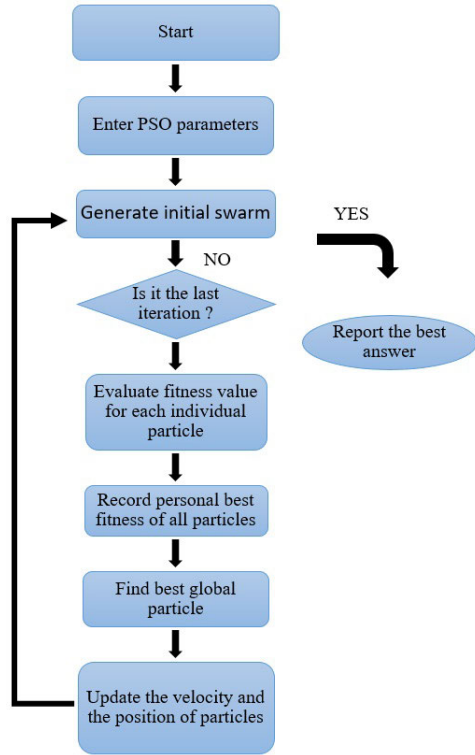


Figure 6-18: PSO sequential flowchart

In this study, the PSO algorithm has been employed along with MLP as a unique intelligence algorithm. The goal of the PSO algorithm is to find the optimal objective function.

6.4.1.3 Feature selection (FS) technique

Feature selection (FS) in various machine learning and data mining fields is a subset of feature extraction. This technique is preferred in cases where the readability and interpretation of the subjects are important because the discounted values are preserved as the main features in the reduced space. This method of dimensionality leads to the creation of a quality database without deleting helpful information. It also allows combining features with different data models. This task is essential because a large number of features are often used in different applications. Therefore, the need to choose a limited set from them becomes apparent. Furthermore, limitations and considerations such as avoiding the problems of dimensionality, memory limitations, reducing

computations required and running time require selecting the minimum number of features that can be used to predict future data. The feature selection process is divided into four parts: production method, performance evaluation, stop criteria, and validation method (Figure 6-19).

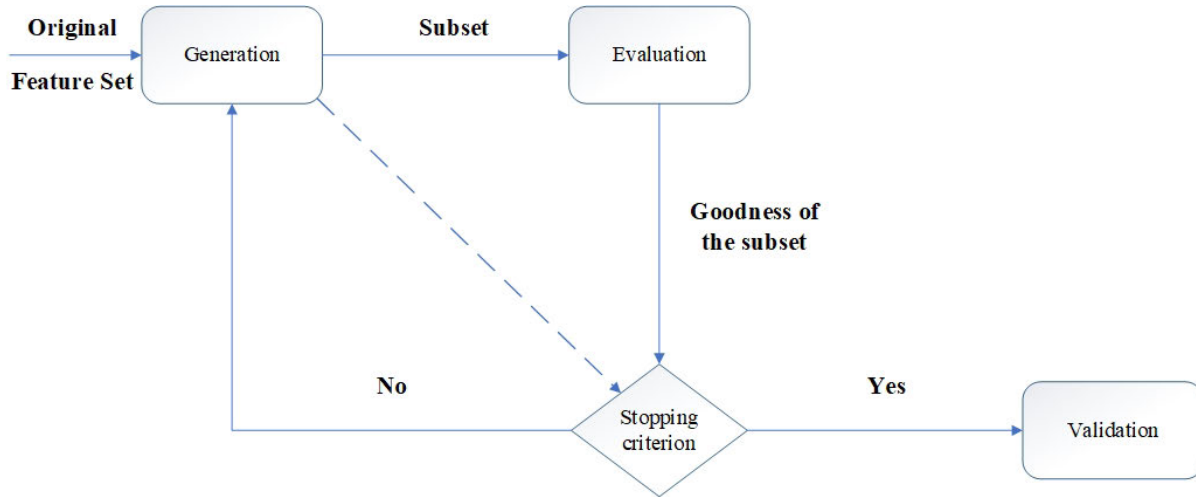


Figure 6-19: Feature selection technique steps

In this study, some of the noticeable features of CFS frames including bolt distance, section thickness, upright length and ultimate load capacity are generated through one or more conversions on the input features. While mapping points from one ample space to another in a smaller space, many points may overlap. Feature extraction helps to find new dimensions that have the minimum overlapping. This approach is related to the problem area and is commonly used in image processing, where specific features are extracted according to the requirements of the problem.

6.4.1.4 MLP-PSO-FS architecture

Figure 6-20 shows a sequential combination diagram of PSO-FS and MLP. In PSO, congestion generally begins with a set of random solutions, and each one is called a particle. Likewise, the particle swarm moves in complex space. A function (f) is evaluated at each step by input. In the global version of the PSO, p_i represents the most appropriate point in the entire population. A new velocity is obtained for each i particle in each iteration according to the best individual neighbourhood positions ($p_i(t) \rightarrow$ and $p_{i \rightarrow ig}(t)$). The new speed can be obtained as follows:

$$v_{i \rightarrow} (t + 1) = wv_{i \rightarrow} (t) + c_1\phi_{1 \rightarrow} \cdot (p_{i \rightarrow} (t) - x_{i \rightarrow} (t)) + c_2\phi_{2 \rightarrow} \cdot (p_{i \rightarrow} (t) - x_{i \rightarrow} (t)) \quad (6.3)$$

As long as the speed exceeds the specified limit, it will be reset to its proper range in some cases. Depending on the speed, each particle changes its position according to the following equation:

$$s_{i \rightarrow} (t + 1) = s_{i \rightarrow} (t) + v_{i \rightarrow} (t + 1) \quad (6.4)$$

Where:

$s_{i \rightarrow}$ = particle's position

$v_{i \rightarrow}$ = particle's velocity

$p_{i \rightarrow}$ = most appropriate position

w = inertia weight

c_1 and c_2 = acceleration coefficients

$\phi_{1 \rightarrow}$ and $\phi_{2 \rightarrow}$ = uniformly-distributed random vectors in $[0,1]$

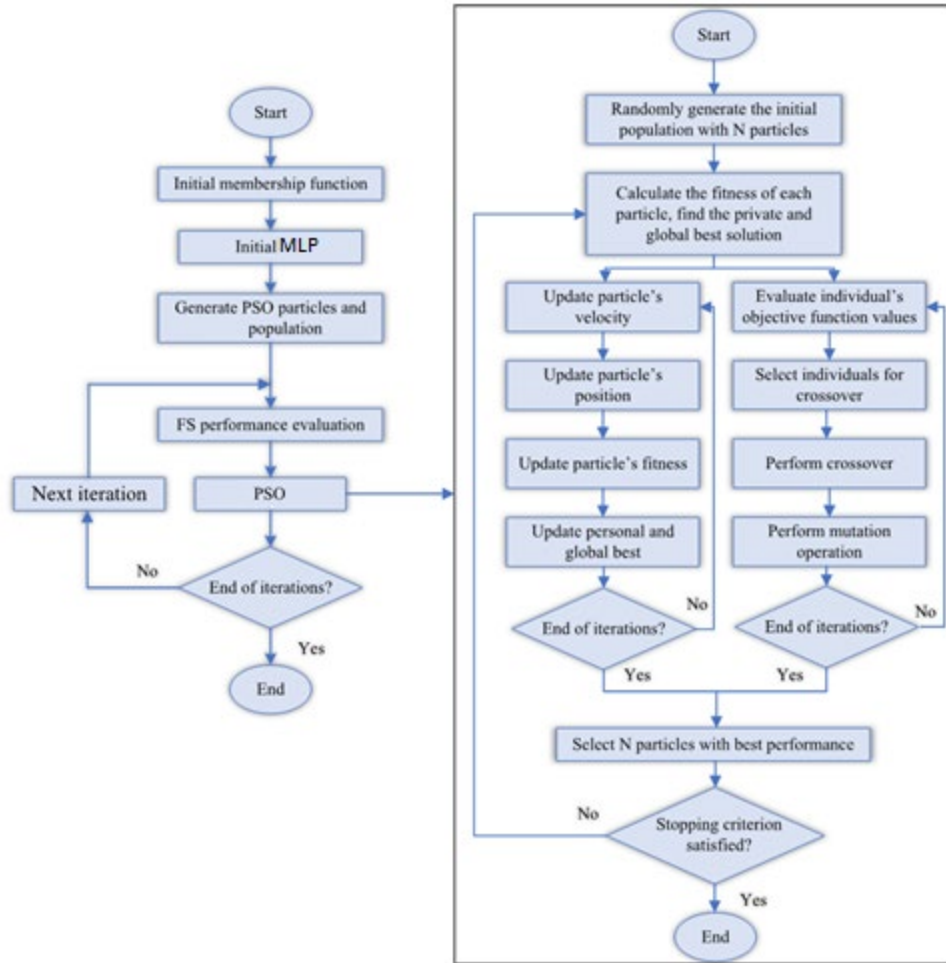


Figure 6-20: flowchart of the sequential combination of hybrid MLP-PSO-FS algorithm.

6.4.1.5 Performance Evaluation

In this paper, five objective criteria, including R, NS, RMSE, MAE and WI, have been used to evaluate the accuracy of the results and the reliability of the proposed neural network [27-30,43]. Nash-Sutcliffe (NS) efficiency is a normalised statistic that determines the relative amount of residual variance compared to the variance of calculation (Nash and Sutcliffe [61]). The Nash-Sutcliffe performance shows how well the observed data graph versus the simulated one corresponds to a 1: 1 line. $NS = 1$ corresponds to the model of full compliance with the observed data. $NS = 0$, indicating that the model predictions are as accurate as the average of the observed data, $-\infty < NS < 0$, indicates that the observed average is a better prediction of the model. Mean absolute error (MAE) and mean square error (RMSE) are two of the most common criteria used to measure the accuracy of continuous variables. MAE measures the average size of errors in a set

of predictions regardless of their direction. This average test is the absolute difference between prediction and actual observation that all individual differences have equal weight. RMSE is a quadratic scoring rule that also measures the average error rate. This square root is the average square difference between prediction and actual observation. From an interpretation point of view, MAE is superior among other criteria . RMSE does not describe moderate error alone and has other implications that are more difficult to understand. On the other hand, one of the distinct advantages of RMSE over MAE is that RMSE avoids the use of absolute values, which is undesirable in many mathematical calculations.

$$R = \frac{\sum_{i=1}^M (O_i - \bar{O}_i) \cdot (P_i - \bar{P}_i)}{\sqrt{\sum_{i=1}^M (O_i - \bar{O}_i)^2 \sum_{i=1}^M (P_i - \bar{P}_i)^2}} \quad [\text{Range} = (0-1); \text{superior value} = 1] \quad (6.5)$$

$$NS = 1 - \frac{\sum_{i=1}^N (P_i - O_i)^2}{\sum_{i=1}^N (O_i - \bar{O}_i)^2} \quad [\text{Range} = (-\infty, 1); \text{superior value} = 1] \quad (6.6)$$

$$RMSE = \sqrt{\frac{1}{N} \sum_{i=1}^N (P_i - O_i)^2} \quad [\text{Range} = (0, +\infty); \text{superior value} = 0] \quad (6.7)$$

$$MAE = \frac{\sum_{i=1}^M |P_i - O_i|}{N} \quad [\text{Range} = (0, +\infty); \text{superior value} = 0] \quad (6.8)$$

$$WI = 1 - \frac{\sum_{i=1}^N (O_i - P_i)^2}{\sum_{i=1}^N (|P_i - \bar{O}_i| + |O_i - \bar{O}_i|)^2} \quad [\text{Range} = (0,1); \text{outstanding value} = 1] \quad (6.9)$$

Where:

O_i and P_i = measured and estimated values, respectively;

\bar{O}_i and \bar{P}_i = mean of the measured and estimated values, respectively;

According to equations 6.5 to 6.9, in the case of R and NS value, a higher value up to 1 represents a suitable fit between measured and predicted values, which negative value shows that the model's performance is worse than the average of the developed models. WI is a stabiliser criterion for prediction error, and as well as the NS criteria, the values close to 0 represents low accuracy while the values close to 1 reveal the decisive estimation.

6.4.1.6 Algorithm results and discussion

According to several running and processes of the developed MPF (combination of MLP, PSO, and Feature-selection techniques), a neural network dataset has been derived and ultimately formed from 10511 rows of data and five-column of values. Regarding the database, this prediction consists of six inputs and one target output. In order to select the most suitable combination of the inputs for the evaluation matrix of the displacement and load, the multi-layer perceptron (MLP) was tuned by particle swarm optimisation (PSO) and carried out as the neural network model. The variables affecting load are indicated in the functional relationship as follows:

$$Ultimate\ Load = f(length, bolts\ spacing, thickness, A_g \times \sigma_y, Load)$$

The MLP neural network is suitable for prediction, especially in problems with stochastic irregularities [62]. In the first stage, regarding the selected training data, MLP was fitted for the best possible prediction of the displacement and load separately. MATLAB (version 2019) software was utilised to predict the load using the MPF network. The best result is given in Table 6-5 and Table 6-6 and for both displacement and normalized load.

Table 6-5: Best achieved results for displacement estimation

Phase	Network Result					
	R ²	R	NS	RMSE	MAE	WI
Test	0.999	1.000	1.000	0.001	0.000	1.000
Train	1.000	1.000	1.000	0.000	0.000	1.000

Table 6-6: Best achieved results for normalised load estimation

Phase	Network Result					
	R ²	R	NS	RMSE	MAE	WI
Test	0.907	0.800	0.435	1.678	1.203	0.882
Train	0.847	0.820	0.511	1.590	1.137	0.895

The parameters of the PSO algorithm are population size, iterations, inertia weight, damping ratio, personal and global learning coefficient, which are provided in Table 6-7. MLP neural network parameters are hidden layers and training functions, as shown in Table 6-8. The parameter characteristics used for FS are also indicated in Table 6-8.

Table 6-7: Parameter characteristics were used for PSO in this study.

FIS Clusters	Population Size	Iterations	Inertia Weight	Damping Ratio	Learning coefficient	
					Personal	Global
10	150~350	45~100	1	0.98	2	3

Table 6-8: Parameter characteristics used for MLP and FS.

Parameter characteristics used for the MLP	
Hidden Layers	Training Function
10	Levenberg-Marquardt back-propagation (LMBP)
Parameter characteristics used for FS	
Number of runs	Number of functions(n_f)
3	1~5

The main reason for employing the feature-selection method along the neural network was eliminating the residual inputs to achieve the most precise estimation. A database may have a large

amount of input data, but certainly, not all inputs are suitable for use in the neural network, some of them have virtually no effect on output prediction, and some may cause network deviation. Therefore, finding the best combination is very time consuming and tedious if it has a large number of work inputs. Implementing the neural network and studying its results for this number of repetitions is impossible considering the different combinations of neural network settings. We may lose the best combination, but using the feature selection technique, with only five runs, all possible input states will be checked, and the best combination will be determined.

6.5. Displacement prediction

Following the prediction process, available inputs were tested with five different scenarios to predict the displacement of the upright frames under the axial compressive load. Table 6-9 presents the five combinations of the MPF and the quality of input selection. According to this Table, the load itself was the most significant input on the displacement prediction, and Thickness stands in second place. In order to avoid ambiguity, Table 6-10 shows the best-predicted results by MPF network by tabulating the value of evaluation criteria for 45 and 250 as iteration and population, respectively.

Table 6-9: Selected input composition based on feature-selection method for deflection case.

Feature	Number of inputs				
	1	2	3	4	5
Length				X	X
Bolt spacing			X	X	X
Thickness		X	X	X	X
Shape factor ($A_g \times \sigma_y$)					X
Axial load	X	X	X	X	X

Table 6-10: Calculated accuracy criteria for the performance of the implemented models (Iteration = 45).

Train
The MPF network

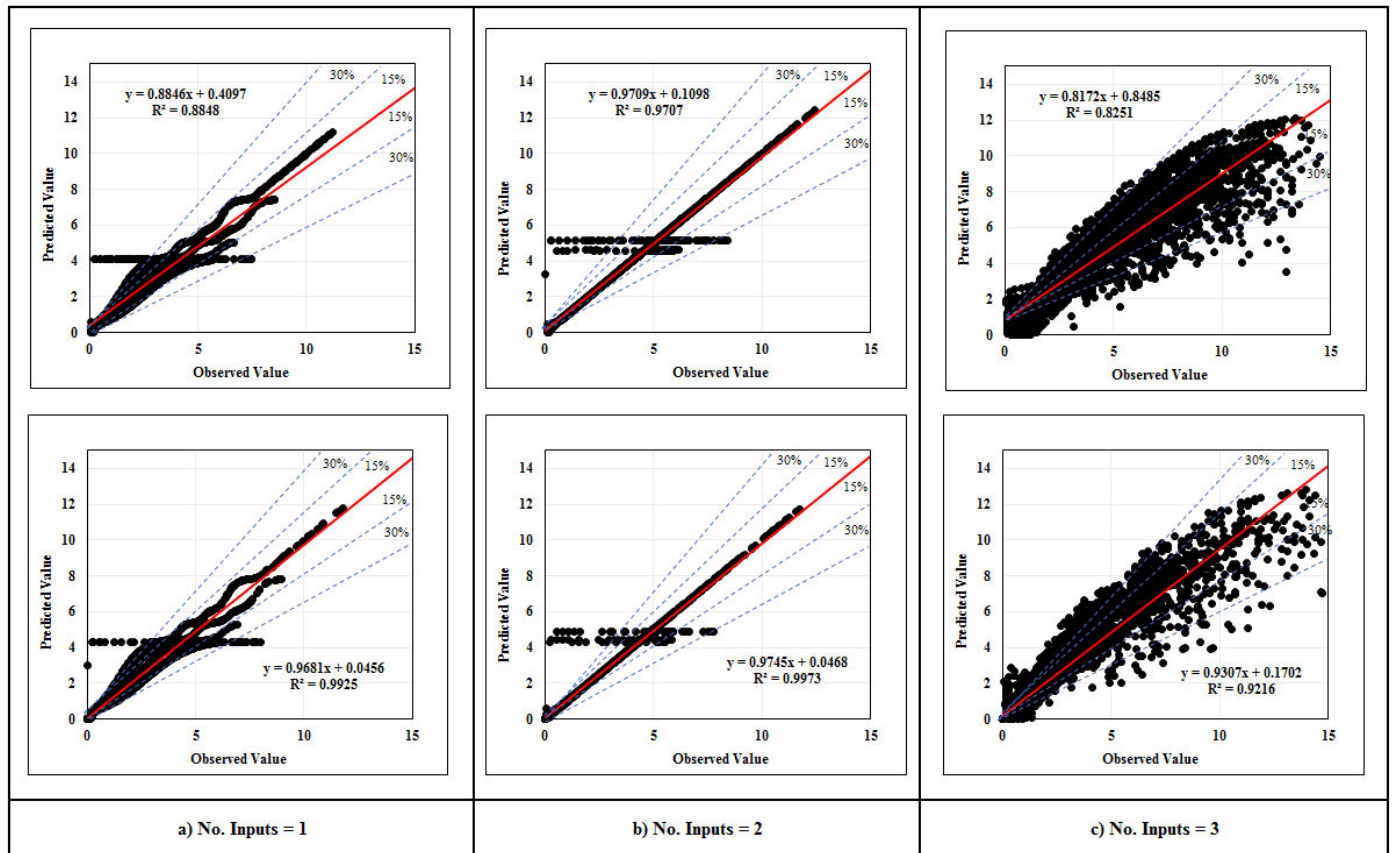
Iteration	Population	n _f	R ²	R	NS	RMSE	MAE	WI
45	250	1	0.885	0.941	0.870	0.035	0.026	0.969
45	250	2	0.971	0.985	0.970	0.018	0.003	0.993
45	250	3	0.825	0.996	0.992	7.244	5.270	0.998
45	250	4	0.999	1.000	1.000	0.001	0.000	1.000
45	250	5*	1.000	1.000	1.000	0.000	0.000	1.000
Test								
The MPF network								
Iteration	Population	n _f	R ²	R	NS	RMSE	MAE	WI
45	250	1	0.992	0.935	0.854	0.038	0.028	0.965
45	250	2	0.997	0.978	0.955	0.022	0.004	0.989
45	250	3	0.921	0.907	0.798	7.199	5.246	0.951
45	250	4	0.999	1.000	1.000	0.001	0.000	1.000
45	250	5*	0.999	1.000	1.000	0.001	0.000	1.000

* most precise predicted value in comparison to the measured value

Table 6-9 has indicate the quality of presence for each input parameter, where the axial load has the most participation among other parameters while shape factor has the lowest participation. Table 6-10 also indicated that the 5th combination of inputs leads to the best prediction in the test phase; moreover, the 5th combination presented the most accurate results in the training phase. On the other hand, since the test results are more substantial scale for accuracy, the 5th combination has represented the best estimation of upright displacement by the MPF network.

Figure 6-21 illustrates the predicted and measured displacement by the MPF model in scatter diagrams. Figure 6-21(a) shows the train and test phase of the model with a single input, whose performance parameters are shown in Table 6-10. Figure 6-21(b) depicts the testing and training phase of the model with two inputs. According to this procedure, it is obvious that MPF networks have shown acceptable performance where the number of inputs increased to 5 inputs. Figure 6-21

(d) and Figure 6-21(e) represent the best-achieved predictions amongst other models; also, there is a slight difference between these two models in the prediction capability mentioned in Table 6-10. As can be seen, some improvement in the performance of the MLP has been resulted in this phase by using the PSO algorithm such that the r and R^2 values have increased and the RMSE value has decreased.



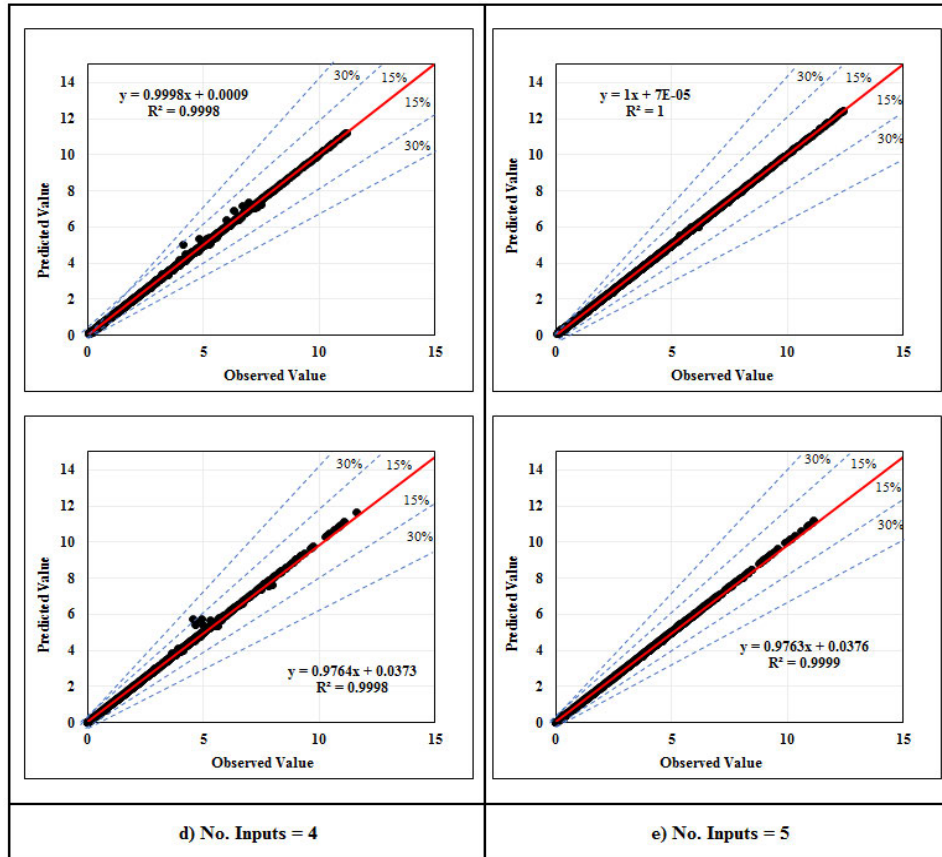


Figure 6-21: Regression of the train (above charts) and test (below charts) phase results with measured values of displacement for (a) One input, (b) Two inputs, (c) Three inputs, (d) Four input, (e) Five inputs

Considering Table 6-9 and Figure 6-21, the shape factor had an insignificant role in the prediction, while Figure 6-21(c) represented that the shape factor effect as an additional parameter is able to make a distraction in the prediction process. On the contrary, Length has a good effect on the precision of the displacement prediction that is shown in Figure 6-21(d) and (e). In the case of horizontal dots in 6-21(a) and (b) it could be related to the accidental selecting of MLP algorithm or some minor overtraining during the prediction phase that is insignificant and does not affect the prediction. Figure 6-22 shows the tolerance diagram based on the prediction and measured results of the models in the testing and training phase. As can be realised, both of the MPF with five input model have been capable of closely predicting most of the test samples.

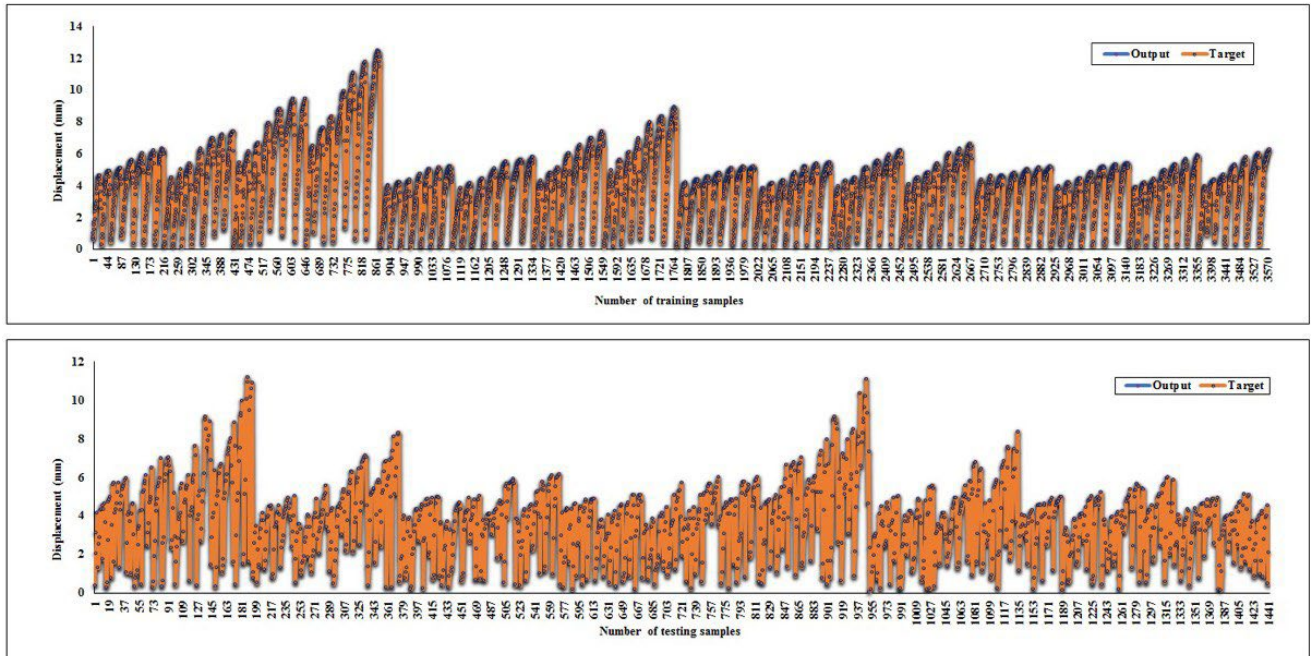


Figure 6-22: The MPF (five inputs) prediction vs experimental diagram: (above) train phase, (bellow) test phase

As shown in Table 6-10 and Figure 6-22, the best performance parameters for the MPF neural network are $RMSE = 0.001$, $r = 1.000$, $R^2 = 0.999$, $NS = 1.000$, $MAE = 0.0$, $WI = 1.000$. Considering that the best result for RMSE is the lowest result and for r , the best positive correlation coefficient is 1, then numbers closer to 1 are considered better results. Also, for higher numbers, higher R^2 shows a more suitable regression diagram. Also, for NS and MAE, smaller results and WI, larger results indicate better performance. Figure 6-23 has revealed the error histogram of the MPF model in the best prediction with 45 iterations and 250 populations utilising five inputs, where the convergence of the error in both test and train phases have shown the same pattern with an acceptable range.

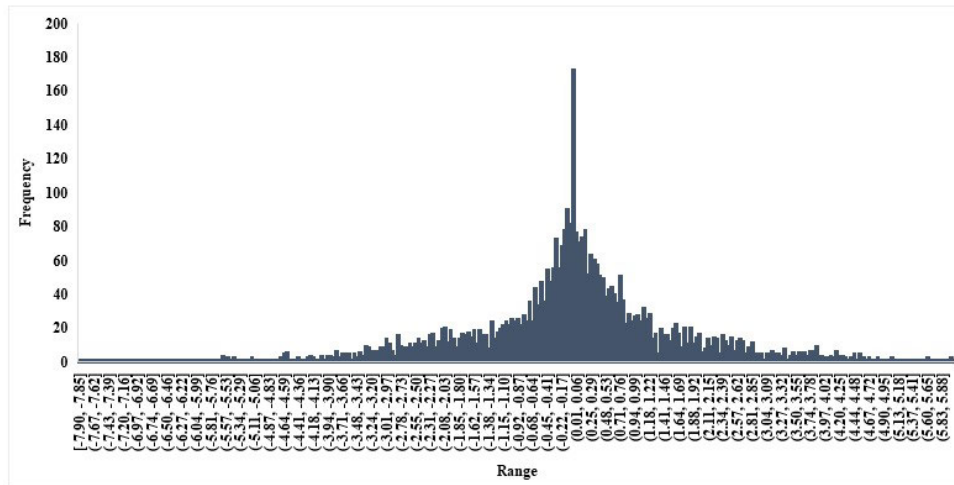
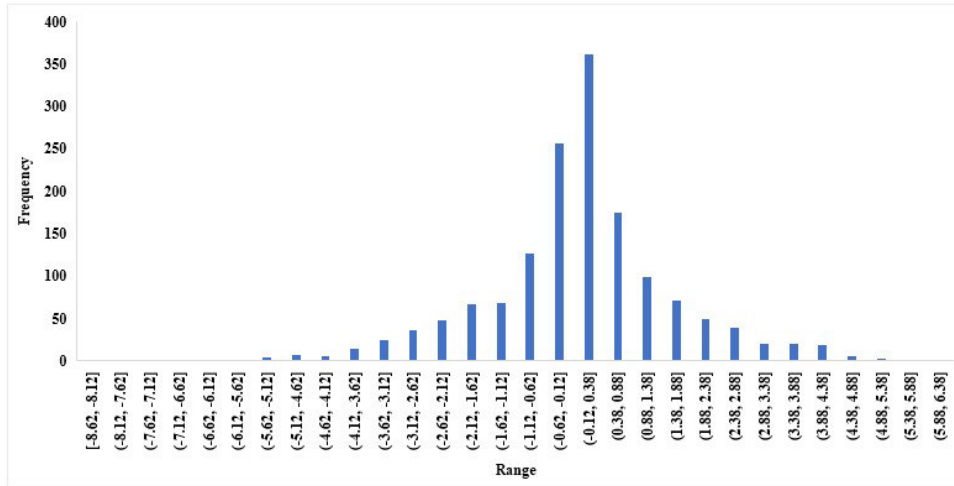


Figure 6-23: The MPF (five inputs) Error histograms: (above) train phase, (below) test phase

6.6. Ultimate Load Prediction

In order to find the best scenario of populations and iterations by considering an endless number of repetitions, and following the adjusting process, according to the feature-selection results, bolt spacing plays the most critical role in predicting ultimate load. Table 6-11 indicated the order of each input and their effect based on the combination participation. After the mentioned process, the model with 150 iterations and 250 populations has been selected, and the results of the prediction were tabulated in Table 6-12. As mentioned earlier, this technique does not require

testing all possible combinations, and it is sufficient to test only once for each set of n members. For example, if we want to determine the best combination of inputs with four members, we run the network only once and set the value of nf to five, and the network of 6 inputs that has the most impact on the answer is selected. As shown in Table 6-12, the results are almost identical for two to four inputs, while the five inputs represented a noticeable accuracy compared to other combinations.

Table 6-11: Selected input composition based on feature-selection method for load case.

Feature	Number of inputs				
	1	2	3	4	5
Length	X			X	X
Bolt spacing		X	X	X	X
Thickness			X	X	X
Shape factor ($A_g \times \sigma_y$)				X	X
Displacement		X	X		X

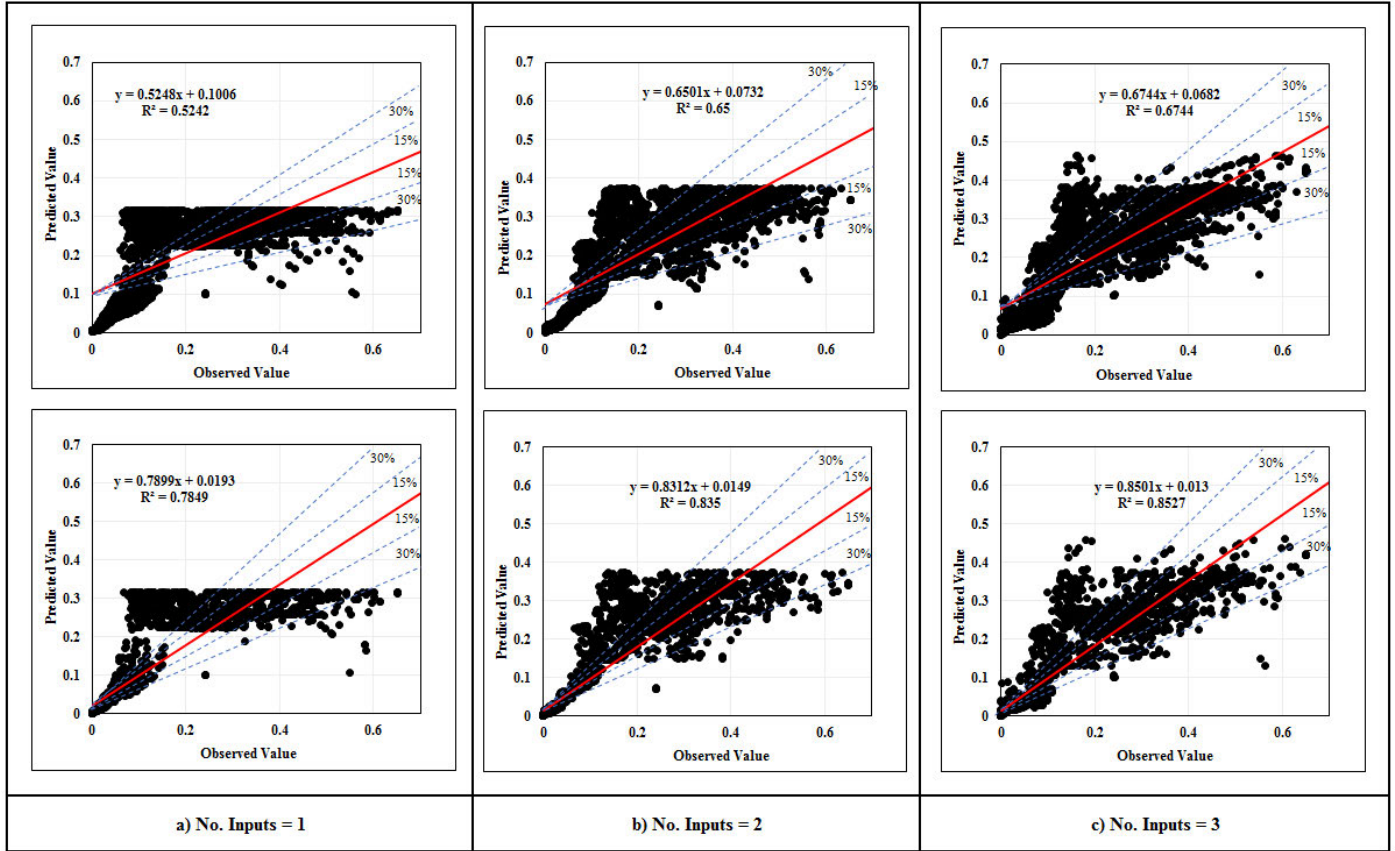
Table 6-12: Calculated accuracy criteria for the performance of the implemented models (Iteration = 150).

Train								
The MPF network								
Iteration	Population	nf	R ²	R	NS	RMSE	MAE	WI
150	250	1	0.524	0.709	0.011	1.966	1.386	0.816
150	250	2	0.650	0.796	0.422	1.672	1.121	0.879
150	250	3	0.674	0.812	0.484	1.620	1.148	0.890
150	250	4	0.683	0.818	0.503	1.575	1.125	0.894
150	250	5*	0.847	0.820	0.511	1.590	1.137	0.895
Test								
The MPF network								
Iteration	Population	nf	R ²	R	NS	RMSE	MAE	WI

150	250	1	0.785	0.697	-0.034	1.984	1.400	0.809
150	250	2	0.835	0.782	0.357	1.762	1.189	0.869
150	250	3	0.853	0.806	0.464	1.655	1.159	0.886
150	250	4	0.812	0.822	0.489	1.639	1.163	0.894
150	250	5*	0.907	0.800	0.435	1.678	1.203	0.882

*the most precise predicted value in comparison to the measured value

In Table 6-11, the composition of parameters in the order of feature-selection decision is indicated in which the bolt spacing is shown in most of the input groups, while the shape factor has the lowest participation. Figure 6-24 indicates the result of the MPF models in the prediction of the ultimate load. Predicting the load faced more challenges rather than displacement prediction. Figure 6-24 illustrates the training and testing phase of the MPF model with 150 times of iteration. Upper regressions present the training phase, and the lower ones present the test phase, and by looking at Figure 6-24(a) to (e) difference between the qualities of the prediction is obvious. The best achieved result is related to the model with 5 inputs along 150 iteration and 250 population including $R^2= 0.907$, $r= 0.8$, $NS= 0.435$, $MAE= 1.203$, $RMSE= 1.678$ and $WI= 0.882$ in the test phase and the same values in the train phase with acceptable variation. RMSE and MAE are both more than 1 with 0.28% as tolerance which indicates the same behaviour of the predicted data around the standard deviation. Except for the NS value, other evaluation criteria have proven the reliability of prediction and the neural network. According to Figure 6-24 and Table 6-12, employing the MPF network is conservative for upright ultimate axial load capacity prediction.



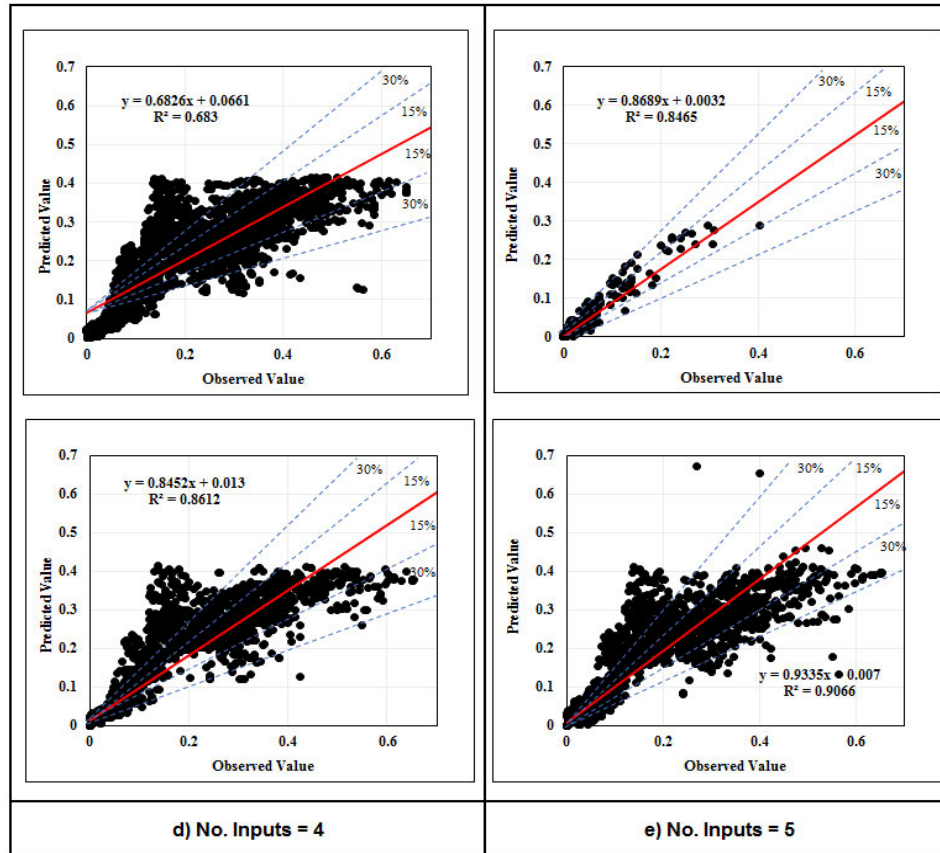


Figure 6-24: Regression of the train (above charts) and test (below charts) phase results with measured values of normalized load for (a) One input, (b) Two inputs, (c) Three inputs, (d) Four input, (e) Five inputs

Based on Figure 6-24 and Table 6-11, shape factor has the most effect on the normalised load prediction. The capability of the models in the prediction of each test sample is shown in Figure 6-25. A highly close prediction of the models and better performance of the MPF model is evident in this figure.

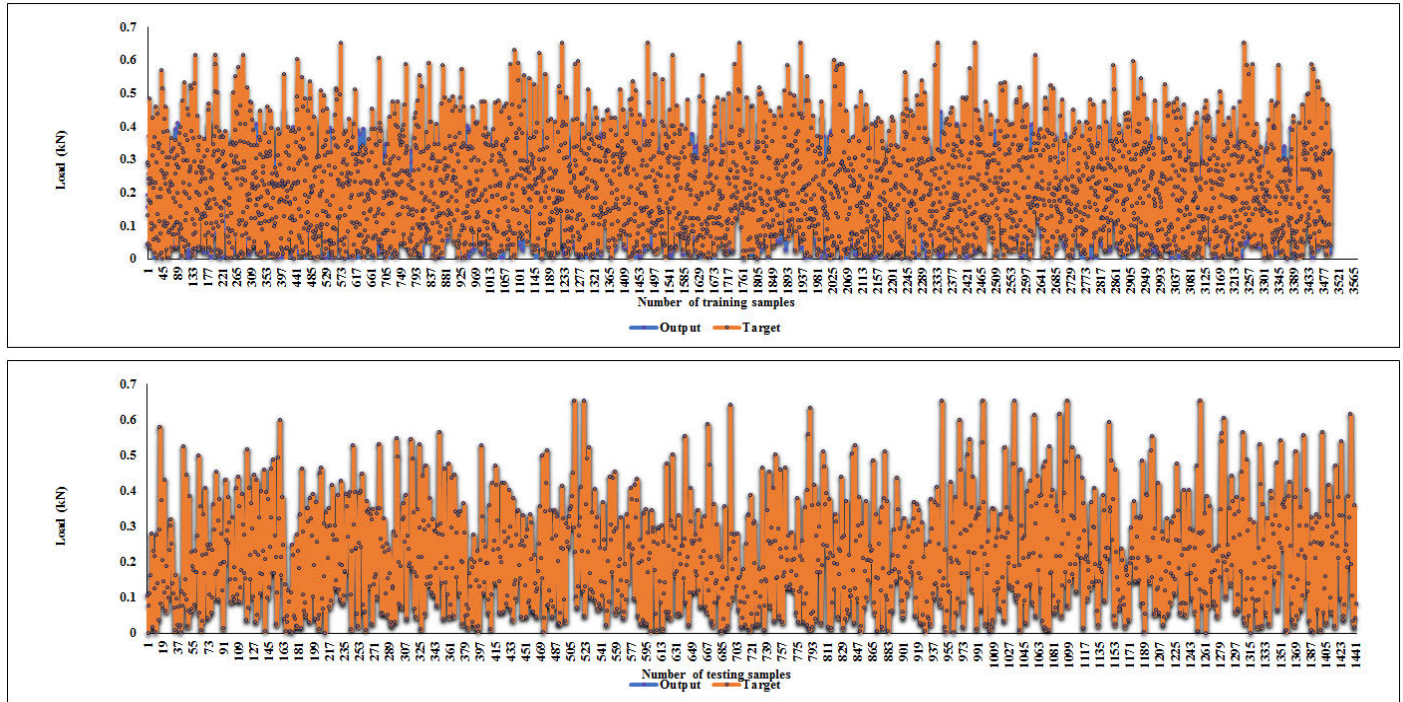


Figure 6-25: The MPF (five inputs) prediction vs experimental diagram: (above) train phase, (bellow) test phase

As shown in Table 6-11 and Figure 6-25, the best performance parameters for the MPF neural network are $RMSE = 1.678$, $r = 0.800$, $R^2 = 0.861$, $NS = 0.435$, $MAE = 1.203$, $WI = 0.882$. Considering that the best result for RMSE is the nominal value and for r the best positive correlation coefficient is 1, then numbers closer to 1 are considered better results. Also, for higher numbers, R^2 shows a suitable regression diagram. In addition, for NS and MAE, smaller results indicate better performance. Figure 6-26 represented the error histogram for the best load estimation by the developed neural network and proven the acceptable error range in both train and test phase with a similar convergence pattern.

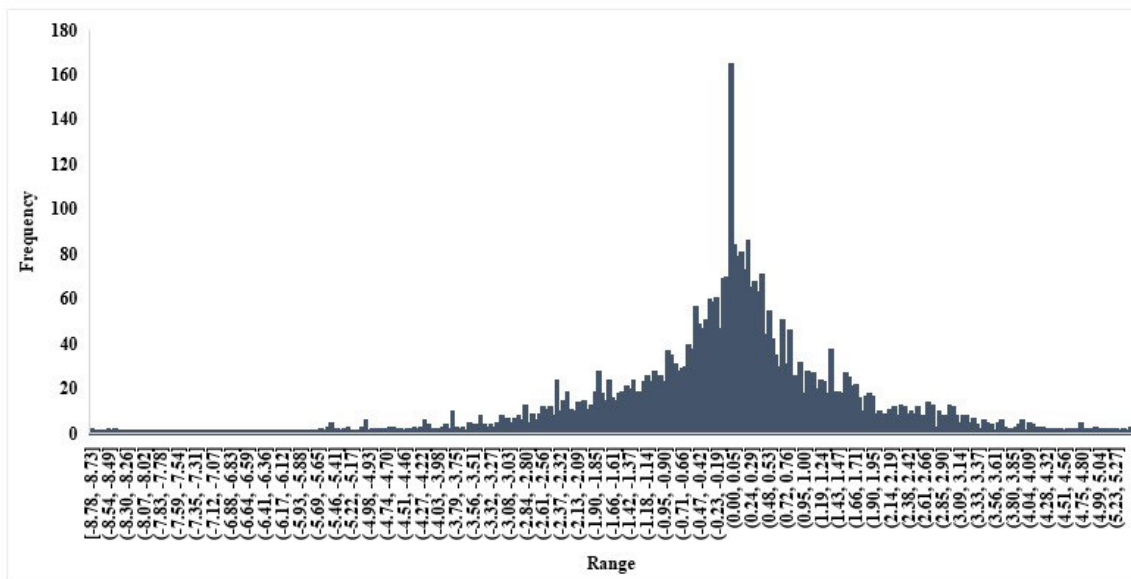
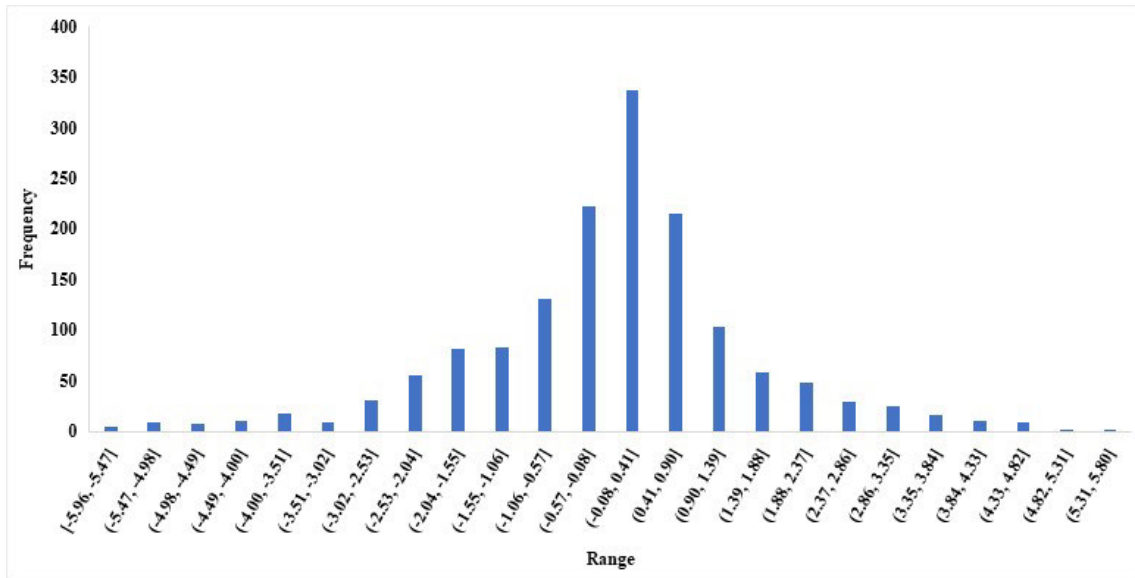


Figure 6-26: The MPF (five inputs) Error histograms: (above) train phase, (below) test phase

6.7. Conclusion

Uprights in racking systems typically deal with axial load or compressive forces, which may become a problem for the stability of these structures. On the other hand, strengthening the

upright frames is a controversial subject for researchers to choose an optimum approach for reinforcing them and finding the cost-effective and low time-consuming way. In this study, a new reinforcement system in the CFS upright frames has been investigated by numerical approaches. In this study for the first time feature-selection technique has used to select the best possible input composition and identify the most effective parameter in the prediction of load-displacement results. First, FE models in ABAQUS software were created and verified by the test results. Therefore, models with different thicknesses, lengths, and reinforcement spacing were finally compared to define the system's performance. secondly, in order to predict the FE results a new combination of intelligence methods has been developed by integrating the evolutionary feature-selection technique with neural network and particle swarm optimisation. The MPF network has been used to predict significant characteristics, including ultimate axial load and displacement. The feature selection technique is applied to avoid trying all possible input modes and wasting time. On the other hand, it provides the best possible input combination that may be overlooked in other methods. The dataset used contains 10511 rows of experimental data, which included different inputs. FE results have been successfully validated by linear regression and MPF results.

- According to the FE results, using reinforcement more closely has increased ultimate load capacity among all models, especially in models with 1.6 mm thickness. By comparing the thicknesses, the model with 2.5 mm thickness presented the most load capacity increase among other thicknesses. The model with 1800 mm length and 50 mm spacing represented the most capacity among other models. Models with 3600 mm length were preformed more ductile behaviour in comparison with other models.
- Neural network prediction revealed a harmonious relation between load and displacement. Results of the MPF algorithms in the displacement prediction phase represented that the model's prediction with 45 iterations and 250 population is better than others. Five inputs combination represented the best prediction of the upright displacement with the best performance parameters including $RMSE = 0.001$, $r = 1.000$, $R^2 = 0.999$, $NS = 1.000$, $MAE = 0$, $WI = 1.000$. In the case of load prediction, the model with 150 iterations, 250 population and five input combination predicted the most accurate values along best precision values including $RMSE = 1.678$, $r = 0.800$, $R^2 = 0.907$, $NS = 0.435$, $MAE = 1.203$, $WI = 0.882$.

Finally, the new reinforcing system has been successfully investigated throughout the present study. The models with 1800 and 2400 mm length and 2.5 mm thickness performed more efficiently than others; however, all simulated lengths and thicknesses represented relevant results. As a suggestion for further studies, other types of Intelligence approaches could be investigated to predict and optimise other specifications of cold-formed structures.

6.8. References

1. Taheri, E.; Firouzianhaji, A.; Mehrabi, P.; Hosseini, B.V.; Samali, B. Experimental and numerical investigation of a method for strengthening cold-formed steel profiles in bending. *Applied Sciences* **2020**, *10*, 3855.
2. Firouzianhaji, A.; Usefi, N.; Samali, B.; Mehrabi, P. Shake Table Testing of Standard Cold-Formed Steel Storage Rack. *Applied Sciences* **2021**, *11*, 1821.
3. Zhang, W.; Tang, Z.; Yang, Y.; Wei, J.; Stanislav, P. Mixed-Mode Debonding Behavior between CFRP Plates and Concrete under Fatigue Loading. *Journal of Structural Engineering* **2021**, *147*, 04021055.
4. Sun, L.; Li, C.; Zhang, C.; Su, Z.; Chen, C. Early monitoring of rebar corrosion evolution based on FBG sensor. *International Journal of Structural Stability and Dynamics* **2018**, *18*, 1840001.
5. Yang, N.; Bai, F. Damage analysis and evaluation of light steel structures exposed to wind hazards. *Applied Sciences* **2017**, *7*, 239.
6. Sharafi, P.; Mortazavi, M.; Usefi, N.; Kildashti, K.; Ronagh, H.; Samali, B. Lateral force resisting systems in lightweight steel frames: Recent research advances. *Thin-Walled Structures* **2018**, *130*, 231-253.
7. Fanaie, N.; Tahriri, M. Stability and stiffness analysis of a steel frame with an oblique beam using method of least work. *Journal of Constructional Steel Research* **2017**, *137*, 342-357.
8. Zhao, X.; Chen, B.; Li, Y.; Zhu, W.; Nkiegaing, F.; Shao, Y. Forced vibration analysis of Timoshenko double-beam system under compressive axial load by means of Green's functions. *Journal of Sound and Vibration* **2020**, *464*, 115001.
9. Zhao, X.; Zhu, W.; Li, Y. Analytical solutions of nonlocal coupled thermoelastic forced vibrations of micro/nano-beams by means of Green's functions. *Journal of Sound and Vibration* **2020**, *481*, 115407.
10. Niu, Z.; Zhang, B.; Li, D.; Ji, D.; Liu, Y.; Feng, Y.; Zhou, T.; Zhang, Y.; Fan, Y. A mechanical reliability study of 3-dB waveguide hybrid couplers in submillimeter and terahertz bands. *Frontiers of Information Technology & Electronic Engineering* **2021**, *22*, 1104-1113.
11. Javidan, M.M.; Kang, H.; Isobe, D.; Kim, J. Computationally efficient framework for probabilistic collapse analysis of structures under extreme actions. *Engineering Structures* **2018**, *172*, 440-452.
12. Ahmadi, R.; Rashidian, O.; Abbasnia, R.; Mohajeri Nav, F.; Usefi, N. Experimental and numerical evaluation of progressive collapse behavior in scaled RC beam-column subassembly. *Shock and Vibration* **2016**, *2016*.
13. Shayanfar, M.A.; Javidan, M.M. Progressive collapse-resisting mechanisms and robustness of RC frame-shear wall structures. *Journal of Performance of Constructed Facilities* **2017**, *31*, 04017045.
14. Javidan, M.M.; Kim, J. Variance-based global sensitivity analysis for fuzzy random structural systems. *Computer-Aided Civil and Infrastructure Engineering* **2019**, *34*, 602-615.
15. Fanaie, N.; Kazerani, S.; Soroushnia, S. Numerical study of slotted web drilled flange moment frame connection. *International Journal of Numerical Methods in Civil Engineering* **2017**, *1*, 16-23.
16. Shariati, M.; Tahmasbi, F.; Mehrabi, P.; Bahadori, A.; Toghroli, A. Monotonic behavior of C and L shaped angle shear connectors within steel-concrete composite beams: an experimental investigation. *Steel Compos Struct* **2020**, *35*, 237-247.
17. Koen, D.J. Structural capacity of light gauge steel storage rack uprights. University of Sydney., 2008.

18. Davies, J.M.; Leach, P.; Taylor, A. The design of perforated cold-formed steel sections subject to axial load and bending. *Thin-walled structures* **1997**, *29*, 141-157.
19. Trouncer, A.; Rasmussen, K. Flexural–torsional buckling of ultra light-gauge steel storage rack uprights. *Thin-walled structures* **2014**, *81*, 159-174.
20. Standard, B. Steel static storage systems—Adjustable pallet racking systems—Principles for structural design. *Bs En* **2009**, *15512*, 15512.
21. Gilbert, B.P.; Rasmussen, K.J. Bolted moment connections in drive-in and drive-through steel storage racks. *Journal of Constructional Steel Research* **2010**, *66*, 755-766.
22. Dinis, P.B.; Young, B.; Camotim, D. Strength, interactive failure and design of web-stiffened lipped channel columns exhibiting distortional buckling. *Thin-Walled Structures* **2014**, *81*, 195-209.
23. Roure, F.; Pastor, M.; Casafont, M.; Somalo, M. Stub column tests for racking design: Experimental testing, FE analysis and EC3. *Thin-walled structures* **2011**, *49*, 167-184.
24. Casafont, M.; Pastor, M.M.; Roure, F.; Peköz, T. An experimental investigation of distortional buckling of steel storage rack columns. *Thin-Walled Structures* **2011**, *49*, 933-946.
25. Lu, D.; Yu-ting, Z.; Yuan-liang, Y.; Yan-zhi, L. Optimization on bearing capacity and ductility of cold-formed thin-walled steel flexural member. *工程力学* **2021**, *38*, 93-101.
26. Phan, D.T.; Mojtabaei, S.M.; Hajirasouliha, I.; Lau, T.; Lim, J.B. Design and optimization of cold-formed steel sections in bolted moment connections considering bimoment. *Journal of Structural Engineering* **2020**, *146*, 04020153.
27. Phan, D.T.; Mojtabaei, S.M.; Hajirasouliha, I.; Ye, J.; Lim, J.B. Coupled element and structural level optimisation framework for cold-formed steel frames. *Journal of Constructional Steel Research* **2020**, *168*, 105867.
28. Mojtabaei, S.M.; Hajirasouliha, I.; Becque, J. Optimized Design of Cold-Formed Steel Elements for Serviceability and Ultimate Limit States. *ce/papers* **2021**, *4*, 481-486.
29. Shariati, M.; Trung, N.-T.; Wakil, K.; Mehrabi, P.; Safa, M.; Khorami, M. Moment-rotation estimation of steel rack connection using extreme learning machine. *STEEL AND COMPOSITE STRUCTURES* **2019**, *31*, 427-435, doi:<https://doi.org/10.12989/scs.2019.31.5.427>.
30. Shariati, M.; Mafipour, M.S.; Mehrabi, P.; Shariati, A.; Togholi, A.; Trung, N.T.; Salih, M.N. A novel approach to predict shear strength of tilted angle connectors using artificial intelligence techniques. *Engineering with Computers* **2020**, 1-21.
31. Togholi, A.; Mehrabi, P.; Shariati, M.; Trung, N.T.; Jahandari, S.; Rasekh, H. Evaluating the use of recycled concrete aggregate and pozzolanic additives in fiber-reinforced pervious concrete with industrial and recycled fibers. *Construction and Building Materials* **2020**, *252*, 118997.
32. Shariati, M.; Faegh, S.S.; Mehrabi, P.; Bahavarnia, S.; Zandi, Y.; Masoom, D.R.; Togholi, A.; Trung, N.-T.; Salih, M.N. Numerical study on the structural performance of corrugated low yield point steel plate shear walls with circular openings. *Steel and Composite Structures* **2019**, *33*, 569-581.
33. Xu, C.; Zhang, X.; Haido, J.H.; Mehrabi, P.; Shariati, A.; Mohamad, E.T.; Nguyen, H.; Wakil, K. Using genetic algorithms method for the paramount design of reinforced concrete structures. *Structural Engineering and Mechanics* **2019**, *71*, 503-513, doi:<https://doi.org/10.12989/sem.2019.71.5.503>.
34. Li, X.; Yang, H.; Zhang, J.; Qian, G.; Yu, H.; Cai, J. Time-Domain Analysis of Tamper Displacement during Dynamic Compaction Based on Automatic Control. *Coatings* **2021**, *11*, 1092.
35. Armaghani, D.J.; Hasanipanah, M.; Amnieh, H.B.; Bui, D.T.; Mehrabi, P.; Khorami, M. Development of a novel hybrid intelligent model for solving engineering problems using GS-GMDH algorithm. *Engineering with Computers* **2019**, 1-13.
36. Guo, H.; Zhou, J.; Koopialipoor, M.; Armaghani, D.J.; Tahir, M. Deep neural network and whale optimization algorithm to assess flyrock induced by blasting. *Engineering with Computers* **2019**, 1-14.
37. Xiao, G.; Song, K.; He, Y.; Wang, W.; Zhang, Y.; Dai, W. Prediction and experimental research of abrasive belt grinding residual stress for titanium alloy based on analytical method. *The International Journal of Advanced Manufacturing Technology* **2021**, 1-15.
38. Mousavi, A.A.; Zhang, C.; Masri, S.F.; Gholipour, G. Structural damage detection method based on the complete ensemble empirical mode decomposition with adaptive noise: a model steel truss bridge case study. *Structural Health Monitoring* **2021**, 14759217211013535.
39. Xiang, G.; Zhang, Y.; Gao, X.; Li, H.; Huang, X. Oblique detonation waves induced by two symmetrical wedges in hydrogen-air mixtures. *Fuel* **2021**, *295*, 120615.
40. Ao, H.; Thoi, T.N.; Huu, V.H.; Anh-Le, L.; Nguyen, T.; Chau, M.Q. Backtracking Search Optimization Algorithm and its Application to Roller Bearing Fault Diagnosis. *The International Journal of Acoustics and*

- Vibration* **2016**, *21*, doi:10.20855/ijav.2016.21.4439.
41. Mi, C.; Huang, Y.; Fu, C.; Zhang, Z.; Postolache, O. Vision-Based Measurement: Actualities and Developing Trends in Automated Container Terminals. *IEEE Instrumentation & Measurement Magazine* **2021**, *24*, 65-76.
 42. Zhang, B.; Chen, Y.-X.; Wang, Z.-g.; Li, J.-Q.; Ji, H.-h. Influence of Mach Number of Main Flow on Film Cooling Characteristics under Supersonic Condition. *Symmetry* **2021**, *13*, 127.
 43. Shariati, M.; Mafipour, M.S.; Mehrabi, P.; Ahmadi, M.; Wakil, K.; Trung, N.T.; Togholi, A. Prediction of concrete strength in presence of furnace slag and fly ash using Hybrid ANN-GA (Artificial Neural Network-Genetic Algorithm). *Smart Structures and Systems* **2020**, *25*, 183.
 44. El-Kassas, E.; Mackie, R.; El-Sheikh, A. Using neural networks in cold-formed steel design. *Computers & Structures* **2001**, *79*, 1687-1696.
 45. Liu, C.; Gao, X.; Chi, D.; He, Y.; Liang, M.; Wang, H. On-line chatter detection in milling using fast kurtogram and frequency band power. *European Journal of Mechanics-A/Solids* **2021**, 104341.
 46. Yu, N.-t.; Kim, B.; Yuan, W.-b.; Li, L.-y.; Yu, F. An analytical solution of distortional buckling resistance of cold-formed steel channel-section beams with web openings. *Thin-Walled Structures* **2019**, *135*, 446-452.
 47. Gholami, A.; Bonakdari, H.; Zaji, A.H.; Akhtari, A.A. A comparison of artificial intelligence-based classification techniques in predicting flow variables in sharp curved channels. *Engineering with Computers* **2019**, 1-30.
 48. Paknahad, M.; Shariati, M.; Sedghi, Y.; Bazzaz, M.; Khorami, M. Shear capacity equation for channel shear connectors in steel-concrete composite beams. *Steel and Composite structures* **2018**, *28*, 483-494.
 49. Xiang, G.; Gao, X.; Tang, W.; Jie, X.; Huang, X. Numerical study on transition structures of oblique detonations with expansion wave from finite-length cowl. *Physics of Fluids* **2020**, *32*, 056108.
 50. Du, Y.; Pan, N.; Xu, Z.; Deng, F.; Shen, Y.; Kang, H. Pavement distress detection and classification based on YOLO network. *International Journal of Pavement Engineering* **2020**, 1-14.
 51. Shariati, M.; Mafipour, M.S.; Mehrabi, P.; Zandi, Y.; Dehghani, D.; Bahadori, A.; Shariati, A.; Trung, N.T.; Salih, M.N.; Poi-Ngian, S. Application of Extreme Learning Machine (ELM) and Genetic Programming (GP) to design steel-concrete composite floor systems at elevated temperatures. *Steel and Composite Structures* **2019**, *33*, 319-332.
 52. Shariati, M.M., M.S.; Mehrabi, P.; Bahadori, A.; Zandi, Y.; Salih, M.N.A.; Nguyen, H.; Dou, J.; Song, X.; Poi-Ngian, S. . Application of a Hybrid Artificial Neural Network-Particle Swarm Optimization (ANN-PSO) Model in Behavior Prediction of Channel Shear Connectors Embedded in Normal and High-Strength Concrete. *Applied Sciences* **2019**, *9*, 55-34, doi:<https://doi.org/10.3390/app9245534>.
 53. Perera, R.; Varona, F.B. Flexural and shear design of FRP plated RC structures using a genetic algorithm. *Journal of structural engineering* **2009**, *135*, 1418-1429.
 54. Shahgoli, A.F.; Zandi, Y.; Heirati, A.; Khorami, M.; Mehrabi, P.; Petkovic, D. Optimisation of propylene conversion response by neuro-fuzzy approach. *International Journal of Hydromechatronics* **2020**, *3*, 228-237.
 55. Yadollahpour, A.; Nourozi, J.; Mirbagheri, S.A.; Simancas-Acevedo, E.; Trejo-Macotela, F.R. Designing and implementing an ANFIS based medical decision support system to predict chronic kidney disease progression. *Frontiers in physiology* **2018**, *9*, 1753.
 56. Özkan, A.O.; Kara, S.; Salli, A.; Sakarya, M.E.; Güneş, S. Medical diagnosis of rheumatoid arthritis disease from right and left hand Ulnar artery Doppler signals using adaptive network based fuzzy inference system (ANFIS) and MUSIC method. *Advances in Engineering Software* **2010**, *41*, 1295-1301.
 57. Al-Qaness, M.A.; Ewees, A.A.; Fan, H.; Abd El Aziz, M. Optimization method for forecasting confirmed cases of COVID-19 in China. *Journal of Clinical Medicine* **2020**, *9*, 674.
 58. Mehrabi, P.; Honarbari, S.; Rafiei, S.; Jahandari, S.; Alizadeh Bidgoli, M. Seismic response prediction of FRC rectangular columns using intelligent fuzzy-based hybrid metaheuristic techniques. *Journal of Ambient Intelligence and Humanized Computing* **2021**, doi:10.1007/s12652-020-02776-4.
 59. Feng, Y.; Mohammadi, M.; Wang, L.; Rashidi, M.; Mehrabi, P. Application of Artificial Intelligence to Evaluate the Fresh Properties of Self-Consolidating Concrete. *Materials* **2021**, *14*, 4885.
 60. Taheri, E.; Firouzianhaji, A.; Usefi, N.; Mehrabi, P.; Ronagh, H.; Samali, B. Investigation of a method for strengthening perforated cold-formed steel profiles under compression loads. *Applied Sciences* **2019**, *9*, 5085.
 61. Nash, J.E.; Sutcliffe, J.V. River flow forecasting through conceptual models part I—A discussion of principles. *Journal of hydrology* **1970**, *10*, 282-290.
 62. Taheri, E.; Esgandarzadeh Fard, S.; Zandi, Y.; Samali, B. Experimental and Numerical Investigation of an Innovative Method for Strengthening Cold-Formed Steel Profiles in Bending throughout Finite Element

Modeling and Application of Neural Network Based on Feature Selection Method. *Applied Sciences* **2021**, *11*, 5242.

7. Conclusion and Future Works

In this research, the influence of a novel reinforcement technique was investigated on the axial and flexural behaviour of upright frames. Extensive axial tests were performed on 72 upright frames and nine single uprights with various heights and thicknesses, and then the obtained results were examined. In the suggested reinforcement system, bolts and spacers were attached along the upright height. Laboratory results indicated that once the distortional buckling failure mode governs, the reinforcement system is considerably influential in improving the load-bearing capacity. However, the applicability of this approach is not as effective for taller frames as for the shorter ones. This demonstrates that the proposed reinforcing technique has less influence on other buckling modes (flexural, torsional, flexural-torsional, and local) and mainly influences distortional buckling mode. Besides, thicker uprights had higher axial capacity enhancement when strengthened with bolts and spacers in comparison with thinner uprights. It was also found that as well as improving ultimate load capacity, the reinforcement had a substantial effect on the buckling failure mode of upright frames with low lengths (1200 mm, 1800 mm, and 2400 mm).

In order to examine the influence of the reinforcement approach on the flexural strength of CFS upright sections, several empirical tests were carried out. Eighteen samples were made, and experimental tests of standard monotonic four-point bending tests were conducted to assess their bending capacity. All the samples were built with perforated CFS uprights with 2400 mm length and 1.6 mm thickness. Samples without reinforcement and samples with reinforcement at 200 mm and 300 mm pitches were examined along both their minor and major axes direction, respectively. For the minor axis experiment, the samples comprised single uprights. However, for the major axis tests, the samples were made by combining two uprights as a frame using conventional diagonal bracing to retain the set-up stability for precise evaluation of the flexural strength of reinforced and unreinforced uprights. According to the obtained results, along both the minor axis and the major axis experiments, the governing failure modes were local, distortional and a combination of them. The bending moment capacity of samples increases using the proposed reinforcement as the half wavelength of sections changes. Compared with unreinforced samples, the ultimate flexural capacity using reinforcement at 200 mm pitches is improved by about 13.8% and 17% along major axis and minor axis experiments, respectively. At pitches of 300 mm, the bending moment capacity of reinforced samples, compared with unreinforced ones for the major axis and minor

axis tests increase by about 6.97% and 5.5%, respectively. It was deduced that the flexural performance of all open CFS sections could be improved using the considered reinforcement as a highly beneficial and economical method.

In addition, in this study, FEM models were developed in ABAQUS platform and validated by experimental results to examine the performance of CFS upright frames strengthened by the reinforcement technique under axial and flexural loads. Later, in a parametric study, the axial and flexural behaviour of uprights with various thicknesses, lengths and reinforcement spacings were modelled and assessed. The results of FEM utilising ABAQUS showed that with closer reinforcements, the models demonstrate a stiffened behaviour as expected. It was also shown that FEM could simulate the structural performance of the CFS section.

Moreover, a feature-selection method was employed for determining the best input composition and identifying the most influential factor in predicting the results of load-displacement. Also, the evolutionary feature-selection technique was integrated with neural network and particle swarm optimisation to develop the new hybrid intelligent models, which were used for data prediction. In order to predict the important characteristics, such as ultimate axial and flexural load and displacement, the MPF network was employed. The feature selection method was deployed to reduce the processing time and avoid trying all possible input modes. On the other hand, this technique is able to provide the best combination of input that might be ignored in other approaches. The considered database includes series of laboratory and FEM data with various inputs. The results of FEM modellings were verified successfully by linear regression and MPF results.

In the end, the new reinforcing technique was successfully investigated in the current research. The performance of models with 1800 and 2400 mm lengths was better than other ones, but all lengths and thicknesses presented improved outcomes. Besides, by using the developed neural network, the FEM results were verified, and considerable precision in predicting the load and displacement was observed.

In future investigations, other type of CFS sections could be considered for experimental and numerical evaluations. Developing other types of AI algorithms is also suggested to predict and estimate other characteristics of CFS systems. In order to have a better understanding of the

performance of open perforated profiles strengthened with bolts and spacers, and other reinforcements methods, more experimental and numerical studies should be performed. Also, the FEM is required for a parametric evaluation of various types of reinforcement techniques.

8. References

Abaqus, V. *6.14 Documentation*; Dassault Systemes Simulia Corporation: Johnston, RI, USA **2014**; Volume 651.

Ahmadi, R.; Rashidian, O.; Abbasnia, R.; Mohajeri Nav, F.; Usefi, N. Experimental and numerical evaluation of progressive collapse behavior in scaled RC beam-column subassemblage. *Shock and Vibration* **2016**, *2016*.

Ahmadi, R.; Rashidian, O.; Abbasnia, R.; Nav, F.M.; Usefi, N. Experimental and numerical evaluation of progressive collapse behavior in scaled RC beam-column subassemblage. *Shock Vib.* **2016**, *2016*, Article ID 3748435.

Al-Musawi, A.A.; Alwanas, A.A.H.; Salih, S.Q.; Ali, Z.H.; Tran, M.T.; Yaseen, Z.M. Shear strength of SFRCB without stirrups simulation: implementation of hybrid artificial intelligence model. *Eng. Comput.* **2020**, *36*, 1–11.

Al-Qaness, M.A.; Ewees, A.A.; Fan, H.; Abd El Aziz, M. Optimization method for forecasting confirmed cases of COVID-19 in China. *Journal of Clinical Medicine* **2020**, *9*, 674.

Anbarasu, M.; Amali, D.; Sukumar, S. New approach to improve the distortional strength of intermediate length web stiffened thin walled open columns. *KSCE J. Civ. Eng.* **2013**, *17*, 1720–1727.

Anbarasu, M.; Kumar, S.B.; Sukumar, S. Study on the effect of ties in the intermediate length cold formed steel (CFS) columns. *Struct. Eng. Mech.* **2013**, *46*, 323–335.

Anbarasu, M.; Sukumar, S. Effect of connectors interaction in behaviour and ultimate strength of intermediate length cold formed steel open columns. *Asian J. Civ. Eng. (BHRC)* **2013**, *14*, 305–317.

Anbarasu, M.; Sukumar, S. Finite Element-Based Investigation on Performance of Intermediate Length Thin-walled Columns with Lateral Stiffeners. *Arab. J. Sci. Eng.* **2014**, *39*, 6907–6917.

Anbarasu, M.; Sukumar, S. Influence of Spacers on Ultimate Strength of Intermediate Length Thin walled Columns. *Steel Compos. Struct. Int. J.* **2014**, *16*, 437–454.

Ao, H.; Thoi, T.N.; Huu, V.H.; Anh-Le, L.; Nguyen, T.; Chau, M.Q. Backtracking Search Optimization Algorithm and its Application to Roller Bearing Fault Diagnosis. *The International Journal of Acoustics and Vibration* **2016**, *21*, doi:10.20855/ijav.2016.21.4439.

Armaghani, D.J.; Hasanipanah, M.; Amnieh, H.B.; Bui, D.T.; Mehrabi, P.; Khorami, M. Development of a novel hybrid intelligent model for solving engineering problems using GS-GMDH algorithm. *Engineering with Computers* **2019**, 1-13.

AS 4084. *Steel Storage Racking*; Standards Australia: Sydney, Australia, 2012.

Baldassino, N.; Hancock, G. Distortional Buckling of Cold-Formed Steel Storage Rack Section including Perforations. In Proceedings of the 4th International Conference on Steel and Aluminum Structures, Espoo, Finland, 20-23 June 1999.

Broomhead, D.S.; Lowe, D. *Radial Basis Functions, Multi-Variable Functional Interpolation and Adaptive Networks*; Royal Signals and Radar Establishment Malvern: Worcestershire, UK, 1998; RSRE-MEMO-4148.

Calderoni, B.; De Martino, A.; Formisano, A.; Fiorino, L. Cold formed steel beams under monotonic and cyclic loading: Experimental investigation. *J. Constr. Steel Res.* **2009**, *65*, 219–227, doi:10.1016/j.jcsr.2008.07.014.

Cardoso, F.S.; Rasmussen, L.J. Finite element (FE) modelling of storage rack frames. *J. Constr. Steel Res.* **2016**, *126*, 1–14, doi:10.1016/j.jcsr.2016.06.015.

Casafont, M.; Pastor, M.M.; Roure, F.; Peköz, T. An experimental investigation of distortional buckling of steel storage rack columns. *Thin-Walled Structures* **2011**, *49*, 933-946.

Chen, C.; Shi, L.; Shariati, M.; Toghroli, A.; Mohamad, E.T.; Bui, D.T.; Khorami, M. Behavior of steel storage pallet racking connection—A review. *Steel Compos. Struct.* **2019**, *30*, 457–469, doi:10.31224/osf.io/jzdpq.

Chu, X.-T.; Kettle, R.; Li, L.-Y. Lateral-torsion buckling analysis of partial-laterally restrained thin-walled channel-section beams. *J. Constr. Steel Res.* **2004**, *60*, 1159–1175, doi:10.1016/j.jcsr.2003.11.001.

Dai, L.; Zhao, X.; Rasmussen, L.J. Flexural behaviour of steel storage rack beam-to-upright bolted connections. *Thin Walled Struct.* **2018**, *124*, 202–217, doi:10.1016/j.tws.2017.12.010.

Davies, J.M.; Leach, P.; Taylor, A. The design of perforated cold-formed steel sections subject to axial load and bending. *Thin-walled structures* **1997**, *29*, 141-157.

Dinis, P.B.; Young, B.; Camotim, D. Strength, interactive failure and design of web-stiffened lipped channel columns exhibiting distortional buckling. *Thin-Walled Structures* **2014**, *81*, 195-209.

Du, Y.; Pan, N.; Xu, Z.; Deng, F.; Shen, Y.; Kang, H. Pavement distress detection and classification based on YOLO network. *International Journal of Pavement Engineering* **2020**, 1-14.

El-Kassas, E.; Mackie, R.; El-Sheikh, A. Using neural networks in cold-formed steel design. *Computers & Structures* **2001**, *79*, 1687-1696.

Fanaie, N.; Kazerani, S.; Soroushnia, S. Numerical study of slotted web drilled flange moment frame connection. *International Journal of Numerical Methods in Civil Engineering*

2017, 1, 16-23.

Fanaie, N.; Tahriri, M. Stability and stiffness analysis of a steel frame with an oblique beam using method of least work. *Journal of Constructional Steel Research* **2017**, *137*, 342-357.

Feng, Y.; Mohammadi, M.; Wang, L.; Rashidi, M.; Mehrabi, P. Application of Artificial Intelligence to Evaluate the Fresh Properties of Self-Consolidating Concrete. *Materials* **2021**, *14*, 4885.

Firouzianhaji, A. The Effect of Connection Flexibility on the Seismic Performance of Industrial Racking Systems. Ph.D. Thesis, UTS, Sydney, Australia, 2016.

Firouzianhaji, A.; Usefi, N.; Samali, B.; Mehrabi, P. Shake Table Testing of Standard Cold-Formed Steel Storage Rack. *Appl. Sci.* **2021**, *11*, 1821, doi:10.3390/app110418214.

Gholami, A.; Bonakdari, H.; Zaji, A.H.; Akhtari, A.A. A comparison of artificial intelligence-based classification techniques in predicting flow variables in sharp curved channels. *Engineering with Computers* **2019**, 1-30.

Gilbert, B.P.; Rasmussen, K.J.R. Bolted moment connections in drive-in and drive-through steel storage racks. *J. Constr. Steel Res.* **2010**, *66*, 755–766.

Gilbert, B.P.; Savoyat, T.J.M.; Teh, L.H. Self-shape optimisation application: Optimisation of cold-formed steel columns. *Thin Walled Struct.* **2012**, *60*, 173–184.

Guo, H.; Zhou, J.; Koopialipoor, M.; Armaghani, D.J.; Tahir, M. Deep neural network and whale optimization algorithm to assess flyrock induced by blasting. *Engineering with Computers* **2019**, 1-14.

Hancock, G. Design for distortional buckling of flexural members. *Thin Walled Struct.* **1997**, *27*, 3–12, doi:10.1016/0263-8231(96)00020-1.

Hancock, G.; Rogers, C. Design of cold-formed steel structures of high strength steel. *J. Constr. Steel Res.* **1998**, *46*, 167–168, doi:10.1016/s0143-974x(98)80013-8.

Hancock, G.J. Design of Cold-formed Steel Structures: To Australian/New Zealand Standard AS/NZS 4600: **1996**; *Institute of Steel Construction*: Sydney, Australian, 1998.

Hornik, K.; Stinchcombe, M.; White, H. Multilayer feedforward networks are universal approximators. *Neural Netw.* **1989**, *2*, 359–366.

Huang, X.; Yang, J.; Liu, Q.-F.; Zhu, J.; Bai, L.; Wang, F.-L.; Wang, J.-H. A simplified flange–lip model for distortional buckling of cold-formed steel channel-sections with stiffened web. *Int. J. Mech. Sci.* **2018**, *136*, 451–459, doi:10.1016/j.ijmecsci.2017.12.034.

Javidan, M.M.; Kang, H.; Isobe, D.; Kim, J. Computationally efficient framework for probabilistic collapse analysis of structures under extreme actions. *Eng. Struct.* **2018**, *172*,

440–452.

Javidan, M.M.; Kang, H.; Isobe, D.; Kim, J. Computationally efficient framework for probabilistic collapse analysis of structures under extreme actions. *Engineering Structures* **2018**, *172*, 440–452.

Javidan, M.M.; Kim, J. Variance-based global sensitivity analysis for fuzzy random structural systems. *Comput. Aided Civ. Infrastruct. Eng.* **2019**, *34*, 602–615.

Kasaeian, S.; Usefi, N.; Ronagh, H.; Dareshiry, S. Seismic performance of CFS strap-braced walls using capacity-based design approach. *J. Constr. Steel Res.* **2020**, *174*, 106317.

Kaveh, A.; Vaez, S.H.; Hosseini, P. Simplified dolphin echolocation algorithm for optimum design of frame. *Smart Struct. Syst.* **2018**, *21*, 321–333.

Kaveh, A.; Vaez, S.R.H.; Hosseini, P.; Fathali, M.A. A New Two-Phase Method for Damage Detection in Skeletal Structures. *Iran. J. Sci. Technol. Trans. Civ. Eng.* **2019**, *43*, 49–65.

Keshtegar, B.; Bagheri, M.; Yaseen, Z.M. Shear strength of steel fiber-unconfined reinforced concrete beam simulation: Application of novel intelligent model. *Compos. Struct.* **2019**, *212*, 230–242.

Koen, D.J. Structural capacity of light gauge steel storage rack uprights. University of Sydney., 2008.

Koopialipour, M.; Fahimfar, A.; Ghaleini, E.; Momenzadeh, M.; Jahed Armaghani, D. Development of a new hybrid ANN for solving a geotechnical problem related to tunnel boring machine performance. *Eng. Comput.* **2020**, *36*, 1–13.

Laím, L.; Rodrigues, J.P.; Da Silva, L.S. Experimental and numerical analysis on the structural behaviour of cold-formed steel beams. *Thin Walled Struct.* **2013**, *72*, 1–13, doi:10.1016/j.tws.2013.06.008.

Lakusic, S.; Usefi, N.; Nav, F.M.; Abbasnia, R. Finite element analysis of RC elements in progressive collapse scenario. *J. Croat. Assoc. Civ. Eng.* **2016**, *68*, 1009–1022, doi:10.14256/JCE.1550.2016.

Li, X.; Yang, H.; Zhang, J.; Qian, G.; Yu, H.; Cai, J. Time-Domain Analysis of Tamper Displacement during Dynamic Compaction Based on Automatic Control. *Coatings* **2021**, *11*, 1092.

Liao, X.; Khandelwal, M.; Yang, H.; Koopialipour, M.; Murlidhar, B.R. Effects of a proper feature selection on prediction and optimization of drilling rate using intelligent techniques. *Eng. Comput.* **2020**, *36*, 499–510.

Liu, C.; Gao, X.; Chi, D.; He, Y.; Liang, M.; Wang, H. On-line chatter detection in milling using fast kurtogram and frequency band power. *European Journal of Mechanics-A/Solids* **2021**, 104341.

Lu, D.; Yu-ting, Z.; Yuan-liang, Y.; Yan-zhi, L. Optimization on bearing capacity and ductility of cold-formed thin-walled steel flexural member. *工程力学* **2021**, *38*, 93-101.

Majidi, L.; Usefi, N.; Abbasnia, R. Numerical study of RC beams under various loading rates with LS-DYNA. *J. Central South Univ.* **2018**, *25*, 1226–1239, doi:10.1007/s11771-018-3820-x.

Manikandan, P.; Arun, N. Behaviour of Partially Closed Stiffened Cold-Formed Steel Compression Member. *Arab. J. Sci. Eng.* **2016**, *41*, 3865–3875.

Mehrabi, P.; Honarbari, S.; Rafiei, S.; Jahandari, S.; Alizadeh Bidgoli, M. Seismic response prediction of FRC rectangular columns using intelligent fuzzy-based hybrid metaheuristic techniques. *J. Ambient Intell. Humaniz. Comput.* **2021**, 1–19, doi:10.1007/s12652-020-02776-4.

Mehrabi, P.; Shariati, M.; Kabirifar, K.; Jarrah, M.; Rasekh, H.; Thoi Trung, N.; Shariati, A.; Jahandari, S. Effect of pumice powder and nano-clay on the strength and permeability of fiber-reinforced pervious concrete incorporating recycled concrete aggregate. *Constr. Build. Mater.* **2021**, *287*, 122652.

Mi, C.; Huang, Y.; Fu, C.; Zhang, Z.; Postolache, O. Vision-Based Measurement: Actualities and Developing Trends in Automated Container Terminals. *IEEE Instrumentation & Measurement Magazine* **2021**, *24*, 65-76.

Michael Davies, J.; Leach, P.; Taylor, A. The design of perforated cold-formed steel sections subject to axial load and bending. *Thin-Walled Struct.* **1997**, *29*, 141–157.

Moen, C.D.; Schafer, B. Elastic buckling of cold-formed steel columns and beams with holes. *Eng. Struct.* **2009**, *31*, 2812–2824, doi:10.1016/j.engstruct.2009.07.007.

Moen, C.D.; Schafer, B.W. Experiments on cold-formed steel columns with holes. *Thin-Walled Struct.* **2008**, *46*, 1164–1182.

Mojtabaei, S.M.; Hajirasouliha, I.; Becque, J. Optimized Design of Cold-Formed Steel Elements for Serviceability and Ultimate Limit States. *ce/papers* **2021**, *4*, 481-486.

Mousavi, A.A.; Zhang, C.; Masri, S.F.; Gholipour, G. Structural damage detection method based on the complete ensemble empirical mode decomposition with adaptive noise: a model steel truss bridge case study. *Structural Health Monitoring* **2021**, 14759217211013535.

Muftah, F.; Sani, M.S.H.M.; Kamal, M.M.M. Flexural Strength Behaviour of Bolted Built-Up Cold-Formed Steel Beam with Outstand and Extended Stiffener. *Int. J. Steel Struct.* **2018**, *19*, 719–732, doi:10.1007/s13296-018-0157-0.

Nandini, P.; Kalyanaraman, V. Strength of cold-formed lipped channel beams under interaction of local, distortional and lateral torsional buckling. *Thin-Walled Struct.* **2010**, *48*, 872–877.

Nash, J.E.; Sutcliffe, J.V. River flow forecasting through conceptual models part I—A discussion of principles. *Journal of hydrology* **1970**, *10*, 282-290.

Nav, F.M.; Usefi, N.; Abbasnia, R. Analytical investigation of reinforced concrete frames under middle column removal scenario. *Adv. Struct. Eng.* **2017**, *21*, 1388–1401, doi:10.1177/1369433217746343.

Niu, Z.; Zhang, B.; Li, D.; Ji, D.; Liu, Y.; Feng, Y.; Zhou, T.; Zhang, Y.; Fan, Y. A mechanical reliability study of 3-dB waveguide hybrid couplers in submillimeter and terahertz bands. *Frontiers of Information Technology & Electronic Engineering* **2021**, *22*, 1104-1113.

Özkan, A.O.; Kara, S.; Salli, A.; Sakarya, M.E.; Güneş, S. Medical diagnosis of rheumatoid arthritis disease from right and left hand Ulnar artery Doppler signals using adaptive network based fuzzy inference system (ANFIS) and MUSIC method. *Advances in Engineering Software* **2010**, *41*, 1295-1301.

Paknahad, M.; Shariati, M.; Sedghi, Y.; Bazzaz, M.; Khorami, M. Shear capacity equation for channel shear connectors in steel-concrete composite beams. *Steel and Composite structures* **2018**, *28*, 483-494.

Perera, R.; Varona, F.B. Flexural and shear design of FRP plated RC structures using a genetic algorithm. *Journal of 807 structural engineering* **2009**, *135*, 1418-1429.

Phan, D.T.; Mojtabaei, S.M.; Hajirasouliha, I.; Lau, T.; Lim, J.B. Design and optimization of cold-formed steel sections in bolted moment connections considering bimoment. *Journal of Structural Engineering* **2020**, *146*, 04020153.

Put, B.M.; Trahair, N.S.; Pi, Y.-L. Bending and Torsion of Cold-Formed Channel Beams. *J. Struct. Eng.* **1999**, *125*, 540–546, doi:10.1061/(ASCE)0733-9445(1999)125:5(540).

Rhodes, J.; Schneider, F.D. *The Compressional Behaviour of Perforated Elements*; Saint Louis, Missouri, USA, 1994.

Rogers, C.; Schuster, R. Flange/web distortional buckling of cold-formed steel sections in bending. *Thin Walled Struct.* **1997**, *27*, 13–29, doi:10.1016/0263-8231(96)00017-1.

Roure, F.; Pastor, M.M.; Casafont, M.; Somalo, M.R. Stub column tests for racking design: Experimental testing, FE analysis and EC3. *Thin-Walled Struct.* **2011**, *49*, 167–184.

Safa, M.; Shariati, M.; Ibrahim, Z.; Toghroli, A.; Bin Baharom, S.; Nor, N.M.; Petkovic, D. Potential of adaptive neuro fuzzy inference system for evaluating the factors affecting steel-concrete composite beam's shear strength. *Steel Compos. Struct.* **2016**, *21*, 679–688, doi:10.12989/scs.2016.21.3.679.

Sanikhani, H.; Deo, R.C.; Yaseen, Z.M.; Eray, O.; Kisi, O. Non-tuned data intelligent model for soil temperature estimation: A new approach. *Geoderma* **2018**, *330*, 52–64.

Sedghi, Y.; Sedghi, Y.; Zandi, Y.; Shariati, M.; Ahmadi, E.; Azar, V.M.; Toghroli, A.; Safa, M.; Mohamad, E.T.; Khorami, M.; Wakil, K. Application of ANFIS technique on performance of C and L shaped angle shear connectors. *Smart Struct. Syst.* **2018**, *22*, 335–340.

Shafaei, S.; Ronagh, H.; Usefi, N. Experimental evaluation of CFS braced-truss shear wall under cyclic loading. In Proceedings of the Advances in Engineering Materials, Structures and Systems: Innovations, Mechanics and Applications, Proceedings Of The 7Th International Conference On Structural Engineering, Mechanics And Computation, September 2-4, 2019, Cape Town, South Africa, UK, 2019; pp. 192–196.

Shahgoli, A.F.; Zandi, Y.; Heirati, A.; Khorami, M.; Mehrabi, P.; Petkovic, D. Optimisation of propylene conversion response by neuro-fuzzy approach. *Int. J. Hydromechatron.* **2020**, *3*, 228–237.

Sharafi, P.; Mortazavi, M.; Usefi, N.; Kildashti, K.; Ronagh, H.; Samali, B. Lateral force resisting systems in lightweight steel frames: Recent research advances. *Thin Walled Struct.* **2018**, *130*, 231–253, doi:10.1016/j.tws.2018.04.019.

Sharafi, P.; Rashidi, M.; Samali, B.; Ronagh, H.; Mortazavi, M. Identification of Factors and Decision Analysis of the Level of Modularization in Building Construction. *J. Archit. Eng.* **2018**, *24*, 04018010, doi:10.1061/(asce)ae.1943-5568.0000313.

Shariati, M.; Faegh, S.S.; Mehrabi, P.; Bahavarnia, S.; Zandi, Y.; Masoom, D.R.; Toghroli, A.; Trung, N.T.; Salih, M.N.A. Numerical study on the structural performance of corrugated low yield point steel plate shear walls with circular openings. *Steel Compos. Struct.* **2019**, *33*, 569–581.

Shariati, M.; Mafipour, M.S.; Mehrabi, P.; Ahmadi, M.; Wakil, K.; Trung, N.T.; Toghroli, A. Prediction of concrete strength in presence of furnace slag and fly ash using Hybrid ANN-GA (Artificial Neural Network-Genetic Algorithm). *Smart Struct. Syst.* **2020**, *25*, 183–195.

Shariati, M.; Mafipour, M.S.; Mehrabi, P.; Bahadori, A.; Zandi, Y.; Salih, M.N.A.; Nguyen, H.; Dou, J.; Song, X.; Poi-Ngian, S. Application of a Hybrid Artificial Neural Network-Particle Swarm Optimization (ANN-PSO) Model in Behavior Prediction of Channel Shear Connectors Embedded in Normal and High-Strength Concrete. *Appl. Sci.* **2019**, *9*, 5534, doi:10.3390/app

Shariati, M.; Mafipour, M.S.; Mehrabi, P.; Shariati, A.; Toghroli, A.; Thoi Trung, N.; Salih, M.N.A. A novel approach to predict shear strength of tilted angle connectors using artificial intelligence techniques. *Eng. Comput.* **2020**, 1–21, doi:10.1007/s00366-019-00930-x.

Shariati, M.; Mafipour, M.S.; Mehrabi, P.; Zandi, Y.; Dehghani, D.; Bahadori, A.; Shariati, A.; Trung, N.T.; Salih, M.N.; Poi-800 Ngian, S. Application of Extreme Learning Machine (ELM) and Genetic Programming (GP) to design steel-concrete 801 composite floor systems at elevated temperatures. *Steel and Composite Structures* **2019**, *33*, 319-332. 802

Shariati, M.; Tahmasbi, F.; Mehrabi, P.; Bahadori, A.; Toghroli, A. Monotonic behavior of

C and L shaped angle shear connectors within steel-concrete composite beams: an experimental investigation. *Steel Compos Struct* **2020**, *35*, 237-247.

Shariati, M.; Trung, N.T.; Wakil, K.; Mehrabi, P.; Safa, M.; Khorami, M. Estimation of moment and rotation of steel rack connection using extreme learning machine. *Steel Compos. Struct.* **2019**, *31*, 427–435.

Shariati, M.M., M.S.; Mehrabi, P.; Bahadori, A.; Zandi, Y.; Salih, M.N.A.; Nguyen, H.; Dou, J.; Song, X.; Poi-Ngian, S. Application of a Hybrid Artificial Neural Network-Particle Swarm Optimization (ANN-PSO) Model in Behavior Prediction of Channel Shear Connectors Embedded in Normal and High-Strength Concrete. *Applied Sciences* **2019**, *9*, 55-34, doi:<https://doi.org/10.3390/app9245534>.

Shayanfar, M.A.; Javidan, M.M. Progressive Collapse-Resisting Mechanisms and Robustness of RC Frame–Shear Wall Structures. *J. Perform. Constr. Facil.* **2017**, *31*, 04017045.

Shen, Y.; Chacón, R. Effect of Uncertainty in Localized Imperfection on the Ultimate Compressive Strength of Cold-Formed Stainless Steel Hollow Sections. *Appl. Sci.* **2019**, *9*, 3827.

Standard, B. Steel static storage systems—Adjustable pallet racking systems—Principles for structural design. *BS EN* **2009**, *15512*, 15512.

Sun, L.; Li, C.; Zhang, C.; Su, Z.; Chen, C. Early monitoring of rebar corrosion evolution based on FBG sensor. *International Journal of Structural Stability and Dynamics* **2018**, *18*, 1840001.

Taheri, E.; Esgandarzadeh Fard, S.; Zandi, Y.; Samali, B. Experimental and Numerical Investigation of an Innovative Method for Strengthening Cold-Formed Steel Profiles in Bending throughout Finite Element Modeling and Application of Neural Network Based on Feature Selection Method. *Applied Sciences* **2021**, *11*, 5242.

Taheri, E.; Firouzianhaji, A.; Mehrabi, P.; Hosseini, B.V.; Samali, B. Experimental and numerical investigation of a method for strengthening cold-formed steel profiles in bending. *Applied Sciences* **2020**, *10*, 3855.

Taheri, E.; Firouzianhaji, A.; Mehrabi, P.; Vosough Hosseini, B.; Samali, B. Experimental and Numerical Investigation of a Method for Strengthening Cold-Formed Steel Profiles in Bending. *Appl. Sci.* **2020**, *10*, 3855, doi:10.3390/app

Taheri, E.; Firouzianhaji, A.; Usefi, N.; Mehrabi, P.; Ronagh, H.; Samali, B. Investigation of a Method for Strengthening Perforated Cold-Formed Steel Profiles under Compression Loads. *Appl. Sci.* **2019**, *9*, 5085, doi:10.3390/app9235085.

Talikoti, R.; Bajoria, K. New approach to improving distortional strength of intermediate length thin-walled open section columns. *Electron. J. Struct. Eng.* **2005**, *5*, 69–79.

Toghroli, A.; Mehrabi, P.; Shariati, M.; Trung, N.; Jahandari, S.; Rasekh, H. Evaluating the use of recycled concrete aggregate and pozzolanic additives in fiber-reinforced pervious concrete with industrial and recycled fibers. *Constr. Build. Mater.* **2020**, *252*, 118997.

Trouncer, A.N.; Rasmussen, K.J.R. Flexural–torsional buckling of ultra light-gauge steel storage rack uprights. *Thin-Walled Struct.* **2014**, *81*, 159–174.

Trung, N.T.; Shahgoli, A.F.; Zandi, Y.; Shariati, M.; Wakil, K.; Safa, M.; Khorami, M. Moment-rotation prediction of precast beam-to-column connections using extreme learning machine. *Struct. Eng. Mech.* **2019**, *70*, 639–647.

Usefi, N.; Ronagh, H.; Kildashti, K.; Samali, B. Macro/Micro Analysis of Cold-Formed Steel Members Using ABAQUS and OPENSEES. In *Volume of Abstracts, Proceedings of the 13th International Conference on Steel, Space and Composite Structures (SS18)*; The University of Western Australia: Perth, Australia, 2018.

Usefi, N.; Ronagh, H.; Mohammadi, M. Finite Element Analysis of Hybrid Cold-Formed Steel Shear Wall Panels. In *International Structural Engineering and Construction*, 2018; ISEC Press: Fargo, ND, USA, 2018; Volume 5.

Usefi, N.; Ronagh, H.; Sharafi, P. Numerical modelling and design of hybrid cold-formed steel wall panels. *Thin-Walled Struct.* **2020**, *157*, 107084.

Usefi, N.; Ronagh, H.R.; Mohammadi, M. Finite element analysis of hybrid cold-formed steel shear wall panels. In *Streamlining Information Transfer between Construction and Structural Engineering, Proceedings of the Fourth Australasia and South-East Asia Structural Engineering and Construction Conference*, ISEC Press, Brisbane, Australia, 3–5 December 2018.

Usefi, N.; Sharafi, P.; Ronagh, H. Numerical models for lateral behaviour analysis of cold-formed steel framed walls: State of the art, evaluation and challenges. *Thin Walled Struct.* **2019**, *138*, 252–285, doi:10.1016/j.tws.2019.02.019.

Veljkovic, M.; Johansson, B. Thin-walled steel columns with partially closed cross-section: Tests and computer simulations. *J. Constr. Steel Res.* **2008**, *64*, 816–821.

Visy, D.; Szedlák, M.; Geleji, B.B.; Ádány, S. Flexural buckling of thin-walled lipped channel columns with slotted webs: Numerical and analytical studies. *Eng. Struct.* **2019**, *197*, 109399, doi:10.1016/j.engstruct.2019.109399.

Wang, H.; Zhang, Y. Experimental and numerical investigation on cold-formed steel C-section flexural members. *J. Constr. Steel Res.* **2009**, *65*, 1225–1235, doi:10.1016/j.jcsr.2008.08.007.

Wang, L.; Young, B. Beam tests of cold-formed steel built-up sections with web perforations. *J. Constr. Steel Res.* **2015**, *115*, 18–33, doi:10.1016/j.jcsr.2015.08.001.

Wang, L.; Young, B. Behavior of cold-formed steel built-up sections with intermediate stiffeners under bending. I: Tests and numerical validation. *J. Struct. Eng.* **2015**, *142*, 04015150.

Wu, M.-J.; Huang, X.-H.; Zhu, J. Distortional buckling of a CFS channel section with and without stiffened flanges. *J. Mech. Sci. Technol.* **2019**, *33*, 2623–2632, doi:10.1007/s12206-019-0510-z.

Xiang, G.; Gao, X.; Tang, W.; Jie, X.; Huang, X. Numerical study on transition structures of oblique detonations with expansion wave from finite-length cowl. *Physics of Fluids* **2020**, *32*, 056108.

Xiang, G.; Zhang, Y.; Gao, X.; Li, H.; Huang, X. Oblique detonation waves induced by two symmetrical wedges in hydrogen-air mixtures. *Fuel* **2021**, *295*, 120615.

Xiao, G.; Song, K.; He, Y.; Wang, W.; Zhang, Y.; Dai, W. Prediction and experimental research of abrasive belt grinding residual stress for titanium alloy based on analytical method. *The International Journal of Advanced Manufacturing 769 Technology* **2021**, 1-15.

Xu, C.; Zhang, X.; Haido, J.H.; Mehrabi, P.; Shariati, A.; Mohamad, E.T.; Nguyen, H.; Wakil, K. Using genetic algorithms method for the paramount design of reinforced concrete structures. *Structural Engineering and Mechanics* **2019**, *71*, 503-513, doi:https://doi.org/10.12989/sem.2019.71.5.503.

Yadollahpour, A.; Nourozi, J.; Mirbagheri, S.A.; Simancas-Acevedo, E.; Trejo-Macotela, F.R. Designing and implementing an ANFIS based medical decision support system to predict chronic kidney disease progression. *Frontiers in physiology* **2018**, *9*, 1753.

Yang, N.; Bai, F. Damage Analysis and Evaluation of Light Steel Structures Exposed to Wind Hazards. *Appl. Sci.* **2017**, *7*, 239.

Yaseen, Z.M.; Deo, R.C.; Hilal, A.; Abd, A.M.; Bueno, L.C.; Salcedo-Sanz, S.; Nehdi, M.L. Predicting compressive strength of lightweight foamed concrete using extreme learning machine model. *Adv. Eng. Softw.* **2018**, *115*, 112–125.

Ye, J.; Hajirasouliha, I.; Becque, J.; Pilakoutas, K. Development of more efficient cold-formed steel channel sections in bending. *Thin Walled Struct.* **2016**, *101*, 1–13, doi:10.1016/j.tws.2015.12.021.

Ye, J.; Jiang, L.; Wang, X. Seismic Failure Mechanism of Reinforced Cold-Formed Steel Shear Wall System Based on Structural Vulnerability Analysis. *Appl. Sci.* **2017**, *7*, 182, doi:10.3390/app7020182.

Ye, J.; Wang, X. Piecewise Function Hysteretic Model for Cold-Formed Steel Shear Walls with Reinforced End Studs. *Appl. Sci.* **2017**, *7*, 94, doi:10.3390/app7010094.

Yu, C.; Schafer, B.C. Distortional Buckling Tests on Cold-Formed Steel Beams. *J. Struct.*

Eng. **2006**, *132*, 515–528, doi:10.1061/(asce)0733-9445(2006)132:4(515).

Yu, N.-T.; Kim, B.; Yuan, W.-B.; Li, L.-Y.; Yu, F. An analytical solution of distortional buckling resistance of cold-formed steel channel-section beams with web openings. *Thin Walled Struct.* **2019**, *135*, 446–452, doi:10.1016/j.tws.2018.11.012.

Yuan, W.-B.; Yu, N.-T.; Li, L.-Y. Distortional buckling of perforated cold-formed steel channel-section beams with circular holes in web. *Int. J. Mech. Sci.* **2017**, *126*, 255–260, doi:10.1016/j.ijmecsci.2017.04.001.

Zhang, W.; Tang, Z.; Yang, Y.; Wei, J.; Stanislav, P. Mixed-Mode Debonding Behavior between CFRP Plates and Concrete under Fatigue Loading. *Journal of Structural Engineering* **2021**, *147*, 04021055.

Zhao, J.; Sun, K.; Yu, C.; Wang, J. Tests and direct strength design on cold-formed steel channel beams with web holes. *Eng. Struct.* **2019**, *184*, 434–446, doi:10.1016/j.engstruct.2019.01.062.

Zhao, O.; Rossi, B.; Gardner, L.; Young, B. Behaviour of structural stainless steel cross-sections under combined loading—Part I: Experimental study. *Eng. Struct.* **2015**, *89*, 236–246, doi:10.1016/j.engstruct.2014.11.014.

Zhao, X.; Chen, B.; Li, Y.; Zhu, W.; Nkiegaing, F.; Shao, Y. Forced vibration analysis of Timoshenko double-beam system under compressive axial load by means of Green's functions. *Journal of Sound and Vibration* **2020**, *464*, 115001.

Zhao, X.; Ren, C.; Qin, R. An experimental investigation into perforated and non-perforated steel storage rack uprights. *Thin-Walled Struct.* **2017**, *112*, 159–172.

Zhao, X.; Wang, T.; Chen, Y.; Sivakumaran, K.S. Flexural behaviour of steel storage rack beam-to-upright connections. *J. Constr. Steel Res.* **2014**, *99*, 161–175.

Zhao, X.; Zhu, W.; Li, Y. Analytical solutions of nonlocal coupled thermoelastic forced vibrations of micro-/nano-beams by means of Green's functions. *Journal of Sound and Vibration* **2020**, *481*, 115407.

Zhou, F.; Young, B. Tests of cold-formed stainless steel tubular flexural members. *Thin Walled Struct.* **2005**, *43*, 1325–1337, doi:10.1016/j.tws.2005.06.005.